ATOMIC LASER-SPECTROSCOPY IN THE UV AND VISIBLE

D.M. Kane

A Thesis Submitted for the Degree of PhD
at the
University of St Andrews

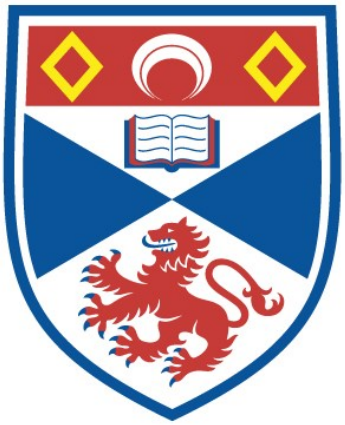

1984

ATOMIC LASER-SPECTROSCOPY IN THE UV AND VISIBLE

A thesis presented by

D M Kane, B Sc Hons

to the

University of St Andrews

in application for the degree of

Doctor of Philosophy

September 1983

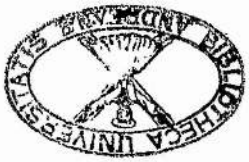

Declaration

I hereby certify that this work has been composed by me, and is a record of work done by me, and has not previously been presented for a Higher Degree.

This research was carried out in the Department of Physics, in the University of St Andrews under the supervision of Dr M H Dunn.

D M Kane

Certificate

I certify that Deborah M Kane, B Sc Hons, has spent nine terms of research work towards the Degree of Doctor of Philosophy of the University of St Andrews under my direction, that she has fulfilled the conditions of the Resolution of the University Court, 1967, No 1, and that she is qualified to submit the following thesis in application for the degree of Doctor of Philosophy.

M H Dunn

Research Supervisor

Acknowledgements

I should like to thank Dr M H Dunn for his help and support throughout the course of this work. I am indebted to Mr F Akerboom for helping to design and constructing all the discharge tubes used in my experiments. I gratefully acknowledge the assistance of Mr R McCraw and colleagues in constructing mechanical apparatus. Mr M Robertson and colleagues, in the electronics workshop, are thanked for their help with instrumentation. I thank Mrs Norma Pacholek for typing part of the manuscript and the computing service of the university for providing text editing facilities. I am grateful to the Association of Commonwealth Universities and the British Council for financial support during this work.

Finally, I thank my parents, Catherine and James Kane, for demonstrating that it is possible to provide family support even when separated by many thousands of miles. I wish to dedicate this thesis to them.

Abstract

This thesis describes the development of an intracavity frequency doubled dye laser from a commercial Spectra-Physics 380D single frequency ring dye laser, and the application of this system to a number of spectroscopic studies in discharges.

Evaluation of the stability of the laser cavity is carried out, by computer calculation, in order to optimise the optical component set used in the frequency doubled dye laser. Using an ADA (ammonium dihydrogen arsenate) crystal, 17 mW of continuous wave ultra-violet, tunable over the range 292-302 nm, has been produced. The linewidth, when the laser is stabilised, is about 500 kHz in the UV.

The CW UV output has been used to measure helium triplet (2^3S) metastable densities in a positive column discharge as a function of pressure (1-8 Torr) and current (2.5-80 mA). A maximum density of 10×10^{12} cm^{-3} is measured for a pressure of 2 Torr and current of 60mA. The measured metastable densities are used in a rate equation analysis to extract values of the rate coefficient for destruction (by collisions with electrons) of the 2^3S metastables (1.6×10^{-8} $cm^3 s^{-1}$ for p = 2 Torr).

A study of the optogalvanic signal generated when irradiating a neon positive column discharge with laser light of wavelength 588.2 nm, corresponding to the $1s_5$-$2p_2$ transition, is carried out. The signal is found to change sign as the dye laser power is increased, for some discharge conditions. Spatial studies of the optogalvanic signal in conjunction with absorption and emission studies are carried out to investigate the evolution of the population densities of levels connected to the $1s_5$ and $2p_2$ levels. A rate equation model is developed which demonstrates the importance of the

$1s_3$ population density in explaining the observed sign reversal.

A high resolution study of two transitions in the UV, in the tungsten spectrum, is presented. The even isotope splittings and the hyperfine splitting between the two strongest hyperfine components on transitions at 294.4 nm and 294.7 nm have been resolved by saturated absorption spectroscopy. From centre of gravity considerations the hyperfine splittings of the three levels involved in the two transitions have been predicted as 1630 MHz for the $^7S_3$ level, -506 MHz for the 369_2 level and 225 MHz for the 368_3 level.

A simple wavemeter using a corner-cube Michelson interferometer is described. Digital counting circuits to provide a direct reading of either the fundamental or second harmonic wavelength have been designed and constructed. Wavelength readings accurate to 1 part in 10^6 are achieved.

Publications from this Thesis

1. Laser absorption measurements of atomic metastable densities, D M Kane and M H Dunn, J.Phys.B:At.Mol.Phys. 16 (1983), 2709-2719.

2. Optogalvanic signals generated in a neon positive column discharge by resonant chopped CW radiation, D M Kane, to be published Opt. Commun.

3. Isotope and hyperfine splittings for two UV transitions in tungsten I, D M Kane and M H Dunn, presented at the Sixth National Quantum Electronics Conference, Brighton, September 1983.

4. Stability calculations for a commercial ring dye laser resonator with two foci, D M Kane and M H Dunn, submitted to Opt. Commun.

CONTENTS

Chapter 1 - Introduction

1 Introduction 1

References

Figures

Chapter 2 - Frequency Doubled Ring Dye Laser

2.1 Introduction 8

2.2 Review of Single Mode Dye Lasers 9

2.3 The Spectra-Physics 380D Ring Dye Laser 17

2.3.1 Unidirectional Device 18

2.3.2 The Birefringent Filter 20

2.3.3 Air Spaced Etalon 22

2.3.4 Thin Etalon 23

2.3.5 Scanning Dual Galvanometer Mounted Quartz Plates 24

2.3.6 Frequency Stabilisation 25

2.4 Stability Region Calculations

2.4.1 Ray Propagation by the Matrix Method 26

2.4.2 Application to the Spectra-Physics 380D Cavity 31

2.4.3 Results 34

2.5 Second Harmonic Generation 37

2.6 Experimental SHG in the 380D 42

2.7 Further Improvements 49

References

Figures

Chapter 3 - Laser Absorption Measurement of the Helium 2^3S Metastable Density

3.1 Introduction 50

3.2 Principle of the Laser Absorption Method 53

3.3 Application to Helium 2^3S Metastables 55

3.4 Rate Equation Analysis 58

3.5 Summary 65

References

Figures

Chapter 4 - Optogalvanic Spectroscopy in Neon

4.1 Introduction 67

4.2 Review of Optogalvanic Spectroscopy 68

4.3 The $1s_i$ and $2p_k$ Energy Levels in Neon 74

4.4 Experimental Studies at 588.2nm in Neon 76

4.4.1 Axial Optogalvanic/Absorption Studies 78

4.4.2 Time Variation of the Axial Optogalvanic Signals 80

4.4.3 Transverse Optogalvanic Studies 82

4.4.4 Optogalvanic/Emission Studies 84

4.4.5 Results in Other Discharges 86

4.5 Rate Equation Analysis 86

4.5.1 Analysis 87

4.5.2 Numerical Results and Discussion 90

4.6 Summary and Conclusion 95

References

Figures

Chapter 5 - Saturated Absorption Spectroscopy in Tungsten I

5.1 Introduction 99

5.2 Saturated Absorption Spectroscopy 101

5.2.1 Saturation Spectroscopy in Two Level Atoms 102

5.2.2 Crossover Resonances 108

5.3 Theory of Isotope Shifts 109

5.4 Previous Results From Isotope Shift Measurements in Tungsten I 115

5.5 Saturated Absorption Spectra 117

5.6 Summary 125

References

Figures

Appendix A - The Wavemeter

Introduction A1

The Interferometer A2

Method of Alignment A3

The Preset Count A5

The Electronics A7

References

Figures

Appendix B - Stability Region Calculations - Computer Programs B1

- Alignment Procedure for Incorporating the Frequency Doubling Elements B2

Appendix C - Computer Programs Used in Analysing Helium 2^3S Metastable Densities C1

Appendix D - Change in the Electron Density in a Discharge D1

Appendix E - Method of Solving Neon Positive Column Rate Equations E1

- Computer Programs

CHAPTER 1

INTRODUCTION

1 Introduction

Development of tunable lasers and their use in laser spectroscopy are two tightly interconnected fields of research. The need for specific wavelengths of laser light to carry out key fundamental experiments motivates many advances in tunable laser technology. Conversely, developments leading to extended wavelength ranges, decreased linewidth and increased frequency stability in tunable lasers are all rapidly exploited by spectroscopists.

Today, there is a wide variety of tunable laser sources available, such as CW and pulsed dye lasers, F-centre lasers and tunable diode lasers, etc. Also, there is a large number of nonlinear techniques (such as second harmonic generation (SHG), sum and difference frequency mixing, parametric oscillation, four wave mixing) which can be used to generate wavelengths not directly obtainable in single laser transitions. Combining the basic wavelength range obtained from tunable lasers with that obtained by nonlinear techniques, most of the wavelength spectrum from the UV (~210nm) to the near infra red (~3μm) is covered.

In the present work an intracavity frequency doubled ring dye laser is developed from a Spectra-Physics 380D laser to provide a single frequency CW source of UV radiation in the range 290-300nm. This laser is then used in a variety of spectroscopic studies including measurements of helium metastable densities in a positive column discharge, optogalvanic studies in a neon positive column discharge and sub-Doppler resolution studies in tungsten.

Laser spectroscopy first became practical with the development of reliable dye lasers. (For a recent review of dye lasers see Schafer [1]). The absorption/emission spectrum of an organic dye is shown in figure 1.1. Also shown in figure 1.1 is the excitation and stimulated emission cycle caused by optically pumping an organic dye. If a suitable resonator is provided, laser oscillation can occur over a broad band corresponding to transitions from the lowest vibrational level of the first excited singlet level to the excited vibrational levels of the ground state of the dye molecule. The general strategy for converting a laser with gain over a broad band into a source of tunable coherent radiation is shown in figure 1.2. Several frequency selective elements (prisms, gratings, birefringent tuning plates, Fabry Perot etalons) are usually required to obtain oscillation on only a single longitudinal cavity mode (where the spacing in frequency between longitudinal modes is c/2L, L being the cavity length).

The generation of CW UV radiation by frequency doubling CW dye laser radiation in a nonlinear crystal is now a standard technique. Many nonlinear materials have been used as frequency doublers [2] (potassium dihydrogen phosphate and its isomorphs, lithium formate, lithium iodate, potassium pentaborate and urea, for example). The wavelengths obtainable using these materials by angle tuning and temperature tuning are summarised in figures 1.3 and 1.4. A considerable increase in the efficiency of SHG can be obtained by placing the nonlinear crystal inside the dye laser cavity, where the available fundamental power is much higher.

Chapter 2 is concerned with the development of an intracavity frequency doubled dye laser based on the Spectra-Physics 380D. It starts with a review of single mode dye laser development, concentrating on ring dye lasers. Such systems may be designed to give optimum visible output power or to provide high intracavity powers for efficient intracavity second harmonic generation (SHG). In the latter case a very small amount of the fundamental power is coupled out of the cavity. The single mode dye lasers are described in terms of fundamental power output, linewidth (with or without stabilisation) and second harmonic power generated (where the system has been used for SHG). Following the review of single-mode dye lasers the intracavity elements of the Spectra-Physics 380D ring dye laser, which is used in the present work, are described. The types of elements are common to most ring dye lasers. As the 380D is to be used for intracavity SHG in an ADA crystal, it is necessary to consider the effect which introducing the crystal has on the stability of the cavity. Computer calculations of the stability regions for the tangential and sagittal planes of the 380D cavity are performed. It is found that to achieve optimum overlap of the stability regions when using a 15mm long ADA crystal, a 15mm long quartz rhomb should be included in the same arm of the cavity as the ADA crystal and a 1.5mm long quartz rhomb should replace the standard astigmatism compensator in the dye jet arm of the cavity. When using a 20mm long ADA crystal, a 20mm long quartz rhomb should be included in the same arm as the crystal and no astigmatism compensator should be placed in the jet arm.

The principles of SHG are outlined in Chapter 2, before the results of intracavity frequency doubling in the 380D are presented. A maximum UV power of 17mW has been measured outside the cavity (corresponding to 29mW being generated in the crystal). This was generated by 25W of intracavity fundamental power. More typically, 12mW of usable UV power was easily obtained. Experimentally, it was found that the reduction in intracavity power caused by the introduction of an astigmatism compensating rhomb (1-5mm long) in the dye jet arm far outweighed any advantage of more complete overlap of the stability regions for the tangential and sagittal planes of the cavity. Thus, the optimum set of frequency doubling optics is a 20mm long ADA crystal and a 20mm long quartz rhomb in the auxiliary waist arm of the cavity, with no astigmatism compensator in the dye jet arm. This combination gives maximum overlap of the stability regions whilst minimising the number of intracavity elements. The UV power generated is reduced from optimum by phase mismatch effects caused by absorption in the crystal. This absorption is estimated.

In Chapter 3 measurements of helium 2^3S metastable densities in a positive column discharge are presented. These are obtained using the single-mode UV output of the frequency doubled ring dye laser as the radiation source to measure the absorption on the 2^3S-5^3P transition at 294.51nm. The advantages of using laser absorption are: (i) it allows direct measurement of the absorption at line centre; (ii) the gas temperature may be calculated from the measured Doppler-width of the absorption line profile; and (iii) the geometry is simple. There are also advantages in using a UV transition rather than a visible transition: (i) the larger Doppler width implies that it is much less likely that fine structure will lead to a non-Gaussian absorption profile; and (ii) the upper level of the transition is higher in

energy and, therefore, is less populated (the population density of the lower level is only obtained in the limit of negligible upper level population density).

The improved accuracy of the measured He 2^3S densities, over those obtained by absorption measurements using broad band sources, allows a new approach to the rate equation analysis for the He 2^3S metastables. The experimental metastable densities are used in the rate equation describing the He 2^3S density to deduce values of the rate coefficients for excitation of He 2^3S by electron collisions and the destruction of He 2^3S metastables by electron collision leading to the creation of more highly excited species. It is found that the He 2^3S density at higher pressures (4-8 Torr) is larger than that predicted by the excitation and destruction processes usually assumed to affect this density. Several additional excitation processes for the 2^3S state are examined in an attempt to account for this discrepancy.

The absorption experiment in helium demonstrates the usefulness of a single-mode ring dye laser as a discharge diagnostic tool. This theme is expanded in Chapter 4 which describes optogalvanic spectroscopy on the $1s_5$-$2p_2$ transition at 588.2nm in neon. In optogalvanic spectroscopy it is the change in ionisation in a discharge caused by resonant laser irradiation that is detected (indirectly). For a transition originating on a metastable state, like the neon $1s_5$-$2p_2$ transition, this normally corresponds to a decrease in the ion density due to irradiation. In the experiments described, a reversal in the sign of the optogalvanic signal on a metastable transition as the irradiating pump power is increased is observed, for the first time. This reversal corresponds to a decrease in the ion density for small irradiating powers changing to an

increase in the ion density for higher irradiating powers. The reversal occurs only for a limited range of pressures and currents. A rate equation analysis is devised to find a mechanism which leads to such a reversal. It is found that the increasing density of the $1s_3$ metastable state caused by irradiation at 588.2nm can qualitatively explain the observed reversal. Previously it has been assumed that this level does not affect the change in ionisation caused by irradiation on the $1s_5$-$2p_i$ transitions.

The most pursued application of single mode dye lasers in laser spectroscopy has so far been high resolution studies. A number of techniques, including saturated absorption, intermodulated fluorescence, polarisation spectroscopy, intermodulated optogalvanic spectroscopy and two photon spectroscopy [3,4], resolve resonances below the Doppler width. Other techniques, using a collimated atomic beam crossed transversely with a laser beam or an accelerated ion beam co-linear with a laser beam, reduce the effective Doppler width and this is detected in laser induced fluorescence.

In many instances the precision achieved by high resolution laser spectroscopy is not as good as that achieved by radio-frequency techniques, but the two are largely complementary. This is demonstrated by the measurement of the hydrogen 1S Lamb shift by Doppler free laser spectroscopy [5,6] and the measurement of isotope shifts. These measurements can not be performed by radio-frequency methods. Often the limitation in the precision of the measured frequency separations arises from the calibration of the measured spectra using interferometers.

In Chapter 5 a saturated absorption experiment, measuring the even isotope shifts and one hyperfine splitting in WI, is described. The saturated absorption spectra on two UV transitions at 294.440nm and 294.698nm (air at 15°C, 1 atmosphere) are generated. The even isotope peaks are separated by about 100 MHz. The relative shifts between pairs of even isotopes, $\Delta(182-184)/\Delta(184-186)$, is measured as 1.14 ± 0.05 at 294.440nm and as 1.10 ± 0.05 at 294.698nm. These values are in agreement with previous measurements on visible transitions with larger splittings, performed by emission spectroscopy. Two of the hyperfine components, due to W^{183}, have also been resolved.

In Appendix A a corner-cube wavemeter which is used for measuring the wavelength of the ring dye laser output (either fundamental or second harmonic) is described. The mechanical and electronic design has been refined so that wavelength measurement is routine.

References

1. F P Schäfer ed., (Springer-Verlag, 1977), Dye Lasers. (New, updated edition to be published soon).
2. R S Adhav (June, 1983), Laser Focus, p73.
3. W Demtroder (Springer-Verlag, 1982), Laser Spectroscopy.
4. M D Levenson (Academic Press, 1982), Introduction to Nonlinear Laser Spectroscopy.
5. S A Lee, R Wallenstein and T W Hänsch (1975), Phys.Rev.Lett. 35, 1262.
6. C Wieman and T W Hänsch (1975), Phys.Rev.Lett. 36, 307

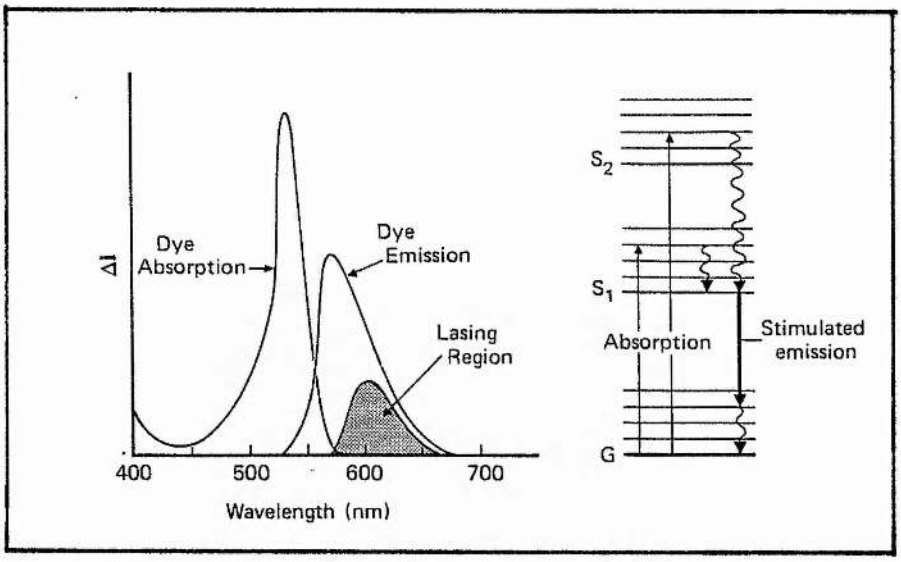

Figure 1.1 The absorption and emission spectrum of rhodamine 6G and the dynamics of stimulated emission. G-ground state; S1, S2-first and second excited singlet states. The loss of singlets through conversion to triplets is not shown.

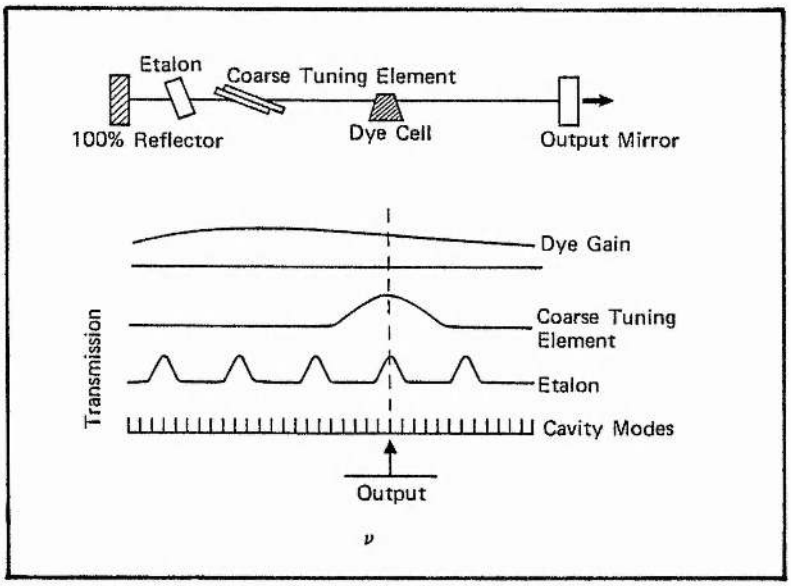

Figure 1.2 A typical single-mode tunable laser cavity and the principles of operation. The gain available over the wide lasing region of the dye is channelled into a narrow frequency interval by a series of frequency selective elements.

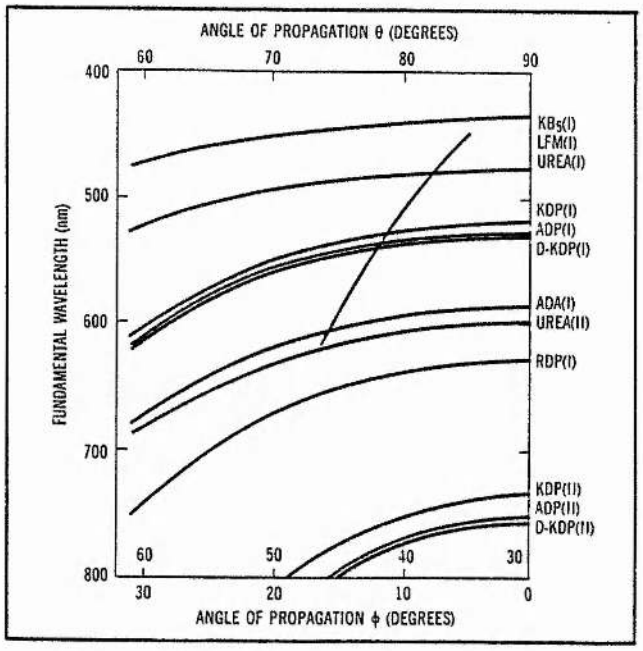

Figure 1.3 Angle-tuning curves for type I and type II phase matched SHG crystals. The 0-30° angle range is for KB$_5$; 30-60° is for LFM; 60-90° is for KDP isomorphs and urea (after Adhav [2]).

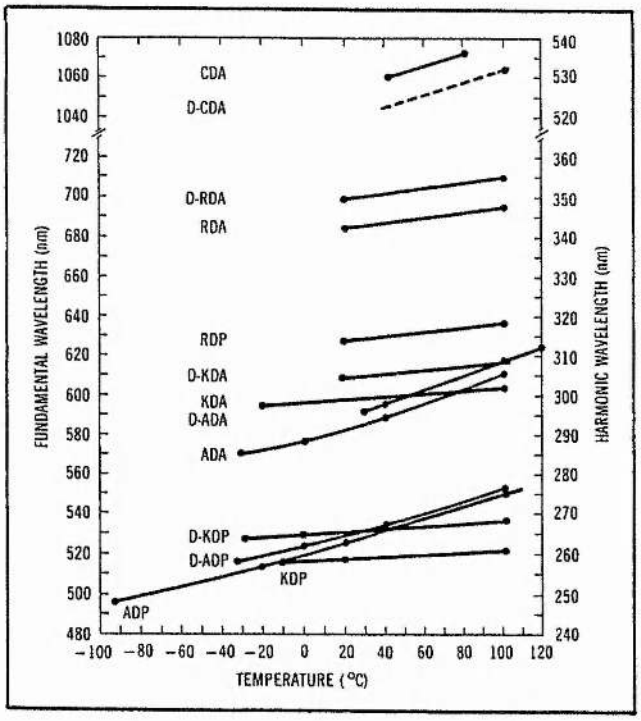

Figure 1.4 Temperature-tuning curves for 90° phase-matched type I SHG in KDP isomorphs (after Adhav [2]).

CHAPTER 2

FREQUENCY DOUBLED

RING DYE LASER

2.1 Introduction

For the spectroscopic studies proposed, a laser source providing tunable output in the UV and visible with a linewidth of less than 1 MHz is required. This suggests a single mode dye laser which may be used as a source for second harmonic generation (SHG). The development of such lasers, in particular ring dye lasers, and their use for intracavity second harmonic generation is reviewed. A Spectra-Physics 380D ring dye laser has been used in this work and the intracavity elements and stabilisation of this cavity are outlined.

The 380D ring dye laser cavity has two foci. The dye jet is located at one and the other is auxiliary. The auxiliary focus provides a point of high intracavity fundamental intensity which may be exploited for efficient SHG. The cavity, as delivered, is astigmatically compensated but the introduction of a Brewster angled ADA (ammonium dihydrogen arsenate) crystal at the auxiliary beam waist causes astigmatism in the beam. To minimise this astigmatism, compensating quartz rhombs may also be introduced. It is desirable to have these rhombs with the same optical pathlength as the nonlinear crystal so that beam walk-off is also corrected. Computer calculations modelling the 380D cavity are performed. These calculations predict optics combinations for intracavity SHG which give a cavity well compensated against astigmatism.

The principles of SHG are outlined. The effects of non-optimum focusing of the fundamental beam in the nonlinear crystal and thermally induced phase mismatch are formalised. The performance of the 380D ring dye laser for intracavity SHG in ADA is characterised experimentally. The optics combinations predicted to give a well astigmatically compensated cavity are compared in terms of SHG

efficiency. The UV power generated shows a marked decrease, at high intracavity powers, over that expected from the theory of Boyd and Kleinman [54]. This decrease is well described in terms of thermally induced phase mismatch. A maximum of 17mW of usable UV radiation is generated using 4.5W of 514.5nm Ar^+ laser power to pump the dye laser.

2.2 Review of Single Mode Dye Lasers

For the purpose of spectroscopic studies of atoms and molecules, using both Doppler-limited and sub-Doppler techniques, a single frequency scanable laser is the most versatile and useful tool. Dye lasers are excellent tunable light sources due to the broad fluorescence spectrum of the active medium. In the twenty years dye lasers have been available, considerable effort has been made to decrease the effective bandwidth, increase the output power and efficiency, and to increase the coverage of the frequency spectrum by the introduction of new dyes and the use of nonlinear techniques for frequency conversion.

The first single frequency CW dye laser reported [1] was a standing wave cavity incorporating a Brewster angle dispersing prism and an uncoated glass etalon (thickness 2mm, n=1.75) as shown in figure 2.1. A bandwidth of 35 MHz, stable to 180 MHz for several minutes, was achieved with this system and the output was demonstrated to be a single longitudinal cavity mode. It required very careful cavity adjustment to achieve this. Nevertheless, the single mode output was tuned over 3 GHz, by very small changes in the angle of M_2, before other longitudinal modes were observed to oscillate.

In a cavity similar to that in figure 2.1, but, replacing the 2mm thick etalon by one 10mm long with reflective coatings (R=63%), Schröder et al [2] obtained 10 mW of single mode output power with a free running linewidth as small as 2 MHz, using 1.5W of 514.5nm Ar^+ pump power. This corresponds to an efficiency of less than 2%. The use of a high reflectivity etalon has greatly reduced the efficiency of the dye laser (which can be as much as 35%), due to absorption and reflection losses. This small linewidth was achieved by stabilising the dye temperature to 1/100 ^{o}C, reducing the fluctuations in the pump power to less than 20mW, optimising the design of the dye cell to avoid turbulent flow in the pumped region and making the whole system mechanically rigid. With a later, similar cavity design [3] they achieved 50 mW of single mode output power for 1.7W pump power. Increasing the pump power beyond this level leads to multi-mode operation. This is a basic characteristic of all standing wave CW dye lasers using prisms (or birefringent filters) and etalons to obtain single mode operation. It is due to the effect of spatial hole burning. The standing wave inside the laser generates an inversion grating in the dye because the population inversion generated by the pump laser is depleted only at the antinodes of the standing wave of the oscillating cavity mode. The gain for a second mode in the non-depleted population inversion regions will eventually be sufficient to overcome the greater losses for that mode, as the pump power is increased. Thus additional modes with their antinodes occurring in the non-depleted population inversion regions will start to oscillate. To be able to increase the pump power and maintain single mode operation more highly selective etalons (larger reflectivities) to discriminate against adjacent modes are required. The greater round trip loss introduced, due to absorption and front surface reflection losses, further reduces the efficiency of the

laser. Thus, these systems have inherent power limitations.

Another approach to obtain single mode operation in a standing wave laser is to use an intra-cavity Michelson interferometer for frequency selection. The first such laser reported, with a single Michelson mode selector replacing the output mirror [4], is shown in figure 2.2a. A double Michelson mode selector and triple Michelson mode selector [7] are shown in figure 2.2b. Results obtained with Michelson mode selectors are summarised in Table I.

The disadvantages of these systems are the delicate path difference adjustments that must be made to achieve single mode operation and the "optical leaks" which result from imperfect destructive interference of the beams in directions A_1, A_2 and A_3 in figure 2.2b. Comparison of the single frequency efficiency reported using a triple Michelson interferometer [7] with that obtained in a prototype for the Spectra-Physics 380D ring dye laser is shown in figure 2.2c. The ring laser has a higher efficiency at low powers but at higher powers the results for the triple Michelson standing wave laser tend asymptotically to those obtained with the ring laser. The advantage of these Michelson mode selectors is that they are low loss and may be fitted on any conventional standing wave dye laser at a reasonable price. However, they are difficult to align and scan and their use is not common.

Investigations of flashlamp pumped ring dye lasers [8-9] had shown their bandwidth to be considerably less than that of equivalent linear dye lasers and their output to be more stable. This motivated work to obtain a CW ring dye laser, operation of which was first achieved by Green et al [10]. The ring dye laser cavity they used is shown in figure 2.3. In a ring laser cavity, two essentially

Table I

Results Using Michelson Mode Selectors

Michelson Mode Selector	Pump Power (W)	Dye	Max.Single Mode Output Power in Main Beam (mW)	Linewidth (MHz)
Single [4]	0.6-0.8	Rh6G	3-4	15
Single [5]	0.7	Rh6G	5	30
Double [6]	5	Rh6G	>250	± 2
Double [7]	5	Rh6G	600	30
Triple [7]	7	Rh6G	1000	30
Double [7]	4.5	Oxazine	250	

independent travelling waves are generally produced. These two waves interfere to generate a standing wave as they do in a linear cavity. By introducing a small differential loss between the two directions of propagation it is possible to produce a single travelling wave and thus minimise the spatial hole burning effects due to the standing wave. Thus, a reduction in the bandwidth is expected for a ring laser operating in a single direction. Green et al used a passive unidirectional device to obtain single travelling wave operation. Mirror 5 in figure 2.3 feeds back part of the light transmitted through M4 from the counter clockwise wave into the clockwise wave direction. With mirror 5 properly aligned the standing wave ratio was 50:1 near threshold, dropping to 10:1 at 20% above threshold. In standing wave operation, 4 or 5 modes oscillated corresponding to a bandwidth of 20 GHz. This was reduced to 3.5 GHz with a standing wave ratio of 10:1. With the addition of a single uncoated etalon with a FSR of 15 GHz, stable single frequency operation was achieved. The linewidth was less than 20 MHz with a long term stability of better than 50 MHz. But, with the use of a passive optical isolator, this system was not suited for obtaining high output powers due to the increase in coupling between the counter clockwise and clockwise directions caused by light scattered from the optical elements in the cavity.

Schröder et al [11] constructed a high power single-mode CW ring dye laser also using a passive unidirectional device but incorporating a prism and two Fabry Perot etalons (t_1 = 0.16mm, R_1 = 60%, t_2 = 2mm, R_2 = 30%) to achieve single mode operation (figure 2.4). With this system they obtained single mode output powers of 1.2W at 595nm for 7W pump power at 514nm, corresponding to a slope efficiency of 19%. Converting this laser to a standing wave cavity, by the insertion of M_2 and M_3 dotted in figure 2.4, the 2mm thick Fabry Perot etalon had

to be coated for a reflectivity of 60% in order to achieve single mode output up to a pump power of 7W. A single mode output power of 200mW was obtained with a conversion efficiency of 4% in the standing wave laser.) This laser was used for the first intracavity second harmonic generation in a ring dye laser [11]. Using an ADA crystal and the same etalons as in the standing wave laser, 55mW of single mode UV power was generated in bistable operation. Further developments of ring dye laser systems have been heavily weighted towards achieving high intracavity fundamental powers for efficient SHG.

Wagstaff and Dunn [12] developed a single mode ring dye laser with intracavity SHG in ADA from what had previously been a standing wave system [13]. This system is shown in figure 2.5. Initially the frequency selection was achieved using a three plate birefringent filter and a 2mm solid etalon. A 2mm thick quartz plate (placed in the cavity at Brewster's angle and tilted about this on a scanning galvanometer) was used for scanning the fundamental frequency of the laser. A Faraday rotator in combination with a quartz rotatory plate (section 2.3.1) was used to achieve unidirectional operation. A linewidth of $\pm$20 MHz in the UV with a longer term drift of $\pm$100 MHz maximum excursion for times up to 1 min was measured using a confocal interferometer. The angles of incidence on the mirrors of the cavity α, β and γ, were chosen to compensate for astigmatism and coma. With this cavity, 3mW of single mode UV was then generated for 4.5W, 514.5nm pump power. This could be tuned in the range 292 - 302nm and, using a simple servo control circuit, the laser frequency was locked to an external reference cavity and could be scanned continuously through 6GHz in the UV. This system was modified to include a two-plate birefringent filter, an air-spaced etalon composed of two Littrow prisms [14], and a 0.2mm solid etalon, as the frequency selective elements. The scanning range was then increased to 30 GHz

while the other characteristics remained unchanged. The unidirectional device was also modified to reduce its physical size.

Spectra-Physics Inc (Jarrett and Young) published the first details of their 380 series of ring dye lasers in 1979 [15]. They obtained as much as 0.9W of single frequency 580nm radiation from Rh6G using 4W of 514.5nm Ar^+ laser pump. Intracavity SHG in a 20mm long ADA crystal generated 20mW of single frequency UV radiation.

A computer-controlled ring dye laser with intracavity SHG was developed by Marshall et al [16]. This had single mode UV outputs of up to 10mW with a bandwidth of 100 MHz, continuously tunable over an interval of 3200 GHz in the wavelength range 285 - 311 nm (the ADA crystal could be cooled or heated to achieve this wavelength range). This system superseded an earlier one using extracavity SHG in a 25mm long ADA crystal to give up to 1mW of single frequency UV [17]. The cavity design is similar to that of the 380 series except the angles of incidence on the cavity mirrors are much smaller. It incorporates analogous intracavity elements for unidirectional operation, frequency selectivity, and scanning.

The first report of intracavity doubling of a single mode ring dye laser using a dye other than Rh6G was made by Webster et al [18]. They designed a six mirror cavity specifically for operation using coumarin 515 (coumarin 30). Using a three plate birefringent filter and an uncoated etalon (FSR = 16.2 GHz) to obtain single mode operation, they were able to generate 60μW of single mode UV at 254nm (bandwidth <50 MHz) in a cooled ADP crystal with its end faces cut at Brewster's angle. The UV was tunable in the range 250-260nm. This radiation was used to generate partial scans of the 253.7nm transition in Hg with sub-Doppler resolution.

Couillaud et al [19] reported the use of the Coherent Radiation model 699-21 CW ring dye laser [20] to produce single frequency UV powers of more than 10mW near 296nm, continuously scanable over 60 GHz, by pumping with 19W (all lines) from an Ar^+ laser. The intracavity nonlinear crystal replaces the astigmatism compensating rhomb normally fitted at the auxiliary waist and so the cavity is fully compensated if a nonlinear crystal of dimensions and refractive index similar to the standard rhomb is used. Using Rh6G in a water based Ammonyx LO solution, as much as 5.6W of single frequency fundamental radiation was generated with 24W (all lines) of Ar^+ laser pumping [20].

The Spectra-Physics 380A ring dye laser has been used by Eliel et al [21,22] to obtain single frequency UV radiation to use in transverse crossed atomic beam/laser beam spectroscopic studies. Initially they placed a 20mm right angle faced ADA crystal at the auxiliary waist and generated 0.5mW of UV with a 2 MHz linewidth and 7 GHz scanwidth, tunable from 292-305nm [21], using 2.5W 514.5nm pump power. Subsequently they obtained 25mW single frequency UV with a 2 MHz bandwidth and a scan range of 30 GHz at 4W pump power [22]. This improvement was achieved by placing a 20mm Brewster angle faced ADA crystal at the auxiliary waist and a 20mm fused silica compensating rhomb between the crystal and M2 (see figure 2.16) to compensate for beam displacement. Empirically it was found that removing the standard astigmatism compensating rhomb from between M_1 and M_2 increased the single frequency UV coupled out of the cavity from 10mW to 25mW. This method is the one adopted in the present work where a Spectra-Physics 380D ring dye laser is employed. Runge et al [23] adopted a similar scheme in a 380D ring dye laser and generated 10mW of single frequency UV for 7W of 514.5nm pump power using a 20mm

long Brewster-cut ADA crystal without any compensating rhombs.

For a number of applications involving transient conditions, a rapid scanning rate of the single frequency output is required. Modifications to the Coherent Radiation 699 ring dye laser have been outlined by Phillips [24] to give continuous scans of up to 8 GHz with repetition rates of several kilohertz, observing maximum scanning rates of 60 THz/sec. Rea and Hanson [25] modified a Spectra-Physics 380C ring dye laser to allow scan repetition rates in excess of 4 kHz and extended the single mode scanning range from 30 GHz to 75 GHz.

Active stabilisation of the Coherent Radiation 699 ring dye laser had proved difficult when UV was being generated by intracavity SHG. For this reason, Bloomfield et al [26] used a passive enhancement cavity for second harmonic generation. This was a second 699 cavity without the frequency selection elements or unidirectional device. This cavity, with a finesse of 20, was pumped with 1.4W of single frequency 589.0nm radiation from a coherent 699-21 ring dye laser. A 23mm ADA crystal with Brewster surfaces was placed in one of the beam waists; 90° phase matching was employed with the crystal temperature stable to 0.03°C. The peak single frequency UV thus generated was more than 50mW. The enhancement cavity was locked on resonance by analysing the reflected light from the input mirror [27]. Using the same passive cavity Couillaud et al [28] generated 4mW of single frequency CW UV radiation near 265nm by sum frequency-mixing. The outputs of a Rh6G ring dye laser (1.25W) and a 488nm Ar^{+} laser (3.5W) were mixed in a crystal of ADP. Subsequently, they generated single mode CW UV radiation between 243nm and 247nm by sum frequency-mixing the outputs of an ultraviolet Ar^{+} laser at 363.8nm and a red LD700 dye laser in ADP. Powers of about 100μW, but up to 1mW have been produced [29], [30]. Radiation around 243nm is required for the two photon

excitation of the hydrogen Lyman alpha line. This forms part of the continuing series of experiments measuring the 1S Lamb shift by Doppler free spectroscopic techniques.

Majewski [31] developed a single frequency UV radiation source based on intracavity SHG using an angle-tuned $LiIO_3$ crystal in a 380D ring dye laser. Using Rh6G and DCM dyes he obtained a tuning range of 293-330nm with a maximum obtainable power of 15mW and linewidth between 180 and 500 kHz. The cavity was modified by separating the thin optically active quartz plate in the unidirectional device (figure 2.8) from the Faraday rotator and moving it towards M_3 (figure 2.6). The cavity power could then be optimised by a simple tilt or displacement of the plate. Also, to minimize the coupling between the birefringent filter and the crystal a single plate birefringent filter was used and, simultaneously, the thin etalon was repositioned towards M_4 (figure 2.6). Continuous scans up to 75 GHz (fundamental) were then obtained.

2.3 The Spectra-Physics 380D Ring Dye Laser

The following is a brief discussion of the intracavity elements of the Spectra-Physics 380D ring dye laser (figure 2.6). The performance of this laser operating with different dyes is shown in figure 2.7 [32].

2.3.1 Unidirectional Device

If a ring laser is allowed to oscillate in the two possible directions, a standing wave is generated and spatial hole burning in the gain medium will occur. A far more serious limitation in single mode operation of ring dye lasers is bistable operation. The laser switches from one direction of oscillation to the other as microbubbles and velocity fluctuations in the dye jet perturb oscillation. This bistable behaviour has been predicted theoretically [33]. In ring dye lasers with a large amount of backscattering the switching is suppressed [34] but this is an unfavourable design criterion for obtaining high values of stable output power. Thus, the need to enforce unidirectional operation is crucial to obtaining useful single mode operation of a ring dye laser.

The most successful unidirectional device to date is a Faraday rotator coupled with a compensating plate [12], [15], [35] depicted in figure 2.8. The Faraday rotator consists of a length of a glass with a high Verdet constant, V, low absorption, high thermal conductivity and small rate of change of refractive index with temperature. The rotator is surrounded by suitable magnets to give a large axial magnetic field. Crystalline quartz, FR-5, and SF-2 are commonly used glasses and disc magnets, fabricated from cobalt samarium in a polymer base, give large axial magnetic fields. The expected rotation of the polarisation direction, is given by

$$\theta = VBL \quad \text{min arc} \tag{1}$$

where B is the magnetic field and L the length of the glass. As the magnetic field has opposite signs for the two directions of travel through the Faraday rotator, the linear polarisation of these

directions are rotated by $+\theta$ and $-\theta$ respectively. This is followed by a rotatory plate, usually of crystalline quartz cut with the optic axis normal to the faces of the plate. The natural rotatory power of crystalline quartz is 21° mm^{-1} at 633nm so lengths of the order 0.1 - 0.2mm are required. Both directions of oscillation have their polarisation direction rotated by $+\phi$ by this plate. If ϕ is equal to θ then one direction of oscillation has zero net rotation while the other has a net rotation of 2θ. This latter wave will suffer Fresnel losses at the Brewster-angled surfaces of the cavity (jet, birefringent filter, SHG crystal, compensating and scanning rhombs). The rotation should be sufficient that these losses are large enough to completely suppress this direction of oscillation. A small loss is sufficient ($\backsim$ 1%) because of the strong competition between the two directions of circulation.

Coherent Inc. have developed two related devices using Brewster angled Faraday glass elements [36]. One is constructed by optically contacting a piece of left-handed optically active quartz crystal to a similar piece of right- handed quartz of slightly different thickness. This rhomb is then placed in an axial magnetic field and the Faraday rotation and the optical activity rotation take place in this same composite length of crystalline quartz. This unidirectional device is useful for the blue end of the visible spectrum where there is sufficient Faraday rotation in a short length of quartz.

2.3.2 The Birefringent Filter

The overall gain for a dye laser is maximum for an output polarisation parallel to the pump polarisation [37]. Brewster angled surfaces in the cavity are placed to conserve this polarisation. In the case of the 380 series of ring dye lasers the Ar^+ pump laser polarisation is rotated by 90° to allow a horizontal ring cavity geometry. With the polarisation thus defined it is possible to use a single birefringent plate (usually crystalline quartz), with refractive index that is a function of the polarisation of the light, as a frequency selective element. The linearly polarised light incident on the plate is, for most wavelengths, transformed into elliptically polarised light which then suffers reflection losses at each subsequent Brewster surface. However, for some wavelengths, the net rotation will be zero. These wavelengths are therefore selected for oscillation.

The wavelength transmitted with zero net rotation depends, firstly, on the angle between the incident polarisation vector and the optic axis and, secondly, on the thickness of the plate. Tunability is achieved by rotating the plate in its own plane as this changes the angle between the optic axis of the quartz and the polarisation direction. Several plates with thicknesses of integer ratio and identical orientations of the optic axis will transmit the same wavelength. The linewidth of transmission is inversely proportional to the thickness of the plates so by stacking several plates(having integral thickness ratios) together, a very narrow linewidth may be obtained.

Calculation of the transmission characteristics of a set of birefringent plates is an eigen-value problem specific to the particular laser cavity design. Bloom [38] has solved this problem for a simple ring resonator using the Jones- matrix formalism. Holtom and Teschke [39] used Stokes formalism to evaluate favourable thickness ratios for a three plate birefringent filter for suppressing sidebands. The optimum design was L:2L:9L, where L is the thickness of the thinnest plate. Favourable transmission was also predicted for a filter L:2L:15L. Preuss and Gole [40] developed a simplified Jones matrix treatment where they assumed the favoured polarisation eigen-mode of the cavity oscillates, ignored the optical activity and birefringent splitting in the crystalline quartz, assumed the loss of the component perpendicular to the laser polarisation was 100% at each Brewster interface and took no account of interaction between the birefringent filter and the laser. Thus they obtained an approximate transmission function of a three plate birefringent filter (figure 2.9a) by multiplying the transmission functions of the individual birefringent plates. The results they obtained for a L:2L:15L design with L = 0.381mm, with the plates set at an angle $\theta = 32.8^{\circ}$ to the ray axis and an angle $\phi = 50^{\circ}$ between the optic axis and the cavity polarisation vector are shown in figure 2.9b. The composite curve has the FSR of the thinnest plate and the resolution of the thickest plate. The plates have to be cut so that their thicknesses are in the required integral ratio to better than one part in 10^4 to achieve the overlap of transmission maxima shown in figure 2.9b.

If continuous tuning is to be obtained the optic axes of all three plates need to be aligned accurately in the same plane. Mudare and O'Shea [41] have developed a method based on maximising the tuning range of the dye laser as the birefringent plates are added. Dunn

[42] has developed an alignment method where the plates are mounted in their holder so the optic axis is at approximately 45° to the plane of polarisation of the laser. Then a linearly polarised HeNe laser oriented to give minimum reflection from the front surface of the thinnest plate, is used, and the subsequent plates are rotated to minimise all reflected spots. Ideally there should be no reflected spots at all.

The three plate birefringent filter in the Spectra-Physics 380 is an L:4L:16L design giving a measured bandwidth of 0.03nm without the unidirectional device (UD) in the cavity and a bandwidth of less than 0.01nm with the UD in the cavity, for our system.

2.3.3 Air Spaced Etalon

The 380D has a plane parallel, electronically tunable, temperature stabilised Fabry-Perot etalon with a FSR of 75 GHz (d = 2mm). The mirrors are coated with a 20% reflective coating. The width of the air space between the mirrors is controlled by the length of a hollow cylindrical piezoelectric element. Inclusion of the air spaced etalon along with the three plate BRF and unidirectional device gives stable single mode operation.

The FSR of an air spaced etalon like that shown in figure 2.10 is

$$FSR = c/2d \tag{2}$$

The transmission coefficient is the well known Airy function

$$T = (1-R)^2/((1-R)^2 + 4R\sin^2(\omega/c)d) \tag{3}$$

assuming there is no absorption, where ω is the optical radian

frequency. It is necessary to alter the etalon spacing so that the desired frequency of oscillation corresponds to a maximum in the transmission of the etalon. This is achieved by the etalon lock loop circuitry. The etalon spacing is dithered at 2 kHz to impress a small amplitude modulation on the laser's power output. The magnitude and phase of the modulation determine which direction in frequency and how much the etalon must be driven to place the peak of its transmission closer to the lasing cavity mode.

2.3.4 Thin Etalon

The thin etalon is a thin uncoated piece of fused silica approximately 0.11mm thick. Its FSR is

$$FSR = c/2nd \tag{4}$$

is about 900 GHz. This etalon is not used for tuning and its large FSR and low finesse ensure negligible losses due to its non-optimum orientation when scanning. It is included to help prevent mode hopping during scanning.

In some laser cavities [12] the thin etalon is tilted to track the cavity mode during scanning. A thin etalon can also be used as a tuning device. The increase in the cavity length L produced by tilting the intracavity etalon by a small angle θ is approximately $d\theta^2(n-1)/2n$, so that the shift in a given cavity resonance is $-\nu[d\theta^2(n-1)/2nL]$.

2.3.5 Scanning Dual Galvanometer Mounted Quartz Plates

The effective length of the cavity is changed by counter-rotating two quartz plates (~ 4mm thick) inserted in the cavity at Brewster's angle. The advantage of using two counter-rotating plates is that the beam is not displaced.

The arrangement of the quartz plates is shown in figure 2.11. The increase in cavity length (ΔL) when the two quartz plates are inserted in the laser cavity at an angle θ is given by

$$\Delta L = 2(nt_2 - t_1)$$
$$= 2((nd/\cos\phi) - d/\cos\phi)\cos(\theta-\phi)) \qquad (5)$$

where t_2, t_1, d, θ and ϕ are shown figure 2.11. For a given θ, ϕ may be calculated using Snell's law, $n\sin\phi = \sin\theta$. The change in length was calculated for rotating the plate by $\pm 1^\circ$ about Brewster's angle. The difference, $\delta L = (\Delta L(\theta_B) - \Delta L(\theta))$ is plotted as a function of $(\theta - \theta_B)$ in figure 2.12 for several plate thicknesses.

To obtain a 30 GHz continuous frequency scan the length of the cavity must be changed by δL.

$$\delta L = (\Delta\nu/\nu)L \qquad (6)$$

For a wavelength of 590nm and a cavity length of 1.25m this requires δL to be 75μm, to achieve a 30 GHz change in frequency. From figure 2.12 this corresponds to tilting the two Brewster plates through $\pm$ 0.56° or a total angle of 1.1°.

2.3.6 Frequency Stabilisation

Changes in the optical length of the cavity, caused by temperature or refractive index changes or turbulence and bubbles in the dye jet, lead to frequency instability of the single frequency dye laser output. Thus for applications requiring a linewidth of less than 1MHz or long term frequency stability, the laser frequency must be locked to an external frequency reference [43]. A thermally stabilised, confocal Fabry-Perot (FP) interferometer is used as a scanable, stable, frequency reference for the 380D [32]. This interferometer employs very broadband optics to avoid reference FP optics changes when the dye is changed. This limits the reflectivity obtainable to (60 $\pm$ 7%) from 400 - 1000nm, yielding a finesse of about 2.3 - 3.8 for the confocal FP. The slope of the interferometer fringe at the lock point determines the optical gain which is to be maximised. With the low finesse it is necessary to decrease the FSR of the interferometer to increase the optical gain. The FSR was chosen as 500 MHz. However, with the FSR of the reference FP of the same order as the cavity mode spacing (200 MHz) a cavity mode hop could result in locking to another fringe. For this reason the transmission of a second confocal interferometer with FSR 10 GHz is used to restore the laser frequency following a mode hop.

A block diagram of the stabilisation system is shown in figure 2.13. The FP's act as frequency-to-amplitude converters. The photodiode detected signals from the slave and reference interferometers are normalised to the intensity signal by a fast analog-divider integrated circuit. The normalised reference signal is conditioned to provide an error signal which is fed back to the galvo plates and to the PZT mounted mirror M2. The PZT-mounted mirror is added to correct for high-frequency FM noise (up to 10 KHz). The

galvanometer servo loop is restricted to low frequencies (<200 Hz). Normally, the slave signal is used to servo the passband of the slave interferometer to the desired spacing determined by the reference FP. During mode hops the reference signal is replaced by the slave signal. The slave fringe is held fixed during mode hop conditions so that the slave signal can be used to return the laser to its original frequency prior to the mode hop, through feed back to the dye laser galvanometers. Scanning is stopped while the slave is in command and restarts when the original frequency is re-established.

To scan the laser the locked frequency of the reference interferometer must be scanned. The optical length of the reference FP is varied by rotating a quartz plate mounted on a galvanometer located within the interferometer cavity. The 10 GHz interferometer is scanned by moving one of the mirrors which is mounted on a PZT. The rms linewidth achieved by this stabilisation system is approximately 150 kHz.

2.4 Stability Region Calculations

2.4.1 Ray Propagation by the Matrix Method

An optical ray at one point in an optical system may be described by the vector $\begin{bmatrix} x \\ n\alpha \end{bmatrix}$, where n is the refractive index of the medium in which it is propagating, α is the angle it makes to the optic axis and x is the distance it is from the optic axis. In the paraxial approximation the ray vector at a second point is linearly related to that at any other point. This is conveniently expressed in

Table II

Ray Transfer Matrices of Elementary Optical Structures

Symbol	System	Ray Transfer Matrix
Translation D, L	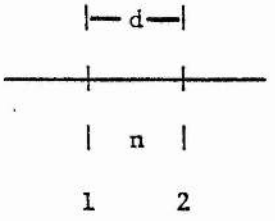	$\begin{bmatrix} 1 & d/n \\ 0 & 1 \end{bmatrix}$
Thin Lens in vacuo, normal incidence F	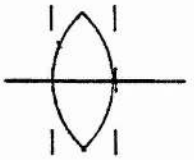	$\begin{bmatrix} 1 & 0 \\ -1/f & 1 \end{bmatrix}$
Thin Lens in vacuo, angle of incidence θ F_x(Sagittal plane)		$\begin{bmatrix} 1 & 0 \\ \frac{-1}{f/\cos\theta} & 1 \end{bmatrix}$
F_y(Tangential plane)		$\begin{bmatrix} 1 & 0 \\ \frac{-1}{f\cos\theta} & 1 \end{bmatrix}$
Transmission through a Brewster surface $\Phi^y_{nn'}$ (Tangential plane)	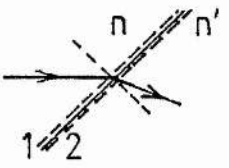	$\begin{bmatrix} n'/n & 0 \\ 0 & n/n' \end{bmatrix}$
$\Phi^x_{nn'}$ (Sagittal plane)		$\begin{bmatrix} 1 & 0 \\ 0 & 1 \end{bmatrix}$

$$\begin{bmatrix} x_2 \\ n\alpha_2 \end{bmatrix} = \begin{bmatrix} A & B \\ C & D \end{bmatrix} \begin{bmatrix} x_1 \\ n\alpha_1 \end{bmatrix} \tag{7}$$

The ray transfer matrices for many optical structures have been documented [44,45]. Those required in the present analysis are listed in Table II.

It should be noted that a lens (or mirror) used at oblique incidence θ, has different focal lengths in the sagittal (xz) and tangential (yz) planes related to the actual focal length f of the lens by $f_x = f/\cos\theta$ and $f_v = f\cos\theta$, respectively [46]. Also, the effect of transmission through a Brewster surface is confined to the tangential plane in which the ray lies.

By matrix multiplication of the individual component matrices of an optical system, a matrix describing a large series of components can be obtained. For this to be useful it is necessary to equate this matrix to something physically meaningful. This is done by finding planes; called principal planes, at distances p_1 and p_2 from the input and output planes of the system described by the final matrix $\begin{bmatrix} A & B \\ C & D \end{bmatrix}$ for which the overall transformation which is given by

$$\begin{bmatrix} 1 & p_2 \\ 0 & 1 \end{bmatrix} \begin{bmatrix} A & B \\ C & D \end{bmatrix} \begin{bmatrix} 1 & p_1 \\ 0 & 1 \end{bmatrix} = \begin{bmatrix} 1 & 0 \\ -1/f_{eff} & 1 \end{bmatrix} \tag{8}$$

is equivalent to that of a thin lens. The image formation condition, $B = 0$, can then be used to find the positions of the focal planes relative to the principal planes for this thin lens. This is depicted in figure 2.14 and the results of making the identities are given in equation (9).

First Principal Plane P_1	$p_1 = n_1(1-D)/C$
Second Principal Plane P_2	$p_2 = n_2(1-A)/C$
First Focal Plane	$f_1 = -n_1/C$
Second Focal Plane	$f_2 = -n_2/C$

(9)

Using these results, if we have a closed ring of optical components then it is possible to collapse this ring between any input and output planes and thus reduce it to a sequence of equivalent identical lenses, describing the elements of the cavity which are not of particular interest, separated by the length of the cavity unreduced which falls between the principal planes. This is depicted in figure 2.15. This infinite series of identical lenses can be treated as the equivalent empty resonator containing, a medium of refractive index n, composed of two identical spherical mirrors with radius of curvature R = $-2n/C$ separated by a distance $d = (L-p_1 - p_2)$.

By tracing a paraxial ray through a given optical system one can determine the transformation of a wavefront of a spherical wave passing through this system, $R = x/n$. For a spherical wave with a radius of curvature R_1 at the input plane of the system one finds the curvature radius R_2 at the output plane

$$R_2 = (AR_1 + B)/(CR_1 + D) \tag{10}$$

The propagation rule for a spherical wavefront, propagating in the z direction, in geometrical optics is

$$R_2 = R_1 + z \tag{11}$$

If a spherical wave passes through a lens of focal length f, it is transformed according to:

$$1/R_2 = 1/R_1 - 1/f$$

(12)

The properties of the Gaussian beams in homogeneous media are well known. A Gaussian beam of light is described by its spot size, $\omega(z)$ and the radius of curvature of the phase front, $R(z)$. As the beam propagates it expands according to

$$\omega^2 = \omega_o^2[1 + (\lambda z/\pi\omega_o^2)^2]$$

(13)

where z is measured from the beam waist. The radius of the phase-front curvature changes along the optic axis according to

$$R(z) = z[1 + (\pi\omega_o^2/\lambda z)^2]$$

(14)

A complex beam parameter q is defined by

$$1/q = 1/R + i(\lambda/\pi\omega^2)$$

(15)

In terms of this parameter the transformation laws (13) and (14) can be written as one equation

$$q_2 = q_o + z$$

(16)

where

$$q_o = i\pi\omega_o^2/\lambda$$

(17)

Redefining z as the distance between any two reference planes in the medium the relation between the input parameter q_1 and the output parameter q_2 can be written as

$$q_2 = q_1 + z$$

(18)

The lens transformation law for the complex beam parameter is then

$$1/q_2 = 1/q_1 - 1/f$$

(19)

The laws of transformation of Gaussian beams, in terms of the complex beam parameter, are formally the same as those for spherical waves in terms of their radii of curvature (11) and (12). Thus in systems reducible to a sequence of thin lenses as discussed above the analogous law to eqn (10) will also hold for the complex beam parameter

$$q_2 = (Aq_1 + B)/(Cq_1 + D) \tag{20}$$

If the $\begin{bmatrix} A & B \\ C & D \end{bmatrix}$ matrix describes one period of an infinite sequence of identical lenses separated by distance d then $q_2 = q_1 = q$ and eqn (20) becomes

$$1/q = -1/2f + i/2\sqrt{4/df - 1/f^2} \tag{21}$$

Equating (21) with (15) gives

$$(\pi\omega_o^2/\lambda_o)^2 = d(4f-d)/4 \tag{22}$$

and the waist occurs at d/2 from the thin lens. Thus from a reduction of the type depicted in figure 2.15 where d, f, p_1 and p_2 are found the spot size may be calculated using (22) and the waist position is given relative to the input and output planes, respectively, by

$$W_1 = d/2 + p_2$$

$$W_2 = d/2 + p_1 \tag{23}$$

A cavity will be stable if $\pi\omega_o^2/\lambda_o$ is real.

2.4.2 Application to the Spectra-Physics 380D Cavity

The matrix method for calculating spot sizes and waist positions has been applied to a number of standing wave and ring resonators [45, 47-50]. It is the intention here to apply this formalism to the 380D ring dye laser cavity to calculate the sagittal and tangential stability regions as a function of the mirror separations, including some or all of the following intracavity elements: (1) The dye jet of length Lj, (2) a jet region astigmatism compensator (AC) of length La, (3) an ADA crystal at the auxiliary waist of length Lc and (4) a crystal region astigmatism compensating rhomb of length Lr. The cavity containing these elements is shown in figure 2.16. The values for mirror radii of curvature and separations quoted are those given by the manufacturer. Eliel et al [22] found empirically that the arrangement, La = 0mm, Lc = 20mm, and Lr = 20mm gave enhanced second harmonic powers generated by intracavity SHG. Removing the AC reduces the intracavity loss and therefore an increase in fundamental and second harmonic power is to be expected. The present analysis demonstrates that this increase is not at the expense of cavity astigmatism compensation.

The Spectra-Physics 380D has its ring in the horizontal (xz) plane but it is redefined to be in the vertical (yz) plane for the purpose of the analysis so that the formalism outlined in 2.4.1, which corresponds to that used by Dunn and Dunn [45], may be applied.

The approach of Dunn and Dunn was to calculate the spot sizes and waist position in the jet or crystal region by collapsing the cavity about the jet or crystal respectively. The spot in the jet or crystal is elliptical because the tangential diameter is increased on entering a material of higher refractive index. For a beam of diameter d

propagating from vacuum to a medium of refractive index n, incident on the surface at Brewster's angle, the tangential beam diameter in the refractory material is $d_n = nd$. Thus if the spot size, $(\pi\omega_o^2/\lambda_o)^2$, calculated by the matrix method, is n^4 times larger in the tangential plane than in the sagittal plane, the beam in vacuum will be of circular cross section. A more direct way of obtaining the beam cross section in air is to compare the tangential and sagittal plane spot sizes obtained by reducing the cavity about the "vacuum" space adjacent to the jet or crystal. Results obtained for cavity reductions about the jet and about d_1 (defined in figure 2.16) are contrasted for the focus in the dye jet. Reductions about the crystal and d_5 are contrasted for the focus in the ADA crystal.

Suppose the cavity is reduced about the dye jet. The $\begin{bmatrix} A & B \\ C & D \end{bmatrix}$ matrix for the tangential plane of the jet region of the cavity is given by the following sequence of matrix multiplications.

$$\begin{bmatrix} A & B \\ C & D \end{bmatrix}_{Jet,yz} = \Phi_{1n_J} D_2 \Phi_{n_A 1} L_A \Phi_{1n_A} D_3 F_{2y} D_4 \Phi_{n_R 1} L_R \Phi_{1n_R} D_5 \Phi_{n_C 1} L_C \Phi_{1n_C} D_6 F_{3y} D_7 F_{1y} D_1 \Phi_{n_J 1}$$

where the matrices D_1, D_2, D_3, D_4, D_5 and D_6 refer to propagation (in vacuo) over distances d_1, d_2, d_3, d_4, d_5 and d_6 as depicted in figure 2.16. The matrices F_{1y}, F_{2y} and F_{3y} describe propagation through equivalent lenses of focal lengths $f_1\cos(\theta_1/2)$, $f_2\cos(\theta_2/2)$, $f_3\cos(\theta_3/2)$, where we have $f_1 = R_1/2$, $f_2 = R_2/2$ and $f_3 = R_3/2$. The refractive indices of the jet, jet astigmatism compensator, crystal and crystal astigmatism compensator are n_J, n_A, n_C and n_R respectively. The matrices L_J, L_A, L_C and L_R describe propagation through the jet, jet astigmatism compensator, crystal and crystal compensating rhomb with lengths of L_j, L_a, L_c and L_r respectively, and the appropriate medium refractive index. Similarly the $\begin{bmatrix} A & B \\ C & D \end{bmatrix}$ matrices for the tangential crystal region, sagittal jet region and

sagittal crystal region are given by

$$\begin{bmatrix} A & B \\ C & D \end{bmatrix}_{Xtal,yz} = \Phi_{1n_C} D_6 F_{3y} D_7 F_{1y} D_1 \Phi_{n_J 1} L_J \Phi_{1n_J} D_2 \Phi_{n_A 1} L_A \Phi_{1n_A} D_3 F_{2y} D_4 \Phi_{n_R 1} L_R \Phi_{1n_R} D_5 \Phi_{n_C 1}$$

$$\begin{bmatrix} A & B \\ C & D \end{bmatrix}_{Jet,xz} = D_2 L_A D_3 F_{2x} D_4 L_R D_5 L_C D_6 F_{3x} D_7 F_{1x} D_1$$

$$\begin{bmatrix} A & B \\ C & D \end{bmatrix}_{Xtal,xz} = D_6 F_{3x} D_7 F_{1x} D_1 L_J D_2 L_A D_3 F_{2x} D_4 L_R D_5$$

The equivalent lens focal lengths for the sagittal plane are $f_{1x} = f_1/\cos(\theta_1/2)$, $f_{2x} = f_2/\cos(\theta_2/2)$ and $f_{3x} = f_3/\cos(\theta_3/2)$.

Analogous matrix calculations have been carried out for reductions about d_1, d_5 and d_6.

A further complication of this cavity is that the mirror separations are not confocal, that is

$$d_{12} \neq f_1 + f_2$$

and (24)

$$d_{23} \neq f_3 + f_2$$

where d_{12} and d_{23} refer to figure 2.17. Thus it is not known a priori where the jet and crystal should be placed to ensure that the beam waists occur inside them. The following numerical approach is taken to achieve this. Firstly the waist positions in the empty, on axis cavity, ω_{jo} and ω_{co}, are calculated by cavity reductions of the form outlined in figure 2.17 for the jet and crystal regions respectively. The distances d_1 and d_6 are then calculated from these waist positions to give the on-axis waist at the midpoint of the jet and crystal respectively.

$$d_1 = \omega_{jo} - L_j/2$$

$$d_6 = \omega_{co} - L_c/2 \qquad (25)$$

The distances d_2 and d_5 are set by the mount positions in the cavity as $d_2 = 4.5$cm and $d_5 = 6.5$cm. Then d_3 and d_4 are calculated from the mirror separations.

$$d_3 = d_{12} - (d_2 + d_1 + L_j + L_a)$$

$$d_4 = d_{23} - (d_5 + d_6 + L_c + L_r) \qquad (26)$$

Incorporating the elements and the off-axis focal lengths changes the positions of the waists and so it is necessary to relocate the jet and crystal at the new waists. This does not change the spot size and so the treatment above is sufficient for calculating the stability regions. An iterative approach of relocating the jet and crystal at the new waist positions and repeating the calculations until there is no change in the waist positions was used. Self consistency was achieved after two iterations in practice.

2.4.3 Results

The spot sizes and the waist positions are calculated, using the expressions given in section 2.4.1, as a function of the mirror separations between $M_1 - M_2$ and $M_2 - M_3$. The distances are adjusted assuming M_1 and M_3 are the mirrors moved. A correction to the cavity length between M_1 and M_3 via M_4 is made at each step. The programs to achieve this are listed in appendix B.

The stability region boundaries for both the sagittal and tangential planes are shown in figures 2.18-2.21 for a selection of intracavity element combinations. Figure 2.18 shows that the empty cavity is poorly compensated astigmatically but with the inclusion of the 5mm standard AC between the jet and M_2, this is corrected (figure 2.19). The standard astigmatism compensator (AC) is incorporated by the manufacturer for just this purpose and thus predicting astigmatism compensation with this optics combination provides a check for the computational method. (To perform calculations of the spot size in the crystal region when there is no crystal in the cavity it is necessary to use a cavity reduction about d_{23}. The error introduced by reducing the cavity about two Brewster surfaces bounding an element of zero length is demonstrated by considering the cavity with the off-axis focal lengths replaced by on-axis focal lengths and setting the lengths of all the intracavity elements to zero. In this limit the calculations for the tangential and sagittal planes should be identical. However, for a reduction about Brewster surfaces this gives $\begin{bmatrix} A & n^2B \\ C/n^2 & D \end{bmatrix}$ for the tangential plane and $\begin{bmatrix} A & B \\ C & D \end{bmatrix}$ for the sagittal plane because the effect of propagating through the two bounding surfaces does not reduce to a unity transformation.) Figure 2.20 shows that when using a 15mm ADA crystal and a 15mm compensating rhomb the additional inclusion of a 1.5mm AC in place of the standard AC gives good overlap of the stability regions. The combination of elements which was found empirically to give good intracavity SHG efficiency [22] is seen to correspond to a well compensated cavity as well (figure 2.21). This latter combination of a 20mm ADA crystal and a 20mm quartz rhomb with no AC, is the optimum combination found as it gives good astigmatism compensation with fewer intracavity elements. Further discussion is confined to this optics set.

Contours of the tangential plane spot size in the jet calculated by cavity reductions about the jet and about d_1 are shown in figure 2.22. The spot size calculated by a reduction about the jet is almost 5 times as large as that for a reduction about d_1. The fourth root of 5 is 1.5 giving the expected n^4 dependence for the beam diameter on propagation at Brewsters angle into an ADA crystal. The contours of the spot size for the sagittal and tangential planes in the jet region, for a reduction about d_1, are given in figure 2.23. There is good agreement between the two, indicating that when overlap of the stability regions is achieved the resulting beam is non-astigmatic in vacuum. Analogous results in the crystal region for a reduction about d_5 are shown in figure 2.24. These show that the beam exiting the crystal appears to be slightly astigmatic. The spot size in the crystal is about one hundred times that in the jet. Thus the radius at the crystal waist is 3.2 times that at the jet waist. This is consistent with the values quoted for the beam radii by the manufacturer, 130μm at the dye jet and 420μm at the auxiliary waist.

The values calculated for the waist position relative to M_1 for the jet focus, for both the tangential and sagittal planes, within the stable regions, are shown in figure 2.25. Analogous results for the crystal waist measured relative to M_3 are given in figure 2.26. It is seen that the waist position for the sagittal plane is about 0.4mm longer than that for the tangential plane in the jet region and about 4mm shorter in the crystal region. But when it is considered that the waist position calculated by cavity reductions about d_6 and d_5 for the crystal region vary by 15mm the values obtained for the two planes are consistent within the uncertainty of the numerical approach.

2.5 Second Harmonic Generation

When a medium is subjected to an electric field the electrons in the material become polarised. For a weak electric field the induced polarization is linearly dependent on the field

$$\underline{P} = \varepsilon_o \chi_1 \underline{E} \tag{27}$$

where χ_1 is the linear susceptibility and ε_o is the permittivity of free space. The linear susceptibility is related to the refractive index n, of the medium by $Re\chi_1 = n^2 - 1$.

In the presence of high electric fields, in certain media the polarisation induced becomes nonlinear in the field

$$\underline{P} = \varepsilon_o(\chi_1 \cdot \underline{E} + \chi_2 \cdot \underline{E} \cdot \underline{E} + \chi_3 \cdot \underline{E} \cdot \underline{E} \cdot \underline{E} + ...) \tag{28}$$

where χ_2 is the second order nonlinear susceptibility and χ_3 is the third order nonlinear susceptibility etc. Nonlinear optical phenomena arising from the χ_2 term include second harmonic generation, three-frequency sum and difference mixing, parametric oscillation, dc rectification and the linear electro- optic effect.

To see that the χ_2 term gives rise to the generation of an electric field at twice the fundamental optical angular frequency, consider the medium to be subject to a harmonic electric field

$$E = E_o \cos(\omega t - k(\omega)z) \tag{29}$$

This wave induces in the medium a non-linear polarisation of the form

$$P_2 = \varepsilon_o \chi_2 E_o^2 \cos^2(\omega t - k(\omega)z) \tag{30}$$

This gives rise to another wave E_2, which is a solution of Maxwell's equation

$$-\nabla^2 E_2 + \mu_o \varepsilon_o (\ddot{E}_2 + \chi_1 \ddot{E}_2 + \chi_2 (\ddot{E})^2) = 0 \tag{31}$$

provided $E_2 \ll E$. A possible solution of this is a wave having twice the frequency of the fundamental wave E and with wave number $k(2\omega)$ to be determined

$$E_2 = E_{20}(z) \cos(2\omega t - k(2\omega)z + \phi_2) \tag{32}$$

where ϕ_2 is a phase factor and E_2 is in general complex. The wave number $k(2\omega)$ and the frequency 2ω are related by the usual dispersion relation

$$(k(2\omega))^2 - \varepsilon_o E_o (1+\chi_1)(2\omega)^2 = 0 \tag{33}$$

The amplitude variation of the second harmonic wave is given by

$$(\partial E_{20}/\partial z) = -i\mu_o \varepsilon_o {}^2 \chi_2 E_o^2 e^{-i\Delta kz}/k(2\omega) \tag{34}$$

where $\Delta k = (k(2\omega) - 2k(\omega))$.

The final amplitude of this second harmonic is obtained by integrating over the length of the medium (L). Assuming E_o is constant (low generation efficiency), the mean SH intensity $I_{2\omega}$ is given by

$$I_{2\omega} = \frac{\omega^2 \chi_2^2 L^2}{2n(2\omega)n(\omega)c^3\varepsilon_o} I_\omega^2 \operatorname{sinc}^2(\Delta kL/2) \tag{35}$$

where $n(\omega)$ and $n(2\omega)$ are the refractive indices at ω and 2ω and I_ω is the fundamental intensity.

The SH intensity is modulated by the sinc^2 term when $\Delta k \neq 0$. The spatial period of the modulation is called the coherence length

$$L_c = \pi/\Delta k = \lambda/4(n(2\omega) - n(\omega)) \tag{36}$$

If $(n(2\omega) - n(\omega)) \neq 0$ then the maximum SH power is generated in a single coherence length but this is usually only a few wavelengths. The largest SH powers will be obtained when $n(2\omega)$ and $n(\omega)$ are equal. The process of obtaining $n_{2\omega} = n_{\omega}$ is called phase matching. The most common method of phase-matching is to use the natural birefringence of the crystalline material to offset the effect of dispersion. In type I phase matching in negative uniaxial crystals ($n_e < n_o$), of which ADA is an example, the fundamental ray is propagated as an ordinary ray and the SH ray as an extraordinary ray. The refractive index of the extra-ordinary ray varies with the angle of its wave normal to the optic axis θ according to

$$1/n_e(\theta) = (\cos^2\theta/n_o^2 + \sin^2\theta/n_e^2)^{1/2} \tag{37}$$

Phase matching is obtained in a wave normal direction such that

$$n_e(2\omega, \theta_{PM}) = n_o(\omega) \tag{38}$$

The nonlinear susceptibility, χ_2 is a tensor and must be evaluated for each crystal symmetry and propagation direction [51]. For the crystal point group 42m, to which ADA belongs, the parameter d_{eff} resulting from the repeated summations in the tensor calculation [52] is given by

$$d_{eff} = -d_{14} \sin\theta \sin 2\phi \tag{39}$$

where θ is the angle of the wave normal to the optic axis and ϕ is the angle to the crystal x-axis. The value d_{14} can be found in standard tables [53]. Only non-centrosymmetric crystals have non-zero values for d_{eff}.

To maximise d_{eff}, ϕ should be chosen to be 45° to the x- and y-axes. The angle θ is determined by the phase matching requirement. For critical phase matching ($\theta_{PM} \neq 90°$) the phase matched wavelength is tuned by changing the angle θ_{PM}. For an angle $\theta_{PM}=90°$ (non critical or 90° phase matching) the phase match wavelength is independent of angle but it is possible to tune the phase match wavelength by changing the temperature provided

$$[(dn_o(\omega)/dT) - (dn_e(2\omega)/dT)] \neq 0 \qquad (40)$$

Temperature tuning of the phase match wavelength is desirable for intracavity SHG because the SH wavelength may be tuned without upsetting the alignment of the cavity. Non critical phase matching with temperature tuning in ADA is used in this work and further discussion is confined to it. A further advantage of 90° phase matching is that beam walk-off does not occur. Beam walk-off refers to the spatial separation of fundamental and SH radiation during propagation through the crystal which occurs when the wave normal direction is not orthogonal to the optic axis in a birefringent material.

Once phase matching is achieved eqn (35) predicts that the SH intensity should increase as L^2 where L is the length of the crystal. In practice the beam must be focused into the nonlinear crystal to increase the value of I_ω and so enhance the SHG efficiency. Equation (35) was derived assuming the fundamental beam to be uniform throughout the material, and so is inappropriate when the beam cross section changes over the length of the crystal. Boyd and Kleinman [54] have developed a theory which takes account of the focusing in the crystal and the Gaussian intensity profile of the fundamental beam. They obtain the following expression for the second harmonic

power in terms of a reduction factor $h(B,\zeta)$

$$P_{2\omega} = \frac{2\omega^2 d_{eff}^2}{n(\omega)^2 n(2\omega)\varepsilon_o c^3} P_\omega^2 Lk\, h(B,\zeta)$$

$$= Kh(B,\zeta)LP_\omega^2 \qquad (41)$$

where B is the walk-off parameter which is zero for 90° phase matching and ζ is the focusing parameter

$$\zeta = L/b \qquad (42)$$

given in terms of the confocal beam parameter $b = \omega_o^2 k$. The factor $h(0,\zeta)$ as a function of ζ is given in figure 2.27. It is seen that $h(0,\zeta)$ has a maximum value for $\zeta = 2.84$. This corresponds to a situation where the fundamental intensity integrated over the length of the crystal is maximised. When the beam is too tightly focused this integral starts to decrease because of the divergence of the beam, even though the maximum intensity achieved at the centre of the crystal is higher.

The fundamental laser beam, with a Gaussian intensity profile, is partially absorbed on passing through the crystal. The resulting heating gives rise to a temperature variation across the beam. This causes a nonuniform variation of the refractive index of the crystal and the resulting phase mismatch leads to a reduction in the generated SH power. Okada and Ieiri [55] have calculated a reduction factor h_T, defined by

$$h_T = P_{2\omega}/P_{2\omega}^o \qquad (43)$$

where $P_{2\omega}$ is the reduced second harmonic power and $P_{2\omega}^o$ is the SH power expected when there are no thermal effects. The thermal reduction factor h_T is given by

$$h_T = (8/a)^2[aSi(a)-(1-\cos a) - 3[\gamma-Ci(a)+\ln(a)]$$
$$+3(a-\sin a)/a - (a/2-\sin a)/a - (1-\cos a)/a^2]$$

where

$$Si(a) = \int_0^a \frac{\sin x}{x}\,dx$$
$$Ci(a) = \int_\infty^a \frac{\cos x}{x}\,dx$$
$$\gamma = \text{Euler's constant} = 0.57721$$

$$a = P_\omega / P_T$$

$$P_T = [2((\partial n_{o,\omega}/\partial T) - (\partial n_{e,2\omega}(90°)/\partial T)|_{T=T_{PM}})P_\omega \delta_1 L/\lambda\kappa_T]^{-1} \qquad (44)$$

T_{PM} - phase matched temperature assumed to occur at r =0

δ_1 - absorption in the crystal

κ_T - thermal conductivity of the crystal

The factor h_T as a function of a is shown in figure 2.28.

2.6 Experimental SHG in the 380D

The cavity of the 380D ring dye laser incorporating the frequency doubling crystal is depicted in figure 2.16, and design features relating to optimising the cavity stability regions have previously been discussed in section 2.4.3. Now, an evaluation of the experimental performance of the system, with regard to second harmonic power generated, conversion efficiency, beam profile, etc. is presented.

The fundamental intracavity power was measured using a UDT PIN-10-UVCAL photodiode calibrated at 588nm using a photodyne Model 66XLA optical power/energy meter. Calibrated neutral density filters (NDF's) were used to attenuate the power to a level which did not saturate the photodiode. The error in all fundamental powers is

$\pm$20%. The SH powers were measured using a UDT PIN 100-UV CAL photodiode and quartz, calibrated NDF's were used to check for saturation effects. These measurements were accurate to $\pm$1%.

With a 15mm, 90° phase matched ADA crystal and a 15mm quartz compensating rhomb in the M2-M3 arm of the cavity and no astigmatism compensator (AC) in the M1-M2 arm, a phase match wavelength curve as a function of crystal temperature shown in figure 2.29 was obtained for an intracavity fundamental power of 4W. A diagram of the intracavity mounts for the ADA crystal and quartz rhomb and their positions in the cavity along with a short description of the method of inserting these elements is given in appendix B. SH wavelengths in the range 292.5 - 301.5nm were obtained for temperatures in the range 22°C - 75°C. The rate of change of SH wavelength with temperature was 0.170nm/°C . The SH wavelength was measured using the corner cube wavemeter described in appendix A; the laser being operated single mode throughout to allow this.

The change in the phase match (PM) wavelength with intracavity power can be used to deduce the increase in crystal temperature due to absorption of the fundamental radiation in the crystal by using the relation between PM wavelength and temperature given in figure 2.29. The measured PM wavelength as a function of intracavity power for two phase match temperatures is shown in figure 2.30. The results from this are summarised in Table III.

The rate of change of PM wavelength with intracavity power $(d\lambda_{SH}/dP_\omega)$, and hence the rate of change of crystal temperature with intracavity power (dT/dP_ω), is constant to within the errors, for the two PM temperatures observed. The absorption in the crystal can be estimated from dT/dP_ω. If the fundamental power incident on the

Table III

Experimentally Determined Thermal Parameters

Phase Match Temp (°C)	$d\lambda_{SH}/dP_{\omega}$ [(nm/W)x10^{3}]	dT/dP_{ω} (°C/W)	P_T (W)	δ_1 (cm^{-1})	β ($K^{-1}x10^{5}$)
30	5.5±0.5	0.032±0.003	1.4	0.0040	7.0
40	6.0±0.2	0.035±0.001	1.4	0.0044	6.4
34.5	10.7±1.0 (both dirns) 5.5 (one dirn)	0.032±0.003	1	0.0079	5.0

crystal is P_ω then the power absorbed per unit length is $P_\omega \delta_1$, and the rise in temperature on axis is given by [8]

$$\Delta T = P_\omega \delta_1 / 2\pi\kappa_T$$

Since this can be written as

$$\Delta T / P_\omega = \delta_1 / 2\pi\kappa_T \qquad (45)$$

the absorption coefficient δ_1 can be estimated if κ_T is known. The values of $d\lambda_{SH}/dP_\omega$ are about ten times smaller than those measured by Ferguson [56].

Initially only a 15mm long Brewster cut ADA crystal was available. As discussed in section 2.4.2 a 1.5mm quartz rhomb in place of the standard AC gives an astigmatically compensated cavity when using a 15mm ADA crystal and 15mm compensating rhomb. A study of the intracavity power as a function of pump power was made, to determine if this was a favourable arrangement for intracavity SHG. The effect on the intracavity power, caused by other optics changes, was also studied. The measured intracavity power as a function of pump power is shown in figure 2.31. The dye laser has the birefringent filter and dual galvo-plates in the cavity when operated multimode. The unidirectional device and air spaced etalon are also included to obtain single mode operation. Comparing curves (a) and (b) made with the 9.4% transmitting output coupler (TOC) there is negligible decrease in intracavity power on replacing M3 with the high UV transmitting equivalent (b). Curve (c) shows the intracavity power when operating single mode with the 9.4% TOC. With the high reflecting output coupler (M4, T = 0.14%) the intracavity power with the ADA crystal and crystal compensating rhomb inserted is shown in curve (d) for the case of no AC and in curve (e) for an AC of length 5mm, 2mm, 1.5mm, 1mm (no difference was observed for the different lengths). The intracavity power is reduced by 20% by the inclusion of

a compensating rhomb in the jet arm of the cavity. Curves (f) and (g) are the analogs of (d) and (e) respectively, for single mode operation. A 10% reduction in intracavity power with the inclusion of an AC is observed in single mode operation. Variations in the intracavity power as a function of pump power occurred for a given optics combination from day to day and the curves plotted correspond to the best performance for each combination.

The inclusion of the AC in some cases increases the overlap of the tangential and sagittal plane stability regions of the cavity. But the reduction in the intracavity power caused by the inclusion of the AC is likely to have a more deleterious effect on the SH efficiency. Thus operation without an AC is best.

The second harmonic power coupled out of the cavity measured as a function of intracavity, multimode, fundamental power using a 15mm long ADA crystal and 15mm long quartz compensating rhomb and various astigmatism compensators in the M1-M2 arm are shown in figure 2.32. The maximum power obtained was 17mW. Comparable powers are achieved in single mode operation. Fitting a line of gradient 2 to the SH powers generated for low fundamental powers predicts values of $Kh(0,\zeta)L$ in equation (41) between $(8.0 - 14.1) \times 10^{-5}\ W^{-1}$. Account has been taken of the Fresnel losses on exiting the crystal ($R = [(n^2-1)/(n^2+1)]^2 = 14.8\%$ for $n = 1.5$), the reflection losses at the mirror ($T = 82\%$) and the Fresnel loss at the fundamental blocking filter ($R = 15\%$). The focusing in the 380D cavity is not optimum for crystal lengths of 15mm and 20mm, as tabulated in table IV.

Table IV

Focusing Parameter ζ and Reduction Factor $h(0,\zeta)$

L/mm	$\zeta = L/b$	$h(0,\zeta)$
15	0.51	0.54
20	0.68	0.60
84	2.84	1.068

The calculated value of $Kh(0,\zeta_{opt}) = Kh(0,2.84)$ for ADA is $2.4 \times 10^{-4} W^{-1}$ [56]. The expected values, taking account of the non-optimum focusing, of $Kh(0,\zeta)L$ are $1.3 \times 10^{-4} W^{-1}$ for a 15mm crystal and $1.9 \times 10^{-4} W^{-1}$ for a 20mm crystal. Thus the expected value occurs in the range of $Kh(0,\zeta)L$ observed experimentally, for a 15mm long crystal. The value of $Kh(0,2.84)$ estimated from the largest experimental value of $Kh(0,0.51)$ is $2.8 \times 10^{-4} W^{-1}$ and is in good agreement with the value of $3 \times 10^{-4} W^{-1}$ observed in other experiments [56].

Optimum focusing occurs for a crystal of length 84mm but such a crystal will not give an improved performance because of increased absorption and astigmatism. It is also impractically large. In fact no improvement in the second harmonic powers achieved was observed for a crystal of length 20mm and this is because of thermal effects.

The SH powers obtained for a given intracavity fundamental power were similar with or without an astigmatism compensator in the jet arm of the cavity. The only difference is that with an AC in the cavity a higher pump power is required to achieve the intracavity fundamental power. Thus improved astigmatism compensation,ie the use of a 1.5mm AC in this case, leads to no measurable improvement in the SH power

generated.

A single set of SH power measurements obtained for operation of the dye laser on many longitudinal modes, is given in figure 2.33. The ratio of the SH power obtained to that calculated using equation (41) and the value of $Kh(0,\zeta)L$ which fits the data, is a measure of the reduction in the SH power due to non uniform heating in the crystal through absorption of the fundamental radiation. Figure 2.34 shows this reduction factor, h_T as a function of intracavity fundamental power for the data in figure 2.33. The dashed line is the function h_T according to the theory of Okada and Ieiri [55] for a value of P_T = 1W. Similar results for a single mode fundamental laser beam are given in figures 2.35 and 2.36 where the dashed curve is a theoretical fit for $P_T = (1.4 \pm 0.2)$W in the latter. However, the fit to the theory is less convincing with many points not falling on the line. This is believed to be due to the increased difficulty in obtaining the optimum SH power in the single mode case where tuning the cavity often changes the fundamental power. Using P_T obtained, it is then possible to find β, given by

$$\beta = [(\partial n_{o,\omega}/\partial T) - (\partial n_{e,2\omega}(90^\circ)/\partial T)] = \lambda \kappa_T / 2P_T \delta_1 L \qquad (46)$$

for λ = 590nm, assuming κ_T = 0.02W cm^{-1} K^{-1}, the value for ADP. The values obtained are included in Table III.

The SH powers generated for the multimode and single mode cases above are approximately the same for a given fundamental power. This is contrary to theoretical predictions [57]. Assuming the time output of a multimode laser is noiselike the SHG process is expected to gain more from the peaks of this noiselike wave than it loses in the troughs because of the P_ω^2 dependence. The ratio of $P_{mm}(2\omega)$ to $P_{sm}(2\omega)$ is approximately

$$P_{mm}(2\omega)/P_{sm}(2\omega) = 2 - 1/N$$

where N is the number of modes. Thus an enhancement factor of 2 is expected for a large number of modes. But this assumes perfect phase matching for all combinations of fundamental modes and as the laser linewidth in the multimode case is about 0.03nm this condition will not be met (a 0.2 °C temperature difference is required to achieve phase match for two wavelengths differing by this amount). Thus some of the fundamental power will not produce any SHG. Also it is possible that the lasing modes switch on and off rather than increasing and decreasing in intensity, in which case no enhancement for multimode operation would be expected.

The bandwidth over which SHG occurred for a set crystal temperature was measured by scanning the single frequency laser fundamental as (50 $\pm$ 10)GHZ in the UV. This corresponds to a 0.03nm bandwidth for the fundamental.

The beam profile of the fundamental and UV beams exiting from mirror M_3 were studied by scanning the beam across a 600μm pinhole in front of a photodiode. A smaller pinhole was not employed since reduction in the pinhole size only led to the resolution of interference effects between the beams from the two surfaces of the scanning mirror. The results of this are shown in figure 2.37. The second harmonic beam diameter at 1/e of its maximum value is 0.59 times the 1/e diameter of the fundamental beam. This compares with the expected ratio of 0.71 comparing a square of a Gaussian with a Gaussian. This suggests that the second harmonic beam does not have a square of a Gaussian intensity profile and this is most likely due to a temperature gradient across the crystal caused by the design of the crystal oven and temperature controlling electronics.

2.7 Further Improvements

As indicated in the latter part of section 2.6 there is a temperature gradient across the crystal. There may also be a lengthwise temperature gradient resulting from the open ended oven used to avoid Fresnel losses at sealing windows. The metal cylinder on which the heater wire is wound was deliberately made longer than the crystal in an attempt to isolate the crystal faces from the cool air in the cavity but this may need to be increased further still. An oven of the type used by Eliel et al [22] consisting of 2 concentric ovens which are independently temperature stabilised may lead to improved temperature uniformity. A temperature difference of 1.5 °C is maintained between the inner and outer oven.

When operating the laser single frequency a 10% modulation in the laser intensity, as the birefringent filter is rotated, is introduced due to an interaction involving the residual non-uniform, birefringence in the thin optically active quartz plate of the unidirectional device, which is stressed by imperfect mounting. Majewski [31] overcame this problem by separating the thin quartz plate from the Faraday rotator, and mounting it on an adjustable stage towards mirror M3. Tilting or displacing the plate was then all that was needed to obtain maximum power at a given frequency. He also found that using a single plate BRF and repositioning the thin etalon towards mirror M_4 reduced the coupling between the BRF and the crystal. Unfortunately in practice the laser would not tune in single FSR's of the air spaced etalon with a single plate BRF in our case. In fact on rotating the BRF the laser frequency changed in steps of 4 or 5 air spaced etalon FSR's. This meant substantial wavelength ranges could not be obtained. However, the separation of the two parts of the unidirectional device should lead to an improvement.

References

1. M Hercher and H A Pike (1971), Opt.Commun. 3, 346.
2. H W Schröder, H Welling and B Wellegehausen (1973), Appl.Phys. 1, 343.
3. H W Schröder, H Dux and H Welling (1975), Appl.Phys. 7, 21.
4. S Liberman and J Pinard (1974), Appl.Phys.Letts. 24, 142.
5. G Marowsky and F K Tittel (1974), Appl.Phys. 5, 181.
6. M Pinard, C G Aminoff and F Laloë (1978), Appl.Phys. 15, 371.
7. M Pinard, M Leduc, G Trenec, C G Aminoff and F Laloë (1979), Appl.Phys. 19, 399.
8. F P Schäfer and H Muller (1971), Opt. Commun. 2, 407.
9. G Marowsky, L Ringwelske and F P Schäfer (1972), Z.Naturforschung 27A, 711.
10. J M Green, J P Hohimer and F K Tittel (1973), Opt.Commun. 7,349.
11. H W Schröder, L Stein, D Frölich, B Fugger and H Welling (1977), Appl.Phys 14, 377.
12. C E Wagstaff and M H Dunn (1979), J.Phys.D:Appl.Phys. 12,355.
13. A I Ferguson and M H Dunn (1977), Opt.Commun. 23, 177.
14. Coherent Inc, private communication.
15. S M Jarrett and J F Young (1979), Opt.Lett. 4, 176.
16. C M Marshall, R E Stickel, F B Dunning and F K Tittel (1980), Appl.Opt 19, 1980.
17. C R Pollock, J Kasper, G K Ernst, W E Ernst, S Blit and F K Tittel (1979), Appl.Opt. 18, 1907.
18. C R Webster, L Wöste and R N Zare (1980), Opt.Commun. 35, 435.
19. B Couillaud, L A Bloomfield, J E Lawler, A Siegel and T W Hänsch (1980), Opt.Commun. 35, 359.
20. T F Johnston, R H Brady and W Proffitt (1982), Appl.Opt. 21,2307.
21. E R Eliel, W Hogervorst, K A H van Leeuwen and B H Post (1981), Opt.Commun. 36, 366.
22. E R Eliel, W Hogervorst, K A H van Leeuwen and B H Post (1981), Opt.Commun. 39, 41.

23. S Runge, A Pesnelle, M Perdrix, D Sevin, N Wolfer and G Watel (1982), Opt.Commun. 42, 45.

24. W D Phillips (1981), Appl.Opt. 20, 3826.

25. E C Rea Jr and R K Hanson (1983), Appl.Opt. 22,518.

26. L A Bloomfield, H Gerhardt, T W Hänsch and S C Rand (1982), Opt. Commun. 42, 247.

27. T W Hänsch and B Couillaud (1980), Opt.Commun. 35, 441.

28. B Couillaud, Ph Dabkiewicz, L A Bloomfield and T W Hänsch (1982), Opt.Lett. 7, 265.

29. L A Bloomfield, B Couillaud, E A Hildum and T W Hänsch (1983), Opt.Commun. 45, 87.

30. B Couillaud, L A Bloomfield and T W Hänsch (1983), Opt.Lett. 8, 259.

31. W A Majewski (1983), Opt.Commun. 45, 201.

32. W G Divens and S M Jarrett (1982), Rev.Sci.Instrum. 53, 1363.

33. G Haag, M Munz and G Marowsky (1981), IEEE J.Quant.Electron. QE-17, 349.

34. R Roy and L Mandel (1980), Opt.Commun. 35, 247.

35. S M Jarrett and T F Young (1978, June), Laser Focus, p16.

36. T F Johnston and W Proffitt (1980), IEEE J.Quant.Electron. QE-16, 483.

37. A E Siegman, D W Phillion and D J Kuizenga (1972), Appl.Phys.Lett. 21, 345.

38. A L Bloom (1974), J.Opt.Soc.Am. 64, 447.

39. G Holtom and O Teschke (1974), IEEE J.Quant.Electron. QE-10, 577.

40. D R Preuss and J L Gole (1980), Appl.Opt. 19, 702.

41. S M Mudare and D C O'Shea (1983), Appl.Opt. 22,640.

42. M H Dunn, private communication.

43. R L Barger, M S Sorem and J L Hall (1973), Appl.Phys.Lett. 22,573.

44. H Kogelnik and T Li (1966), Appl.Opt. 5, 1550.

45. C E Dunn and M H Dunn (1981), Optica Acta 28, 1413.

46. F A Jenkins and H E White (McGraw Hill, 1957), Fundamentals of Optics, p95.

47. C E Wagstaff, M H Dunn, A I Ferguson and S J Bastow (1978), Opt. Commun. 25, 379.

48. D C Hanna (1969), IEEE J.Quant.Electron. QE-5, 483.

49. K K Li (1982), Appl.Opt 21, 967.

50. H P Kortz, R Ifflander and H Weber (1981), Appl.Opt. 20, 4124.

51. A Yariv (Wiley and Sons, 1975), Quantum Electronics, p408.

52. C Flytzanis (Academic Press, 1975), Nonlinear Optics Part A. Ed. H Rabin and C L Tang.

53. S Singh (The Chemical Rubber Co., 1971), Handbook of Lasers, p497. Ed. R J Pressley.

54. G D Boyd and D A Kleinman (1968), J.Appl.Phys 39,3597.

55. M Okada and S Ieiri (1971), IEEE J.Quant.Electron. QE-7, 469.

56. A I Ferguson (1977), Thesis (St Andrews). Chapters 2 and 5.

57. F Zernike and J E Midwinter (Wiley International, 1973), Applied Nonlinear Optics, p108.

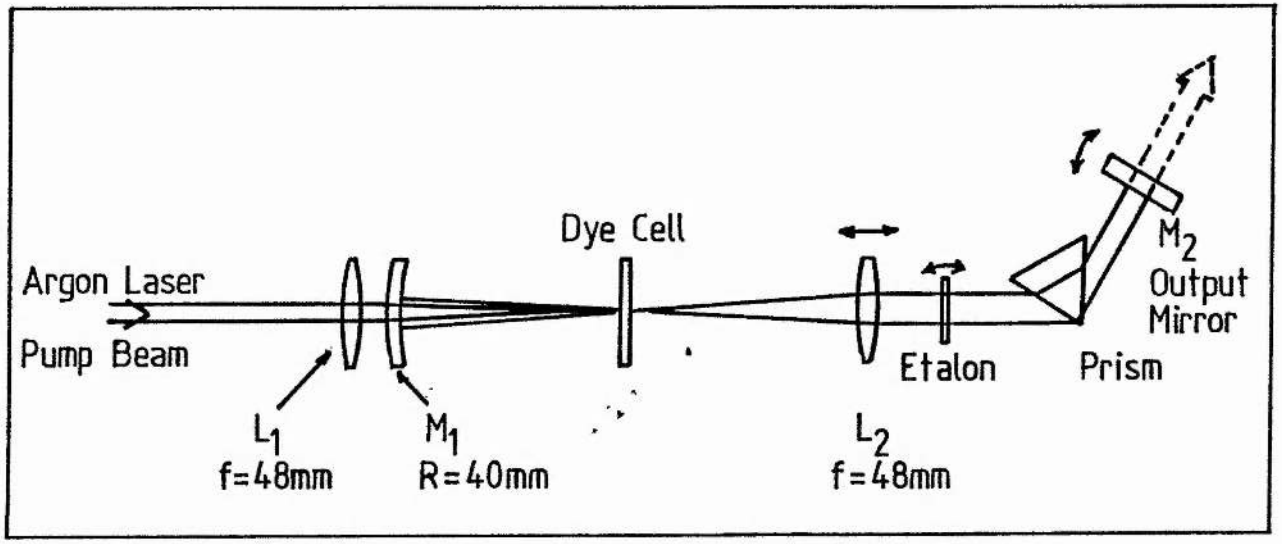

Figure 2.1 First reported single mode standing wave dye laser (after Hercher and Pike [1]).

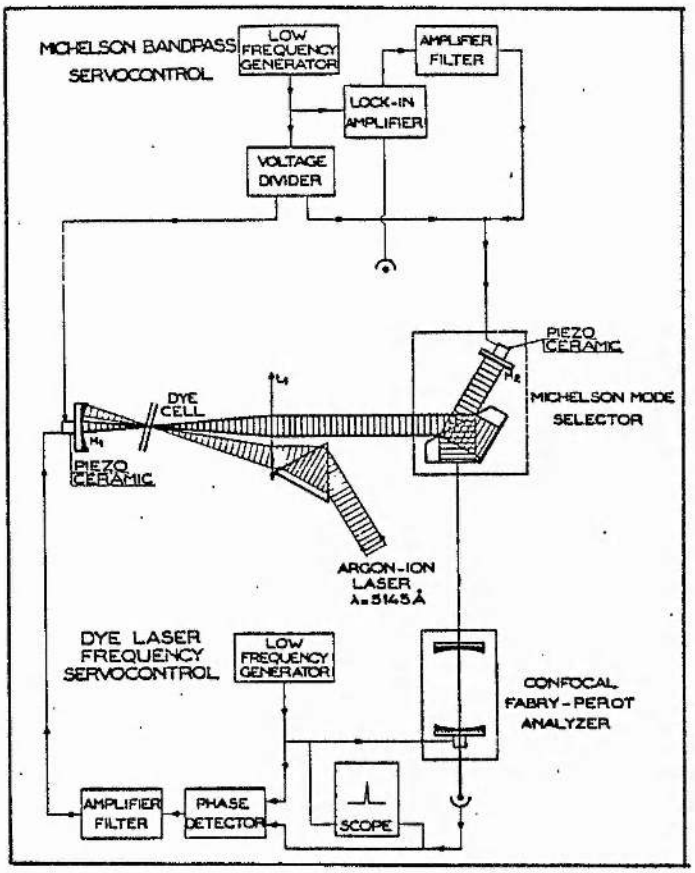

Figure 2.2a Schematic diagram of a single mode dye laser using a single Michelson mode selector (after Liberman and Pinard [4]).

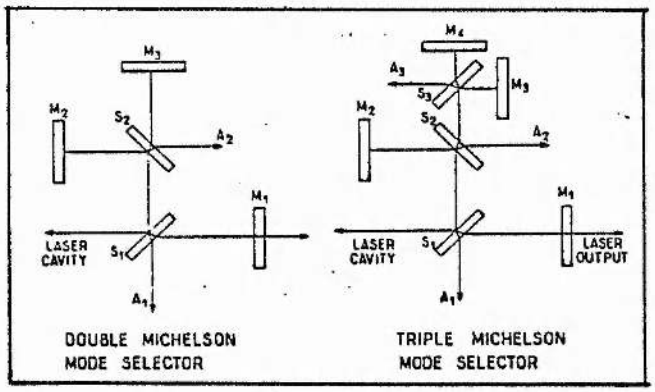

Figure 2.2b Double Michelson and Triple Michelson mode selectors (after Pinard et al [7]).

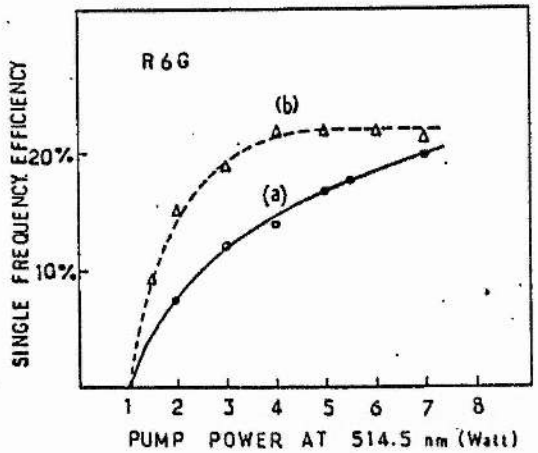

Figure 2.2c Comparison of efficiency achieved with a triple Michelson standing wave dye laser (a) and a Spectra-Physics 380 ring dye laser (b) (after Pinard et al [7]).

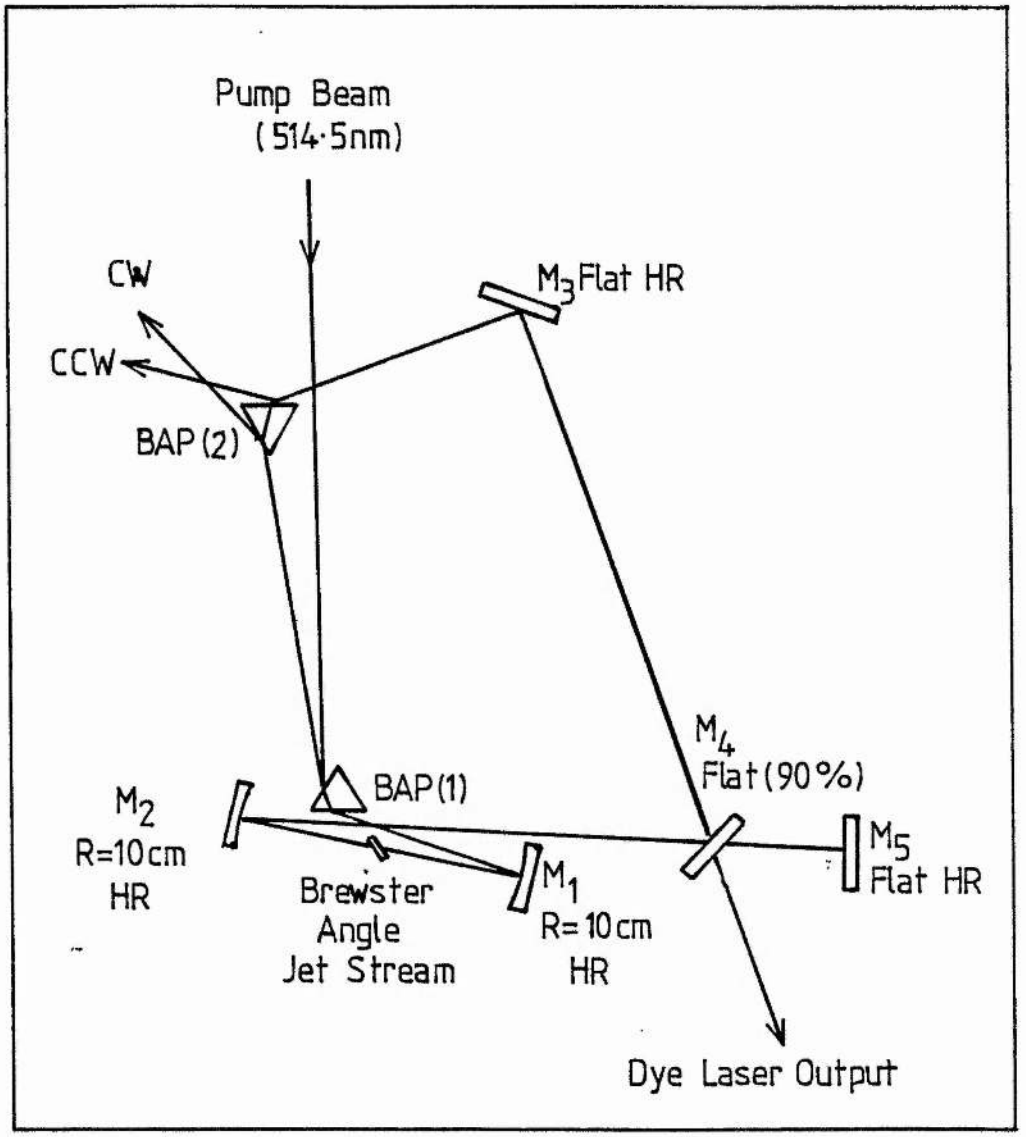

Figure 2.3 Travelling wave CW ring dye laser using a passive unidirectional device (after Green et al [10]) BAP-Brewster angled prism, HR-high reflector.

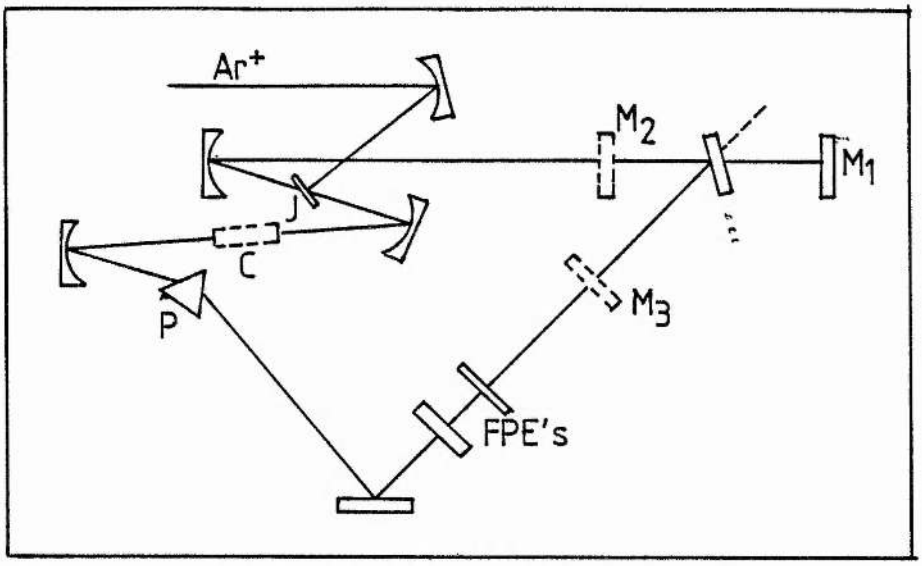

Figure 2.4 Ring dye laser used for intracavity SHG in ADA (after Schroder et al [11]) C-ADA crystal, P-prism, FPE-Fabry Perot etalon, M-mirror

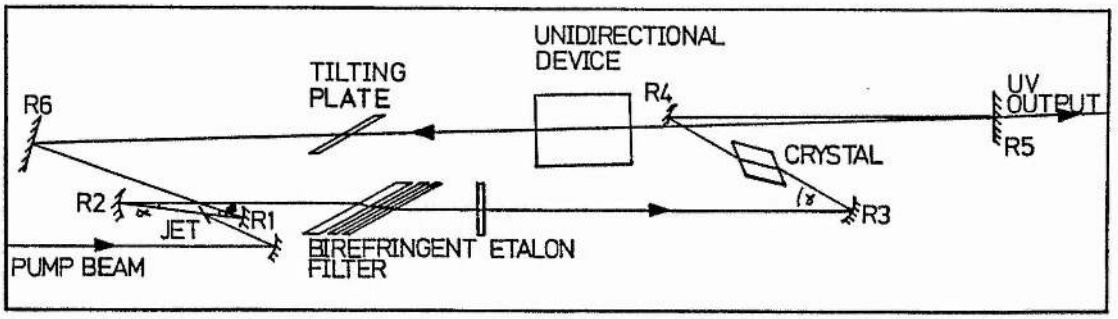

Figure 2.5 St.Andrews single mode intracavity frequency doubled ring dye laser (after Wagstaff and Dunn [12]).

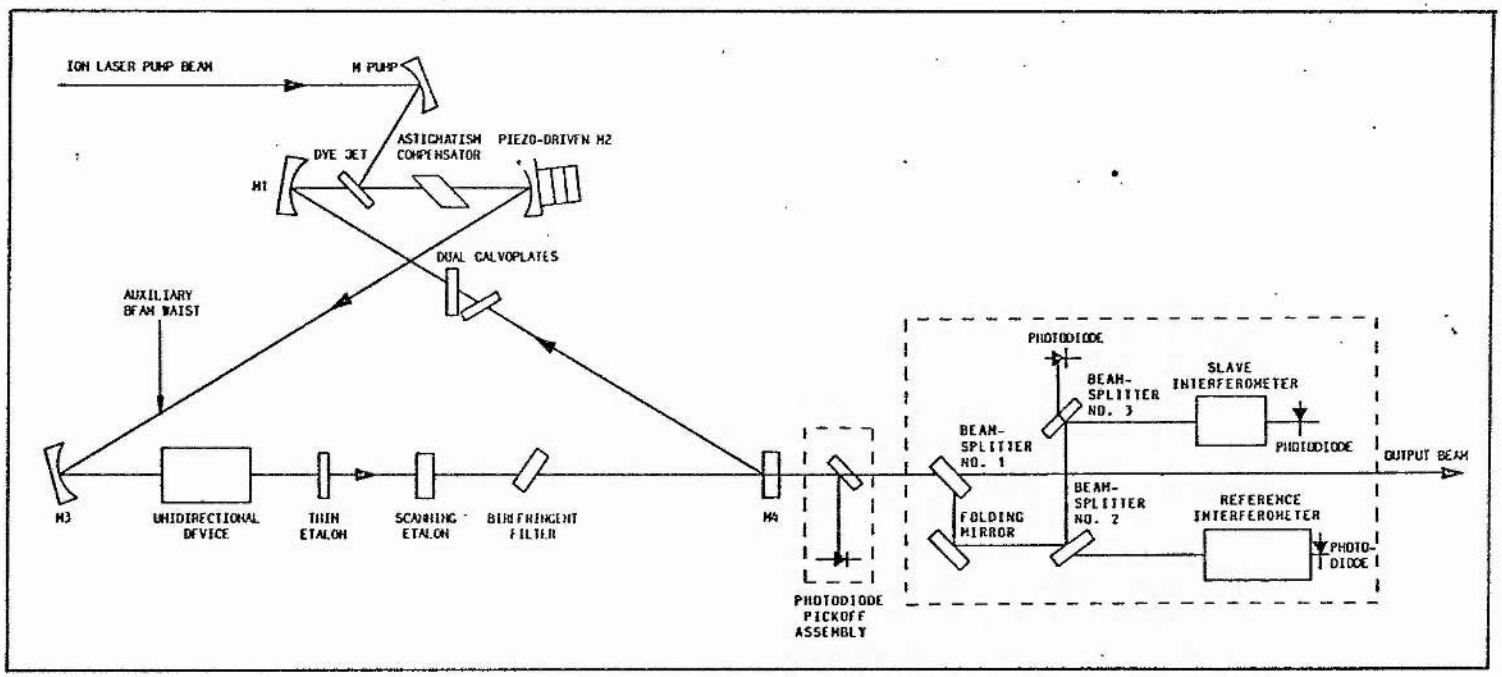

Figure 2.6 Spectra-Physics 380D ring dye laser cavity and reference interferometer cavity (from the manual).

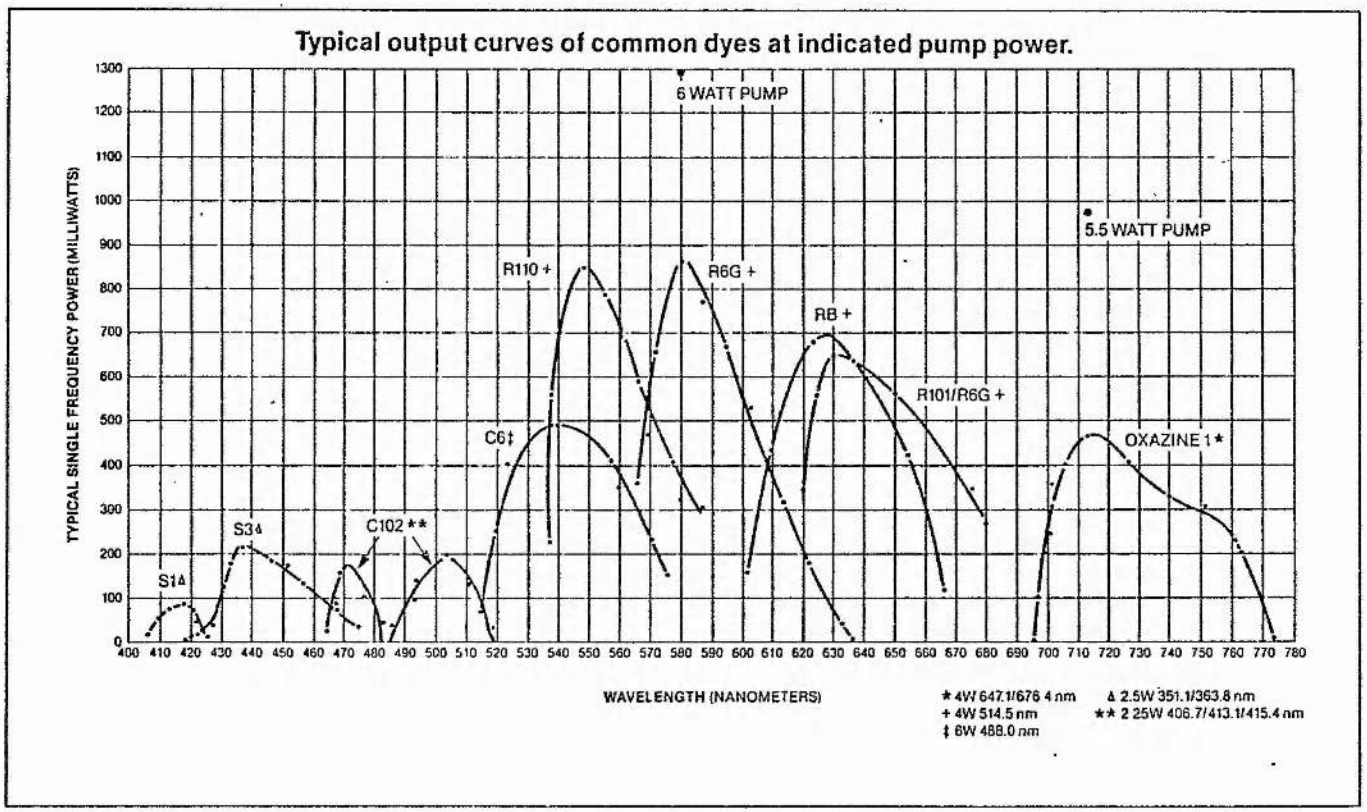

Figure 2.7 Spectra-Physics 380D ring dye laser performance using different dyes (from the manual).

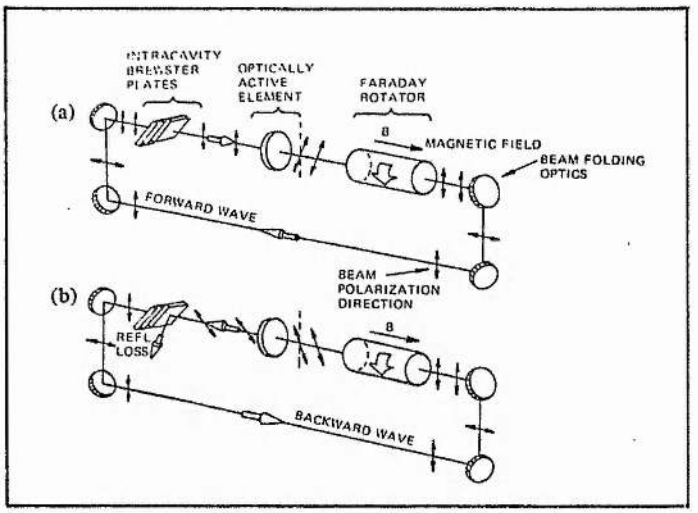

Figure 2.8 Unidirectional device comprised of a Faraday rotator and an optically active element. The backward wave is suppressed. (After Johnston et al [20]).

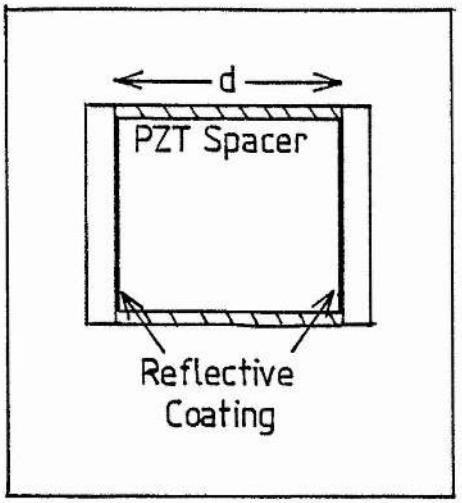

Figure 2.10 Air spaced etalon.

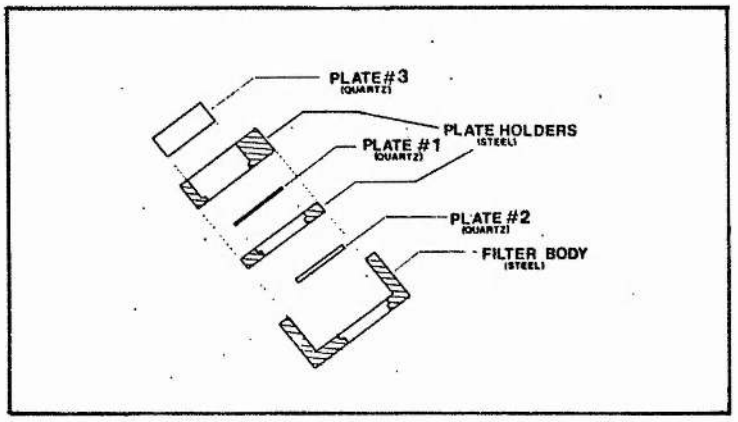

Figure 2.9a Three plate birefringent filter (after Preuss and Gole [40]).

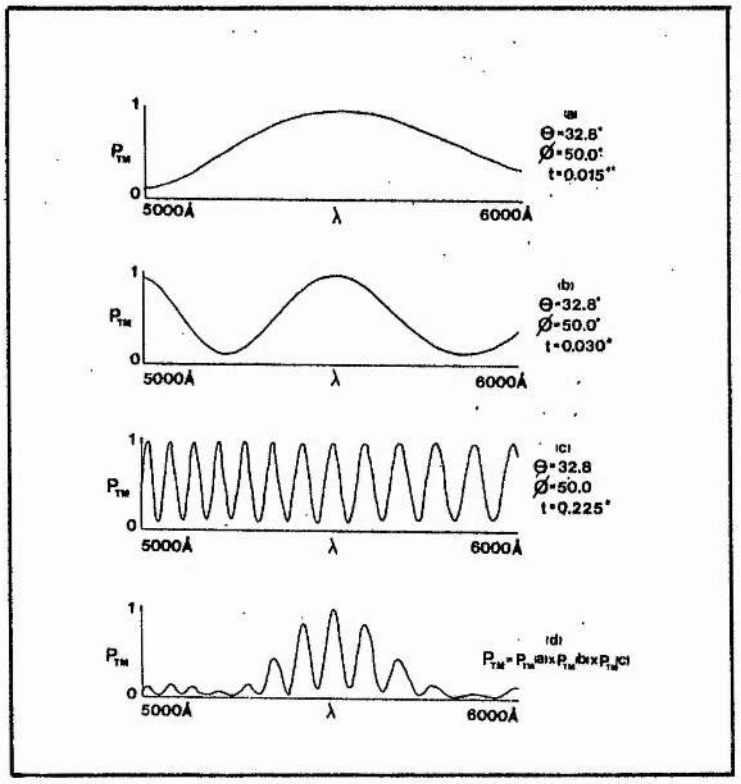

Figure 2.9b Approximate transmission function of the three plate birefringent filter (after Preuss and Gole [40]).

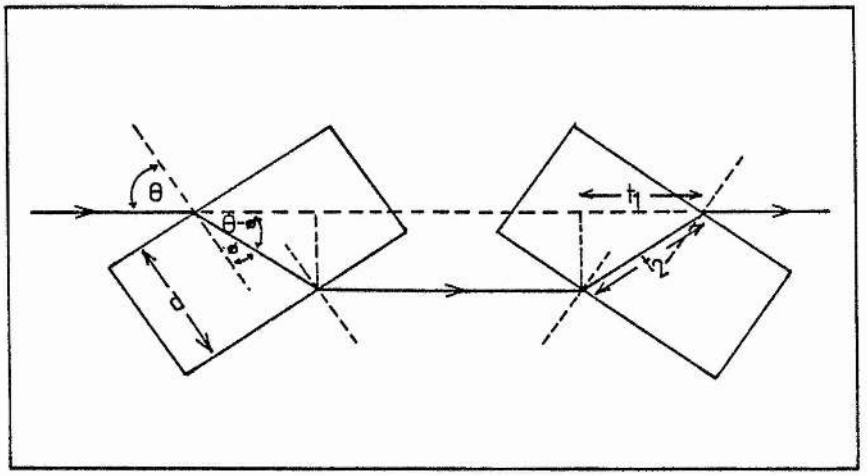

Figure 2.11 Dual quartz plates which are counter rotated to increase the optical path length in the 380D cavity.

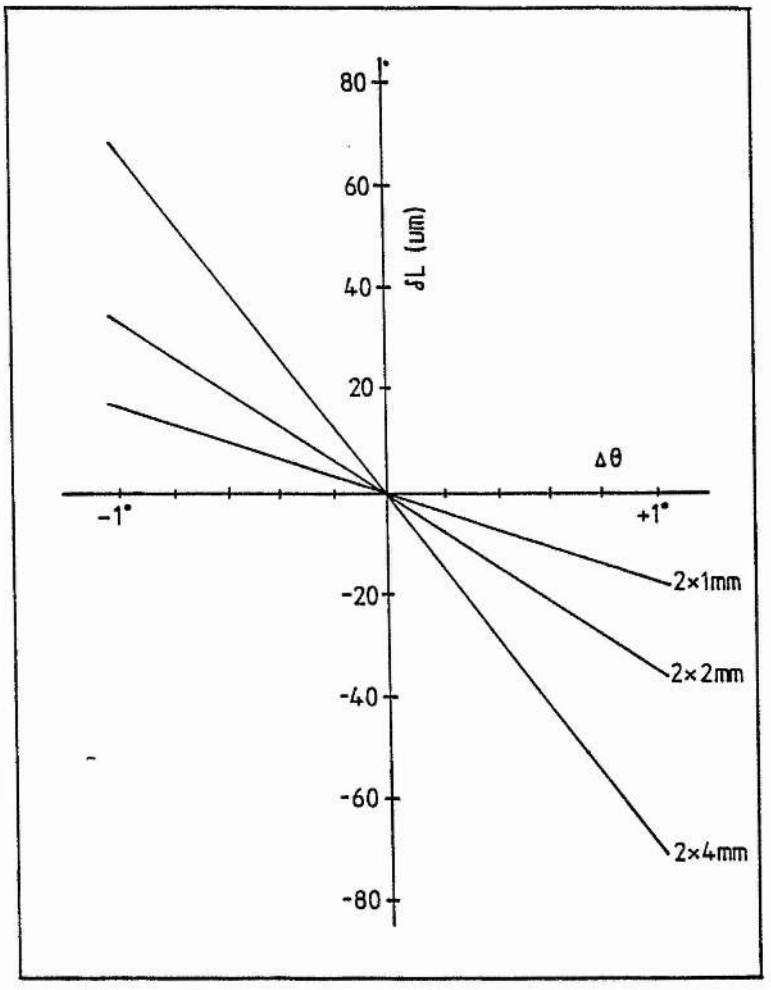

Figure 2.12 The change in the optical pathlength of the cavity for two quartz plates of thickness 1mm, 2mm and 4mm as the plates are rotated by $\pm 1^{\circ}$ about Brewsters angle.

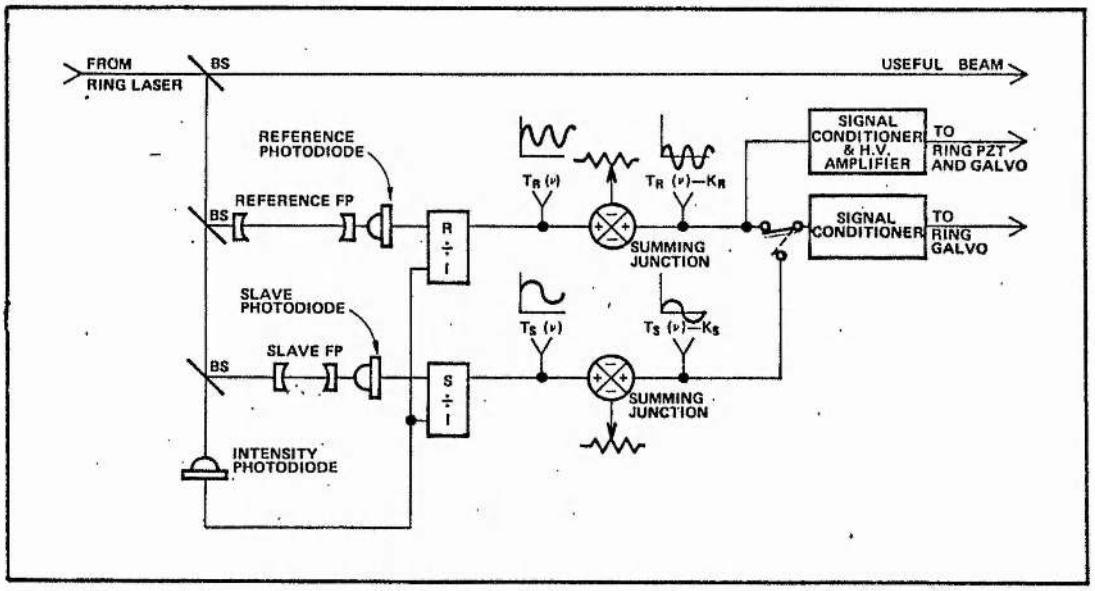

Figure 2.13 Block diagram of the stabilisation system for the Spectra-Physics 380D ring dye laser (after Divens and Jarrett [32]).

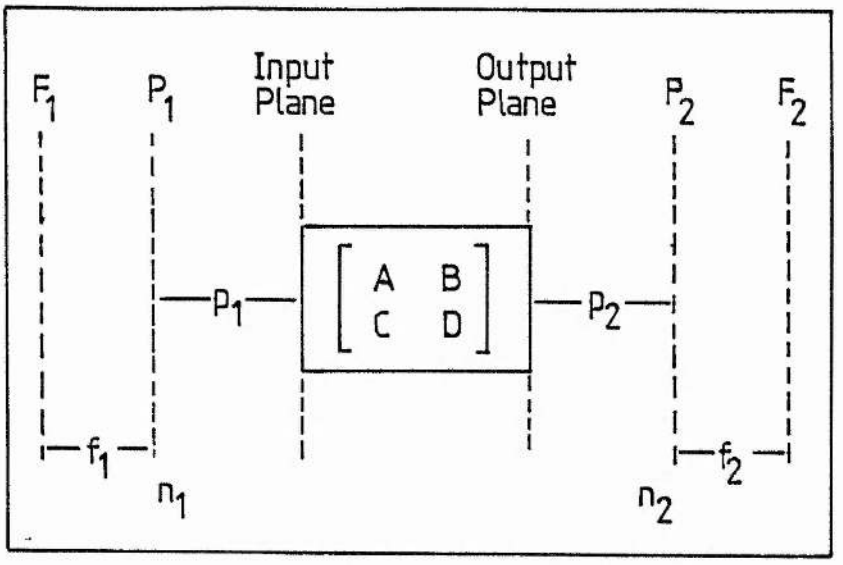

Figure 2.14 Reduction of a complex optical system to an equivalent thin lens (referenced to focal planes F_1 and F_2 through the principal planes P_1 and P_2).

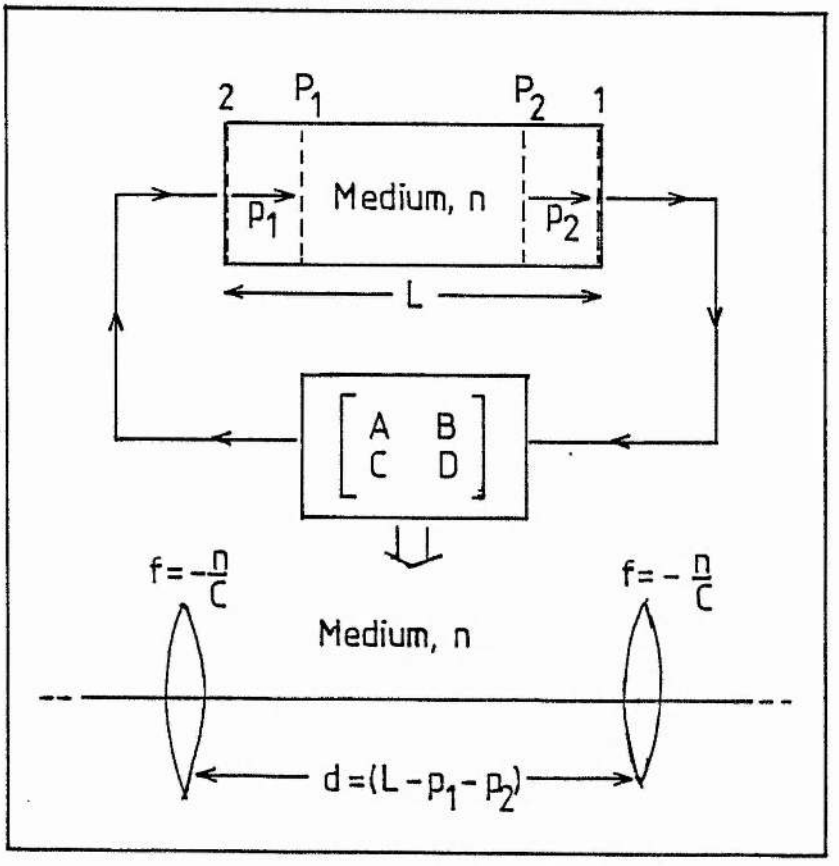

Figure 2.15 Use of an ABCD matrix to describe propagation from one plane in the ring cavity to another and the equivalent sequence of lenses.

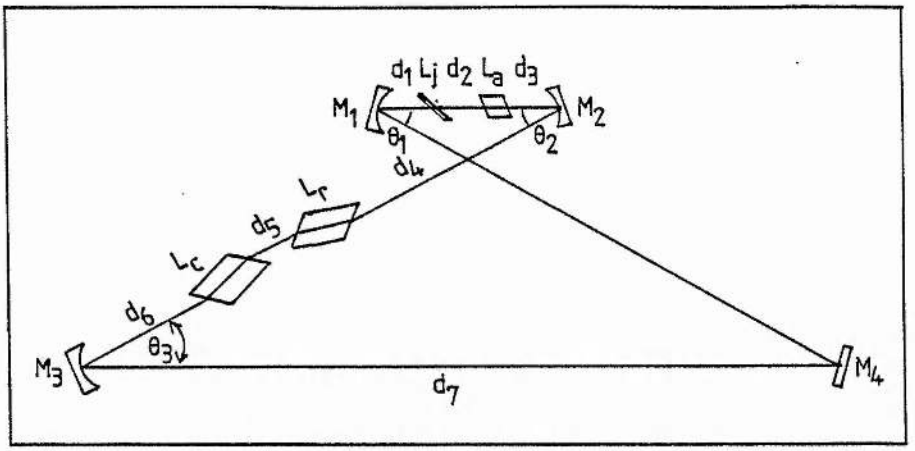

Figure 2.16 The 380D ring dye laser cavity showing the intracavity elements included in the stability region calculations. The distances between the elements are labelled as they are referred to in the text and computer programs. The mirror radii of curvature are: M1-3.5cm, M2-10cm, M3-22.8cm and M4 is plane. The mirror separations are M1-M2 8.4cm, M2-M3 34.5cm, M3-M4 29cm and M4-M1 53.1cm.

Angles are $\theta_1 = 16^{\circ}$. $\theta_2 = \theta_3 = 14^{\circ}$.

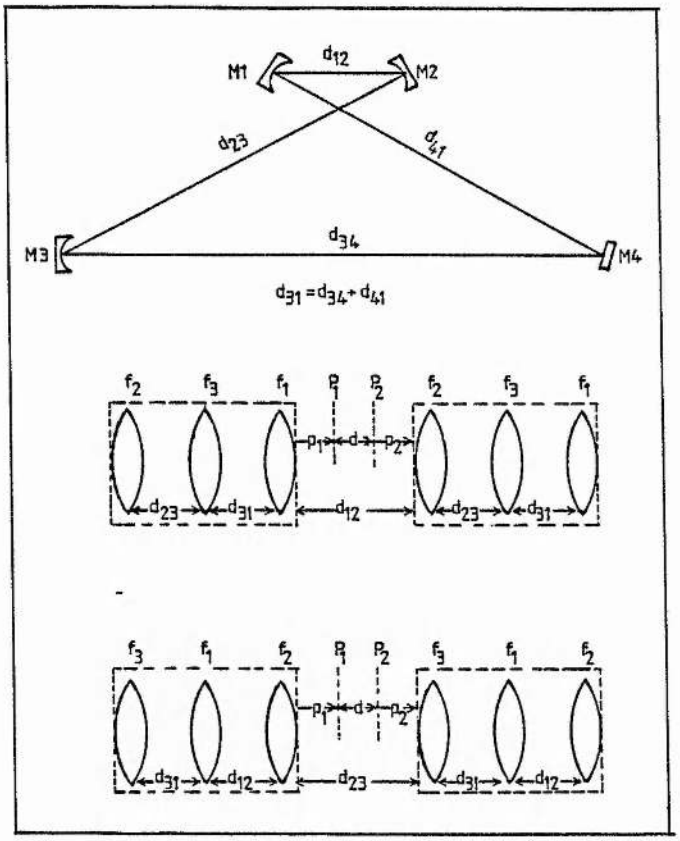

Figure 2.17 Cavity reduction using on-axis focal lengths to obtain an initial position of the beam waists for inserting the dye jet and ADA crystal.

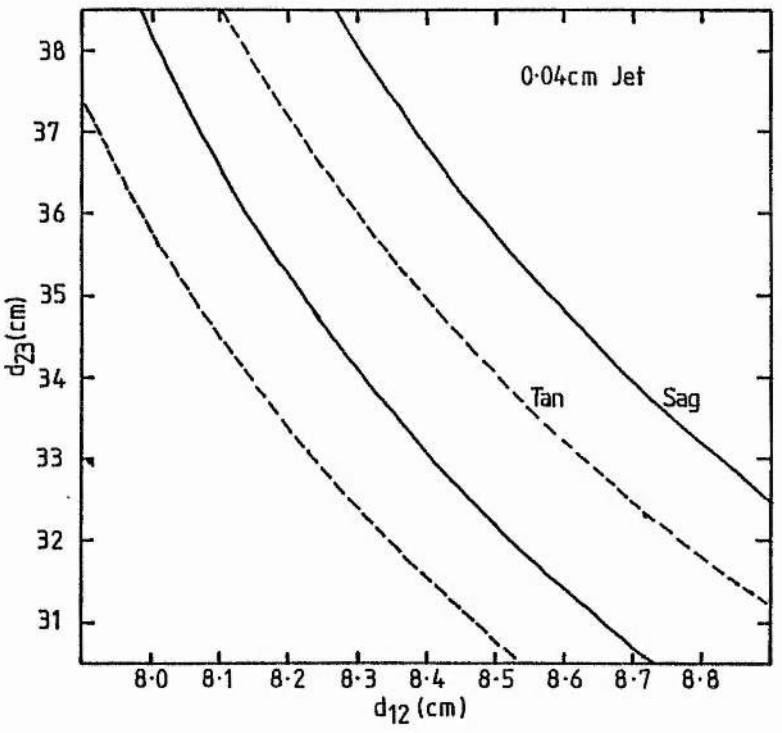

Figure 2.18 Tangential plane and sagittal plane stability regions with only the jet in the 380D cavity. The boundary lines correspond to zero spot size.

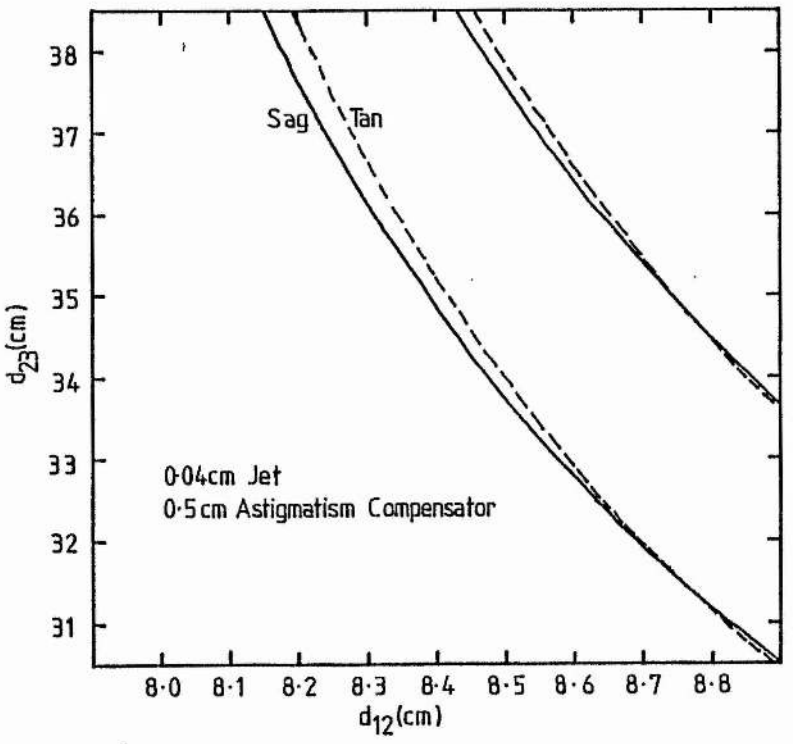

Figure 2.19 Tangential plane and sagittal plane stability regions when the standard astigmatism compensator is included in the jet arm of the cavity.

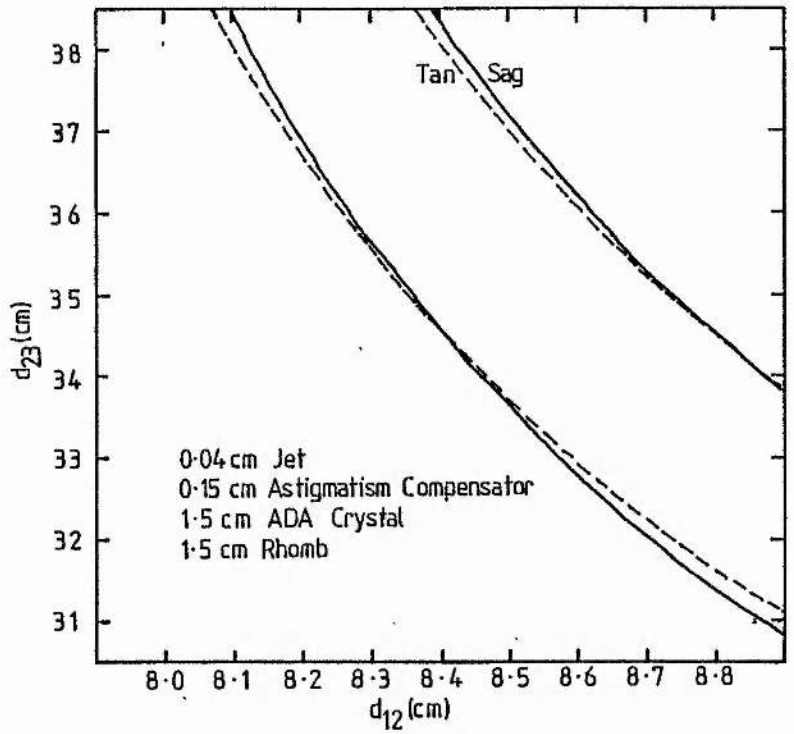

Figure 2.20 Tangential plane and sagittal plane stability regions demonstrating an optics optics combination giving good overlap when using a 15mm long ADA crystal.

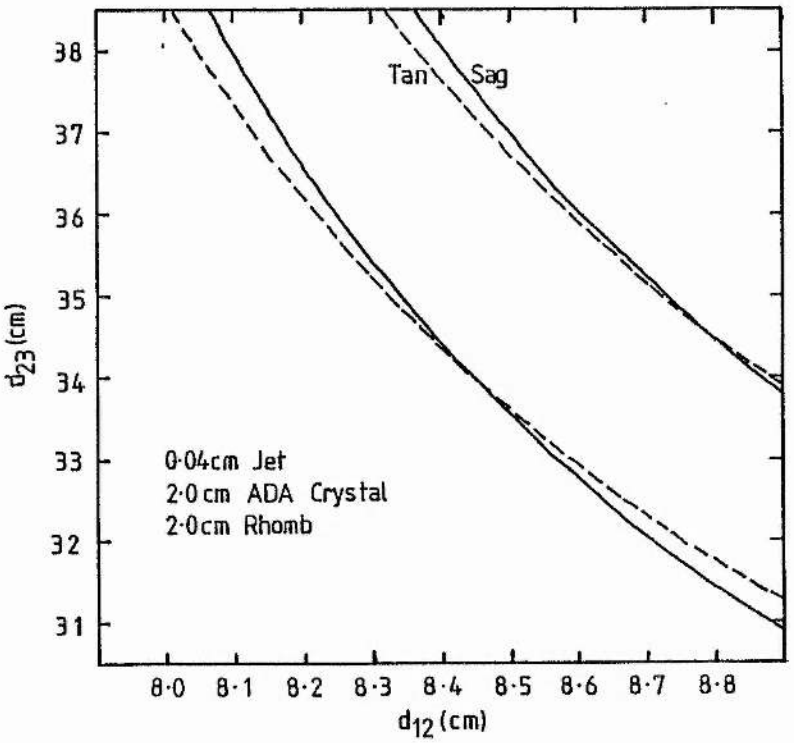

Figure 2.21 Tangential plane and sagittal plane stability regions demonstrating an optics combination giving good overlap when using a 20mm long ADA crystal.

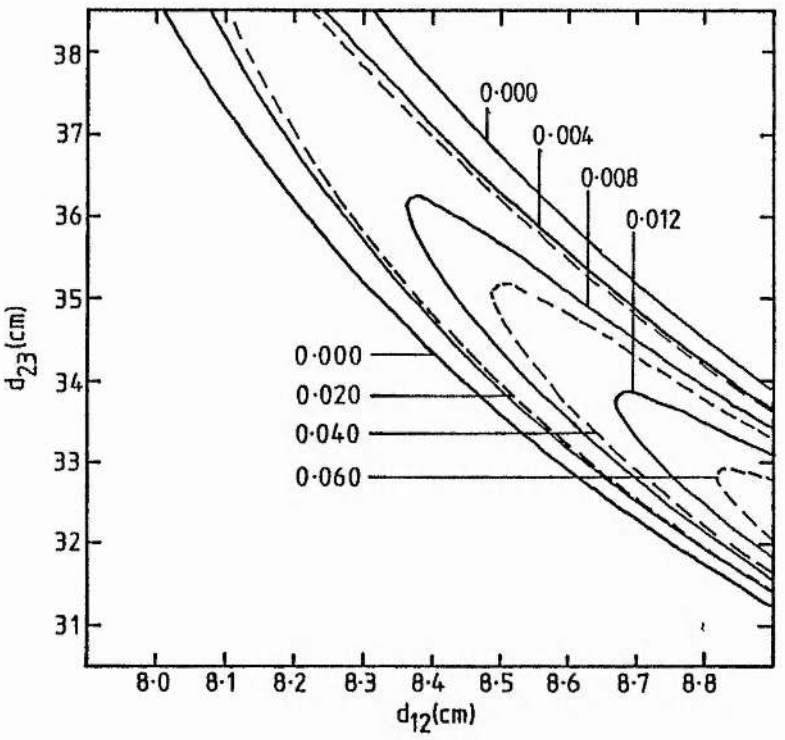

Figure 2.22 Contours of $(\pi\omega_J^2/\lambda_o)^2$ (cm^2) in the jet region calculated for Lc=20mm, Lr=20mm, Lj=0.4mm and La=0; in the tangential plane using a reduction about the Brewster surfaced jet (dashed lines) and a reduction about the region adjacent to it, d_1 (solid lines).

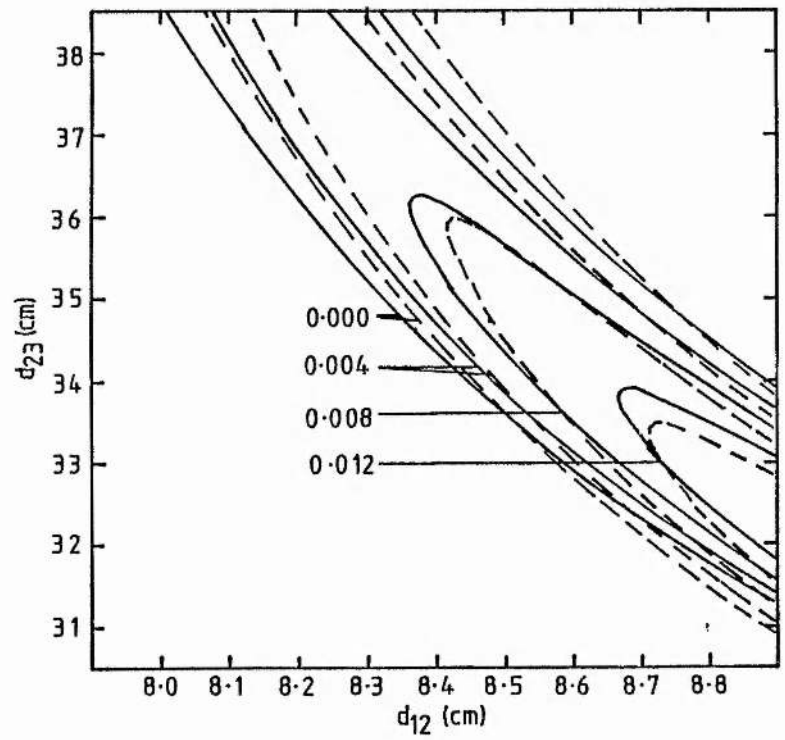

Figure 2.23 Contours of $(\pi\omega_J^2/\lambda_o)^2$ (cm^2) in the jet region calculated for Lc=20mm, Lr=20mm, Lj=0.4mm and La=0; using a reduction about d_1 for the sagittal plane (dashed lines) and tangential plane (solid lines).

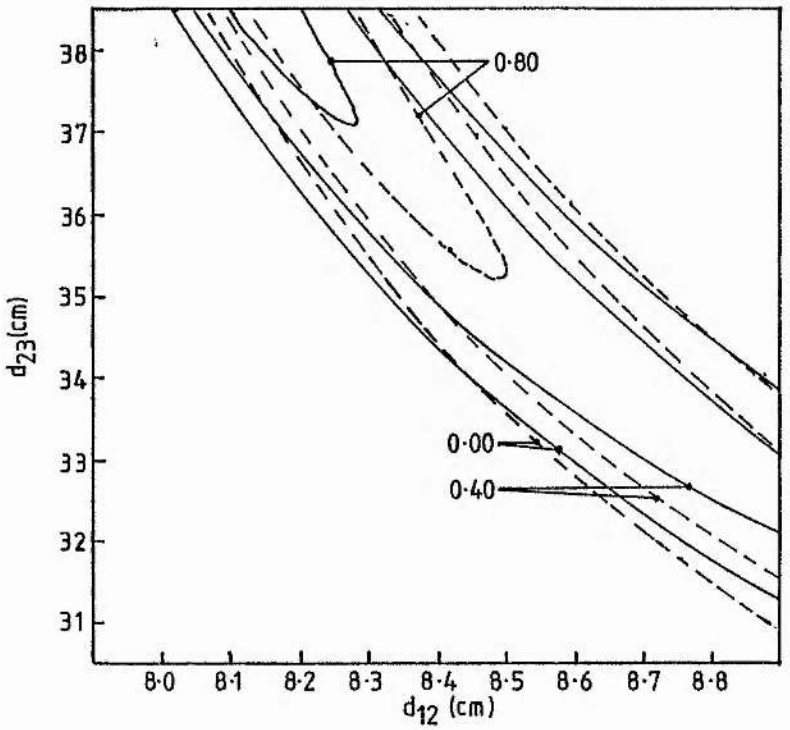

Figure 2.24 Contours of $(\pi\omega_C^2/\lambda\rho)^2$ (cm^2) in the crystal region calculated for Lc=20mm, Lr=20mm, Lj=0.4mm and La=0; using a reduction about d_5 for the sagittal plane (dashed lines) and tangential plane (solid lines).

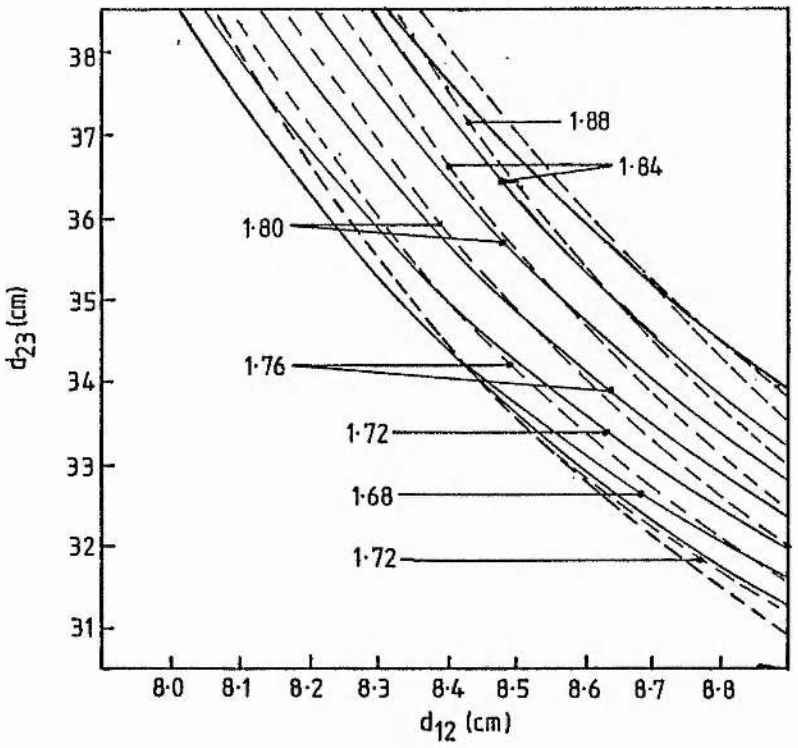

Figure 2.25 Position of the jet waist measured from M1 in cm for the sagittal plane (dashed lines) and tangential plane (solid lines). Lc=20mm, Lr=20mm, Lj=0.4mm and La=0.

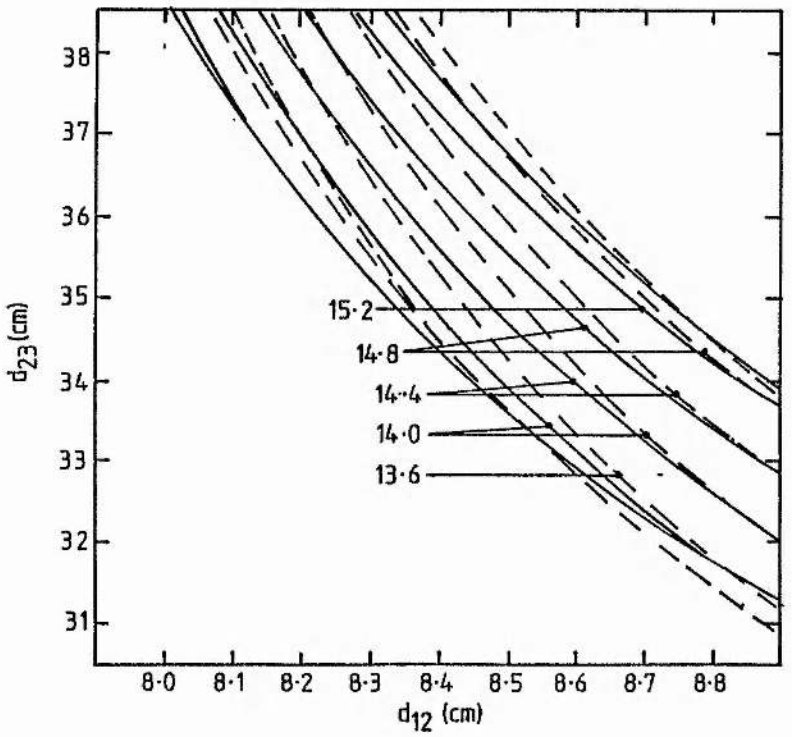

Figure 2.26 Position of the crystal waist measured from M3 in cm for the sagittal plane (dashed lines) and tangential plane (solid lines). Lc=20mm, Lr=20mm, Lj=0.4mm and La=0.

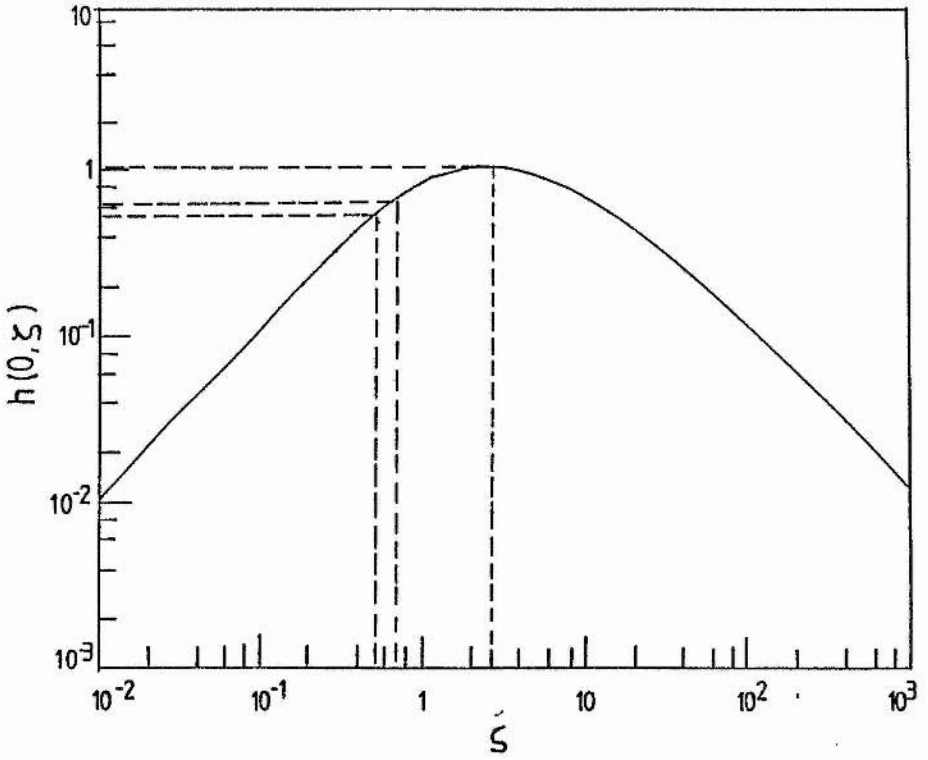

Figure 2.27 Reduction factor $h(0,\zeta)$ where ζ is the focusing parameter (after Boyd and Kleinman [54]).

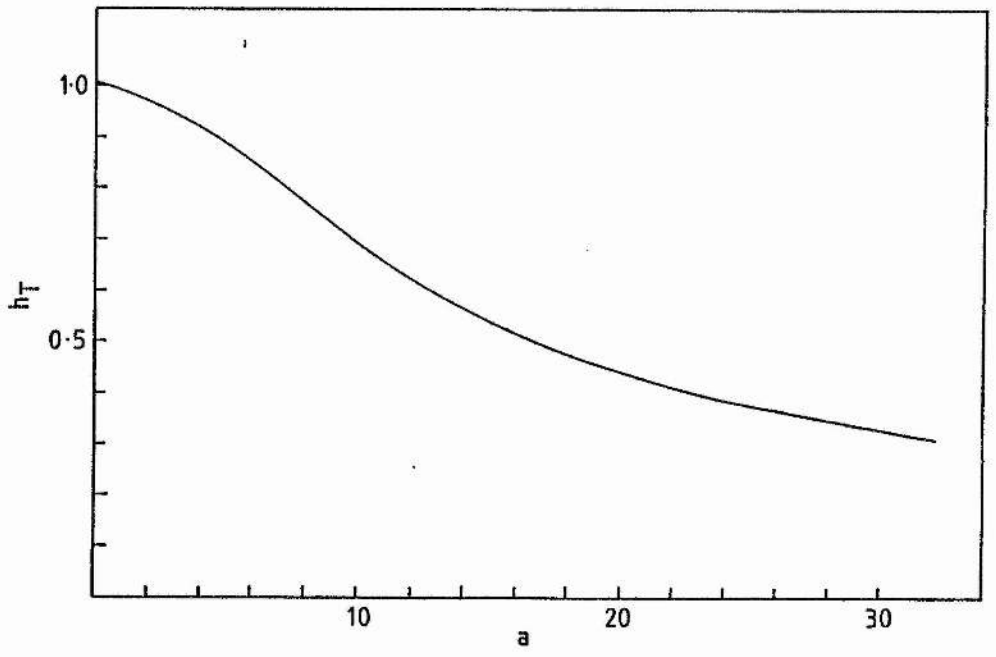

Figure 2.28 Thermal reduction factor h_T according to the theory of Okada and Ieiri [55].

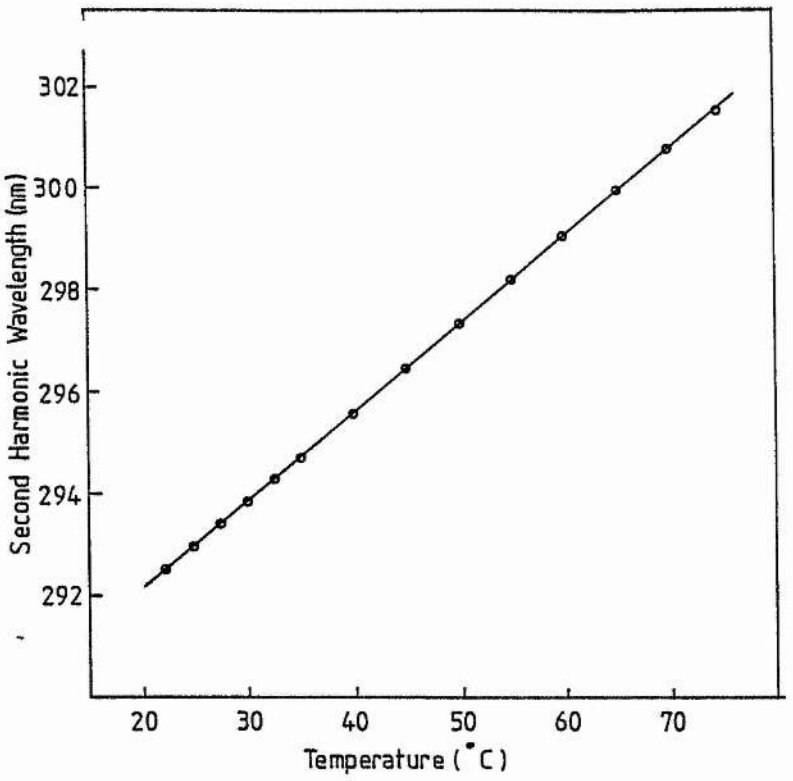

Figure 2.29 Experimental single mode phase match curve as a function of crystal temperature setting for an intracavity power of 4W.

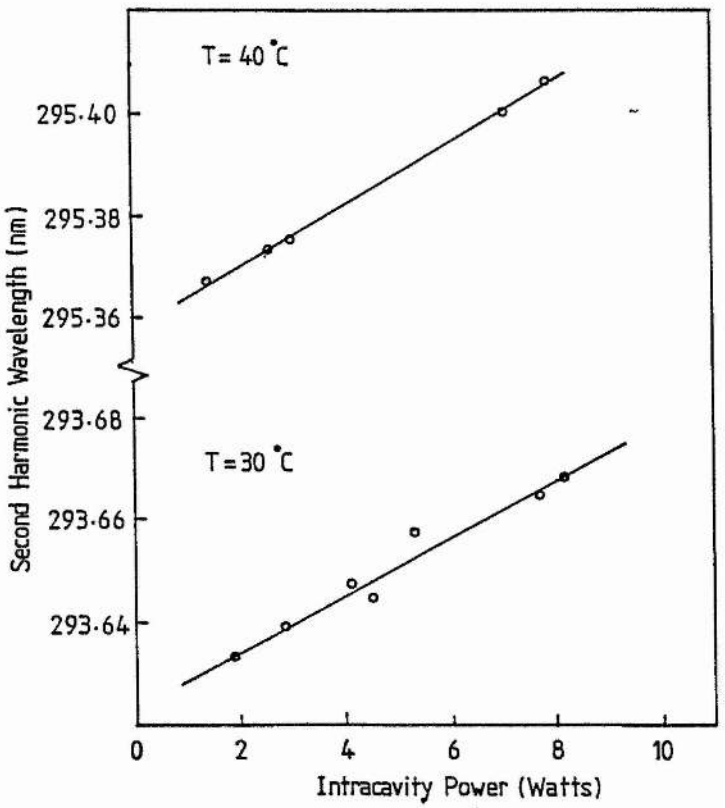

Figure 2.30 Phase match wavelength as a function of intracavity power.

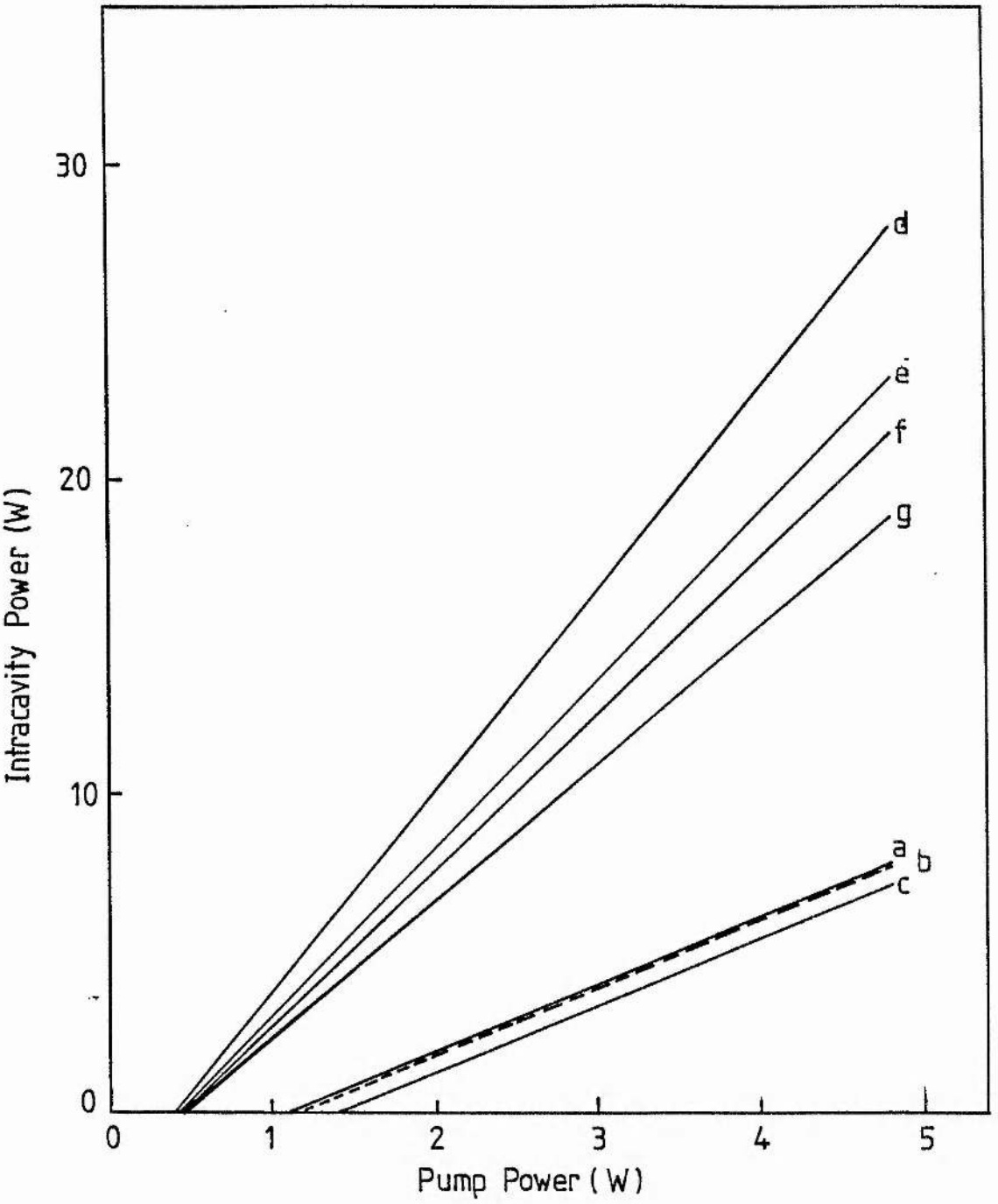

Figure 2.31 Measured intracavity power as a function of pump power. In curves (a), (b) and (c) the 9.4% transmitting output coupler is used. The 0.14% transmitting high reflector was used for the other curves. For curves (a), (b), (d) and (e) the laser is operated multimode. The others refer to single mode operation. Curve (b) shows the minimal reduction in intracavity power when the UV transmitting mirror replaces M3. (d) and (f): Lc=15mm, Lr=15mm, La=0. (e) and (g): Lc=15mm, Lr=15mm, La=1.5mm, 2mm or 5mm.

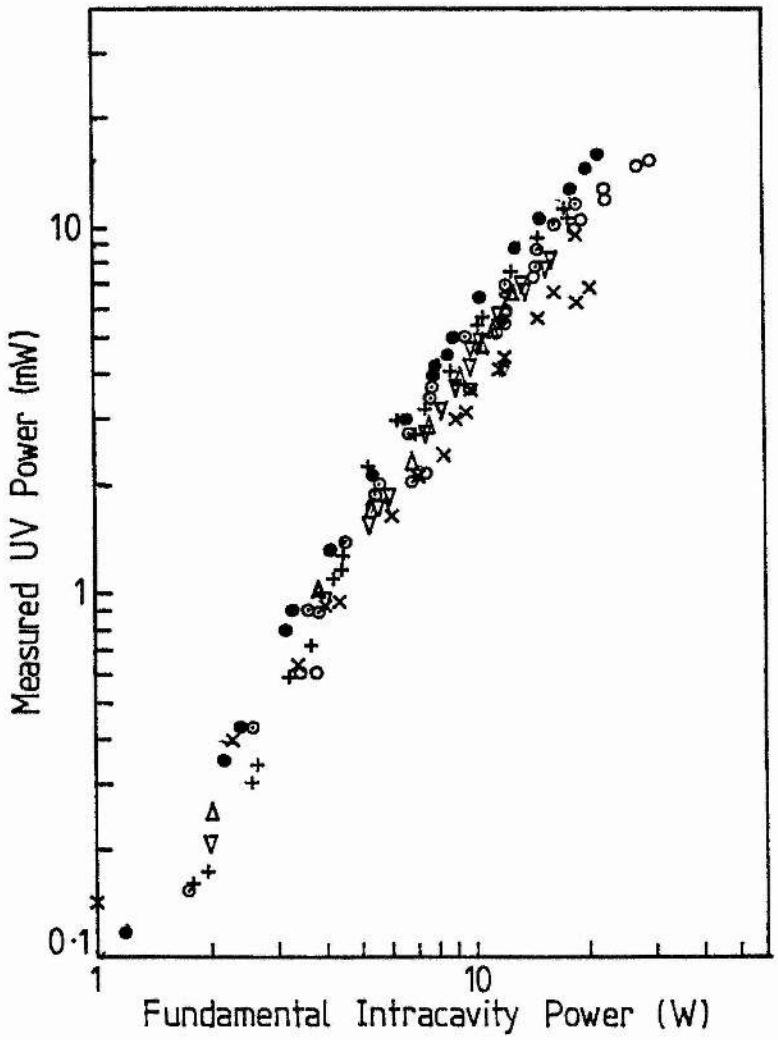

Figure 2.32 Superposition of measured UV powers using Lc=15mm, Lr=15mm and operating the laser multimode. The different symbols refer to different values of La. x o ● La=0; ⊙Δ La=1.5mm; ∇ + La=5mm.

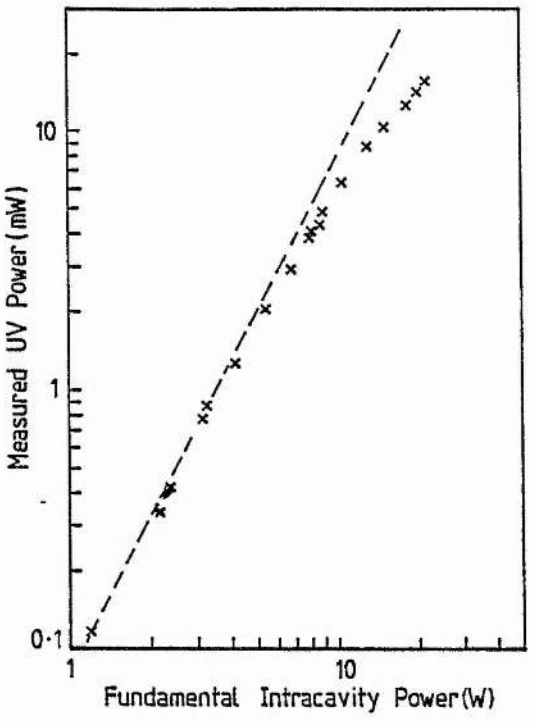

Figure 2.33 Measured UV power as a function of multimode fundamental intracavity power. Lc=15mm, Lr=15mm and La=0.

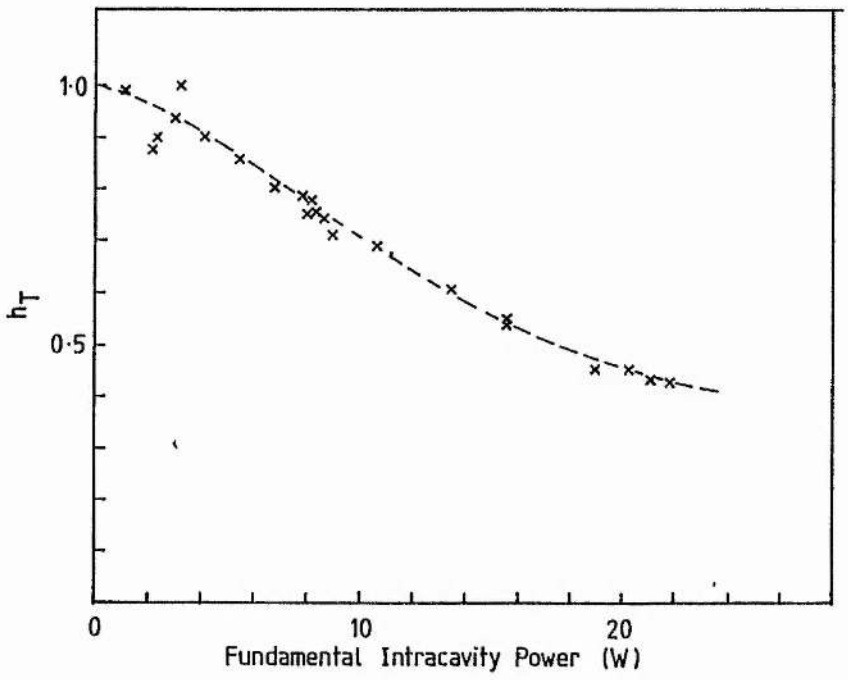

Figure 2.34 Thermal reduction factor calculated from the data in figure 2.33. The dashed line is the reduction factor predicted by the theory of Okada and Ieiri [55] for P_T=1W.

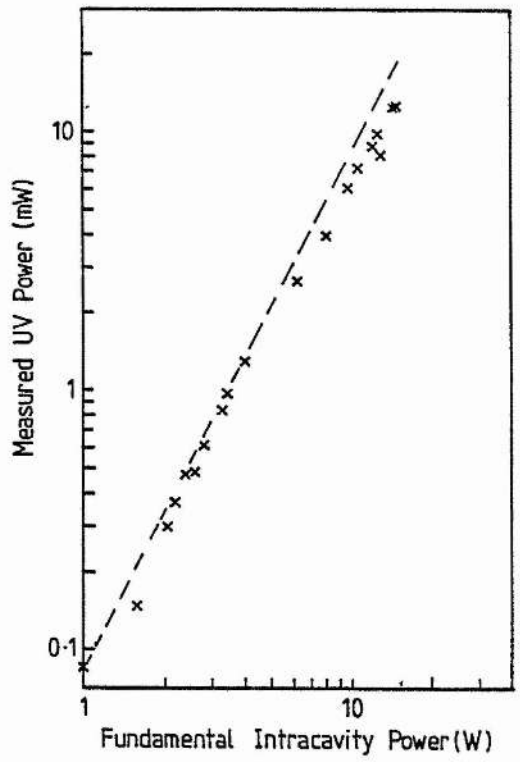

Figure 2.35 Measured UV power as a function of single mode fundamental intracavity power. Lc=15mm, Lr=15mm and La=0.

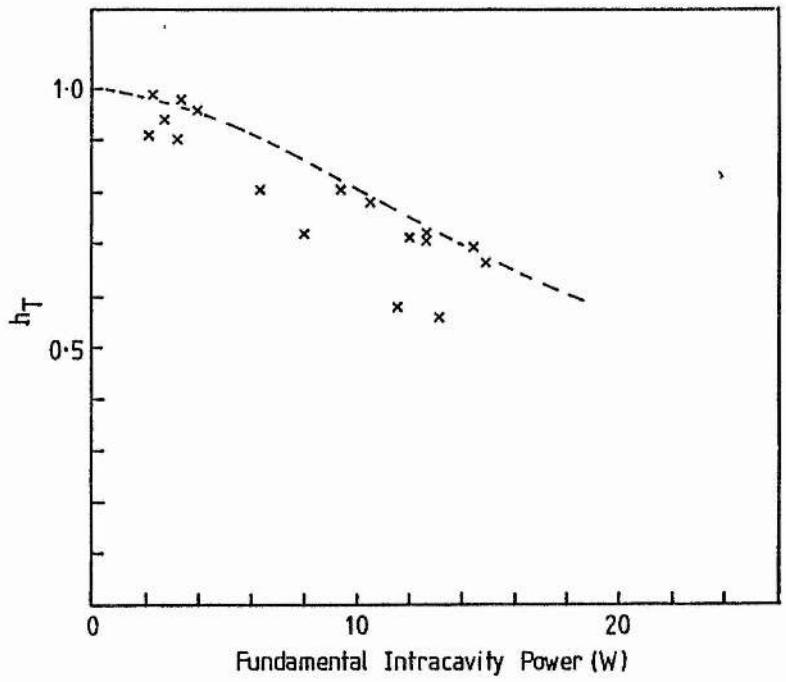

Figure 2.36 Thermal reduction factor calculated from the data in figure 2.35. The dashed line is a fit to the theory of Okada and Ieiri for P_T=1.4 W

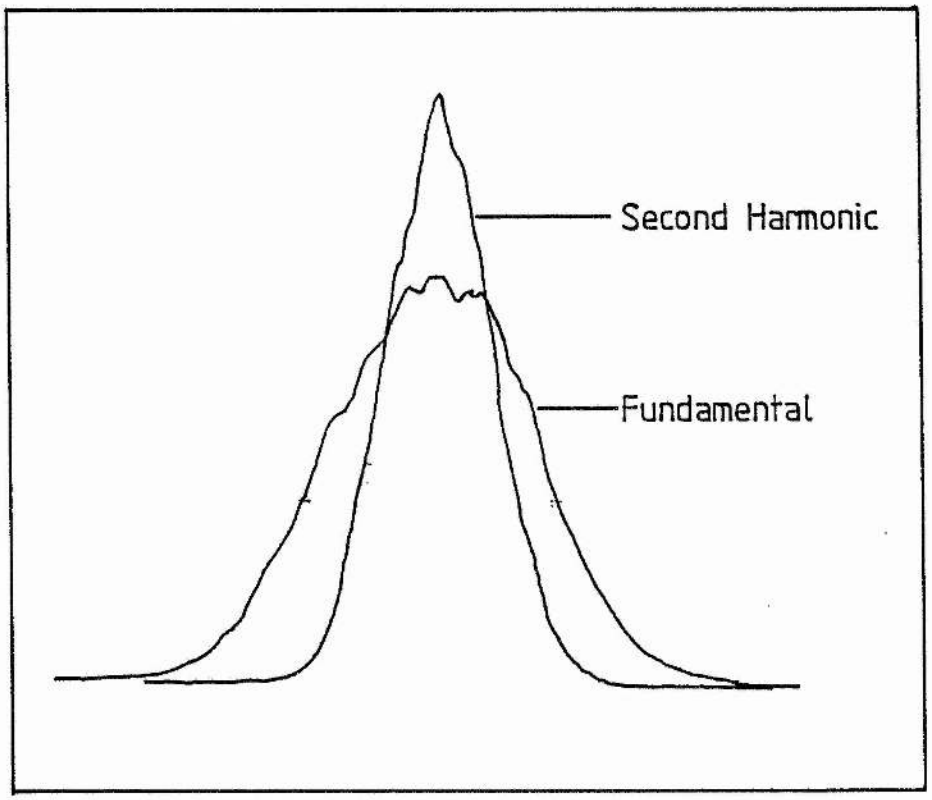

Figure 2.37 Fundamental and SH beam profiles.

CHAPTER 3

LASER ABSORPTION MEASUREMENT OF THE HELIUM 2^3S METASTABLE DENSITY

3.1 Introduction

Atomic metastable energy states may have significant populations in discharges, where they are excited predominantly by collisions of ground state atoms with electrons. In many cases observed discharge phenomena can only be explained by including the collision pathways involving the metastables. Thus quantitative metastable densities are required for the development and checking of discharge models. The He 2^1S and 2^3S metastables are of particular interest because of their role in the population inversion cycles of gas discharge lasers such as the He-Ne and He-metal vapour lasers. The helium triplet metastables are about ten times as numerous as the singlet metastables [5,8]. Therefore the determination of their density will in many cases be sufficient.

Metastable densities have been determined from absorption measurements on transitions with the lower level metastable, by a variety of techniques. Ladenburg and Reiche [1] used two separate but identical discharges, one as the source of light of the required wavelength, the other as absorber. Harrison [2] improved the method by using a single discharge as source and absorber. Light emerging from one end of the discharge tube is reflected back into the tube by a mirror. The intensity of light from the discharge is then monitored at a suitable wavelength with a spectrometer. The absorption coefficient is obtained by comparing the light intensity with and without the mirror covered. The quantity $FF_q^2 G_o(k_o L)$ is deduced from the measurements, where $G_o(k_o L)$ is the Ladenburg-Reiche fractional absorption for a resonant, absorbing source and absorber, L is the length of the absorber, k_o is the absorption coefficient at line centre, F is the mirror reflectivity and F_q the transmissivity of the tube window. Hence this method requires an accurate knowledge of the

reflectivity of the mirror and the transmissivity of the tube window as a function of wavelength and these change as the tube ages. Previous measurements of the He 2^1S and 2^3S densities were carried out by the Harrison method in a discharge similar to that used here [3]. More recently the self absorption method has been modified by monitoring the light emitted from two discharge lengths, one twice the length of the other [4,5]. The two lengths are obtained by constructing a discharge with two anodes or two cathodes. (The latter being the choice when the densities are to be measured as a function of metal vapour partial pressure in, for example, He-Cd discharges.) The discharge is switched from L to 2L and the light intensities from the plasma, I_1 and I_2, are measured. The ratio of these two intensities is directly connected to $G(k_oL)$, and so this technique avoids the uncertainties of the Harrison method with respect to F and F_q.

In all these measurements careful consideration must be given to light collection geometry to ensure that all volume elements of the discharge contribute equally to the light collected [6]. Extracting k_o from the measured quantity $FF_q^2G(k_oL)$ becomes more complicated when the transition of interest is not a simple Doppler broadened line.

The laser absorption method uses a narrow linewidth (<40 MHz) tunable, cw laser as the light source. This laser must be capable of being tuned onto a transition with a metastable lower level. The beam is aligned through the discharge and the transmitted light monitored as the laser is tuned through the line of interest. An absorption profile as a function of frequency is generated and the absorption coefficient at line centre or at any frequency within this profile may be obtained directly. Care must be taken that no scattered laser light or discharge radiation reaches the detector, giving a false zero

intensity. Also checks must be made that the absorption is linear and not saturated.

The remaining difficulty is the uncertainty in the absorption length due to discharge flaring and diffusion of the metastable atoms out of the discharge. This is of the order of the diameter of the discharge and can be large for the short discharge lengths necessary for these absorption studies. (Using this method it would be possible to determine the absorption length more precisely by probing the metastables at the two ends of the discharge through windows inset in the sides of the tube.)

In the present work helium triplet metastable densities have been calculated from measured absorption of resonant, cw, uv laser radiation on the $2^3S - 5^3P$ transition at 294.511nm (in air). Gas temperatures have also been deduced by measuring the Doppler width of this transition. A 3mm bore diameter capillary tube filled to pressures in the range 1 - 8 Torr and run at currents in the range 2.5 - 80 mA was studied. With constant discharge current (60 mA) a maximum value for the triplet metastable density of 10×10^{12} cm^{-3} at about 2 Torr was obtained. The metastable densities show the expected saturation behaviour, saturating at currents above 40 mA. Experimental values are used in conjunction with the rate equation describing the metastable level population in order to estimate the rate coefficient for loss of metastables through electron collisions.

3.2 Principle of the Laser Absorption Method

For a single Doppler broadened line, the absorption coefficient at frequency ν, k_ν, can be written [1]

$$k_\nu = k_o \exp-[\, 2(\ln 2)^{1/2}(\nu-\nu_o)/\Delta\nu_D]^2$$

where we have

$$k_o = \frac{2}{\Delta\nu_D}\left(\frac{\ell n 2}{\pi}\right)^{\frac{1}{2}} \frac{\lambda_o^2}{8\pi} A_{u\ell} N_\ell \frac{g_u}{g_\ell}\left(1 - \frac{g_\ell}{g_u}\frac{N_u}{N_\ell}\right)$$

and

$$\Delta\nu_D = 2\nu_o/c[(2kT/M)\ell n 2]^{\frac{1}{2}} \qquad (1)$$

In the above A_{ul} is the Einstein A coefficient for the transition at wavelength λ_o from level u to level 1. The upper level has population density N_u and statistical weight g_u. The population density of the lower level is N_1 and g_1 its statistical weight. The absorption coefficient on line centre is k_o; $\Delta\nu_D$ is the Doppler width (full width at half maximum) of the transition; ν_o is the optical frequency at line centre, T is the gas temperature and the other symbols have their usual meaning.

By scanning the laser through the transition and monitoring the light transmitted, an absorption profile is obtained from which $k_o L$, where L is the absorption length, and $\Delta\nu_D$ may be measured (provided it is realistic to approximate the actual line profile as a single Doppler broadened line). Thus this method allows the gas temperature to be determined experimentally, in contrast to other absorption methods which require the gas temperature to be measured independently or estimated to provide a Doppler width for substitution into (1).

Provided that $g_u N_u \ll g_1 N_1$ and A_{ul} is known, the metastable population (N_1) can then be determined from

$$N_\ell = k_o \frac{\Delta\nu_D}{2} \left(\frac{\pi}{\ell n 2}\right)^{\frac{1}{2}} \frac{8\pi}{\lambda_o^2 A_{u\ell}} \frac{g_\ell}{g_u}. \qquad (2)$$

Triplet metastable densities have been previously determined from absorption measurements on the $2^3S - 3^3P$ transition at 388.9nm using conventional techniques [3,5]. The 3^3P level population is not negligible, therefore only the reduced metastable density $N_1\{1-g_1N_u/g_uN_1\}$ can be determined. Further, since the Doppler width for the transition at 600K is 6.8 GHz, while the fine structure splittings are 8.1 and 8.8 GHz, it is necessary to treat the line as the sum of three Doppler broadened lines, thus complicating the analysis. The $2^3S - 5^3P$ transition with wavelength 294.511nm, used here, has a Doppler width of 8.9 GHz at 600K and fine structure splittings of 1.66 and 1.80 GHz. Comparing the sum of three Doppler broadened lines, with their centres spaced by the given fine structure splittings and weighted by the intensity ratio 1:3:5, with a single Doppler broadened line with the same centre and maximum (figure 3.1), the width is increased by only 116 - 86 MHz in the range of temperature 350 - 700 K (figure 3.2). The distortion of the single Doppler profile due to the fine structure is thus negligible. Also, the natural width of the transition is less than 1 MHz, (the Einstein A coefficient is $3.02\times10^6 s^{-1}$, 62nd Ed., CRC handbook) and the collisional broadening is estimated as 20 MHz/Torr, being less than 160 MHz for all pressures of interest. The Stark width is calculated to be between 3 and 20 MHz for the electron density range here, using the theoretical broadening constants of Griem [7]. Thus an error in the width of less than 3% is introduced by assuming the line profile to be a single Doppler broadened line. The statistical weights for

this transition are $g_u = 9$ and $g_1 = 3$.

A further advantage of the UV transition is that $g_u N_u$ is considerably less than $g_1 N_1$. The population of the 5^3P level is at least four orders of magnitude less than the 2^3S level population [7]. Thus it is the metastable density that is obtained rather than the reduced number density.

Thus, in using the laser absorption method, the analysis is very much simplified. The Doppler width is measured experimentally and by using the UV transition, with its broad Doppler width and smaller fine structure splittings, complications due to the triplet nature of the transition do not arise.

3.3 Application to Helium 2^3S Metastables

The intracavity, frequency-doubled, Spectra-Physics 380D was used as the laser source. The laser was operated to give single frequency UV radiation. No difference in the absorption profile was observed when operating the laser 'stabiloked' or unstabilised, so most of the results were obtained with the laser unstabilised. There was no evidence of saturation with the available power (11 mW maximum for this crystal) but the power was reduced to about 1 mW to minimise perturbation of the discharge. The UV output beam is collimated, giving a beam 2mm in diameter.

The quartz discharge is similar in design to that used by Browne and Dunn [3] except an additional division in the outer sleeve between the cathode and anode allows the use of a small hole in the inner bore at both ends of the discharge giving improved length definition (see

figure 3.3). It has a 3mm diameter bore and so the 2mm diameter UV laser beam is averaging over two thirds of the radial distribution of the metastables. (With a smaller beam diameter or in wider bore tubes the technique is ideal for measuring radial distributions of metastables). The radial distribution of the metastable density is usually approximated as a zero order Bessel function [8]. Thus with the averaging in the present case the measured metastable density is 85% of the density on axis. Experimentally the metastable density is found to be uniform over the central two thirds of the radial distribution when the current is sufficient for electron collisional destruction to dominate over diffusion to the wall for the central volume of the discharge [16]. This is only the case for the highest currents in the present investigation. Thus to obtain the axial metastable density from the measured densities requires multiplication by a factor varying from 1.2 to 1 in the current range 2.5 to 80mA. The correction factor is slightly larger for a higher pressure at a given current [5]. This correction has not been allowed for in the rate equation analysis that follows, as the radial distribution of metastables was not known. Its inclusion will further increase the disparity of the measured metastable density over the expected metastable density for the case of small currents at the higher pressures investigated. The effective absorption length of the discharge was 23mm. High purity grade (99.995%) helium was used. The filling pressure was measured with a Bourdon gauge calibrated with a McLeod gauge. The tube was pumped out to a pressure of 6×10^{-5} Torr. To obtain a clean discharge the discharge was run at currents in excess of 100mA and then pumped out while still running. This was repeated several times.

The experimental arrangement is shown in figure 3.4. The UV light transmitted through the discharge is detected using a calibrated photodiode (UDT PIN 100UVCAL). A scanning confocal interferometer of 1 GHz free spectral range is used for monitoring the mode structure of the laser to ensure single mode operation. A temperature stabilised, passive confocal interferometer of 752 MHz free spectral range (in the visible) is used to provide frequency markers. The laser is tuned onto the $2^3S - 5^3P$ transition using the 'Kowalski' type wavemeter described in appendix A.

In practice the UV intensity varied slightly over a scan and so the UV beam was split using a 50% beamsplitter and the intensity was continuously monitored with a photodiode. This variation was kept to less than 5% and a linear correction was made to the measured absorption. The program used for calculating the metastable density from the measured absorption is listed in appendix C.

Figure 3.5 shows two of the Doppler broadened profiles obtained on scanning through the 294.51nm transition. Figure 3.6 shows the triplet metastable density, deduced from similar such profiles, as discussed above, as a function of discharge current with helium filling pressure as the other parameter. The error bars arise from variations in consecutive scans in a single run and from repeatability of results on refilling and re-aligning the tube. It was possible with care to obtain results consistent to 0.1% in a single run but on refilling and realigning the variability is of the order of 5-10%. Figure 3.7 shows the variation in Doppler width as a function of discharge current for two helium filling pressures of 1.5 and 8 Torr.

3.4 Rate Equation Analysis

Part of the Grotrian diagram for helium is shown in figure 3.8. The rate equation describing the steady state triplet metastable population in a positive column discharge is of the form [8]

$$\alpha_{01} n_e N_0 + A_{31} N_3 + \alpha_{21} n_e N_2 - \tau_D^{-1} - \beta N_1^2 - \delta N_0^2 N_1 - \alpha_{10} n_e N_1 - \alpha_{11} n_e N_1 - \alpha_{12} n_e N_1 - \alpha_{13} n_e N_1 - \alpha_{14} n_e N_1 = 0 \qquad (3)$$

where N_0, N_1, N_2, N_3 are the population densities of the $1^1S, 2^3S, 2^1S, 2^3P$ levels, respectively, and n_e is the electron density. The first three terms on the left describe, in order, triplet metastable production by (1) direct excitation from the ground state, (2) radiative decay from the level 2^3P and (3) conversion of singlet metastables to triplets by collisions of the second kind with electrons. The remaining terms describe processes destroying the metastables and in order are (4) diffusion to the tube walls, (5) collisions between metastables leading to ionisation, (6) conversion to molecular metastables, (7) collisions of the second kind with electrons resulting in transition to the ground state, (8) step ionisation and (9),(10),(11) step excitation of levels 2^1S, 2^3P and 2^1P by collisions with electrons. Deloche et al [9] in their rate equations for a high pressure helium afterglow also include production terms due to collisions of electrons with atomic and molecular ions and a destruction term due to collisions between atomic and molecular metastables. Using the coefficients quoted in that paper such terms are seen to be negligible in a low pressure positive column.

The ionisation rate for metastable-metastable collisions is $\beta = 1.5 \times 10^{-9} cm^3 s^{-1}$, while the coefficient for conversion of atomic metastables into molecular metastables is $\delta = 1.7 \times 10^{-34} cm^6 s^{-1}$ [9]. Thus, for the pressure range of interest, conversion of atomic metastables to molecular metastables is insignificant compared to the other loss mechanisms and the sixth term is deleted.

From the rate equation for the 2^3P level assuming that step excitation from the 2^1S level is small compared with step excitation from the 2^3S level, [8], we obtain

$$A_{31}N_3 = \alpha_{03} n_e N_0 + \alpha_{13} n_e N_3 \tag{4}$$

Dothan and Kagan [8] also show that the sum of the coefficients for direct excitation of the 2^3S and 2^3P levels is well approximated by the total rate constant for inelastic collisions of ground state helium atoms,

$$\alpha_{01} + \alpha_{03} = \alpha \tag{5}$$

Substituting (4) and (5) into (3) we have

$$\alpha n_e N_0 - N_1 \tau_D^{-1} - \beta N_1^2 - \gamma n_e N_1 = 0$$

where γ is given by

$$\gamma = \alpha_{10} + \alpha_{11} + \alpha_{12} + \alpha_{14} - \alpha_{21}/R \tag{6}$$

Use has been made of the ratio of triplet to singlet metastable atoms, R, obtained from the results of Browne and Dunn [3] to eliminate the number density of the singlet metastables (figure 3.9). Equation (6) is identical to the rate equation used by Browne and Dunn [3] except

for the broader definition of the coefficient γ. Values of γ between 4×10^{-9} and $1 \times 10^{-7} cm^3 s^{-1}$ are quoted in the literature [8,9,10]. To a good approximation the electron temperature is a function of pressure but not of current under our experimental conditions so γ is expected to be a constant for all currents at each pressure.

The model of Dothan and Kagan is only applicable in the pR range 5-100 cm Torr. The pR values here, (0.15 - 1.2 cm Torr), lie outside this range. Also they give all the coefficients as functions of electron temperature which may be estimated but is not explicitly known in the present case. The metastable densities they calculate are about an order of magnitude lower than those measured by Ichikawa and Teii [5] in a similar discharge to that modelled. This arises largely from the calculated values of α used by Dothan and Kagan being too small.

The coefficient α describing the electron excitation is of the form

$$\alpha = \langle \sigma(v_e) v_e \rangle$$

where the brackets denote averaging over the electron energy distribution and $\sigma(v_e)$ is the total cross section for excitation to the triplet metastable state as a function of electron velocity, v_e. The total cross section rises rapidly to a mean value of about $3 \times 10^{-18} cm^2$ just above the threshold of 19.8eV [3]. The fraction of electrons with energies above the threshold for various ranges of E/p have been derived from the electron energy distribution functions of Smit [11] and are listed along with the corresponding value of α in Table I. As the electric field varies as a function of current, α changes with current and pressure in contrast to γ which varies with pressure only, to a good approximation.

Table I

Range of E/p ($V\ Torr^{-1}cm^{-1}$)	Fraction of electrons with energy>20.4eV	α (cm^3s^{-1})
2.7-5	$3.4x10^{-3}(E/p-2.7)$	$2.9x10^{-12}(E/p-2.7)$
5-8	$5x10^{-3}(E/p-3.5)$	$4.2x10^{-12}(E/p-3.5)$
8-20	$6x10^{-3}(E/p-4)$	$5x10^{-12}(E/p-4)$

The other quantities required are taken from Browne and Dunn [3] also, we have

$$\tau_D^{-1}(s^{-1}) = 3 \times 10^4/p \qquad (7)$$

$$n_e(cm^{-3}) = 10^{11}\ (E/p)^{-1} \qquad (8)$$

The volume of the discharge is less than a three hundredth of the volume of the tube and thus the running pressure is equal to the filling pressure, giving

$$N_0 = 3.5 \times 10^{16} p(293/T) \qquad (9)$$

where T is calculated from the measured Doppler width

$$T = 4[\Delta\nu_D/(7.16 \times 1019 \times 10^{-4})]^2 \qquad (10)$$

with $\Delta\nu_D$ in GHz.

The values for the metastable density calculated using the above rate coefficients and $\gamma = 4.2x10^{-9}cm^3s^{-1}$ [9] are shown to be in reasonable agreement with the measured values in figure 3.10. As neither α nor γ are known precisely it should be possible to exploit the improved experimental accuracy to obtain more information about α

and γ. Pairs of values of α and γ which satisfied equation (6) were calculated. Figure 3.11 shows a fit to the experimental data for p = 1 Torr. Superimposed on this graph are the values for α derived from Smit [11]. For all pressures it was found that these values of α at higher currents bunched around a small range of values of γ which displayed the expected trend of increasing with increasing electron temperature (i.e. decreasing pressure). A best value for γ thus obtained was used to calculate the value of α for small currents. These values of α are plotted in figure 3.12 and the bars superimposed on the data points show the range of values obtained allowing for the experimental error and the error in γ. The Smit α values are shown in figure 3.13 for comparison. The computer programs for carrying out these various calculations are listed in appendix C. The main difference is that for p = 4 Torr and 8 Torr the values of α for small currents appear to be much larger than expected. Physically there is no basis for α monotonically decreasing in this manner. Checks indicate that the rate of diffusion of metastables to the wall and the electron density have not been overestimated. The effect of electron temperature varying with current would be to increase γ for small currents requiring α to be larger still. With the gas temperature varying, E/N rather than E/p is a good parameter but the trend in E/N is similar to that in E/p. It would appear there is a further source of triplet metastables which scales with ground state helium density but not with electron density.

Two processes leading to a creation of metastables proportional to the ground state number density, which may be involved in explaining these results, are outlined. Firstly the conversion of singlet metastables to triplets through collisions with ground state atoms and secondly the collision induced singlet to triplet conversion

between states with large angular momentum.

If all of the metastable excess is to be explained in terms of conversion of singlet metastables, which lie 20.61eV above the ground state, to triplets (19.82 eV) through collisions with ground state atom, inclusion of an extra term,

$$\varepsilon N_o N_2 = \varepsilon N_o N_1 / R \qquad (11)$$

where R is the ratio of triplet to singlet metastables, in the rate equation (6), predicts values of ε of the order of $5 \times 10^{-13} cm^3 s^{-1}$, implying a cross section of $3 \times 10^{-18} cm^2$. The cross section estimated is small compared to the gas kinetic cross section and also smaller than the upper bound of $2 \times 10^{-17} cm^2$ obtained for a collision induced triplet to singlet conversion, (He 4^3P - He 4^1L, where L is S,P or D), violating the Wigner spin rule, obtained by Abrams and Wolga [12].

By monitoring the He 2^1S population density in a helium afterglow Phelps [13] measured the cross section for the destruction of singlet metastables through collision with the ground state helium atoms, at 300K, to be $3 \times 10^{-20} cm^2$. Thus this pathway can not totally explain the He 2^3S metastable excess observed here.

Phelps also stated that the destruction of singlet metastables did not lead to the creation of triplet metastables because no build-up in triplet metastable population was observed at early times in the afterglow. Calculations using his rate equations show a 1.4% increase in the 2^3S population density at 4 Torr and an 8.6% increase at 8 Torr in the early afterglow, assuming a rate of destruction of singlet metastables of $5 \times 10^{-13} cm^3 s^{-1}$, leading to triplet production,

as predicted above. These maxima occur in times less than 12μs into the afterglow which are short compared to the 100μs resolution of the Phelps results. It is therefore not known if any triplet metastable creation arises from this process.

In a positive column, in contrast to the afterglow, excited levels are populated by electron collisions with ground state atoms. Thus another possible source of triplet metastables is collision induced singlet to triplet conversion between excited states with large angular momentum where the Wigner Spin Rule no longer applies due to the breakdown of LS coupling. One possible pathway is

$$He(4^1P) + He(1^1S) \rightarrow He(4^3F) + He\ (1^1S)$$

followed by radiative decay through the 3^3D and 2^3P levels to the 2^3S level. Using the populations for the excited levels calculated by Dothan and Kagan [8], radiative decay rates from Wiese et al [14] and the collision cross section, $2x10^{-14}cm^2$, given by Kay and Hughes [15] this leads to a creation rate for triplet metastables an order of magnitude smaller than required. It is worth noting that the calculated populations of the levels, used above, may be an order of magnitude too small by comparison of the measured triplet metastable densities obtained here, which were found to be an order of magnitude larger than those calculated by Dothan and Kagan [8].

Thus it would appear that the extra triplet creation required to explain the experimental results arises from several processes. The cross section derived is only valid if all the excess 2^3S production arises from 2^1S conversion and would need to be decomposed into the individual cross sections for processes demonstrated to occur in the future.

3.5 Summary

The laser absorption method of measuring metastable densities is straightforward and reliable. As indicated, it makes possible simple determination of radially averaged metastable densities and can be readily extended to determine radial distributions and to explore the effective absorbing length of the discharge. The gas temperature is obtained explicitly by measuring the Doppler width of the absorption line. Uncertainties arising from changing transmission of tube windows are avoided and the geometrical arrangement of the light collection apparatus is no longer critical. Thus, most of the difficulties of earlier methods are overcome. The advantage of using a UV transition has also been demonstrated. Metastable densities at very low pressures may be obtained using longer absorption lengths or chopping the laser radiation and using a calibrated phase sensitive detector to measure the percentage absorption.

From the rate equation analysis values for the lumped loss of triplet metastables through collisions with electrons, γ, are deduced. Experimental confirmation of these and the α values used are required. The need for a further source of triplet metastables which scales as the ground state number density is demonstrated and conversion of singlet metastables to triplets through collisions with ground state atoms and collision induced singlet to triplet conversion in states with large angular momentum are tentatively suggested. Measured values of the ratio of the singlet to triplet metastable atom density [3,5] (figure 3.9), indicate there is substantial quenching of the singlet metastables which scales with ground state number density. Whether these singlet metastables are converted to triplets by the types of processes cited above is still to be determined.

It would be useful to apply the laser absorption method to a helium afterglow to check the singlet metastable destruction rates. An intensity stabilised, narrow linewidth laser with no tendency to drift from its stabilised frequency would be required for this. The singlet metastable densities can be measured by the laser absorption method on the $2^1S - 3^1P$ transition at 501.6nm using a Coumarin dye laser. Also the neon $1s_3$ and $1s_5$ metastable densities can be measured on a number of transitions using a Rh6G dye laser, by this method.

References

1. A G C Mitchell and M W Zemansky (1961) Resonance Radiation and Excited Atoms (Cambridge University Press).
2. J A Harrison (1959), Proc. Phys. Soc. 73, 841.
3. P G Browne and M H Dunn (1973), J.Phys. B:Atom. Molec. Phys. 6, 1103 (and references therein).
4. T Goto, M Mori and S Hattori (1976), Appl. Phys. Lett. 29, 358.
5. Y Ichikawa and S Teii (1980), J. Phys. D:Appl. Phys. 13, 1243.
6. P G Browne (1974), Thesis (St Andrews).
7. H R Griem (1964) Plasma Spectroscopy (McGraw-Hill, New York).
8. F Dothan and Yu M Kagan (1981), J. Phys. B:Atom. Molec. Phys. 14, 183.
9. R Deloche, P Monchicourt, M Cheret and F Lambert (1976), Phys. Rev. 13A, 1140.
10. A J Dixon, M F A Harrison and A C H Smith (1976), J. Phys. B:Atom. Molec. Phys. 9, 2617.
11. J A Smit (1936), Physica 3, 543.
12. R L Abrams and G J Wolga (1967), Phys. Rev. Lett. 19, 1411.
13. A V Phelps (1955), Phys. Rev. 99, 1307.
14. W L Wiese, M W Smith and B M Glennon (1966), Atomic Transition Probabilities (NSRDS-NBS4).
15. R B Kay and R H Hughes (1967), Phys. Rev.154, 61.
16. A L McKenzie (1975), Thesis (St Andrews).

Figure 3.1 Comparison of the sum of the three Doppler broadened fine structure components of the He 294.51nm transition with a single Gaussian with the same centre and maximum, for a temperature of 600 K.

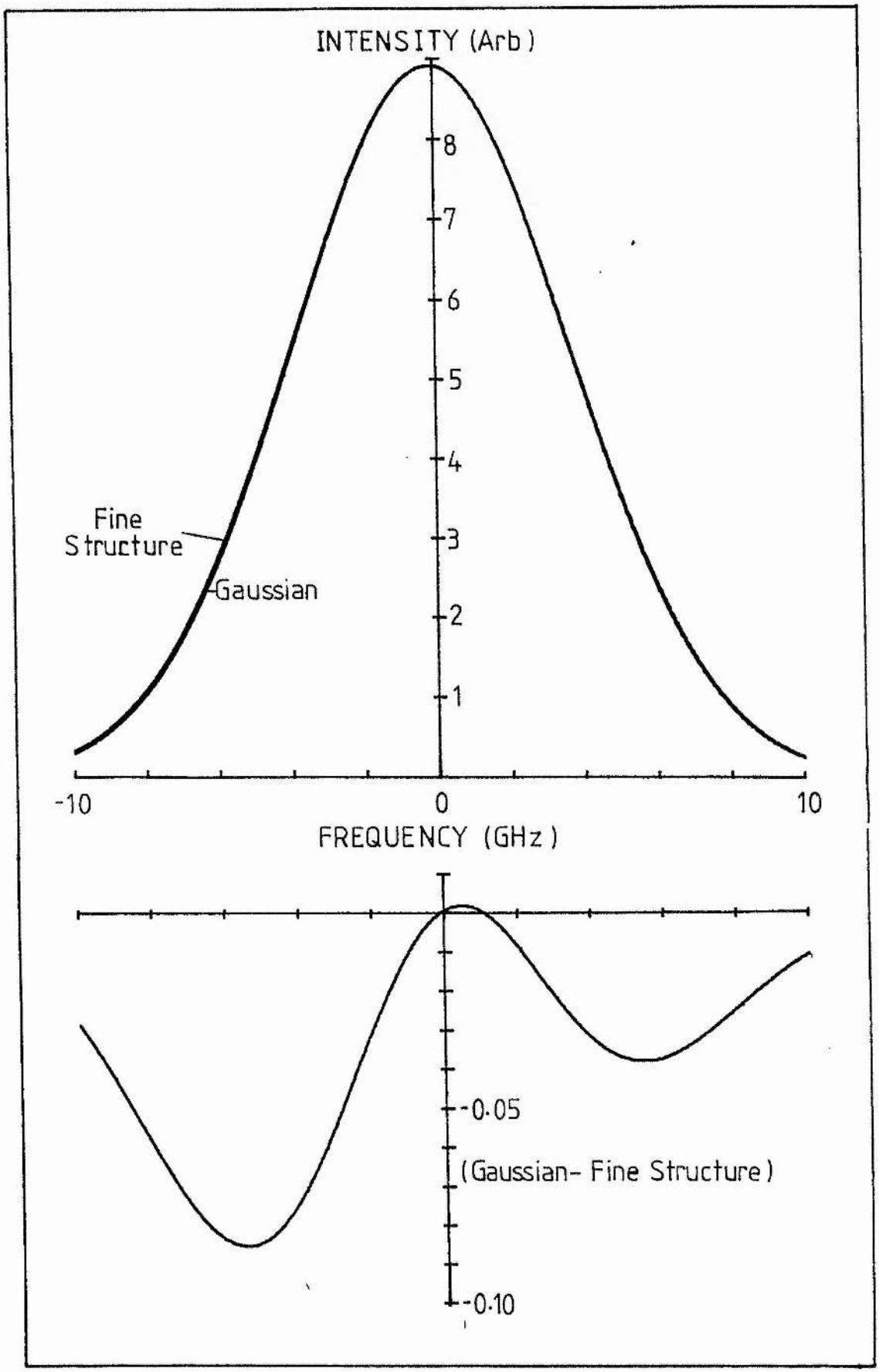

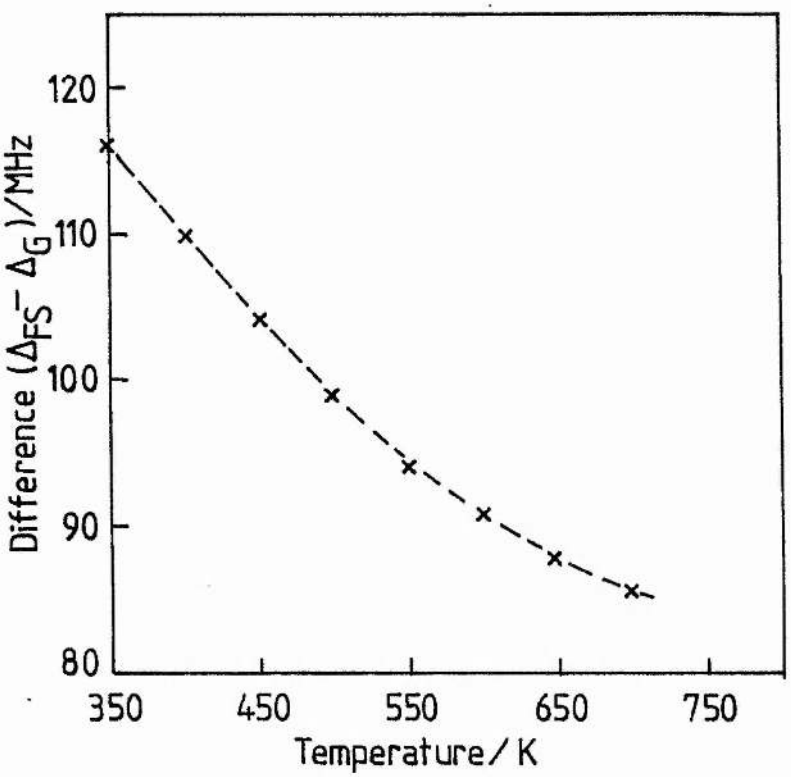

Figure 3.2 The width of the single Gaussian (Δ_G) subtracted from the sum of the Doppler broadened fine structure components (Δ_{FS}) of the He 294.51nm transition, as a function of gas temperature.

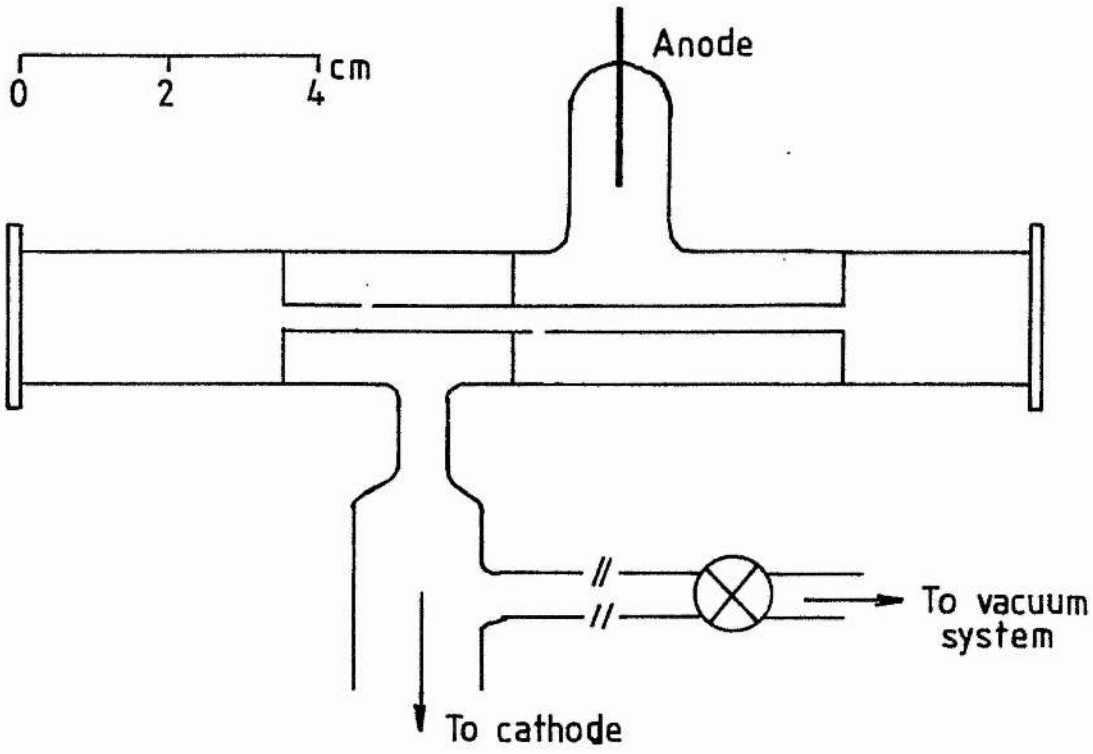

Figure 3.3 Schematic diagram of the discharge tube,to full scale.

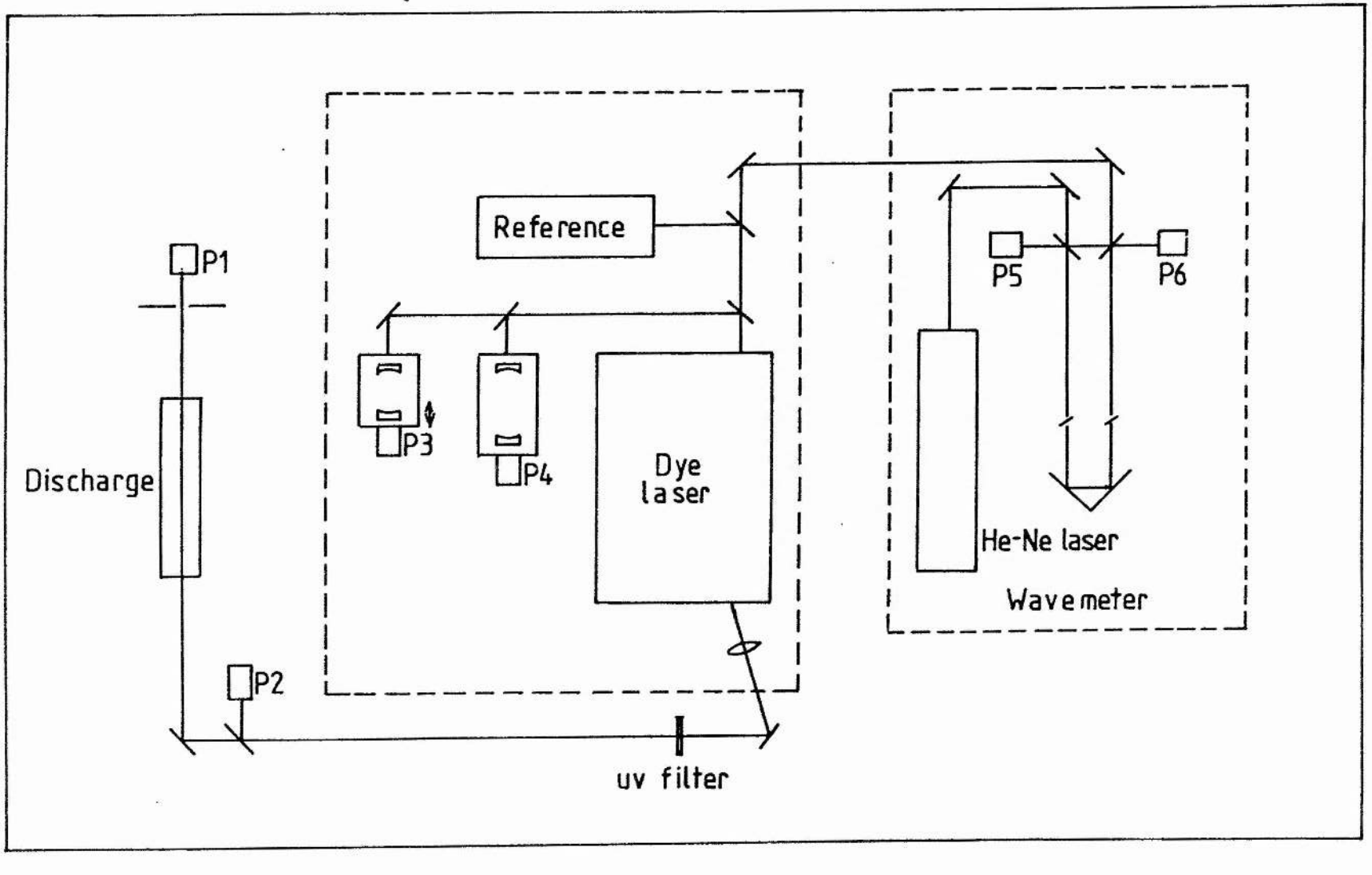

Figure 3.4 Experimental layout.

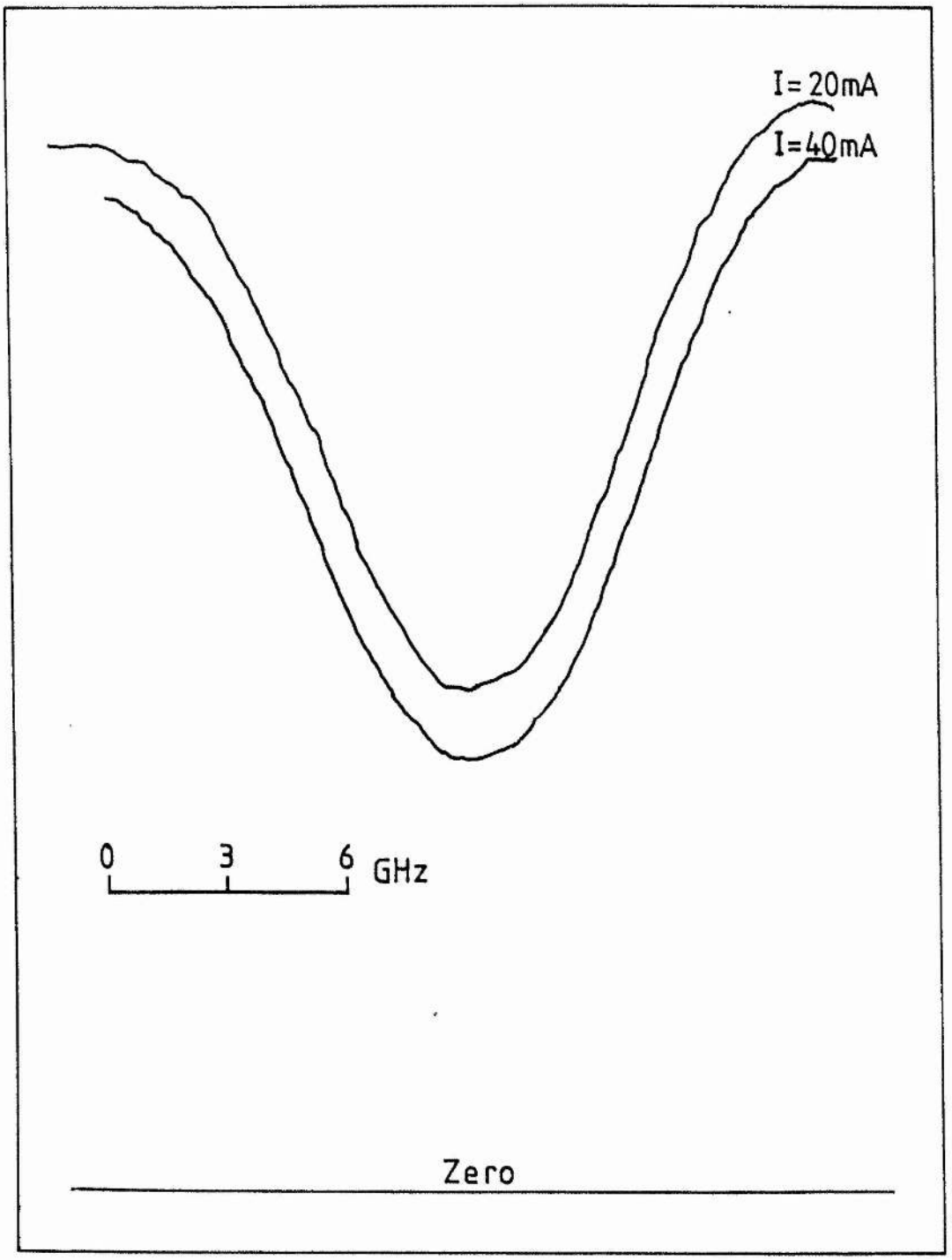

Figure 3.5 Sample Doppler broadened absorption profiles at p=2 Torr for currents of 20 and 40 mA.

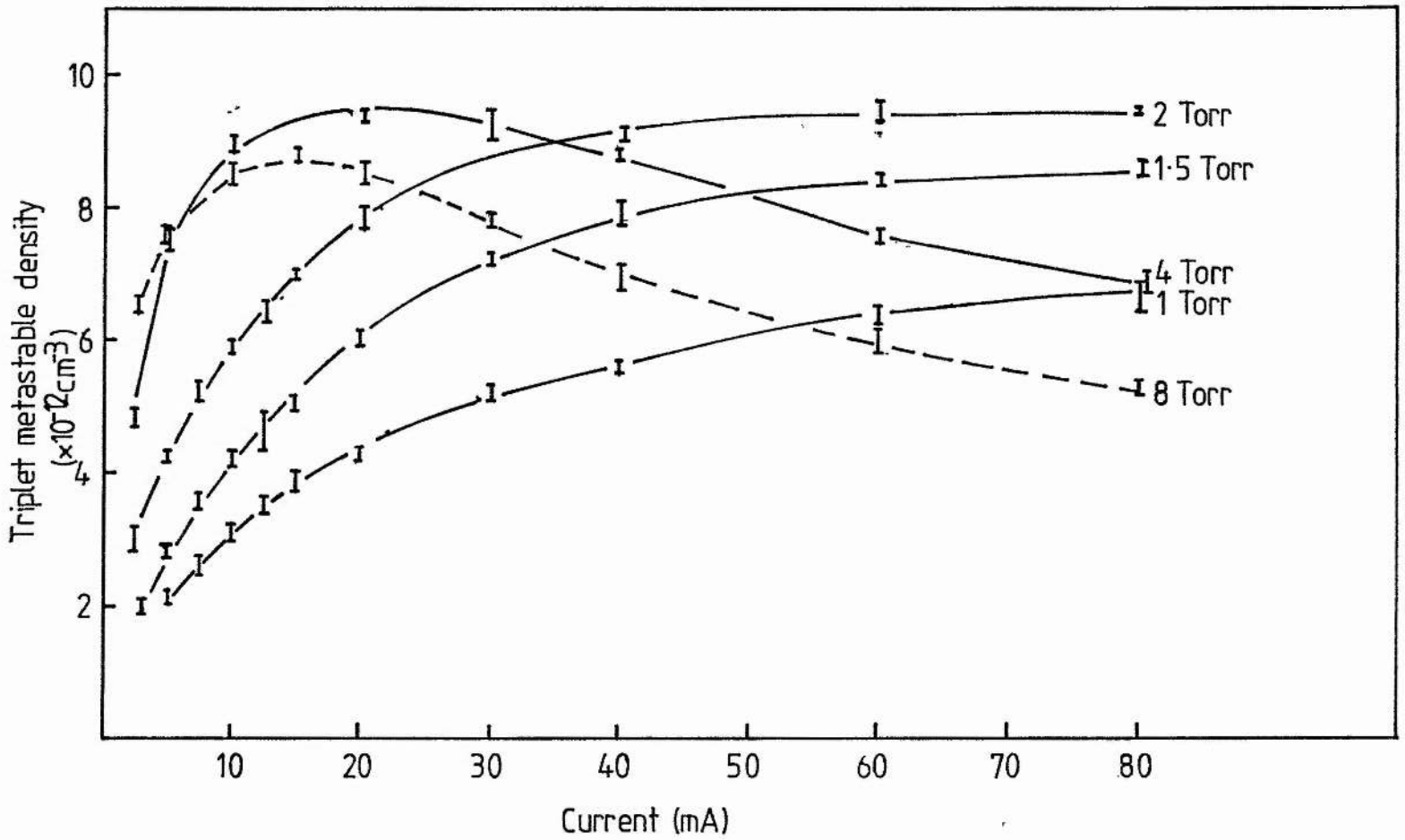

Figure 3.6 Helium triplet metastable density as a function of current for various pressures.

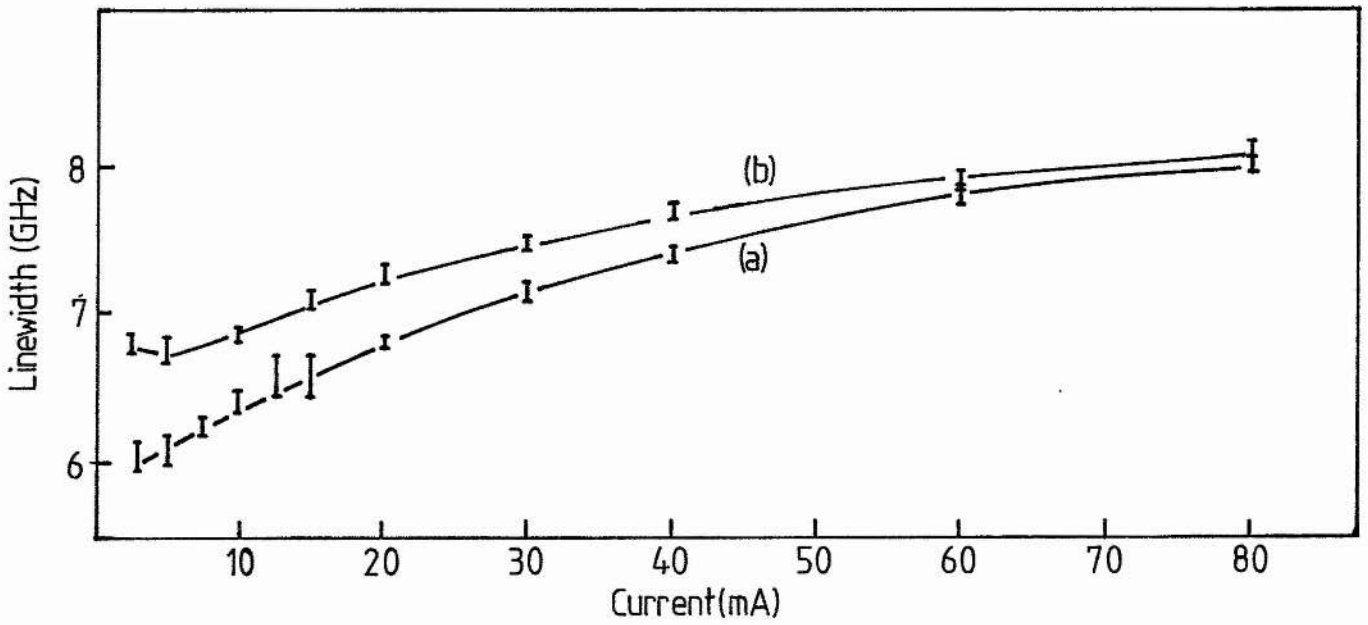

Figure 3.7 The full width at half maximum of the Doppler broadened absorption profile as a function of current for pressures of (a)1.5 and (b)8 Torr.

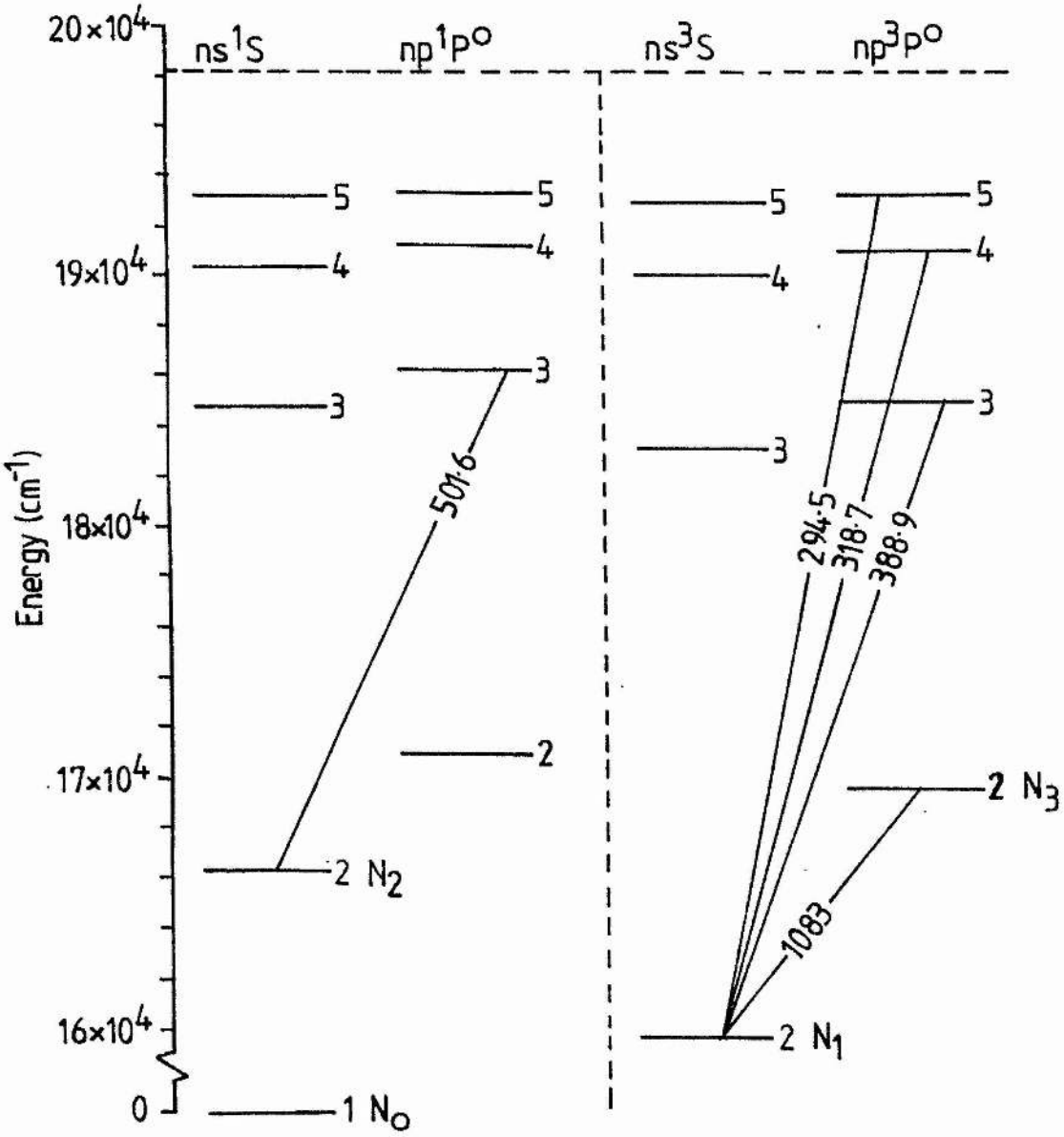

Figure 3.8 Partial Grotrian diagram for helium showing the 294.51nm transition.

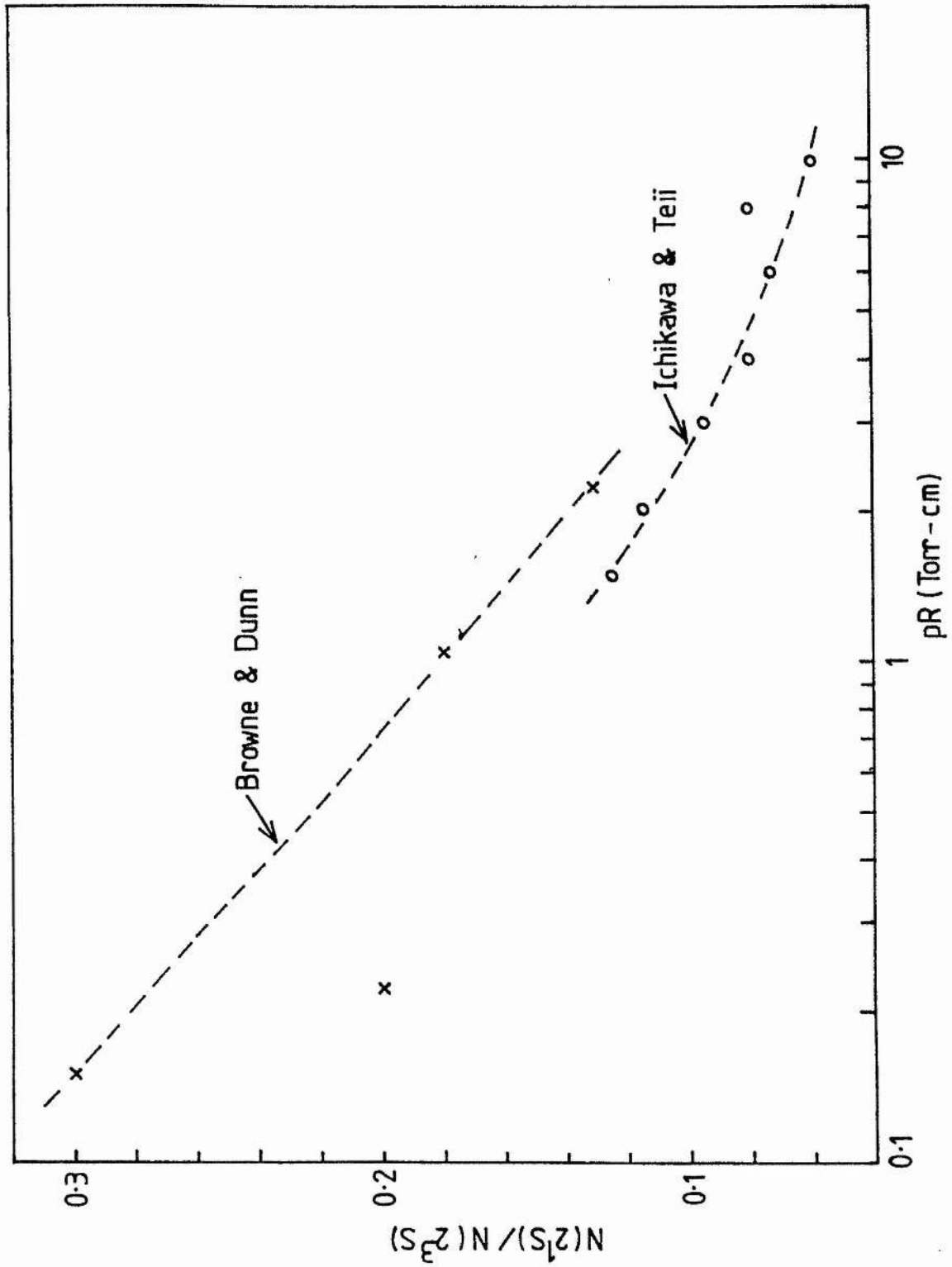

Figure 3.9 The ratio of singlet to triplet metastables as measured by Browne and Dunn [3] and Ichikawa and Teii [5].

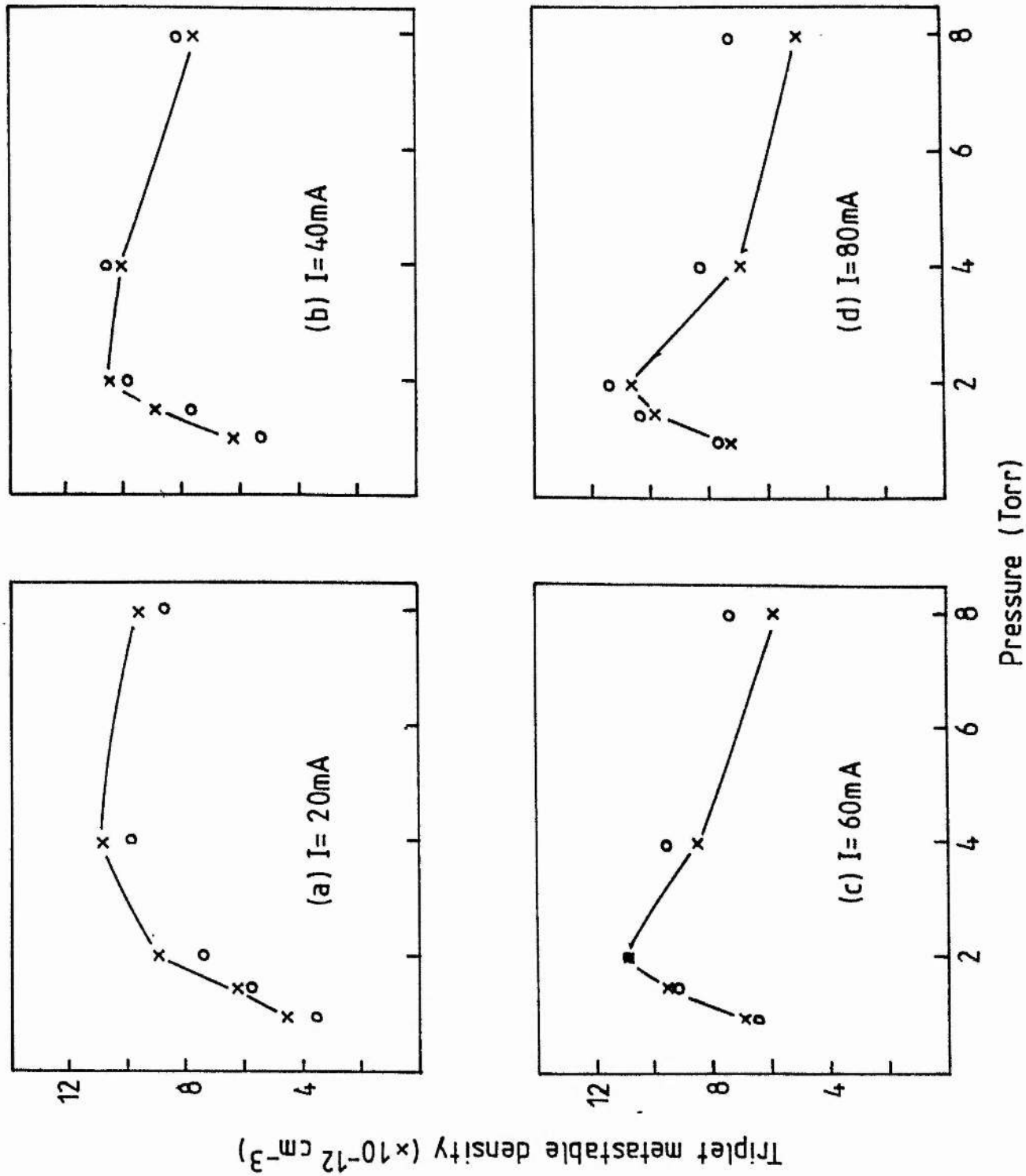

Figure 3.10 Comparison of measured triplet metastable (×) densities with those calculated (o) from the rate equation (6) assuming $\gamma = 4.2 \times 10^{-9}$ cm^3 s^{-1}.

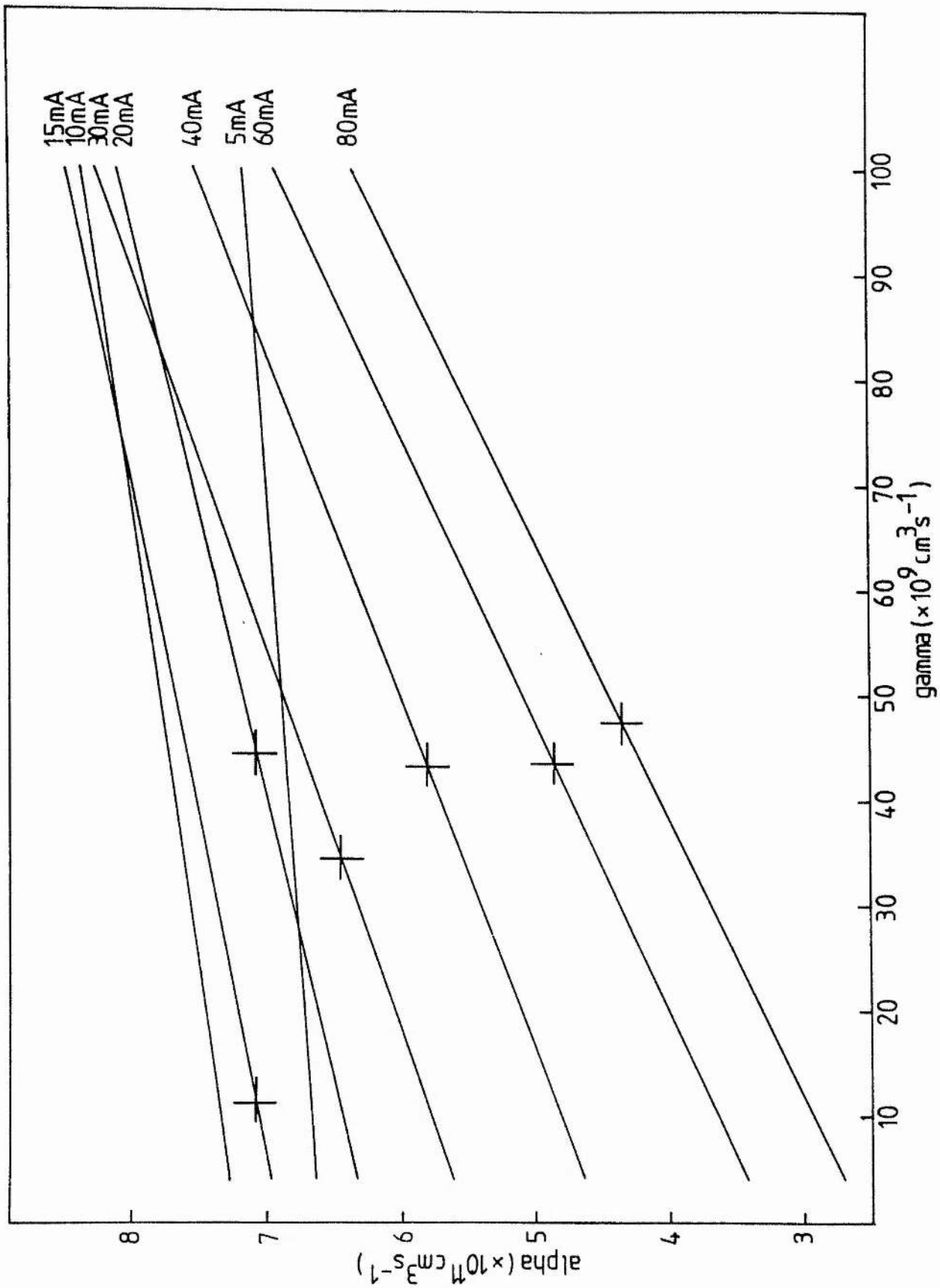

Figure 3.11 Values of α and γ which satisfy equation (6) using the experimental metastable densities, for various currents at a pressure of 1 Torr. Marked are the values of α derived from Smit [11] giving a fit for $\gamma = (4.3 \pm 0.5) \times 10^{-8}$ cm^3 s^{-1}.

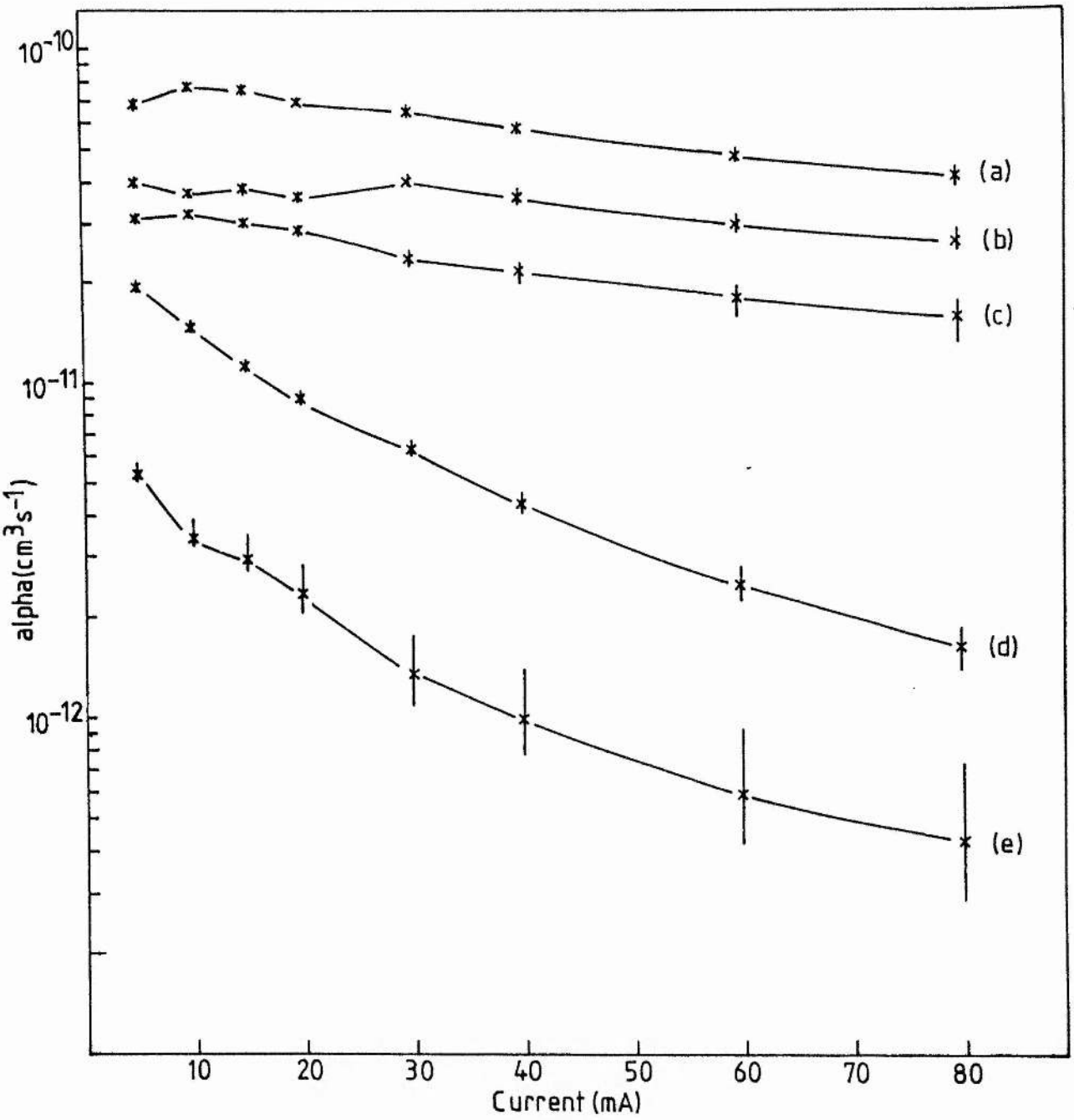

Figure 3.12 The values of α calculated from equation (6) using the best fit γ values and the experimental triplet metastable densities.
(a) p = 1 Torr, $\gamma = (4.3 \pm 0.5) \times 10^{-8} cm^3 s^{-1}$.
(b) p = 1.5 Torr, $\gamma = (2.5 \pm 0.5) \times 10^{-8} cm^3 s^{-1}$.
(c) p = 2 Torr, $\gamma = (1.6 \pm 0.6) \times 10^{-8} cm^3 s^{-1}$.
(d) p = 4 Torr, $\gamma = (0.8 \pm 0.3) \times 10^{-8} cm^3 s^{-1}$.
(e) p = 8 Torr, $\gamma = (0.8 \pm 0.4) \times 10^{-8} cm^3 s^{-1}$.

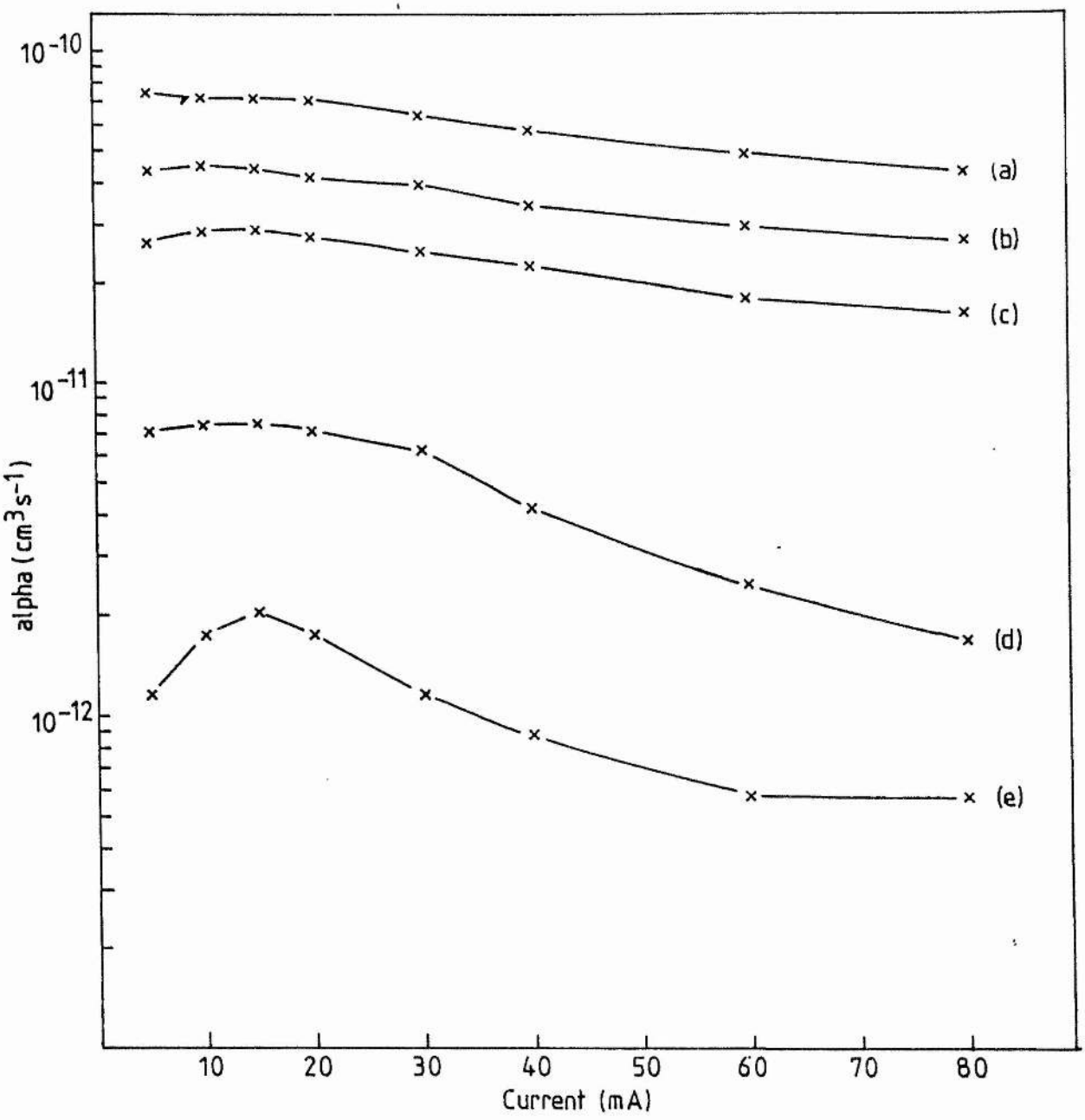

Figure 3.13 The values of α derived from Smit as a Function of current for various pressures. (a) p = 1 Torr. (b) p = 1.5 Torr. (c) p = 2 Torr. (d) p = 4 Torr. (e) p = 8 Torr.

CHAPTER 4

OPTOGALVANIC SPECTROSCOPY IN NEON

4.1 Introduction

The change in ionisation in a discharge, caused by illuminating one discharge with light from another, has been known for almost sixty years. In the past eight years, with the use of tunable dye lasers to irradiate discharges, a renewal of interest in this so called optogalvanic effect has led to its application to a large number of spectroscopic studies. These will be outlined with particular reference to studies in neon.

In this work experimental studies have been carried out in a neon positive column discharge. The optogalvanic line profile for the $1s_5$-$2p_2$ transition (Paschen notation) has been studied as a function of dye laser power (0-300mW) and discharge conditions (2-20 mA, 1-2.5 Torr) for a variety of experimental arrangements, incorporating simultaneous absorption and emission studies. Under certain discharge conditions the sign of the optogalvanic signal changes as a function of dye laser power.

In an attempt to model the above behaviour a set of four rate equations describing the populations of the $1s_5$, $1s_4$, $1s_3$ and $2p_2$ levels in neon, with and without resonant laser irradiation on the $1s_5$-$2p_2$ transition at 588.2nm, are proposed and solved in the steady state. The steady state values are used as initial values for numerical integration of the rate equations to show the time evolution of the various populations as the laser is switched on and off. A qualitative interpretation of the expected optogalvanic signal may be made from the results. In particular, it is seen that build-up in the $1s_3$ metastable density with laser irradiation on the 588.2nm transition can explain the observation of a sign reversal in the

optogalvanic signal in a neon positive column discharge.

4.2 Review of Optogalvanic Spectroscopy

When a discharge is irradiated with light of a wavelength corresponding to an allowed transition of the discharge species the populations within the discharge change thus giving rise to changes in the rate of ionisation. The most common effect is an increase in the ion density caused by increased population density of highly excited states due to optical pumping. These states have higher collisional ionisation rates as a larger percentage of the electrons in the discharge have sufficient energy to cause ionisation. An increase in the ion (and electron) density leads to a drop in the voltage across the discharge tube required to maintain the discharge. This drop in voltage may be measured as an increase in voltage across a ballast resistor in series with the discharge, at its anode, in a constant voltage supply regime. Transitions with a metastable lower level give rise to either increases or decreases in the voltage across the ballast resistor depending upon discharge conditions and the specific coupling mechanisms for the particular atomic or molecular species.

The first observation of this effect, called the optogalvanic effect, was made by Penning[1] who observed an increase in the voltage across a neon discharge when it was illuminated by a second neon lamp. This observation was predated by a related experiment [2] where ion formation was detected by employing thermionic diodes. Subsequent experiments studying the change in voltage across a discharge tube illuminated by another are detailed in references [3-9]. In particular, Drouet and Novak [7] noted that illuminating a neon discharge results in reductions of both the electron density and the

metastable density. They also measured the electron energy distribution and found that illumination caused a shift of electrons to lower energies.

The recent revolution in optogalvanic spectroscopy was started when Green et al [10] used a commercial CW dye laser (linewidth of approximately 0.003nm, tunable over a range 540-675nm, with typical powers of 100-200mW) to investigate the optogalvanic signal induced on transitions of lithium, sodium, calcium, barium, uranium, neon and helium in commercial hollow cathode lamps. The experimental arrangement, which is a standard one for laser linewidth-limited, or Doppler-limited studies, is shown in figure 4.1. The laser beam is chopped at frequency f and the optogalvanic signal produced at this frequency, developed across resistor R, is detected by a lock-in amplifier. Capacitor C is used to block the dc anode voltage. The advantages over fluorescence spectroscopy are that no optical detection apparatus is required, the signal obtained is insensitive to scattered excitation light and background light, and non-volatile species can be studied in hollow cathodes.

The optogalvanic effect has been used to frequency-lock a CW dye laser [11], provide calibration wavelength spectra, measure laser bandwidths (where these exceed the bandwidth of the transitions being used) [12], study line profiles [14] and to measure concentrations of metals in aqueous solutions of metal salts aspirated in a flame [13]. By having the flame inside the laser cavity [25] it has been possible to measure concentrations of Na (1ng/ml) at least an order of magnitude smaller than can be measured quantitatively by atomic absorption in flames.

A number of studies have been undertaken to determine if quantitative measurements of oscillator strengths and line broadening can be obtained from optogalvanic studies [17],[20],[29]. In classical absorption spectroscopy, the integral of the absorption coefficient k over the entire line profile, $\Phi_{ij}(\lambda)$, with centre wavelength λ_{ij} is related to the number of atoms, n_i, in the initial state and the oscillator strength $g_i f_{ij}$, of the transition. For weak absorption ($kl \ll 1$, with l the length of the sample) a simple linear relation,

$$\int k d\lambda = c\lambda_{ij} n_i g_i f_{ij}, \qquad c=\text{const} \tag{1}$$

can be used.

Keller et al [20] and Zalewski et al [17] proposed that the magnitude of the optogalvanic signal, U_{ij}, divided by the laser power P was proportional to the absorption of the laser radiation. Assuming the population of the excited states of the atoms in the discharge to be described by a Boltzmann distribution with an excitation temperature T this gives:

$$U_{ij}/P \propto \lambda_{ij} n_o g_i f_{ij} \exp(-E_i/kT) \tag{2}$$

A good fit to this relation was found for 2p-3s, -4s and -4d (Paschen notation) transitions in neon. Extending the relation to take account of the branching ratio for radiative decay of the $2p_n$ levels to the various $1s_m$ levels and the quantum yield for the decay of $1s_m$ back to the ground state, it gives reasonable agreement for $2p\text{-}1s_5$, $1s_3$ and $1s_2$ transitions as well [17]. The $2p_n\text{-}1s_4$ transitions did not fit into this simple theory. The relation was also verified experimentally using more than 33 lines in uranium with a range of excitation energies, E_i, from 0-10000 cm^{-1} [20]. Deviations from

equation (2) (up to a factor of 2.5) were said to be due to inaccuracies in the calculated oscillator strengths. Bachor et al [29] investigated 15 lines in calcium in the wavelength range 551-559nm and 580-620nm. The oscillator strengths of these transitions are well known. The experimental uncertainty due to current instability, laser power uncertainty and spatial dependence of the optogalvanic signal was estimated as less than 25% with a 67% confidence. The results did not agree with equation (2) within the estimated errors and thus the assumption of a simple Boltzmann distribution appears invalid. Thus it would appear that, for some plasmas, optogalvanic detection is not a suitable method for measuring oscillator strengths since the population distribution in the plasma needs to be well known. Also, the large experimental uncertainty prevents it from being used as a high precision technique in any plasma. Bachor et al [29] also compared the optogalvanic line profile with the absorption profile for thirteen transitions in Ne, Ar and Cu in the current range 20-1500mA. For low currents (<100mA) they found the optogalvanic profile and absorption profiles were identical. For some transitions, as the current increases the half width of the optogalvanic profile becomes larger than the halfwidth of the absorption profile. Then, at higher currents, some profiles show dips at line centre. Bachor et al [29] concluded that reliable optogalvanic profiles may be observed in general for peak absorptions below 20%.

Further laser linewidth-limited or Doppler-limited optogalvanic experiments have included careful mechanistic studies in neon [15-17]; studies on infrared transitions in He [21], transitions in high pressure Hg and Na arc discharges [24], transitions in a prebreakdown neon discharge [26]; and studies of transient signals for neon $1s_i$-$2p_k$ transitions with pulsed and chopped CW laser excitation [28],[31].

There is a most promising future for optogalvanic spectroscopy in investigating gas discharge physics.

It is possible to use optogalvanic detection in a number of the standard experiments of laser spectroscopy. Doppler free spectra, double resonances, Rydberg series and level crossings have all been observed optogalvanically. A number of molecular spectra have also been studied, though, in general, it is quite difficult to get quiet discharge operation for molecular species. A summary of the studies which have appeared in the literature (possibly incomplete) is given in tables I and II.

Doppler free intermodulated optogalvanic spectroscopy (DFIOGS) is analogous to intermodulated fluorescence spectroscopy (discussed in section 5.2). The experimental arrangement is shown in figure 4.2. The CW laser beam is split into two parts of approximately equal intensity, one is chopped at frequency f_1, the other at frequency f_2. These two chopped beams pass through the discharge in opposite directions and, as with saturated intermodulated fluorescence, nonlinear signals at $(f_1 + f_2)$ and $(f_1 - f_2)$ are produced only when both beams interact with the zero velocity class of atoms, with respect to the laser propagation direction. A significant advance was made by using vacuum tube oscillators to excite the discharge. The change in impedance of the rf discharge produced by laser irradiation, by reaction on the oscillator is detected [37],[38]. This allows discharges to be run at low pressures (20-30mTorr) and prevents some of the problems of velocity changing collisions spoiling a signal, for studies on transitions with long lived lower states.

A number of studies of the optogalvanic signal induced in a neon hollow cathode discharge by chopped dye laser light (at wavelengths resonant with transitions between the $1s_m$(m=2,3,4,5) and $2p_n$(n=1 to 10) electronic states) have been carried out [15,16,17]. In general, the impedance of the discharge increases with resonant irradiation on transitions starting from the $1s_3$ and $1s_5$ metastable levels and decreases for transitions from the $1s_2$ and $1s_4$ levels, which may decay radiatively to the ground state. The impedance increase for $1s_3$ and $1s_5$ transitions arises because the metastables (which provide an effective pathway for ionisation) are depleted and thus the electron density decreases. The metastables are depleted because the excitation to the 2p level may be followed by radiative decay to the $1s_2$ and $1s_4$ levels which are radiatively coupled to the ground state. Decreased discharge impedance for transitions which originate in the $1s_2$ and $1s_4$ levels arises because radiative decay of the excited 2p levels increases the metastable populations, and thus the electron density. In both cases ionisation is enhanced through an increase in the population density of the 2p state which is more readily ionised than the 1s state because a greater fraction of the electrons have the required energy. For the case of $1s_{3,5}$-2p transitions, this process competes with metastable population depletion, which leads to decreased ionisation, and is cited by Smyth and Schenck [15] as the reason that the optogalvanic signal changes sign from positive to negative at high currents, in some discharges, on these transitions.

More recently the transient behaviour of the optogalvanic signal generated on $1s_m$-$2p_n$ transitions has been investigated [18,28,31]. With pulsed excitation [18,28] transitions from the $1s_5$ metastable level have an optogalvanic signal, measured across a ballast resistor, of the form of a fast negative voltage spike (5μs) followed by a

slower (30μs) positive pulse. Transitions from the $1s_2$ level give an optogalvanic signal which is essentially a mirror image of that for the $1s_5$ transitions. Using chopped CW laser radiation [31] the transient optogalvanic signal following both the turn-on and turn-off of the irradiation have been studied. These transients were small in magnitude compared with the steady state signal for the $1s_5 - 2p_2$ transition. Uchitomi et al [31] obtained reasonable fits to the transient signals they observed, using a rate equation model allowing collisional mixing among the 2p levels near to the 2p level being optically pumped. The steady state signal for the $1s_5$-$2p_2$ transition was positive, corresponding to a decrease in electron density.

4.3 The $1s_i$ and $2p_k$ Energy Levels in Neon

The lowest excited energy levels in atomic neon are formed by promotion of a 2p electron into the 3s orbital. The four energy levels that arise from this promotion are the result of paired and unpaired electron spins and are labelled: $1s_2$(singlet); $1s_3$, $1s_4$ and $1s_5$(triplet) in Paschen notation to denote their common origin. The $1s_3$ and $1s_5$ levels are metastable with collision free lifetimes of 430s and 24.4s respectively [54]. The $1s_2$ and $1s_4$ levels are coupled radiatively to the ground state and have lifetimes 1.5×10^{-9}s and 2.1×10^{-8}s respectively, without radiation trapping [55].

The next series of levels result from promotion of a 2p electron to a 3p orbital, denoted $2p_k$, k=1 to 10, in Paschen notation. This part of the energy level scheme in neon is shown in figure 4.3.

The arbitrary Paschen notation is commonly used for neon as the coupling scheme which adequately describes the levels, called jl coupling, has cumbersome notation [56]. LS coupling notation is sometimes used. This is reasonably accurate for the 1s levels which become $^1P_1$, $^3P_0$, $^3P_1$ and $^3P_2$ respectively, but is inadequate for the 2p levels.

The levels of noble gas atoms are conveniently classified by the following scheme, which takes account of the fact that the spin-orbit interaction of the electrons of the atomic core is greater than the electrostatic interaction of these electrons with the excited electron. The atomic core is characterised by quantum numbers L, S and j, where L is the orbital angular momentum of the atomic core, S is the spin of the atomic core, and j is the total angular momentum of the atomic core. Due to the electrostatic interaction of the excited electron with the electrons of the atomic core, the state LS_j1 gives a series of levels, each of which is described by the quantum number K corresponding to $\underline{K} = \underline{j} + \underline{1}$. Finally the spin orbit interaction of the excited electron leads to the splitting of each level of LS_j1K into the two J components. The total angular momentum of the atom is denoted by $J=\underline{K}\pm 1/2$.

The level is described by the set of quantum numbers LS_j1KJ when classified by this scheme. The following notation is used:

$$^{2S+1}L_j nl[K]_J$$

The first excited configuration for neon $2p^5 3s$ gives rise to four levels

$$2p^5\ ^2P_{3/2}3s[3/2]_{2,1}$$
$$2p^5\ ^2P_{1/2}3s[1/2]_{1,0}$$

The $2p^5 3p$ configuration gives rise to ten levels:

$$2p^5\ {}^2P_{3/2}3p[1/2]_{0,1}$$
$$2p^5\ {}^2P_{3/2}3p[3/2]_{1,2}$$
$$2p^5\ {}^2P_{3/2}3p[5/2]_{2,3}$$
$$2p^5\ {}^2P_{1/2}3p[3/2]_{1,2}$$
$$2p^5\ {}^2P_{1/2}3p[1/2]_{0,1}$$

4.4 Experimental Studies at 588.2nm in Neon

The basic experimental arrangement is shown in figure 4.4.1. The laser is a Spectra-Physics 380-D ring dye laser operated with Rh6G dye in a single, tunable mode. The output power is attenuated by a Glan-Taylor polariser. A 752MHz free spectral range confocal interferometer is used for frequency calibration. The laser beam is chopped at 10-2000 Hz.

In the investigations in a positive column discharge described here the optogalvanic signal is taken from the cathode side of the discharge tube. This means that an increase in voltage across the tube gives rise to a negative voltage signal. Thus the sign of the optogalvanic signal matches the electron density behaviour, being negative for a decrease in electron density. A negative voltage signal in this work is the same as a positive voltage in the papers referenced above. The line profiles observed show a wealth of structure and indicate that the optogalvanic signal is the result of complicated interactions among the levels of interest.

The quartz discharge tube, shown in plate 1, has a bore diameter of 8mm and the length of discharge in the beam path is 100mm. The cathode is a hollow cylinder of stainless steel 20mm from the discharge length under study at its closest end. Naturally occurring

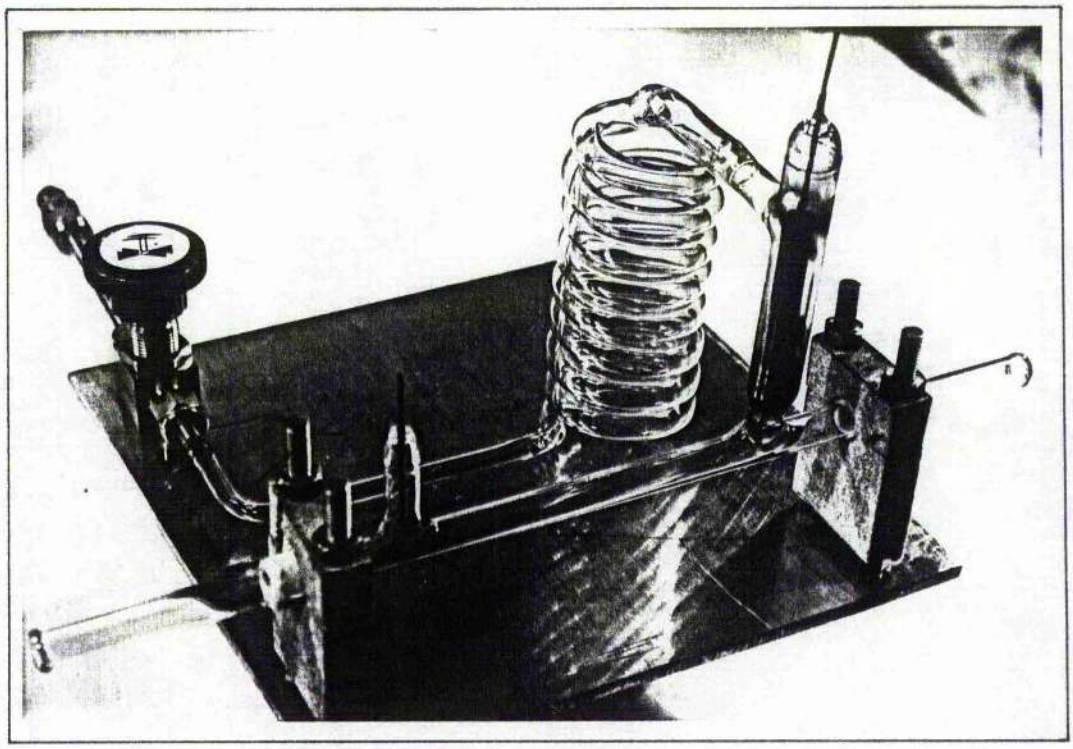

Plate 1 Discharge Tube.

neon is used so all line profiles show the partially resolved peak due to Ne^{22}.

A narrow band amplifier is used for viewing the time behaviour of the optogalvanic signal, to discriminate against the 100kHz oscillations on the discharge tube voltage. The unfiltered signal is monitored simultaneously.

Figure 4.4.1 shows an arrangement for recording the axial optogalvanic profile and the saturated absorption profile simultaneously as the laser frequency is scanned through the 588.2nm neon transition. The other experimental arrangements all utilised similar diagnostics to those shown in figure 4.4.1. A description of the way in which measured changes in voltage across the ballast resistor are related to the change in the electron density is given in appendix D.

In the arrangement shown in figure 4.4.2 the transverse optogalvanic signal is monitored as a function of transverse position of the discharge in the laser beam. The discharge is divided into twenty five 5mm sections for this purpose. The absorption profile can no longer be monitored satisfactorily due to scattering and distortion in the cylindrical discharge tube. In figure 4.4.3 the axial optogalvanic signal is monitored simultaneously with the emission intensity at various transverse positions. Figure 4.4.4 shows the axial optogalvanic signal and the emission intensity of specific neon transitions being monitored as the laser frequency is scanned through the 588.2nm transition. Finally, in figure 4.4.5 the emission intensity is being monitored at various transverse positions in the discharge on both sides of the discharge volume being optically pumped at 588.2nm.

In all the experiments documented the discharge is illuminated from the cathode end of the discharge tube. Further fine structure on the optogalvanic line profiles is observed when the anode end is illuminated first, arising from spikes on the optogalvanic signal.

4.4.1 Axial Optogalvanic/Absorption Studies

Figure 4.5 shows the optogalvanic and saturated absorption line profiles for a pressure of 1 Torr and current of 8mA, for two laser powers. No distortions in either the optogalvanic or saturated absorption profiles are found for currents in the range 2-20mA.The optogalvanic signal is always a negative voltage.

At pressures in the range 1.2-1.5 Torr optogalvanic line profiles like those shown in figure 4.6 are obtained, as a function of laser power, for small discharge currents. The saturated absorption profiles are undistorted in all cases though unfortunately the linear absorption is 100%. The saturated absorption as a function of laser power is shown for a current of 5mA in figure 4.7. For small laser powers the optogalvanic signal is predominantly negative. As the dye laser power increases the signal changes sign to positive for the central frequencies of the line. Also, at higher laser powers the width of the optogalvanic line profile is broader than the width of the absorption profile. This broadening arises because the optogalvanic signal saturates at line centre at laser powers of about 5mW while the signal continues to grow in the wings of the line as the irradiating power increases beyond this. The frequency range for which the signal is positive increases with increasing dye laser

power.

Optogalvanic line profiles for a neon filling pressure of 2 Torr are shown in figure 4.8. The voltage optogalvanic signal is always negative but the line profile shows reproducible peaks on the sides. These behave in a similar manner to the sign reversal occurring at 1.5 Torr, in that they occur further out in the wings of the line as the dye laser power is increased. Again no distortion of the saturated absorption profile is observed and the optogalvanic linewidth is larger than the absorption linewidth.

The results of monitoring the optogalvanic signal at the centre of the 588.2nm transition as the dye laser power is increased smoothly from 0-300mW, for a pressure of 1.5 Torr, are shown in figure 4.9. As the discharge current increases it becomes increasingly difficult to induce the sign change in the optogalvanic signal. For a current of 5mA the voltage optogalvanic signal is negative for small powers, switches to positive at medium powers and then switches back to being negative. This suggests there is a large spatial component to the observed signal caused by differential averaging over a non-uniform axial population distribution.

The irradiating laser power ranges for which the magnitude of the optogalvanic signal divided by the laser power, U_{ij}/P, is a constant are given in table III. A lower power limit is expected in these circumstances because for low irradiating powers only a small section of the discharge is perturbed. The relative size of U_{ij}/P for a neon pressure of 1.5 Torr and for the various currents, followed the expected trend of decreasing with increasing current, due to the decreasing lifetime of the metastable state.

Table III

Power Ranges for which the Optogalvanic Signal is Linear

Pressure Torr	Current mA	Laser Power Range for which U_{ij}/P is constant/mW	U_{ij}/P	Uncertainty
1	9	-		5%
	16	<3	58	5%
1.5	5	2.5-10	90	10%
	8.8	3.6-17.6	80	7%
	13.1	3.5-50	50	8%
	17.5	0-30	35	10%
2	23	3-20	60	20%

For a pressure of 1.5 Torr similar behaviour to that described above is observed on the $1s_5$-$2p_4$ and $1s_5$-$2p_5$ transitions at 594.5nm and 597.6nm, respectively. The transitions $1s_2$-$2p_1$ at 585.2nm, $1s_3$-$2p_2$ at 616.4nm and $1s_4$-$2p_2$ at 603.0nm all gave rise to well behaved optogalvanic line profiles without any sign reversals for the power and current range investigated.

4.4.2 Time variation of the Axial Optogalvanic Signals

Figure 4.10 shows tracings from oscilloscope photographs of the optogalvanic signal, for discrete laser frequencies, as the laser is tuned from the wings of the 588.2nm line to its centre for a pressure of 1.5 Torr and a current of 8mA. This sequence is typical of the

reversal in the negative voltage optogalvanic signal. In other cases the signal became clearly positive as opposed to the zero, steady state, laser-on signal at line centre shown in this sequence. For large $B(\nu)I$, where B is the stimulated emission coefficient (in inverse intensity units per unit time) and I is the laser intensity, the signal shows a negative transient when the dye laser power is switched on and off. At intermediate BI values oscillations are induced in the discharge voltage when the discharge is irradiated and these were almost always observed before the onset of a change in the sign of the optogalvanic signal. With phase sensitive detection for the steady state measurements, the magnitude of the signal will depend on the laser frequency at which the signal is optimised (chosen in the wings of the line here), chopping frequency, duty cycle, the ratio of transient signal to steady state signal in time and beam diameter. When the steady state optogalvanic signal is positive (reversed), the sign reversal behaviour is diminished by increasing the chopper frequency. This decrease in the positive voltage occurs because the proportion of the laser-on time taken up by the negative voltage transient increases. The positive signal at line centre for high laser powers is a steady state signal and does not arise from transients. However, in systems like neon the PSD signal should always be interpreted taking account of the observed time resolved behaviour.

4.4.3 Transverse Optogalvanic Studies

The results of using the experimental arrangement in figure 4.4.2 to investigate the transverse spatial variation of the optogalvanic signal are shown in figures 4.11 and 4.13. Measurements are made at 5mm intervals along the discharge or closer if continuous scans showed important features in the intervening discharge length. For a pressure of 1 Torr the sign of the signal changes smoothly from positive to negative from cathode to anode. Thus the negative axial signal obtained is a spatial average. The effect of spatially averaging over adjacent volumes, with different signs for the optogalvanic signal, is shown in figure 4.12. In figure 4.12 a series of laser scans through the 588.2nm transition recorded with the beam in the region 20-40mm from the cathode end of the discharge tube are shown.The sign of the optogalvanic signal changes in this region. The different spectra are obtained by shifting the discharge tube through the laser beam in steps of one or two millimetres. Complex line profiles are generated in this region, though no sharp discontinuities are observed. The positive optogalvanic signal probably arises from a positive space charge, in front of the cathode, which is diffuse at low pressures. That a negative axial optogalvanic signal is obtained for small dye laser powers, where mainly the cathode end of the discharge is perturbed, is surprising. Integrating the transverse signal measured, over the discharge length, does give a negative result (for currents of 3.8mA, 7.5mA, 12.5mA and 18mA with irradiating powers of 230mW and 30mW), confirming that a negative axial signal will be observed. The signal did not change sign as a function of dye laser power for any transverse position, at a pressure of 1 Torr. This is in contrast to results for pressures of 1.5 and 2 Torr, where at various transverse positions in the discharge, the signal changes

sign from negative to positive as the dye laser power is progressively increased, other discharge conditions being maintained the same.

Figure 4.13 shows the transverse optogalvanic signal for a pressure of 1.5 Torr, current of 5mA and two irradiating laser powers. The signal is always negative for an irradiating power of 3mW but changes sign to be positive at three transverse positions in the discharge when the laser power is increased to 260mW. The discharge is optically thin across its width so this sign change, with increasing dye laser power, is not caused by spatial averaging of differentially perturbed discharge volumes. The top traces show the emission intensity from the discharge, observed transversely. These traces are recorded with the beam passing axially through the discharge. In one trace the laser is tuned to resonance for the 588.2nm transition, in the other it is tuned off resonance. At transverse positions where a positive line centre signal is observed, laser frequency scans through the 588.2nm transition generated line profiles of the form shown in figure 4.6 for high laser powers. Positive signals arise behind the anode and cathode because any ionisation in these regions will give an increase in the electron density.

An attempt was made to measure the $1s_5$, $1s_4$ and $1s_3$ population densities by monitoring the transverse linear absorption profile for the $1s_5$-$2p_2$, $1s_4$-$2p_2$ and $1s_3$-$2p_2$ transitions. These measurements gave $(10\pm2)\times10^{11}cm^{-3}$, $(3.6\pm0.5)\times10^{11}cm^{-3}$ and $(0.6\pm0.2)\times10^{11}cm^{-3}$ for the $1s_5$, $1s_4$ and $1s_3$ level densities respectively, for a pressure of 1.5 Torr and a current of 8.8mA. The errors are derived from spatial variations. These densities are not inconsistent with those measured in more favourable geometries by other experimenters. Ichikawa and Teii [57] obtained values of about 7×10^{11} and $10^{11}cm^{-3}$ for the $1s_5$

and $1s_3$ densities respectively, for 1.5 Torr of neon in a positive column discharge. Zalewski et al [17] measured 4×10^{11}, 3×10^{11} and 10^{11} cm^{-3} for the $1s_5$, $1s_4$ and $1s_3$ densities respectively, in a commercial hollow cathode discharge with the tube initially filled with 7 Torr of neon. The ratio of the $1s_4$:$1s_5$ and the $1s_3$:$1s_5$ densities are (0.37 ± 0.11) and (0.059 ± 0.013) respectively. Only one tranverse position where a sign reversal of the optogalvanic signal is observed could be monitored in absorption. This position showed the largest value (0.072) for the $1s_3$:$1s_5$ population density ratio. The population density measurements are only valid if the $2p_2$ population density is negligible compared to the lower level population density. If this is not the case then the population densities will be underestimated and the $1s_3$ density is the most sensitive to this.

4.4.4 Optogalvanic/Emission Studies

Concentrating on the pressure of 1.5 Torr where the sign reversal of the axial optogalvanic signal as a function of $B(\nu)I$ is observed, it is found that the emission intensity from the discharge had maxima at the three transverse positions where the optogalvanic signal changed from negative to positive with increasing dye laser power. This is depicted in the upper trace of figure 4.13. The maxima are much broader than the lengths of discharge giving rise to sign reversals in the optogalvanic signal but do indicate that these reversals occur in regions of local maxima in the population densities of excited species.

Monitoring the emission at 588.2nm (using the arrangement in figure 4.4.4), as the dye laser frequency is tuned through the transition, it is seen (figure 4.14) that the emission intensity starts to rise at the same frequency that the optogalvanic signal starts to go positive. Thus the reversal onsets when the $2p_2$ population starts to increase. Monitoring the emission intensity of other lines in the 1s-2p group indicates that relaxation among the 2p levels also plays a role in the step ionisation process. For example during a scan generating an optogalvanic line profile like that in figure 4.14 the emission intensity on the $1s_5$-$2p_6$ line at 614.3nm decreased by 8% while the emission intensity on the line $1s_5$-$2p_4$ at 594.4nm increased by 4%, as the dye laser was scanned through the $1s_5$-$2p_2$ transition. A simple depletion of the metastable population without collisional relaxation between the 2p levels would lead to both these intensities decreasing. There is also structure on the emission intensity, as the laser frequency is scanned through the 588.2nm transition, which in some cases follows the distorted line profile of the optogalvanic signal. Other changes in the emission intensity measured with the laser tuned to the centre of the 588.2nm transition and with 260mW of 588.2nm dye laser light passing axially through the discharge are: a 0% change on the $1s_2$-$2p_1$, 585.2nm line; a 2% increase on the $1s_4$-$2p_3$, 607.4nm line and a 14% increase on $1s_3$-$2p_5$, 626.6nm line. The latter is preceded by a reduced emission intensity, with respect to the unperturbed intensity, when optical pumping in the wings of the 588.2nm line.

Using the arrangement in figure 4.4.5 no measurable change in the total emission intensity is caused on either side of the transverse laser beam position, at distances 15mm and greater from the beam position. The smallest separation of laser beam and pinhole

attainable is 15mm.

4.4.5 Results in Other Discharges

The optogalvanic sign reversal observed appears to be unique to this particular discharge, but studies in a 6mm diameter, 20mm discharge length and in a 3mm diameter, 23mm discharge length show time varying behaviour similar to that in figure 4.10. The magnitude of the effect is insufficient to cause a sign reversal but up to a 50% reduction in the signal magnitude at line centre is observed.

4.5 Rate Equation Analysis

A number of rate equation and phenomenological models of the steady state and transient optogalvanic effect have been developed [19,18,22]. Many of them are specific to neon [17,26,31]. For resonant laser irradiation on the $1s_5$-$2p_2$ transition in neon they all predict a steady state decrease in electron density. The above observations in a neon positive column show the electron density decreases with optical pumping of the 588.2nm transition for low laser powers but increases, for certain discharge conditions, at high laser powers. An attempt to model this behaviour is described. All the level populations are treated separately, in contrast to previous models, where the lower levels are paired as the radiative $1s_2$ and $1s_4$, and metastable $1s_3$ and $1s_5$ levels. It is found that if the $1s_3$ density is about one tenth of the $1s_5$ density and the rate coefficients for metastable-metastable collisional ionisation for both $1s_3$ and $1s_5$ metastables are equal, the results of the rate equation analysis here, are consistent with experimental results in neon hollow

cathode discharges [15,17]. When the $1s_3$ density is larger, and/or its cross section for destruction in metastable-metastable collisions leading to ionisation is larger than that for the $1s_5$ metastables, a reversal of the type observed in the experiments presented above is predicted.

4.5.1 Analysis

The neon energy levels involved and the coupling between them, included in the rate equations, are shown in figure 4.3. The collision partner is given and the rate coefficient symbol is in brackets beside it. The processes involved are:

(1)Direct excitation $Ne(^1S_0) + e \rightarrow Ne^* + e$

with rate coefficient α_i, where Ne^* is a metastable or more highly excited atom.

(2)Direct ionisation $Ne^* + e \rightarrow Ne^+ + 2e$

(3)Metastable-metastable collisions with rate coefficient β_i

$$Ne^* + Ne^* \rightarrow Ne^+ + Ne + e$$

(4)Diffusion to the walls with reciprocal lifetime τ_i.

(5)Spontaneous emission on allowed radiative transitions, A_{ik}.

(6)Stimulated absorption on the $1s_5$-$2p_2$ transition.

The rate equations obtained are:

$$dN_5/dt = \alpha_5 N_0 n_e + A_{65} N_6 + BI(g_5/g_6 N_6 - N_5) - \tau_5 N_5 + \tau_5 (N_{50} - N_5) - \gamma_{57} N_5 n_e - \beta_5 N_5^2 \quad (3)$$

$$dN_4/dt = \alpha_4 N_4 n_e + A_{64} N_6 - \gamma_{47} N_4 n_e - A_{40} N_4 \quad (4)$$

$$dN_3/dt = \alpha_3 N_0 n_e + A_{63} N_6 - \gamma_{37} N_3 n_e - \beta_3 N_3^2 - \tau_3 N_3 + \tau_3 (N_{30} - N_3) \quad (5)$$

$$dN_6/dt = \alpha_6 N_0 n_e + BI(N_5 - g_5/g_6 N_6) - \gamma_{67} N_6 n_e - (A_{62} + A_{63} + A_{64} + A_{65}) N_6 \quad (6)$$

The change in the rate of addition to the continuum is proportional to

$$(dN_7/dt) \propto (\gamma_{67} N_6 + \gamma_{57} N_5 + \gamma_{47} N_4 + \gamma_{37} N_3) n_e + \beta_3 N_3^2/2 + \beta_5 N_5^2/2 = \Delta \quad (7)$$

The complete rate equation for dN_7/dt includes terms for the direct ionisation of ground state atoms in collisions with electrons and the ambipolar diffusion loss. As the experimentally determined change in the electron density is only 1-2% a single iteration solution of the rate equations is used.

To avoid having a quartic equation to solve, the $\beta_3 N_3^2$ term is neglected in the calculation of the population densities. This leads to an error in the $1s_3$ metastable density of less than 3%.

The factors $\tau_i (N_{i0} - N_i)$ describe the diffusion of the i^{th} species to or from the surrounding non-illuminated discharge volume. The steady state density of the i^{th} species without illumination is N_{i0}. The best experimental arrangement would be one where the laser beam completely fills the discharge volume but this would give rise to light scattering problems and difficulty in obtaining high intensities. The effect of including this term is to slightly reduce

the laser irradiation induced change in population densities. As long as the diffusion rates for both $1s_5$ and $1s_3$ metastables are close in value no complications arise from this term. The Einstein A coefficient for a transition between levels i and j is designated A_{ij} and the B coefficient is in inverse intensity units per unit time.

To describe switching on the laser light, the steady state equations, $dN_i/dt=0$, are solved for BI=0 and then the equations are numerically integrated with finite BI to yield the time resolved behaviour. The reverse procedure is followed for switching the laser illumination off. The computer programs to obtain these solutions are listed in appendix E. The values of the rate coefficients used are given in table IV. The rate coefficients for the direct excitation of the $1s_5$ and $1s_4$ levels were obtained by fitting the steady state population densities calculated using the rate equations, to those estimated by the laser absorption method (described in chapter 3), in a 20mm length of neon positive column. The rate coefficient for the $2p_2$ level excitation was taken arbitrarily as one tenth of the $1s_5$ direct excitation rate coefficient. These direct excitation rate coefficients are about an order of magnitude smaller than those deduced from calculated electron collision excitation cross sections [58]. A value for β, the rate coefficient for ionisation resulting from metastable-metastable collisions is derived from the work of Biondi [59]. Using a value of the neon metastable density at zero time in the afterglow derived by normalising to results in helium this gives $\beta = 9\times10^{-10}\,cm^3\,s^{-1}$. In the following calculations α_3 and β_3 are regarded as variables. The values for all coefficients are approximate.

Table IV

Rate Coefficients Used in the Rate Equation Analysis

$$\alpha_6 = 1\times10^{-12}\,cm^3s^{-1}$$

$$\alpha_5 = 1\times10^{-11}\,cm^3s^{-1}$$

$$\alpha_4 = 5\times10^{-12}\,cm^3s^{-1}$$

$$\beta_5 = 9\times10^{-10}\,cm^3s^{-1} \qquad [59]$$

$$\gamma_{37} = \gamma_{47} = \gamma_{57} = 6\times10^{-9}\,cm^3s^{-1} \qquad [60]$$

$$\gamma_{67} = 2\times10^{-8}\,cm^3s^{-1} \qquad [26]$$

$$\tau_3 = \tau_5 = 5\times10^{3}\,s^{-1} \qquad [61]$$

$$g_5 = 3$$

$$g_6 = 5$$

$$A_{62} = 2.32\times10^{7}\,s^{-1}$$

$$A_{63} = 1.46\times10^{7}\,s^{-1} \qquad [62]$$

$$A_{64} = 0.56\times10^{7}\,s^{-1}$$

$$A_{65} = 1.15\times10^{7}\,s^{-1}$$

$$A_{40} = 1.3\times10^{4}\,s^{-1} \quad \text{(with radiation trapping)} \qquad [63]$$

$$= 4.76\times10^{7}\,s^{-1} \quad \text{(without radiation trapping)} \qquad [55]$$

In the rate equation analysis no account is taken of the change in electron temperature and electron density caused by superelastic collisions of electrons with excited atoms in the discharge. The change in electron temperature can be found with a knowledge of the change of the ionisation collision cross section with electron energy and the mobility of the atomic states. Once the change in electron temperature is known the change in electron density can be calculated from the energy balance equation for the discharge [19]. The effect of this omission is discussed later (pg.95).

4.5.2 Numerical Results and Discussion

The value $N_o=3.2\times10^{16}cm^{-3}$ corresponds to a pressure of 1.5 Torr at a temperature of 450K. An electron density of $1\times10^{10}cm^{-3}$ corresponds to a current of 5mA. Solving the rate equations using these values of N_o and n_e, the rate coefficients from Table IV and with $\alpha_3=1\times10^{-12}cm^3s^{-1}$ and $\beta_3=9\times10^{-10}cm^3s^{-1}$ gives the population densities shown in figure 4.15. The $1s_5$ population density is significantly depleted and all other population densities increase, though the $1s_4$ population density only slightly.

The changes in the rate of addition to the continuum calculated from these results for five values of β_3 between 1×10^{-9} and $5\times10^{-9}cm^3s^{-1}$ are given in figure 4.16. The effect of the $1s_3$ metastable population density increasing relative to the $1s_5$ density is shown in figure 4.17, where $\beta_3=2\times10^{-9}cm^3s^{-1}$ and α_3 is varied between 1×10^{-12} and $5\times10^{-12}cm^3s^{-1}$. It is seen that either increasing the $1s_3$ population relative to the $1s_5$ population (figure 4.17) or increasing the rate coefficient for ionisation resulting from $1s_3$-$1s_3$

collisions (figure 4.16) leads to reversal behaviour of the type observed experimentally. The electron density initially decreases with increasing BI and then starts to increase as BI increases still further, for all parameters pairs in figure 4.16 and 4.17. Only in two of the traces is the latter increase in electron density sufficient to cause a sign reversal of the optogalvanic signal (figure 4.16(e) and 4.17(e)) in that the final electron density is larger than the initial electron density, but has been less at intermediate values of BI. It is estimated that BI increases smoothly from zero to a maximum value of 2×10^{7} as the dye laser frequency is tuned through the 588.2nm neon transition, in the experiments where a reversal of the sign of the optogalvanic signal is observed, under conditions similar to those being modelled here. Thus the reversal in the sign of the optogalvanic signal predicted from the rate equations occurs in the required range of BI values, from experiment.

The experimentally observed, voltage optogalvanic signals correspond to a 1-2% change in the electron density in the discharge. Using the predicted steady state rates of ionisation, with and without irradiation, and constraining this to correspond to a 2% change in the ion density a direct ionisation rate coefficient of about $1.2 \times 10^{-11} cm^{3} s^{-1}$ is predicted. This is slightly larger than the rate coefficient for $1s_5$ metastable excitation from the ground state. Thus it appears that the depletion of the $1s_5$ level, and the rate of change in the electron density arising from it, are overestimated by the calculation. However, that the $1s_5$ population is significantly depleted is demonstrated by the measured saturated absorption (figure 4.7). The discrepancy is most likely attributable to the approximate values of the rate coefficients, in particular β_3 and β_5, used in the rate equation analysis.

The time resolved population densities are shown in figure 4.18. It is seen that the $1s_5$ metastables are depleted smoothly when the laser is switched on. They then build up smoothly to their initial, unperturbed value when the laser is switched off. The reverse behaviour is observed for the $1s_3$ metastables which increase smoothly when the laser is switched on and decay back to their initial values when the laser is switched off. The $2p_2$ population density increases rapidly when the laser is switched on and then decreases more slowly as the $1s_5$ metastables are depleted. This rapid increase could give rise to a transient increase in the electron density if the rate of ionisation from the $2p_2$ level was high enough. A value of $1x10^{-7}$ cm^3 s^{-1} for the rate γ_{67} gives rise to such a transient increase, which is shown in figure 4.19. Increasing the rate coefficient γ_{67} is equivalent to allowing collisional relaxation among the $2p_2$ levels, if one or more of the ionisation rates of the other 2p levels exceeds that for the $2p_2$ level. The $1s_4$ population density behaviour is similar to that for the $2p_2$ population density except the magnitude of the variation is much smaller and the time taken to reach steady state is longer. Both the $2p_2$ and $1s_4$ population densities decrease smoothly to their unperturbed values when the laser is switched off.

With the rapid increase in the $2p_2$ population density it might be possible to have a population inversion on some or all of the $2p_2$ $-1s_{2,3,4}$ transitions at short times ($<3x10^{-7}$ s). This would give rise to the further complication of stimulated emission on these transitions at short times.

For all the levels under consideration the time to reach the steady state population density is constant for all values of BI when the laser is switched off. This is in contrast to the behaviour when the laser is switched on, when the time to reach equilibrium decreases with increasing BI.

The time resolved change in the rate of addition to the continuum is shown, for different values of BI, for $\alpha_3=1\times10^{-12}cm^3s^{-1}$ and $\beta_3=5\times10^{-9}cm^3s^{-1}$ in figure 4.20, for both switching on and switching off the laser.

The time resolved optogalvanic signal predicted by the above model is qualitatively like that observed in the experiments in a neon positive column discharge (figure 4.10). At small values of BI ($1\times10^4s^{-1}$) the optogalvanic voltage signal, measured at the cathode, is negative (figure 4.20a) and increases in magnitude as BI increases.As BI increases further ($1\times10^5s^{-1}$) a transient in the signal is observed for both switching on and switching off the laser (figure 4.20(b)). The steady state is still a negative voltage, however. As BI is increased still further ($1\times10^6s^{-1}$) the negative transient occurs earlier in time and the steady state signal becomes positive about 10μs after the laser is switched on (figure 4.20(c)). Further increases in BI cause the negative transient to occur at still earlier times (<1μs) and the positive steady state signal saturates (figure 4.20(d) and (e)). The negative transient is observed experimentally to occur at earlier times as BI increased. At a chopping frequency of 2kHz, the transient, (for a pressure of 1.5 Torr and current of 5mA) decreases in duration from 0.3ms to less than 0.05ms as the laser frequency is scanned through the 588.2nm transition. The time resolution attainable is limited by the high

frequency roll off (10kHz) of the narrow band amplifier used to view the signal. As the intensity increases the reversal in the rate of ionisation occurs at a frequency further from line centre in agreement with experiment.

The metastable densities increase with current in the range 2-20mA. Obtaining further fits of α_5, α_4 and α_3 using experimentally determined densities at higher currents, it is found that the reversal behaviour in the rate of addition to the ionisation continuum is suppressed as the electron density increases as shown in figure 4.21. This is also what is observed experimentally. The only qualitative disagreement between experiment and the rate equation analysis arises when considering the behaviour for pressures of 1 and 2 Torr. Experimentally the reversal of sign of the rate of addition to the continuum is only observed for a narrow band of pressures, 1.2-1.8 Torr, in axial studies. There is also a large spatial variation in the experimentally observed optogalvanic signals. In particular, transverse studies showed the sign reversal is only induced in three narrow, transverse sections of the discharge, which correspond to positions of larger excited state densities. Thus it would appear that the appropriate population densities occur only locally within the discharge at p = 1.5 Torr. Sign reversals are also observed for certain transverse positions at p = 2 Torr but the volume involved is apparently an insufficient part of the total discharge volume to dominate the axial behaviour. This suggests that the local enhancement of $1s_3$ population density is the more likely cause of the reversal observed, rather than β_3 being greater than β_5.

Inclusion of the change in electron temperature and electron density due to superelastic collisions will reduce the change in the rate of ionisation and possibly give better agreement between the rate of direct ionisation predicted and that observed. The change in the electron temperature can not be incorporated readily as the cross sections for ionisation as a function of electron energy are not well known. However, by considering the energy balance equation [64] it is seen that the heating in the discharge due to absorption of radiation will lead to an increase in electron temperature and electron density, competing with the decrease in electron density caused by the depletion of the $1s_5$ metastables. (If the increase in electron temperature is calculated independently the increase in electron density could be obtained from measurements of the discharge temperature, with resonant laser irradiation and without. With the use of pure Ne^{20} the temperature could be deduced from the Doppler width of the absorption line profile. Two lasers would be required. But it is doubtful if the required precision could be obtained to make a meaningful correction.) The change in the electrical power input to the discharge due to irradiation is less than 0.5% of the absorbed laser power.

4.6 Summary and Conclusion

As for a hollow cathode discharge the optogalvanic signal on the $1s_5$-$2p_2$ transition at 588.2nm in a positive column discharge corresponds to a decrease in electron density for most discharge conditions. Spatial effects are more prevalent with complex spatial averaging of differentially bleached discharge volumes occurring in

axial studies.

The change in sign from negative to positive of the optogalvanic signal as a function of $B(\nu)I$ for the discharge conditions p=1.5 Torr, I=2.5-20mA has been demonstrated to occur when the $2p_2$ population density starts to increase, by emission studies. That this reversal occurs at several localised transverse positions in the discharge probably results from the non-uniform axial distribution of excited species, also demonstrated by emission studies. This axial distribution also explains the results for the line centre optogalvanic signal as a function of power for I=5mA (figure 4.8), where the signal changed sign to positive and then back to negative with increasing dye laser power, by progressively bleaching through the regions with high excited state densities.

It has been possible to predict reversals in the sign of the optogalvanic signal, with increasing dye laser power, generated in a neon positive column discharge, irradiated by chopped CW dye laser light at 588.2nm, which qualitatively agree with the optogalvanic signals observed. However, for the effect to be caused by an enhancement of the $1s_3$ metastables alone these need to be almost as numerous as the $1s_5$ metastables according to the present analysis. Thus it would seem that the full explanation is much more complicated, possibly requiring the inclusion of the modification of electron energy distribution caused by irradiation, which may be giving rise to enhanced collisional excitation rates for some excited species.

In order to improve the rate equation analysis the change in electron temperature and electron density due to absorption of radiation must be included. The electron density could be calculated from a formulation describing the dynamic discharge rather than from

standard results for positive column discharges. These improvements are to attempt to obtain the correct magnitude of the optogalvanic signal and are not expected to modify the qualitative behaviour. A better knowledge of the ionisation collision cross sections, the gas temperature and the electron temperature would allow these improvements. Also, the optogalvanic signal is dominated at the medium pressures discussed here, by metastable-metastable collisions leading to ionisation [38]. It is therefore very important to measure the cross-sections for $1s_5$-$1s_5$ and $1s_3$-$1s_3$ collisions leading to ionisation. A decrease in these cross sections, compared to the values used here, also reduces the magnitude of the change in the rate of ionisation caused by resonant illumination. Inclusion of the cross terms for metastable-metastable collisions made little difference in the present analysis.

The combination of axial optogalvanic detection while monitoring the emission intensity of the 1s-2p transitions transversely is a sensitive method of obtaining information about the metastable population density while tracing relaxation pathways between the 2p levels. Further experimental investigations of this type would be of value.

Further experiments should be carried out in a shorter, more uniform neon positive column discharge where the $1s_5$ and $1s_3$ population densities may be measured dynamically by the laser absorption method. This would be a two laser experiment, requiring beams of orthogonal polarisation to allow separation, or a "saturation spectrometer" arrangement (figure 4.22). Pure Ne^{20} would be used to simplify the analysis. In the experiments proposed direct measurements of the $1s_3$:$1s_5$ metastable density ratio could be related to the observed optogalvanic line profile.

The sign reversal observed here would appear to be an unusual occurrence but a reduction in the optogalvanic signal at line centre due to the increase in the $1s_3$ metastable density when optically pumping a $1s_5$-$2p_n$ transition appears to be a general effect. Emission and absorption studies here, are not inconsistent with such an increase. When the ratio of $1s_3$:$1s_5$ metastable densities as a function of pressure, and the cross section for ionisation resulting from metastable-metastable collisions for both the $1s_3$ and $1s_5$ metastables are known, the proposed explanation for the sign reversal of the optogalvanic signal can be re-evaluated.

Optogalvanic detection is clearly not capable of giving similar information as absorption studies for high dye laser powers, in a complex system like the neon $1s_m$-$2p_n$ transition group. But, alone, or combined with absorption/emission studies it should prove to be a valuable new tool for discharge studies.

References

1. F M Penning (1928), Physica 8, 137.
   (1930), Physica 10, 47.
   (1931), Physica 11, 183.
   (1932), Physica 12, 65.
   (1928), Z.Physik 46, 335
   (1929), Z.Physik 57,723.
   (1931), Phys.Mag. 11, 961.
   M J Druyvesteyn and F M Penning (1940), Rev.Modern Phys.12, 87.
   (1941), Rev.Modern Phys.13, 72.
2. P D Foot and F L Mohler (1925), Phys.Rev. 26,195.
   F L Mohler, P D Foot and R L Chenaut (1926), Phys.Rev. 27, 37.
3. E W Pike (1936), Phys. Rev. 49, 513.
4. C Kenty (1950), Phys.Rev. 80, 95
5. K W Meissner and W F Miller (1953), Phys.Rev. 92, 896.
6. E Bardareu, I Popescu, C Ghita and G Musa (1965), Rev.Roum.Phys. 10, 785.
7. M G Drouet and J P Novak (1971), Phys.Lett. 34A, 199.
8. D Popescu, M L Pascu, C B Collins, B W Johnson and I Popescu (1973), Phys.Rev. 8A, 1666.
9. N S Kopeika, J Rosenbaum and R Kastner (1976), Appl.Opt. 15,1610, and references there-in.
10. R B Green, R A Keller, G G Luther, P K Schenck and J C Travis (1976), Appl.Phys.Lett. 29, 727.
11. R B Green, R A Keller, G G Luther, P K Schenck and J C Travis (1977), IEEE J.Quant.Electron. QE-13, 63.
12. D S King, P K Schenck, K C Smyth and J C Travis (1977), Appl.Opt. 16, 2617.
13. D S King and P K Schenck (1978), Laser Focus, March, 50.
14. T F Johnston Jr. (1978), Laser Focus, March, 58.
15. K C Smyth and P K Schenck (1978), Chem.Phys.Letts. 55,466.

16. K C Smyth, R A Keller and F F Crim (1978), Chem.Phys.Letts. 55, 473.

17. E F Zalewski, R A Keller and R Engleman Jr. (1979), J.Chem.Phys.70, 1015.

18. G Erez, S Lavi and E Miron (1979), IEEE J.Quant.Electron. QE-15, 1328.

19. D M Pepper (1978), IEEE J.Quant.Electron. QE-14, 971.

20. R A Keller, R Engleman Jr, and E F Zalewski (1979), J.Opt.Soc.Am. 69, 738.

21. D J Jackson, E Arimondo, J E Lawler and T W Hänsch (1980), Opt.Commun. 33, 51.

22. J E Lawler (1980), Phys.Rev. 22A, 1025.

23. R A Keller and E F Zalewski (1980), Appl.Opt. 19, 3301.

24. W J van der Hoek and J A Visser (1980), J.Appl.Phys. 51, 5292.

25. E F Zalewski, R A Keller and C T Apel (1981), Appl.Opt. 20, 1584.

26. S P Kravis and S C Haydon (1981), J.Phys.D:Appl.Phys. 14, 151.

27. C Stanciulescu, R C Bobulescu, A Surmeian, D Popescu, I Popescu and C B Collins (1980), Appl.Phys.Lett. 37, 888.

28. R Schuker, A Ben-Amar and G Erez (1982), Opt.Commun. 42, 29.

29. H A Bachor, P J Mason and R J Sandeman (1982), Opt.Commun. 43,337.

30. J R Nestor (1982), Appl.Opt. 21, 4154.

31. N Uchitomi, T Nakajima, S Maeda and C Hirose (1983), Opt.Commun. 44, 154.

32. J E Lawler, A I Ferguson, J E M Goldsmith, D J Jackson and A L Schawlow (1979), Phys.Rev.Lett. 42, 1044.

33. J E M Goldsmith, A I Ferguson, J E Lawler and A L Schawlow (1979), Opt.Lett. 4, 230.

34. D J Jackson, H Gerhardt and T W Hänsch (1981), Opt.Commun. 37, 23.

35. A Siegel, J E Lawler, B Couillaud and T W Hänsch (1981), Phys.Rev. 23A, 2457.

36. J E Lawler, A Siegel, B Couillaud and T W Hänsch (1981), J.Appl.Phys. 52, 4375.

37. D R Lyons, A L Schawlow and G-Y Yan (1981), Opt.Commun. 38, 35.

38. L Julien and M Pinard (1982), J.Phys.B:Atom. and Molec. 15, 2881.

39. C J Lorenzen and K Niemax (1982), Opt.Commun. 43, 26.

40. N Beverini, M Galli, M Inguscio and F Strumia (1982), Opt.Commun. 43, 261.

41. C R Vidal (1980), Opt.Lett. 5,158.

42. R Engleman Jr, and R A Keller (1980), Opt.Lett. 5, 158.

43. P Camus, M Dieulin and A El Himdy (1982), Phys.Rev. 26A, 379.

44. R Schuker, A Ben-Amar and G Erez (1981), Opt.Commun. 39, 51.

45. D H Katayama, J M Cook, V E Bondybey and T A Miller (1979), Chem.Phys.Lett. 62, 542.

46. J P Grandin and X Husson (1981), J.Phys.B:Atom. and Molec. 14, 433.

47. N Beverini and M Inguscio (1980), Lett.Nuovo Cimento 29,10.

48. P Hannaford and G W Series (1981), J.Phys.B:Atom and Molec. 14, L661.

49. P Hannaford and G W Series (1982), Opt.Commun. 41, 427.

50. P Hannaford and G W Series (1982), Phys.Rev.Lett. 48, 1326.

51. D Feldman (1979), Opt.Commun. 29, 67.

52. C Demuynck and J L Destombes (1981), IEEE J.Quant.Electron. QE-17, 575.

53. T Suzuki (1981), Opt.Commun. 38, 364.

54. N E Small-Warren and L Y Chow Chiu (1975), Phys.Rev. 11A, 1777.

55. W L Wiese, M W Smith, B W Glennon (1966), Natl.Stand.Ref.Data Ser. NBS-4, 128.

56. I I Sobelman (1979), Atomic Spectra and Radiative Transitions (Springer-Verlag), p46.

57. Y Ichikawa and S Teii (1980), J.Phys.D:Appl.Phys. 13, 1243.

58. H S W Massey and E H Burhop (1969), Electronic and Ionic Phenomena (Oxford), p281.

59. M A Biondi (1952), Phys.Rev. 88, 660.

60. D Ton-That and M R Flannery (1977), Phys.Rev. 15A, 517.

61. A R Phelps (1959), Phys.Rev. 114, 1011.

62. S Inatsugu and J R Holmes (1975), Phys.Rev. 11A, 26.

63. T Holstein (1947), Phys.Rev. 72, 1212.

(1951), Phys.Rev. 83, 1159.

64. A L McKenzie (1975), Thesis (St Andrews).

Table I

Summary of Optogalvanic Experiments in Atoms

Atom	Linear	Doppler Free	Double Resonance	Rydberg	Level Crossing
He	10,14,21,22	32,34		45	
Li	10				
Ne	10,11,12,14,15,16,17,18, 26,28,29,30,31,38	33,34,38, 37,40	44,30		38
Na	10,11,12,13,19,23,24,25		42		
Mg	13				
Ar	18,29,30				
Ca	10,29	40			
Mn	13				
Cu	13,29	40			
Sr		39			
Y					50
Zr	23				48,49
Mo		35,36			
Xe				46	
Cs	27		27	27	
Ba	10,11		43	43	
Eu	23				
Hg	24				
Pb	13				
U	10,18,20,23		42		

Table II

Summary of Optogalvanic Experiments in Molecules

Molecule	Reference
NH_2	51,52
NO_2	51,52,53
H_2	51,52
N_2	51,52,53
I_2	52
NH_3	53

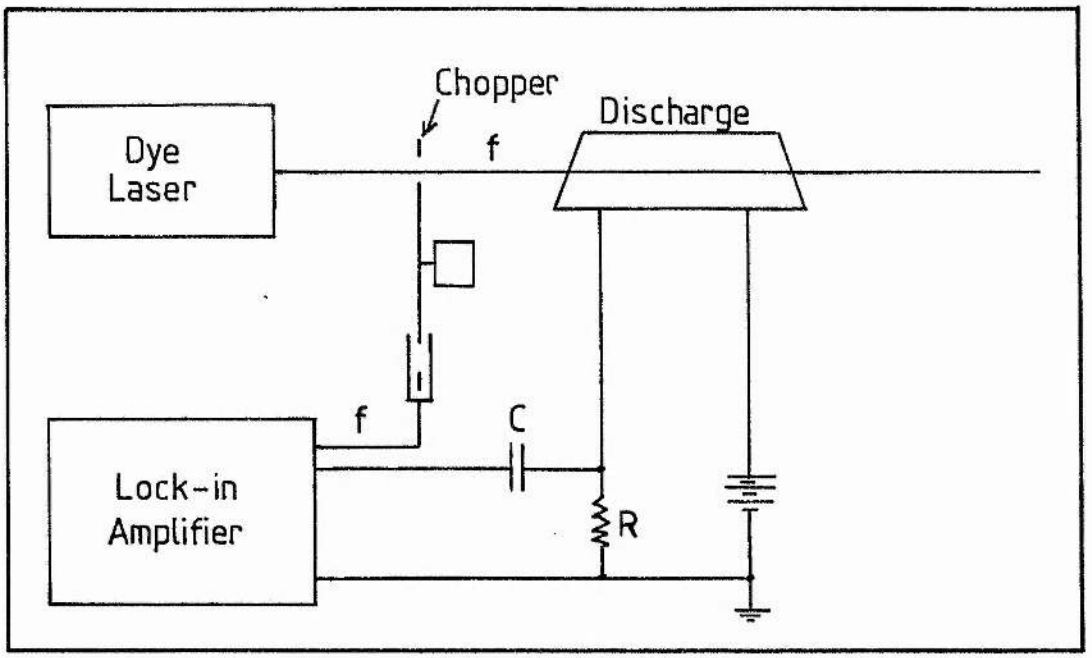

Figure 4.1 Standard experimental layout for Doppler/laser linewidth limited optogalvanic spectroscopy.

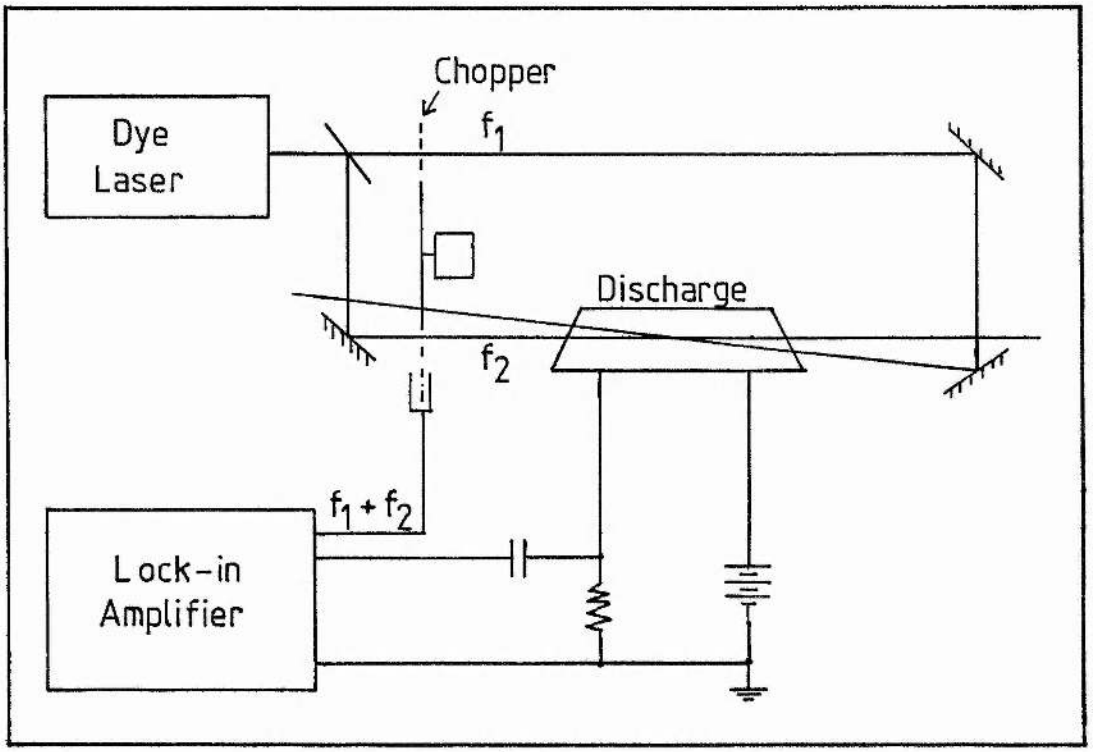

Figure 4.2 Experimental arrangement for Doppler free intermodulated optogalvanic spectroscopy.

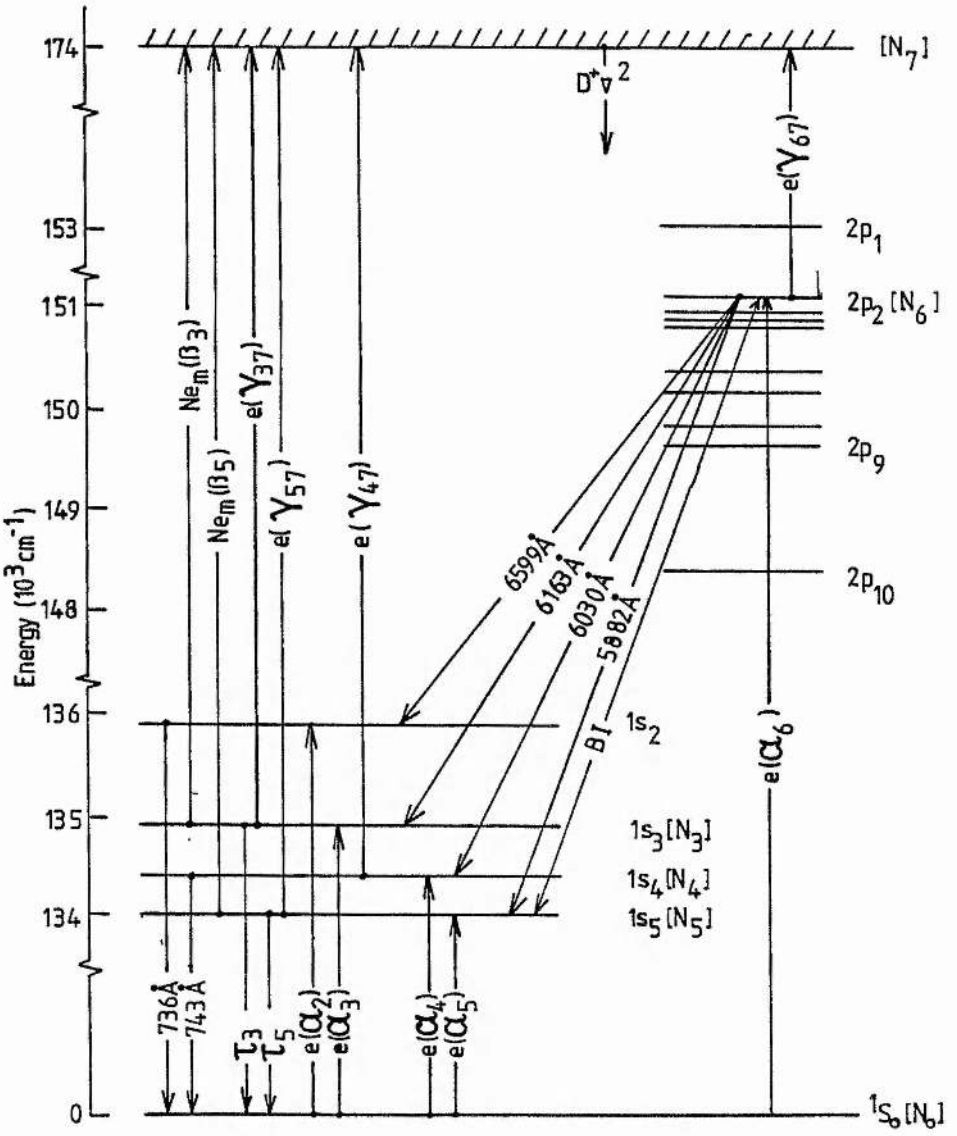

Figure 4.3 Part of the neon energy level scheme showing the energy levels and the coupling between them involved in the present studies.

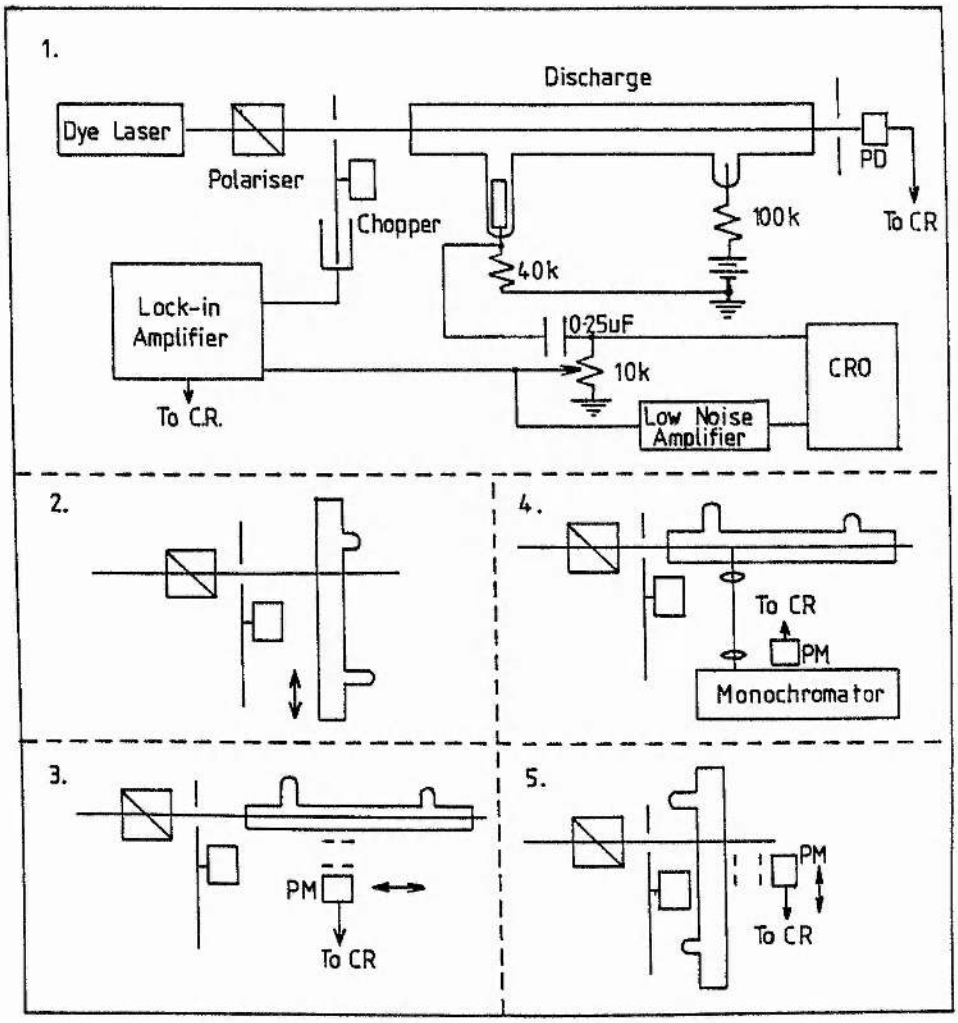

Figure 4.4 Experimental arrangements. CR-chart recorder, PD-photodiode, PM-photomultiplier.

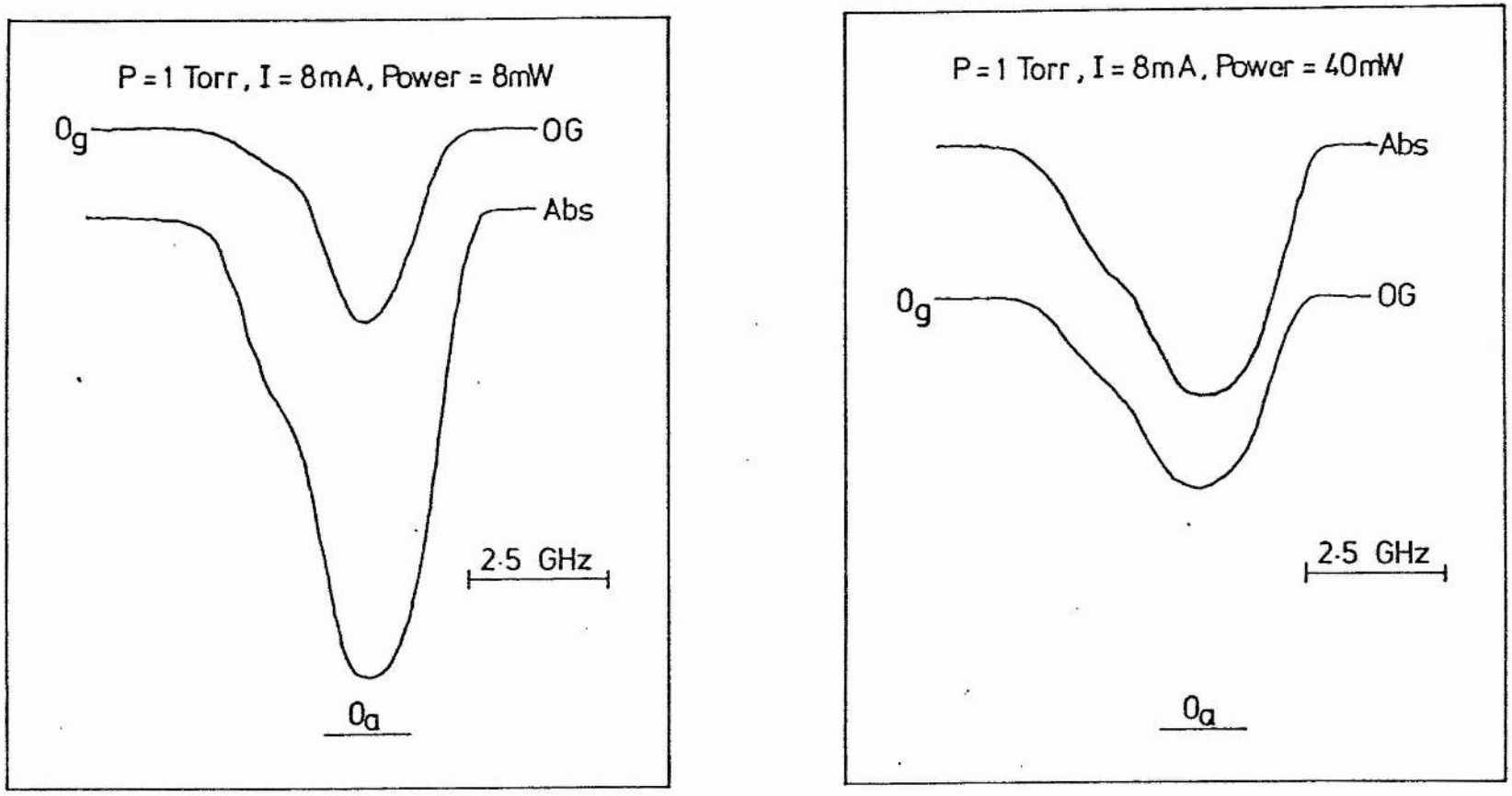

Figure 4.5 Axial optogalvanic and saturated absorption line profiles at 588.2nm, observed simultaneously for p = 1 Torr.

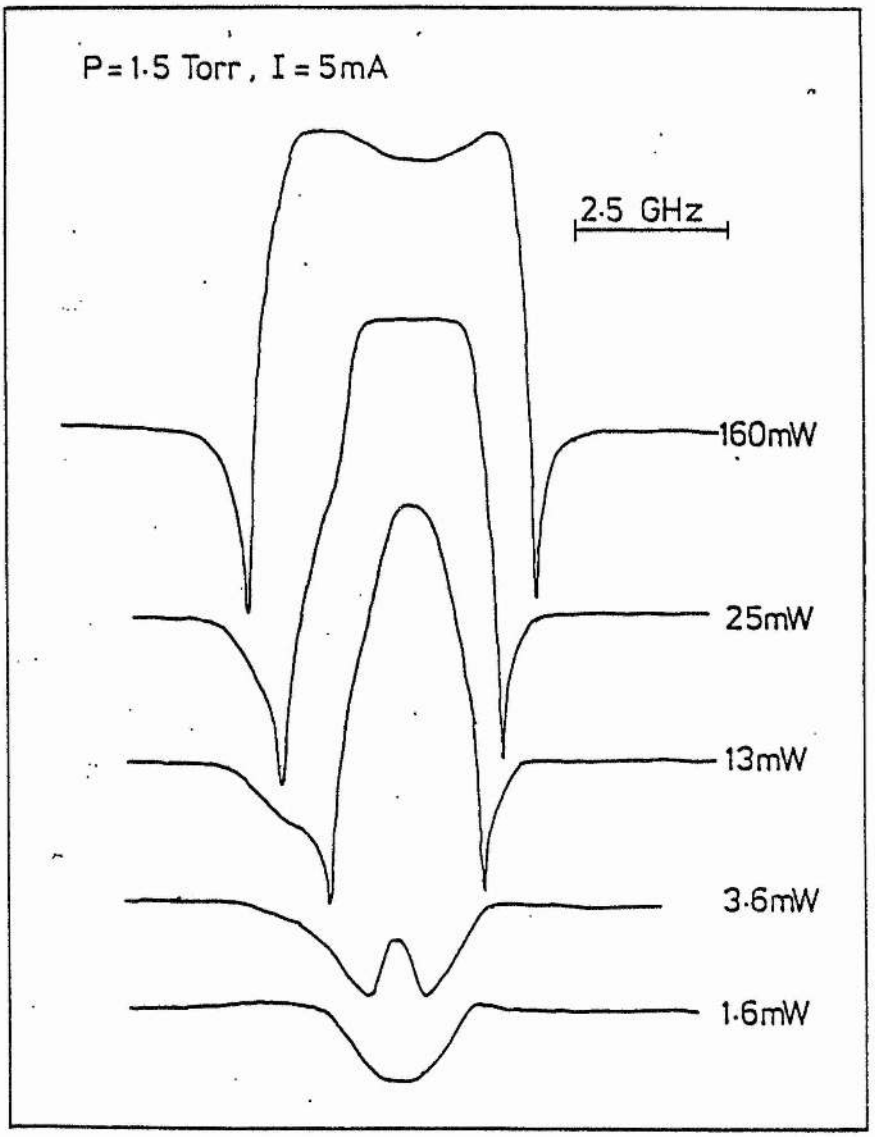

Figure 4.6 Axial optogalvanic line profiles at 588.2nm as a function of dye laser power for p = 1.5 Torr, I = 5mA.

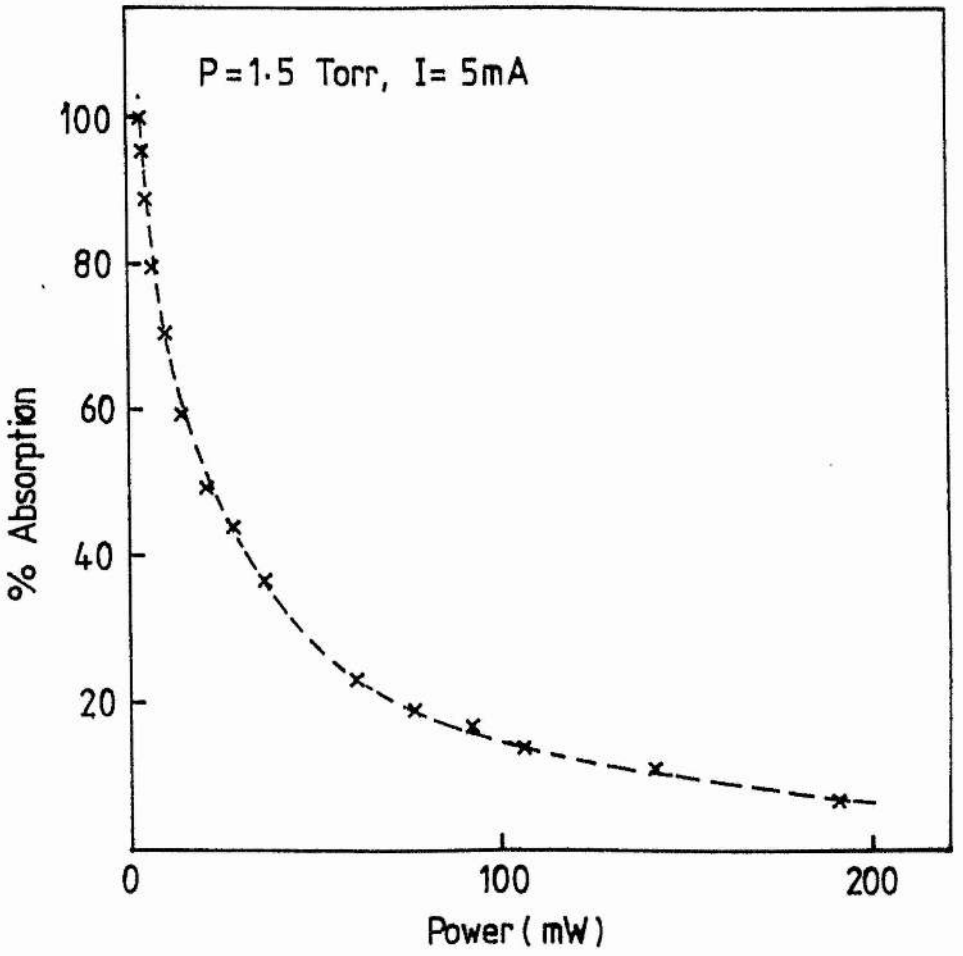

Figure 4.7 Percentage saturated absorption as a function of dye laser power, at line centre, for the $1s_5$-$2p_2$ transition.

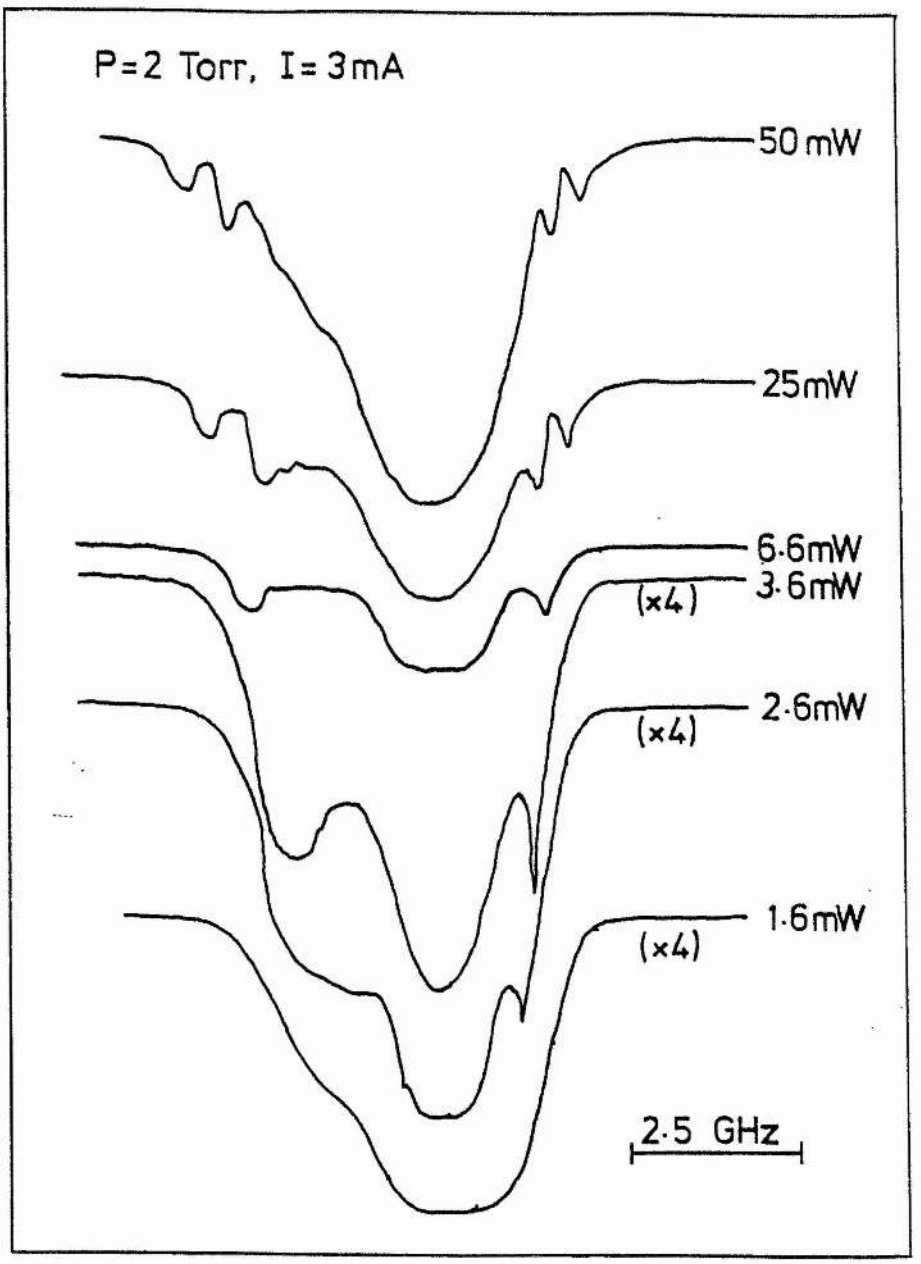

Figure 4.8 Axial optogalvanic line profiles at 588.2nm as a function of dye laser power, for p = 2 Torr and I = 3mA.

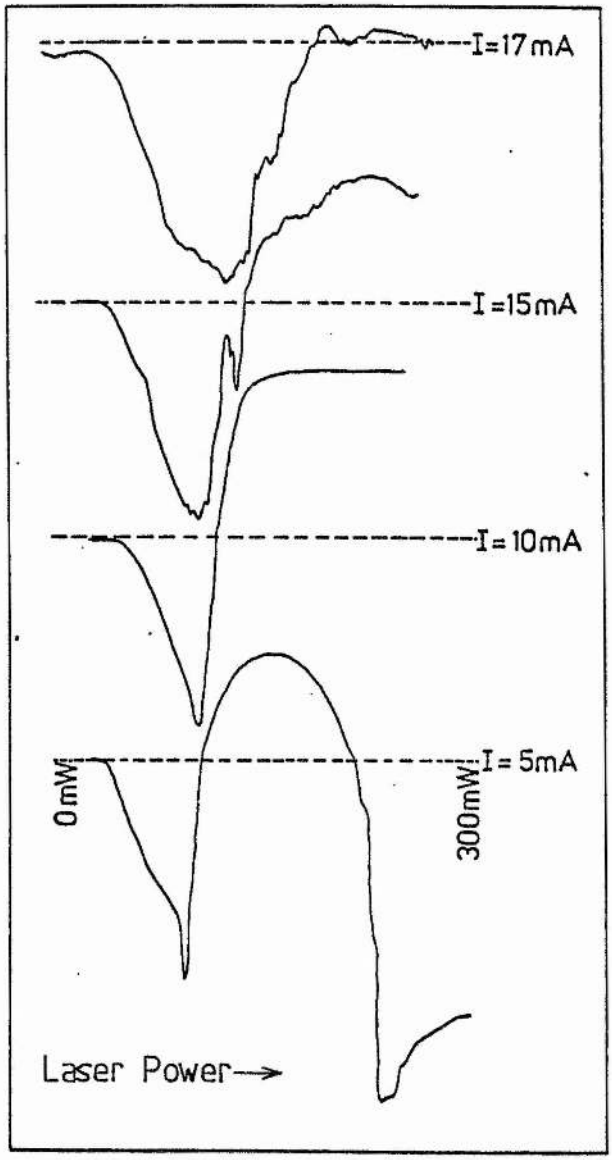

Figure 4.9 Axial optogalvanic signal at the centre of the neon 588.2nm transition as a function of dye laser power for a pressure of 1.5 Torr and various currents.

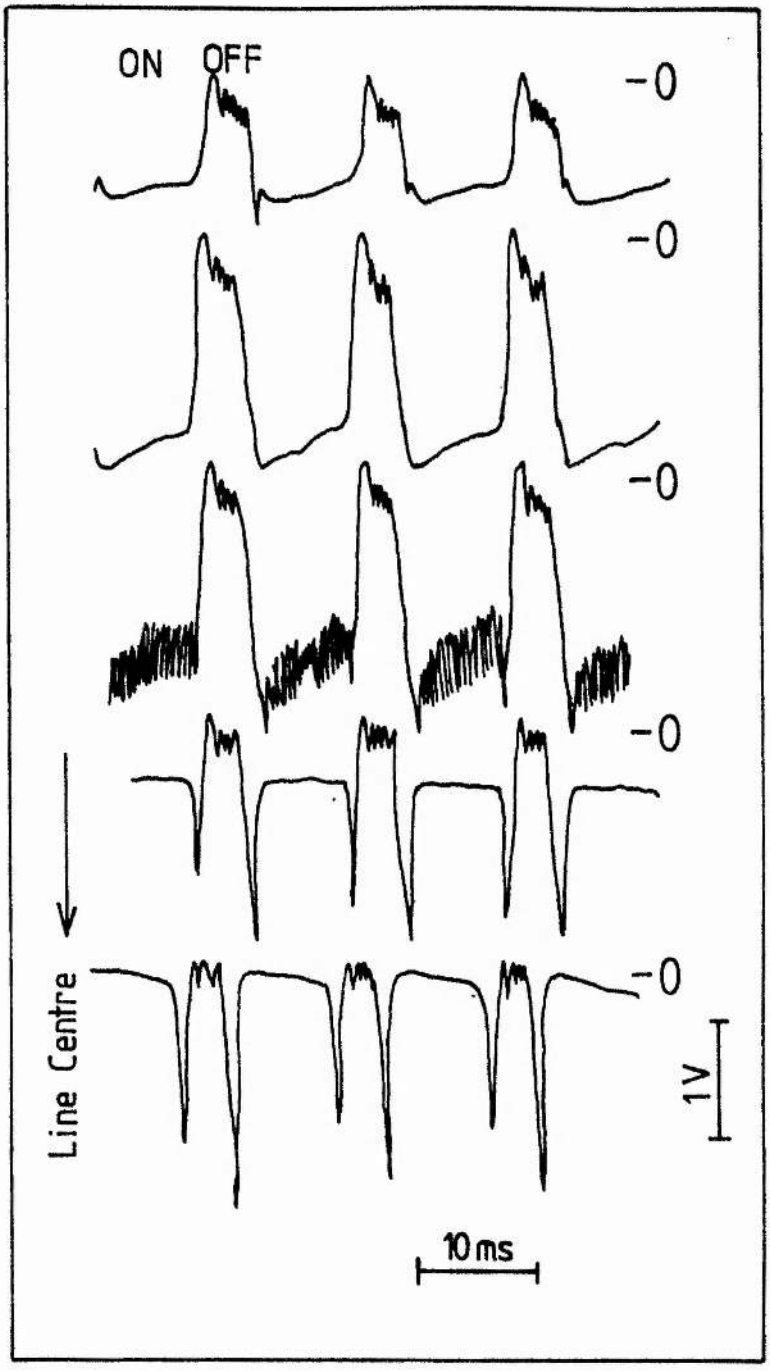

Figure 4.10 Time varying axial optogalvanic signal as the dye laser is tuned into resonance on the neon 588.2nm transition. I = 7mA, p = 1.5 Torr.

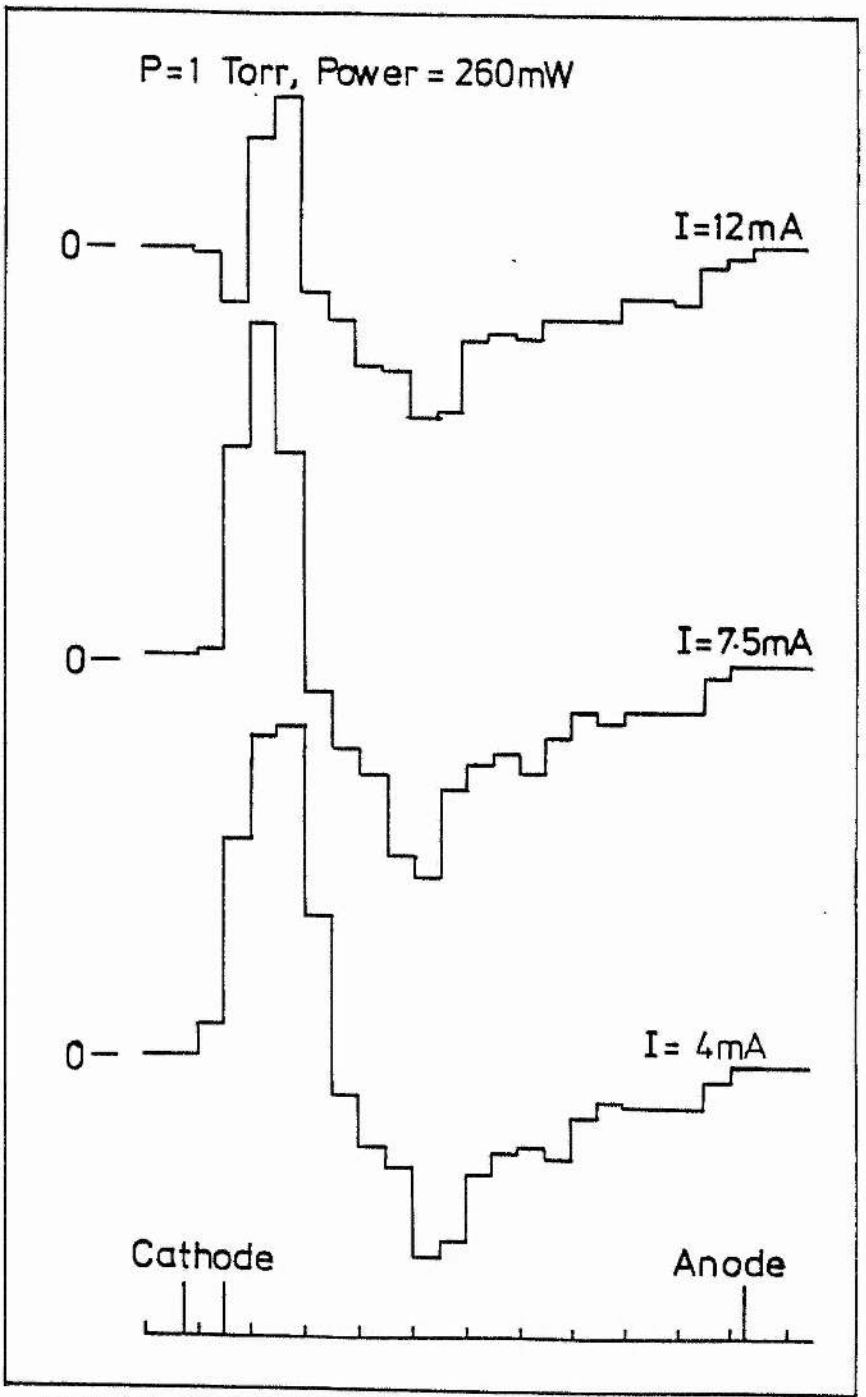

Figure 4.11 Optogalvanic signal at the centre of the neon 588.2nm transition at various transverse positions in the positive column discharge. The discharge length is marked at the bottom in cm.

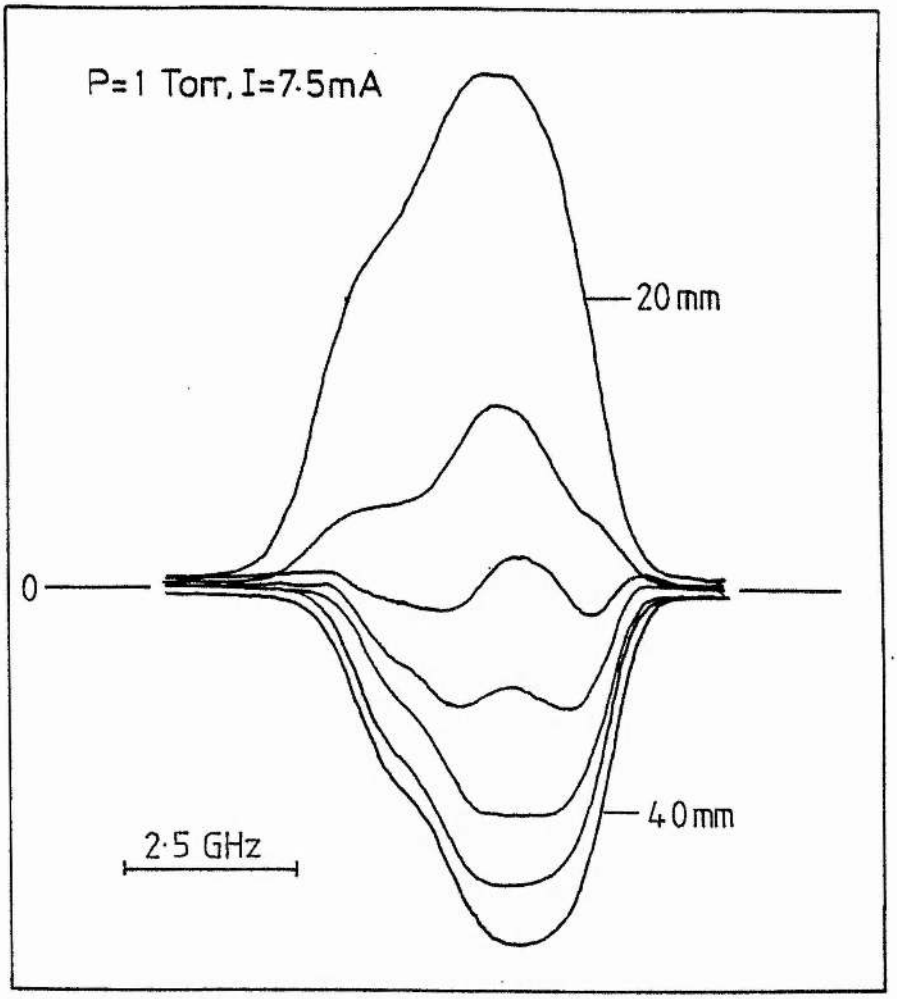

Figure 4.12 Optogalvanic line profiles at 588.2nm for various transverse positions in the region 20–40mm from the cathode, for p = 1 Torr.

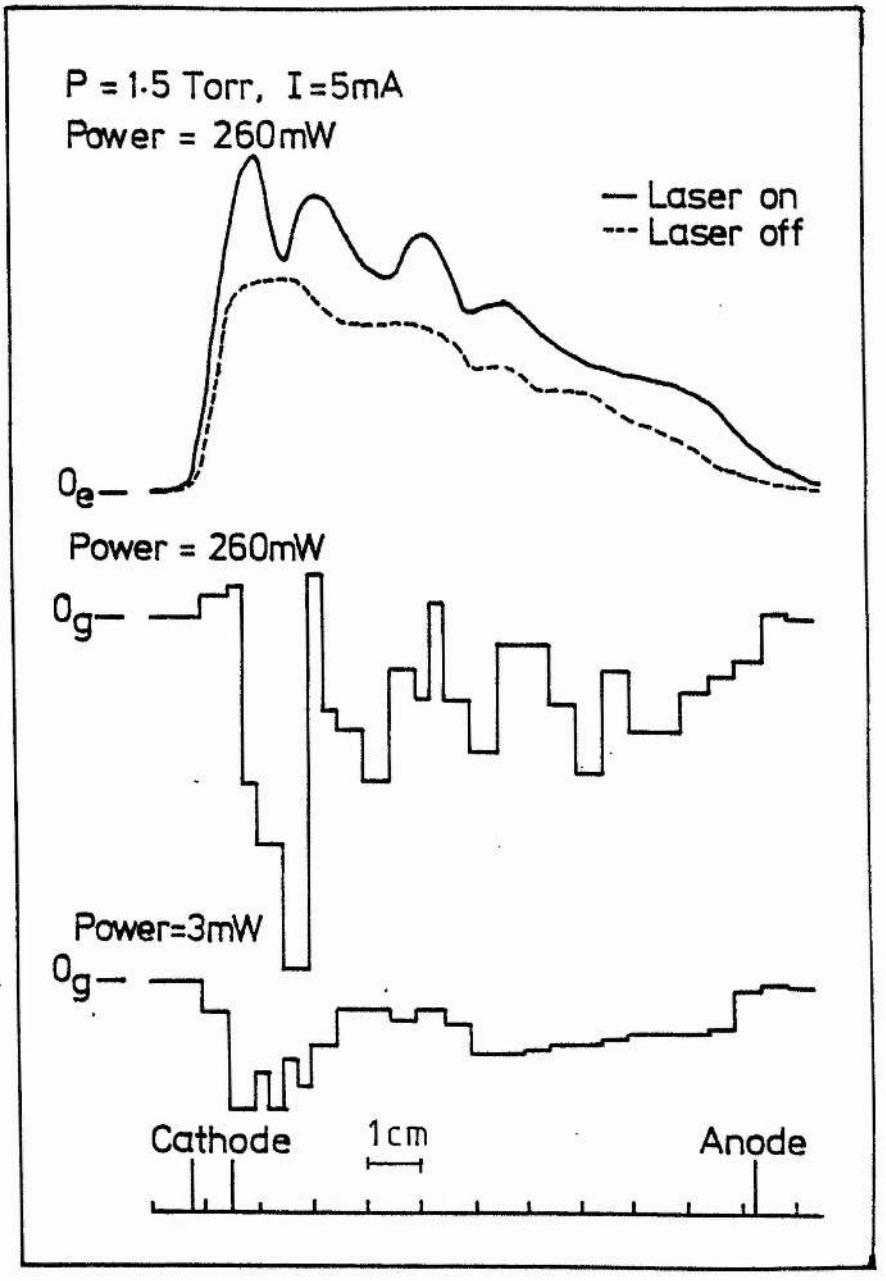

Figure 4.13 Optogalvanic signal at the centre of the neon 588.2nm transition at various transverse positions in the positive column for a pressure of 1.5 Torr. The top trace shows the emission intensity with the laser tuned to the centre of the transition and tuned off the the transition for an irradiating power of 260mW.

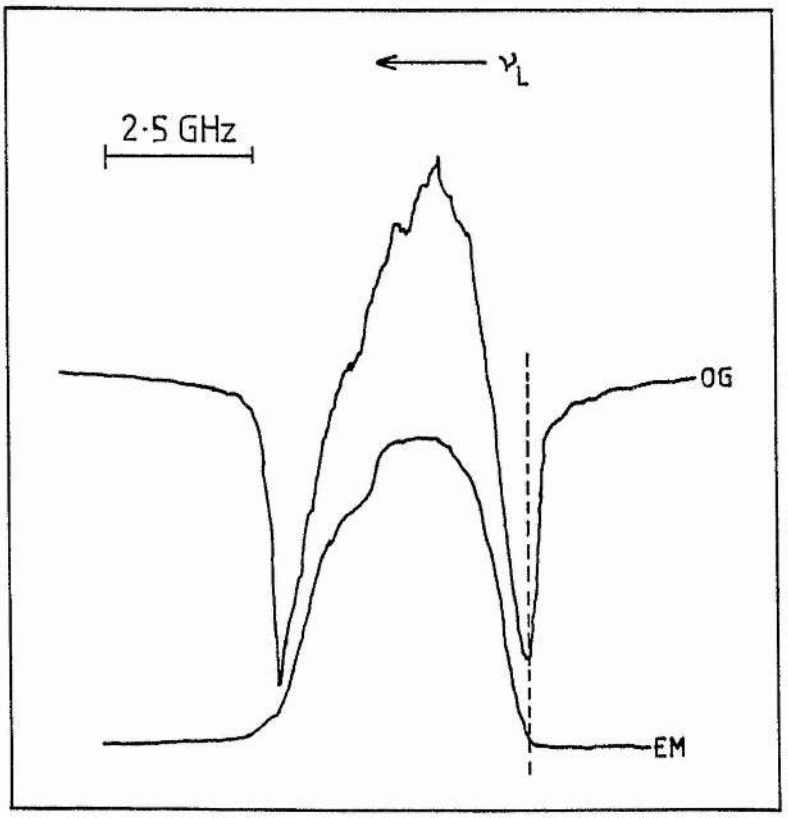

Figure 4.14 Axial optogalvanic and transverse emission line profile at 588.2nm observed simultaneously for p = 1.5 Torr, I = 7mA.

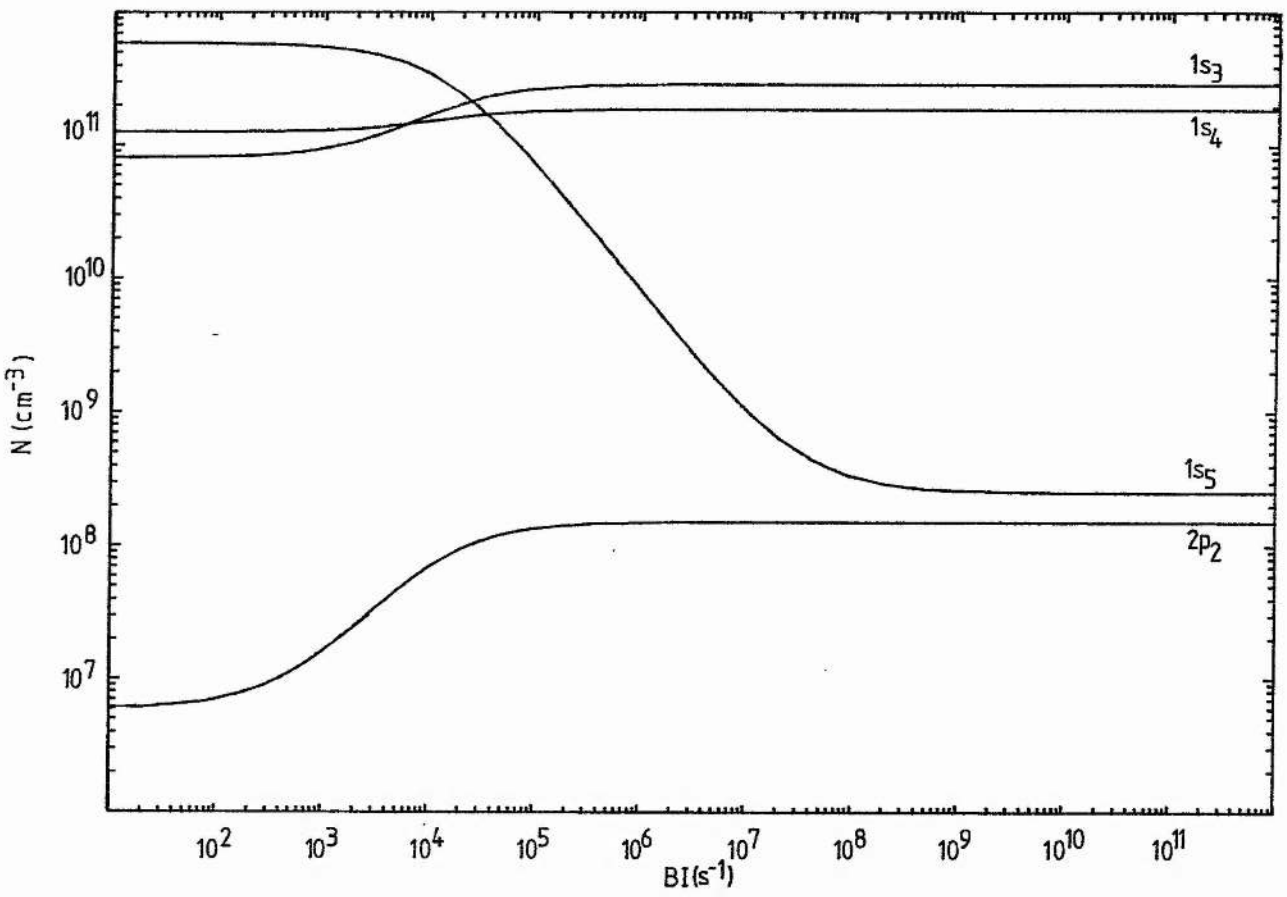

Figure 4.15 Steady state population densities of the $1s_5$, $1s_4$, $1s_3$ and $2p_2$ levels as a function of BI using the rate coefficients in Table IV, $\alpha_3=1\times10^{-12}\,cm^3s^{-1}$, $\beta_3=9\times10^{-10}\,cm^3s^{-1}$, $N_0=3.2\times10^{16}\,cm^{-3}$ and $n_e=1\times10^{10}\,cm^{-3}$.

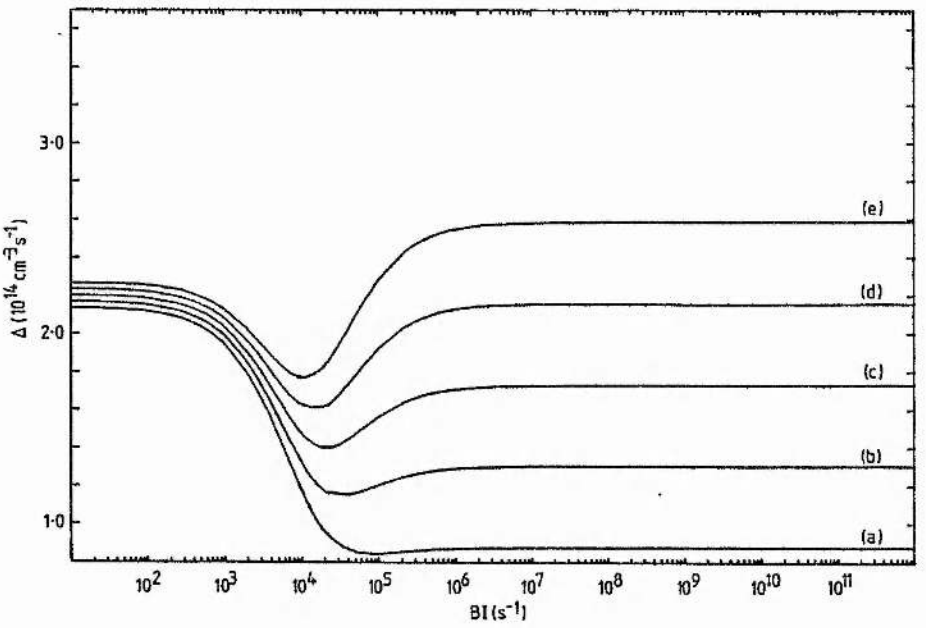

Figure 4.16 Rate of addition to the continuum Δ (as defined in eqn(7)) calculated from the steady state population densities in figure 4.15 for β_3=(a)1x10^{-9},(b)2x10^{-9}, (c)3x10^{-9},(d)4x10^{-9} and (e)5x10^{-9}cm^{3}s^{-1}.

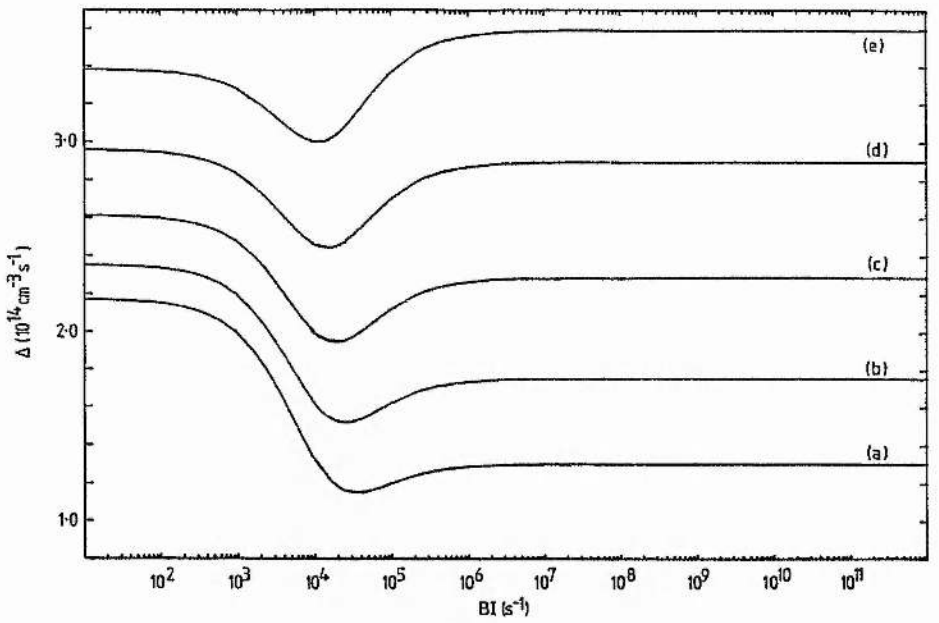

Figure 4.17 Rate of addition to the continuum Δ calculated from the steady state population densities for β_3=2x10^{-9}cm^{3}s^{-1} and α_3=(a)1x10^{-12},(b)2x10^{-12},(c)3x10^{-12},(d)4x10^{-12} and (e)5x10^{-12}cm^{3}s^{-1}.

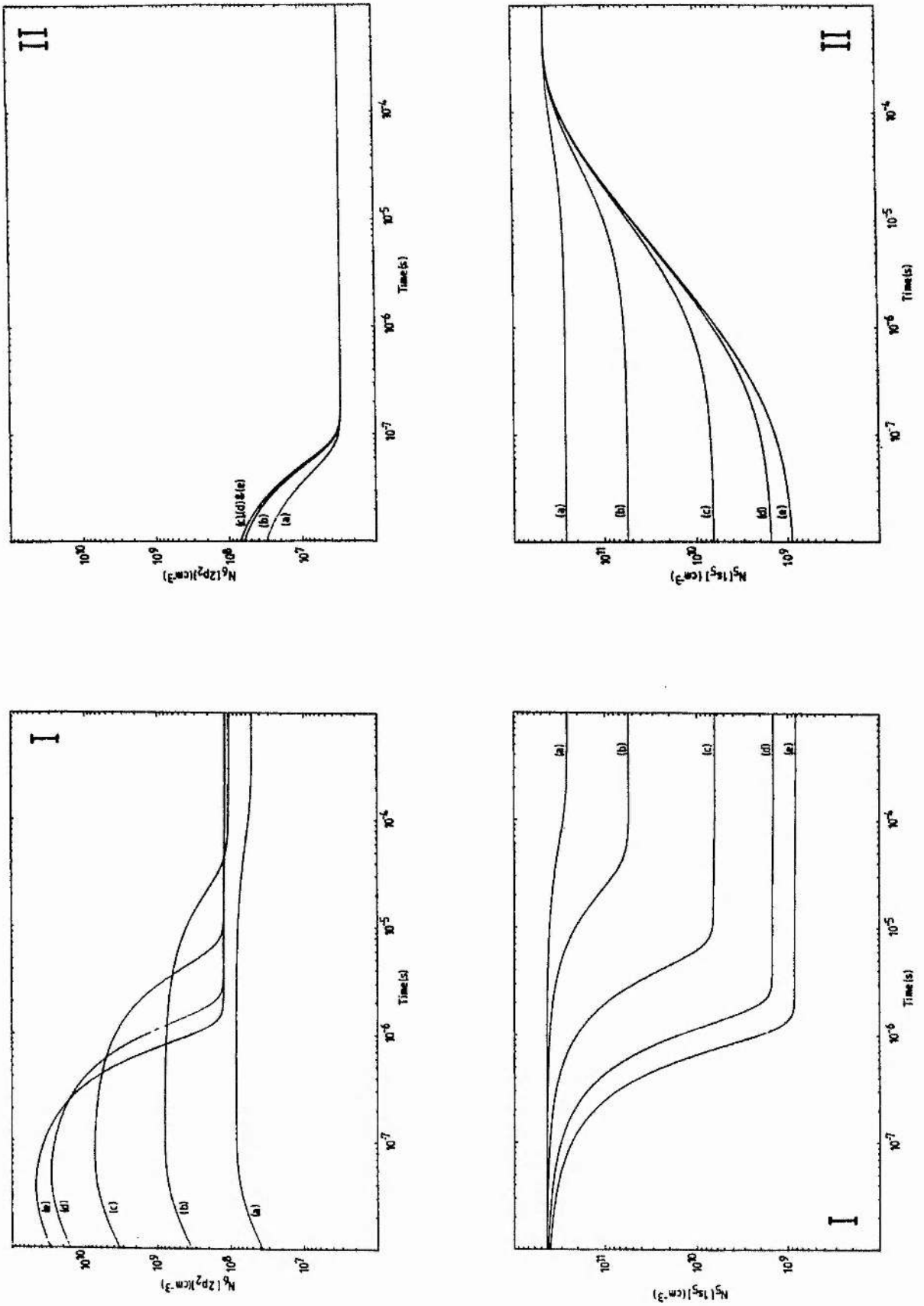

Figure 4.18 Transient behaviour of the $2p_2$, $1s_5$, $1s_4$ and $1s_3$ population densities (I) for switching the laser on and (II) for switching the laser off. Labels refer to the following values of BI: (a)$1x10^4$,(b)$1x10^5$,(c)$1x10^6$, (d)$5x10^6$ and (e)$1x10^7$ s^{-1}.

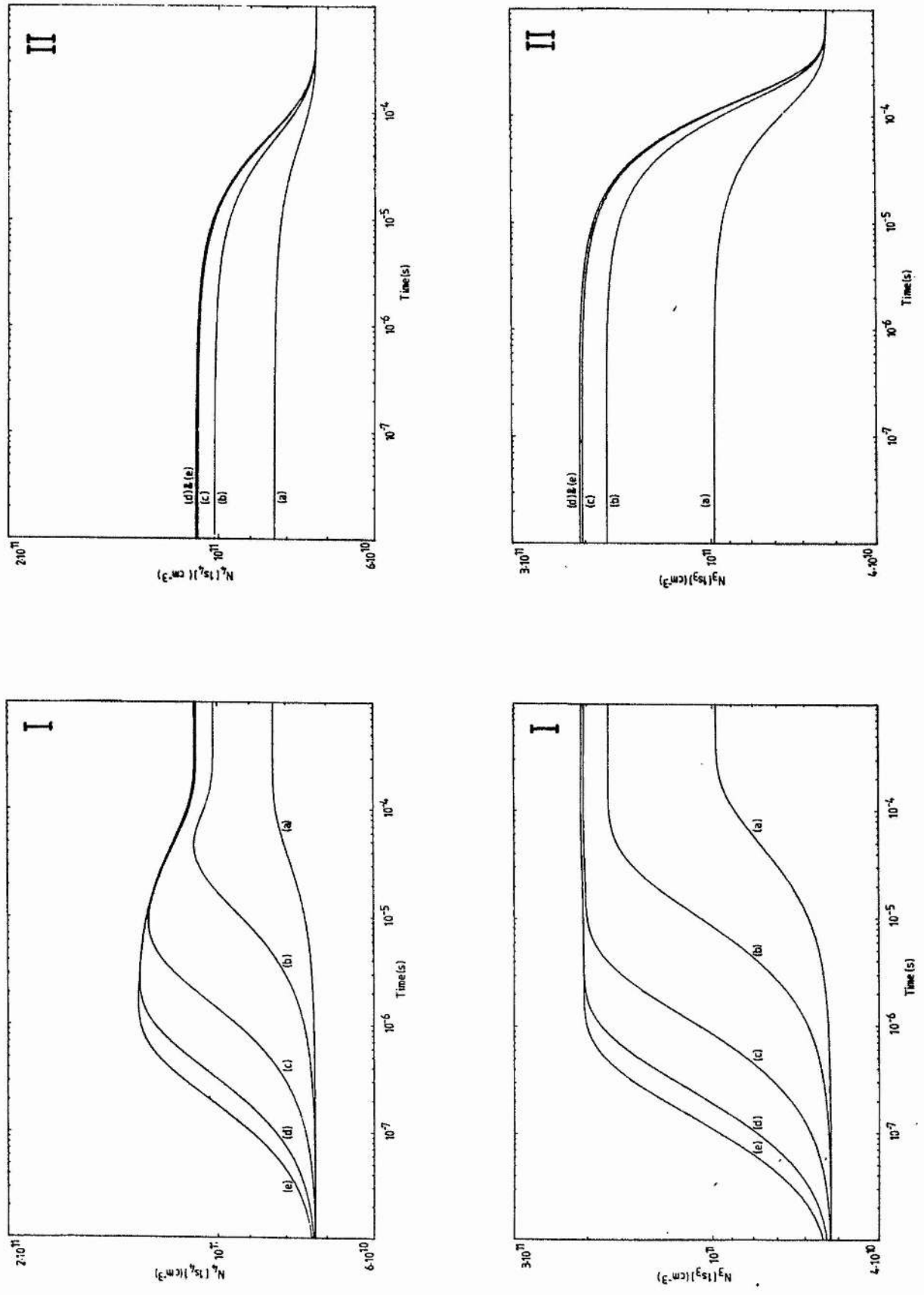

Figure 4.18 Continued.

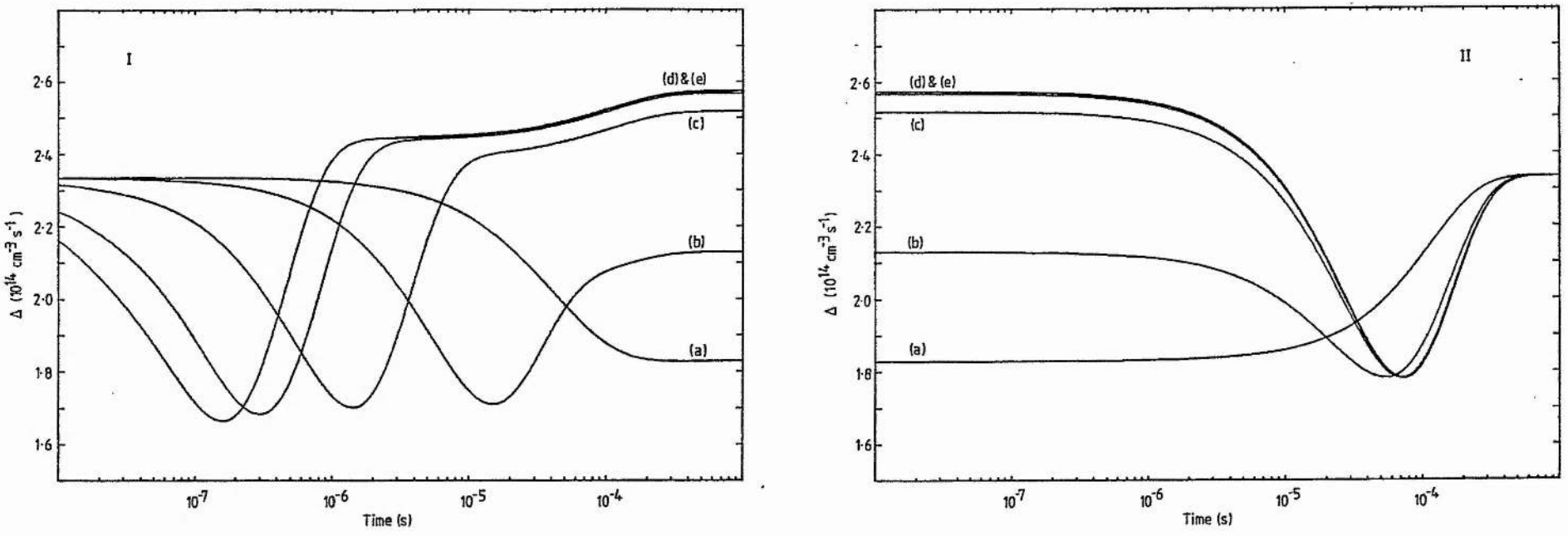

Figure 4.20 Transient rate of addition to the continuum Δ calculated from the transient population densities (I) for switching on and (II) for switching off the laser. $\alpha_3 = 1 \times 10^{-12}\ cm^3 s^{-1}$ and $\beta_3 = 5 \times 10^{-9}\ cm^3 s^{-1}$. The labels refer to the following values of BI: (a)1×10^4, (b)1×10^5, (c)1×10^6, (d)5×10^6 and (e)$1 \times 10^7\ s^{-1}$.

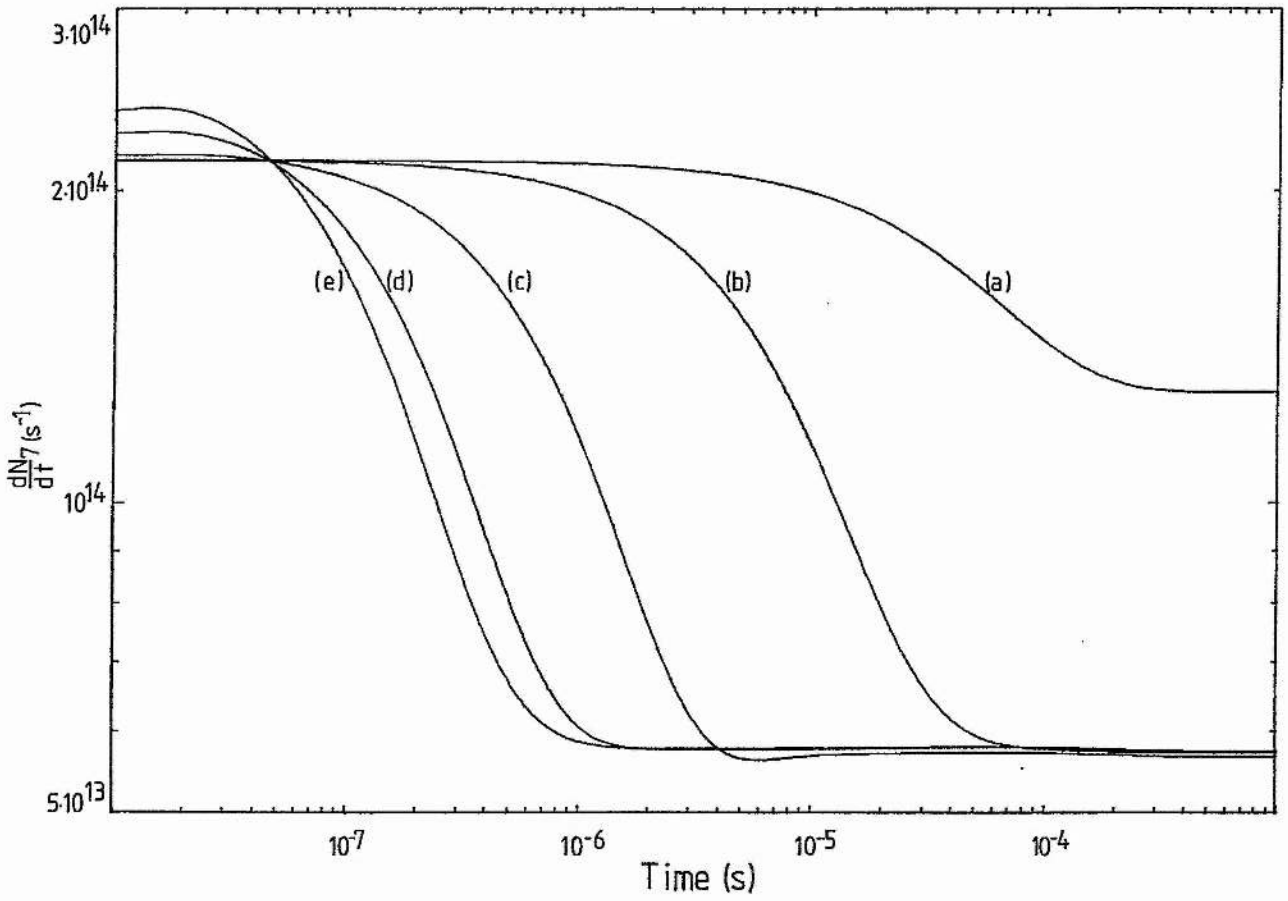

Figure 4.19 Time resolved addition to the continuum when $\gamma_{67} = 2 \times 10^{-7}$ cm^3 s^{-1} for the same values of BI as in figure 4.18.

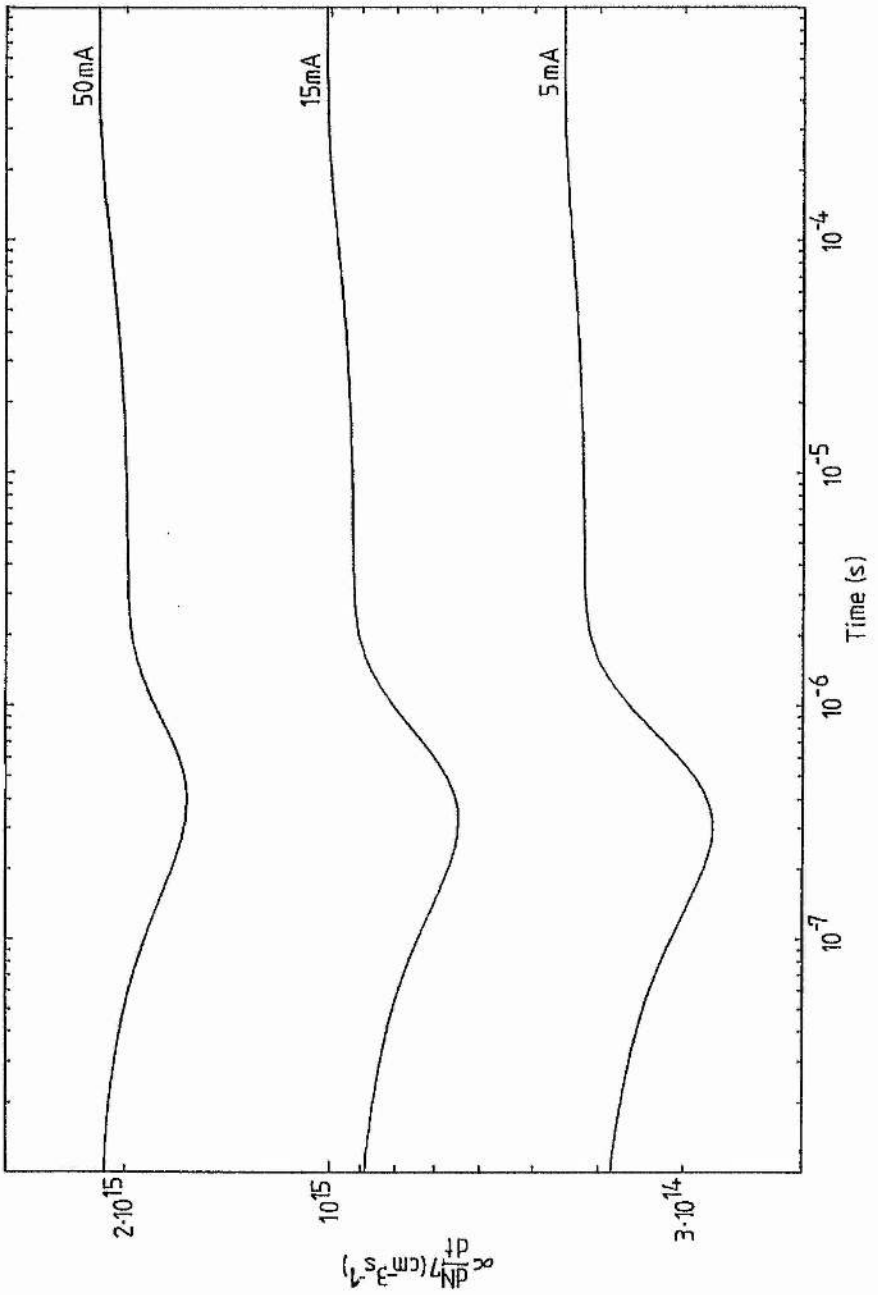

Figure 4.21 Comparison of the time resolved addition to the continuum for switching the laser on for currents of 5mA, 15mA and 50mA. The value of BI is $5 \times 10^6 s^{-1}$.

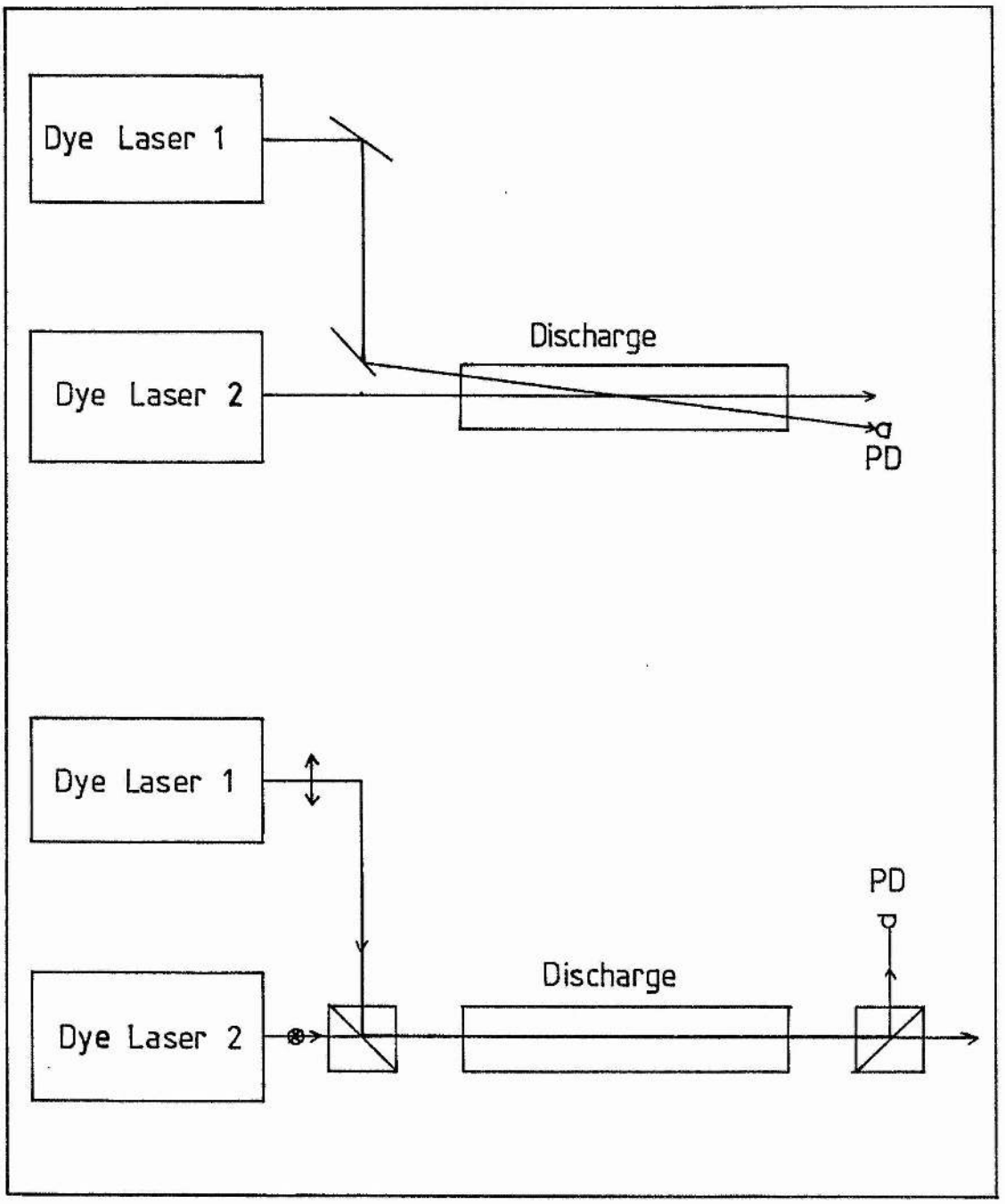

Figure 4.22 Proposed experiment for monitoring the population density of a selected level while monitoring the optogalvanic signal.

CHAPTER 5

SATURATED ABSORPTION SPECTROSCOPY OF TUNGSTEN I

5.1 Introduction

High resolution laser spectroscopic techniques have previously been used to measure the even isotope shifts and hyperfine splittings in a number of atomic species. The naturally occurring isotopes of Mo, Cu and Sr have been studied, on visible transitions, by intermodulated optogalvanic and intermodulated fluorescence spectroscopy, with the atomic species being excited in a hollow cathode discharge [1-3]. Mercury metastables have been excited in a positive column [4] and an rf discharge [5] and the even isotope shifts and hyperfine splittings were measured by saturated absorption spectroscopy on the $6s6d\,^3D_1$-$6s6p\,^3P_o$ transition at 296.73nm. These latter studies achieved the first sub-Doppler resolution attained on a UV transition by laser spectroscopy. Partial sub-Doppler scans of the $6s6p\,^3P_1^o$-$6s^2\,^1S_o$ transition at 253.7nm have been obtained using UV radiation produced by frequency doubling a coumarin 515 ring dye laser in a cooled ADP crystal [6].

Use of a collimated atomic beam crossed transversely with a resonant laser beam gives a much reduced Doppler width and a number of isotope shift measurements have been carried out in samarium [7] and tin [8] by this method. The samarium measurements showed anomalous isotope shifts due to second order hyperfine interactions which had not previously been identified due to the uncertainty of previous measurements. The isotope shifts in tin were measured on the transition $5s^25p^2\,^3P_o$-$5s^25p6s\,^3P_1$ at 286nm. The 286nm radiation was generated by extracavity frequency doubling a Coherent 699 ring dye laser in a cooled ADA crystal.

The present investigation is concerned with isotope shift measurements in tungsten on transitions at 294.7 and 294.4nm. Isotope shifts in tungsten have not previously been measured by classical methods for wavelengths below 370nm, and to date no sub-Doppler studies have been reported for any transitions in the WI spectrum.

Tungsten has the highest melting point of all the metals (3410±20 °C) and is thus not a good candidate for crossed atomic beam/laser beam experiments. It is easily excited in a hollow cathode however and this allows the techniques of saturated absorption, intermodulated fluorescence and intermodulated optogalvanic spectroscopy to be employed.

Tungsten occurs naturally as five isotopes, $_{74}W^{180}$(0.14%), $_{74}W^{182}$(26.41%), $_{74}W^{183}$(14.40%), $_{74}W^{184}$(30.64%) and $_{74}W^{186}$(28.41%). In general the W^{180} isotope is not detected in emission spectra from liquid nitrogen cooled hollow cathode discharges unless a sample of tungsten enriched in this isotope is used.

The ground state configuration for tungsten is $5d^4 6s^2$. Thirteen terms (five of them mixed) and twenty three levels have been identified as belonging to this configuration. Other configurations give rise to similar numbers of levels and the spectrum has an extraordinarily large number of lines as is characteristic of elements with partially filled d shells. Laporte and Mack [9] conducted an exhaustive study and review of the tungsten spectrum. They assign 2567 transitions among 50 even and 250 odd levels. There is considerable term mixing, particularly among the high lying odd levels, and many assignments are given as an energy, a total angular momentum J value and a Lande g value only, as a result. The upper

levels of the two transitions studied here are of this type.

The two transitions studied here; $5d^5 6s\ ^7S_3 - 5d^4 6s6p\ 368_3$ (λ=294.698nm) and $5d^5 6s\ ^7S_3 - 5d^4 6s6p\ 369_2$ (λ=294.440nm), using the notation of Laporte and Mack [9], where odd levels are addressed by the first three numbers of the energy level in wavenumbers and the total angular momentum J is given as a subscript; are among the most intense lines in the arc spectrum. In the present investigation, the even isotope shifts have been measured on both transitions by saturated absorption and the relative shift between W^{182}-W^{184} and W^{184}-W^{186} is in agreement with that obtained on other transitions in tungsten [17-25], where absolute shifts are much larger, using classical spectroscopy. The two strong hyperfine components arising from the W^{183} hyperfine structure have been resolved but the weaker hyperfine components are not resolved.

5.2 Saturated Absorption Spectroscopy

Velocity selective saturation was observed soon after the operation of the first gas laser. Narrow resonances or "Lamb" dips appeared at the centre of inhomogeneously broadened gain lines interacting with counter-propagating laser beams and were recognised as resulting from "holes" burned in the Maxwell-Boltzmann velocity distribution. This phenomenon provided a means for removing the inhomogeneous linewidth in spectroscopic studies by using counter-propagating tunable single frequency laser beams to irradiate the sample. Saturated absorption spectroscopy and related velocity selective techniques are now highly developed and a number of books and articles describing the subject are available [29-32]. The following is a short description of the method of saturation

spectroscopy for a two level atom and a description of broadening mechanisms.

5.2.1 Saturation Spectroscopy in Two Level Atoms

Saturation spectroscopy is based on the velocity selective saturation of an inhomogeneously broadened atomic transition by optical pumping with a monochromatic tunable laser. The population density $n_i(v_z)$ of atoms in the absorbing state E_i in the absence of optical pumping is described by the normalised Maxwellian distribution

$$n_i(v_z)/N_i = f(v_z) = \sqrt{1/\pi \bar{v}_z^2}\exp[-v_z/\bar{v}_z]^2 \tag{1}$$

where the mean velocity is

$$\bar{v}_z = \sqrt{2kT/M} \tag{2}$$

In the presence of the monochromatic light field this distribution is selectively depleted of atoms with velocity components in the interval dv_z such that

$$v_z = (\omega_{ik} - \omega)/k \tag{3}$$

which are Doppler shifted into resonance with the laser frequency ω and are excited from E_i to the higher level E_k with $\omega_{ik} = (E_k - E_i)/\hbar$. Thus a "hole is burnt" into the population distribution $n_i(v_z)$ of the absorbing state and produces simultaneously a peak at the same velocity in the upper state distribution (figure 5.1).

The Doppler broadened linear absorption coefficient for light of very low intensity is

$$\alpha_o(\omega_{ik},\omega) = \int_{-\infty}^{\infty} (n_i(v_z) - n_k(v_z))\sigma_{ik}(v_z)\hbar\omega\, dv_z \tag{4}$$

where $\sigma_{ik}\hbar\omega$ is the absorption cross section per atom. In the strong field case this becomes

$$\alpha(\omega) = \alpha_o(\omega)/(1 + G) \tag{5}$$

where G gives the ratio of the pumping rate to the mean relaxation rate.($G = I/I_{sat}$, I is the irradiating intensity and I_{sat} is defined in eqns (7) and (8)).

At low intensities the width of the hole burnt in the population distribution $n_i(v_z)$ is given by the natural linewidth γ_{ik} but it broadens as the incident intensity increases (figure 5.2).

In order to detect the "Bennet hole" which has been burnt into the population distribution $n_i(v_z)$ by the pump wave, a second light wave, the probe wave, is sent through the sample co-axially with the pump. A narrow dip in the Doppler broadened absorption profile of the probe beam is expected for the probe frequency where both light beams are interacting with the same velocity class of atoms.

It is possible to operate with only one laser, that is to use the same frequency for saturating beam and probe, if the two beams travel in opposite directions so that they experience Doppler shifts of opposite sign. A saturation spectrometer working according to this scheme is shown in figure 5.3. The output of a tunable laser is divided into a strong saturating beam and a weak probe, which pass in opposite directions through the absorbing gas sample. At resonance both beams interact with the atoms with zero axial velocity and the pump beam can bleach a path for the probe. Thus the probe absorption is decreased at this frequency. The saturation signal is detected with higher sensitivity by chopping the pump beam at frequency f and detecting the intensity modulation of the probe at the same frequency

using phase sensitive techniques.

Sorem and Schawlow [33] introduced a method which uses fluorescence detection and offers increased sensitivity with similar convenience to the above method. In this technique, called intermodulated fluorescence, the sample is irradiated with two equal intensity, counter-propagating laser beams which are chopped at frequencies f_1 and f_2 (figure 5.4). A photomultiplier and phase sensitive amplifier are used to detect the modulation of the fluorescence at the sum or difference frequency $f_1 \pm f_2$, which occurs because of the nonlinear mixing of the two intensities in the saturation term.

Hänsch [30] presents a rate equation analysis of saturation spectroscopy in two level atoms. For a sample of gas atoms irradiated by a monochromatic saturating laser beam and a second weak counter-propagating probe beam the rate equation analysis gives the change in the probe absorption $\Delta\alpha_2$ caused by the saturating field, normalised by the Doppler broadened linear absorption coefficient for the probe light α_2 as

$$\frac{\Delta\alpha_2}{\alpha_2} = -\frac{I_1}{2I_{sat}} \frac{\gamma_{ik}^2}{(\omega-\omega_{ik})^2 + \gamma_{ik}^2} \qquad (6)$$

where the saturation intensity I_{sat} is given by

$$I_{sat}^{-1} = \frac{4\pi}{h^2 c} |\mu_{ik}|^2 \gamma_{ik}^{-1} (\gamma_i^{-1} + \gamma_k^{-1} - A_{ik}\gamma_i^{-1}\gamma_k^{-1}) \qquad (7)$$

The intensity of the saturating beam is I_1, γ_{ik} is the natural linewidth of the transition $|i\rangle \rightarrow |k\rangle$, $\gamma_i^{-1} = \tau_i$ is the lifetime of the lower level, $\gamma_k^{-1} = \tau_k$ is the lifetime of the upper level and $|\mu_{ik}|^2$ is the dipole moment. The change in the probe absorption as a function of laser frequency is a Lorentzian centred at ω_{ik} with width γ_{ik}, the

natural linewidth. Substituting the dipole moment in terms of the spontaneous emission rate A_{ik} in equation (7) gives

$$I_{sat} = \frac{h\omega_{ik}^3 \gamma_{ik}}{2\pi c^2 A_{ki}[\tau_i + \tau_k - (g_k/g_i)A_{ki}\tau_i\tau_k]} \tag{8}$$

where g_k and g_i are the statistical weights of the two levels. The saturation intensity decreases with: decreasing frequency, decreasing natural linewidth, increasing transition probability and increasing level lifetimes. A low saturation intensity is expected to be advantageous in carrying out saturated absorption experiments, particularly for transitions in the UV where only small laser powers are available. However, the above analysis is only accurate for $I_1/I_{sat} < 1$. For the case of a large degree of saturation, $I_1/I_{sat} = G >> 1$, it is necessary to solve the equations for the time evolution of the density matrix [34]. This gives

$$\frac{\Delta\alpha_2}{\alpha_2} = \left(1 - b \frac{\bar{\Gamma}^2}{(\omega-\omega_{ik})^2 + \bar{\Gamma}^2}\right) \tag{9}$$

where

$$b = G/(1 + G + (1 + G)^{1/2})$$

and

$$\bar{\Gamma} = \gamma_{ik}(1 + (1 + G)^{1/2})/2$$

The change in the probe absorption now has a width which increases as the saturation parameter increases. This is called power broadening. For a transition with a small saturation intensity I_{sat} it may be difficult to obtain signals which are not power broadened when using a saturating intensity which is easily detectable. The method of intermodulated fluorescence allows up to a two order of magnitude improvement in sensitivity compared with saturated absorption. For this reason intermodulated fluorescence is widely used for studying transitions from long lived metastable levels with low saturation intensities.

There is a number of other broadening mechanisms in addition to natural lifetime broadening and power broadening. In the saturated absorption spectrometer arrangement shown in figure 5.3 there is a small angle between the two interacting beams. This introduces a residual linear Doppler width of approximately $0.6\theta\nu_D$ [29], where ν_D is the Doppler width. For a Doppler width of 1 GHz and an angle of 5 mrad this gives a residual Doppler broadening of 3 MHz. An analogous broadening due to a spherical beam wavefront is estimated as $\Delta\nu = 2\pi(2\ln 2)^{1/2}w\nu/R$, where R is the curvature of the wavefront [29]. Thus a very flat wave surface must be used.

The laser beams interact with the moving atoms for a finite time. This time will be limited by the beam diameter or interaction length, whichever is the smaller. If the interaction time is shorter than the radiative lifetime this will increase the homogeneous linewidth to a value greater than the natural linewidth according to

$$\Delta\nu = 0.89v/L$$

An optical beam expansion may be necessary to prevent transit time broadening in very high resolution experiments.

Non-radiative relaxation processes, predominantly collisions, can lead to pressure broadening. For the special case of collisions between like atoms it is called self-broadening. To accurately predict the reduction of an excited species lifetime due to collisions the interaction potential must be known. This is usually of a very complex form. A simple minded estimate of the increase in the linewidth is given by

$$\Delta\nu = \nu_{nat} + N\sigma\bar{v}/\pi$$

where N is the density of perturbers, $\bar{v}$ is the mean relative velocity, $\bar{v} = [8kT(M_1+M_2)/\ M_1M_2]^{1/2}$, and σ is the collision cross section.

Experimentally pressure broadening in the range 1 to 30 MHz/Torr is observed. Saturated absorption and related velocity selective techniques have provided new methods of measuring these broadening constants.

Pressure broadening results from state changing collisions but it is also possible for a collision to change an atoms trajectory without changing its state. As saturated absorption is a velocity selective technique it is sensitive to such collisions. Weak velocity changing collisions broaden the width of the hole in velocity space. Strong velocity changing collisions remove atoms entirely from the resonant velocity groups. Many collisions are of an intermediate kind and considerable effort has been given to describing these theoretically [35].

When studying transitions in a gas discharge there will also be broadening due to linear and quadratic Stark effects. The former complicates interpretation of the hyperfine structure of the hydrogen Balmer β line where the Stark shift is sufficient to completely resolve the Stark components [36]. The latter occurs for multielectron atoms but the calculated broadening is usually much smaller than the natural linewidth.

The present understanding of the line shapes observed in saturation spectroscopy is not complete. When all the broadening mechanisms are absent the lineshapes are often more complex than expected.

5.2.2 Crossover Resonances

If close lying spectral lines inside the Doppler width belong to transitions with a common level, the saturation spectrum will contain additional resonances which occur midway between the two transitions. Consider a three level system as indicated in figure 5.5. The pump beam saturates the $|i\rangle - |j\rangle$ and $|i\rangle - |k\rangle$ transitions creating two holes in the lower level velocity distribution and two peaks in the upper level velocity distribution. When the laser frequency $\omega = \omega_{ik}$ or $\omega = \omega_{ij}$, the pump and probe interact with the same $v=0$ velocity group and a normal inverted Lamb dip results (figure 5.5a). However, when

$$v_{ij} = -v_{ik}$$

which occurs when $\omega = (\omega_{ij} + \omega_{ik})/2$ the counter-propagating probe beam absorption due to one transition is altered as a result of the pump wave on the other transition (figure 5.5c) which gives rise to a cross-over dip in the absorption exactly half between the Lamb dips corresponding to the $|i\rangle - |j\rangle$ and $|i\rangle - |k\rangle$ transitions.

There is an additional effect that occurs when the upper level is common, as in figure 5.6, due to optical pumping. Atoms excited into the common level $|j\rangle$ can decay to either of the lower levels, $|i\rangle$ or $|k\rangle$. Atoms reaching the state not being pumped can be removed only by the weak probe beam and by slow relaxation processes. Thus an increase in the population of the velocity groups corresponding to the Bennet holes in the other level is observed. A probe wave that interacts with these velocity groups encounters increased absorption as a result of the population peak in the lower level but decreased absorption as a result of the peak in the upper level $|j\rangle$. The former usually dominates leading to a crossover peak inverted with respect to

the Lamb dip peaks in the spectrum, as indicated in figure 5.6. This type of behaviour is well illustrated by saturated absorption spectra of the sodium D_1 and D_2 lines [37].

5.3 Theory of Isotope Shifts

The difference in wavelengths of lines emitted by isotopes of a given element arise from two effects, mass effects and field effects [11-13]. The mass effect is caused by additional kinetic energy due to the motion of the nucleus relative to the centre of mass of the atom and this kinetic energy varies with nuclear mass M according to

$$\Delta E = \underline{P}^2/2M \tag{10}$$

where $\underline{P}$ is the nuclear momentum. The nuclear momentum can be equated to the negative sum over the electron momenta and so ΔE can be expressed as

$$\begin{aligned}\Delta E &= (1/2M)\left(\sum_i \underline{p}_i\right)^2 \\ &= (1/2M)\sum_i (\underline{p}_i)^2 + (1/2M)\sum_{i>j} (\underline{p}_i \cdot \underline{p}_j) \\ &= \Delta E_n + \Delta E_s\end{aligned} \tag{11}$$

The normal mass shift ΔE_n may be evaluated exactly using the virial theorem to give the Bohr reduced mass correction

$$\Delta E_n = -(m/M)E^o \tag{12}$$

The fractional change, $\Delta E_n/E^o$, is the same for all levels. The second term ΔE_s, the specific mass shift, which depends on the particular energy level under consideration, is a symmetrical two electron operator and may be calculated for the case of LS coupling but in general is not susceptible to exact calculation. This term can be either positive or negative in sign and is of the same order as the

normal mass shift. As the total mass shift for a particular level is proportional to 1/M (or 1/A, where A is the mass number) the differences in the total mass effect for two adjacent even isotopes is proportional to $1/M^2$. Thus, Brix and Kopfermann [10] suggest it is safe to neglect the mass shift for Z>60, but as measurements become more precise this assumption is not valid.

The field shift is caused by changes in nuclear size, charge distribution and shape that occur when neutrons are added. In general the nuclear volume is larger for heavier nuclei and as the potential energy of an electron within the nucleus is increased over that associated with the equivalent point charge interaction the electron binding energy is decreased for larger neutron number. Only s and $p_{1/2}$ electrons penetrate the nucleus to any depth ($|\Psi(0)|^2 > 0$) and so most of the field shift is attributed to these, in particular the s electrons. The difference in energy for two adjacent isotopes is given by [12]

$$\delta E_f = R_\infty |\Psi(0)|^2 4\pi (a_H^3/Z) C \tag{13}$$

where a_H is the Bohr radius for hydrogen, Z is the atomic number, R_∞ is the Rydberg constant and $|\Psi(0)|^2$ is the nonrelativistic electron density at the nucleus. The factor C, the isotope shift constant, depends only on the nuclear distribution of the two isotopes under consideration. The equation of Racah, Rosenthal and Breit [14] gives, for the case of an s electron,

$$C=(\gamma+1)/(\Gamma(2\gamma+1))^2 B(\gamma)(2Zr_o/a_H)^2 (\delta r_o/r_o) \tag{14}$$

where we have $\gamma = 1-\alpha^2 Z^2$, $\alpha = e^2/\hbar c$, Γ is the gamma function, r_o is the radius of the nucleus assuming it is spherical and of uniform density and δr_o is the change in the radius caused by the addition of neutrons. The value for a $p_{1/2}$ electron of the same principal quantum

number is about $\alpha^2/(1+\gamma)^2$ that for the s electron [15]. The factor $B(\gamma)$ depends on the distribution of the proton charge in the nucleus. For a uniform distribution of proton charge over the volume of the nucleus we have [14]

$$B(\gamma) = 3[(2\gamma+1)(2\gamma+3)]^{-1}$$

For the charge distributed uniformly over the surface of the nucleus we have [14]

$$B(\gamma) = (2\gamma + 1)^{-1}$$

If the nucleus is deformed to a non-spherical shape and the shape changes as neutrons are added this will cause a further shift. Assuming a uniform distribution with a quadrupole deformation, where r_o is the radius of the uniform sphere with the same volume as the deformed nucleus, the difference in energies for isotopes becomes [12]

$$\delta E_f = \Delta E_{f,sph}[(1+\gamma(5/4\pi)\beta^2)(2\gamma\delta r_o/r_o) + (1+(2\gamma-1)(5/8\pi)\beta^2)\gamma(5/4\pi)\delta(\beta^2)] \quad (15)$$

The deformation parameter β is derived from experimentally determined transition probabilities for the first excited state of the nucleus according to

$$B(E2,\ 0\text{->}2) = a^2\beta^2(1 + 0.36\beta)^2 \quad (16)$$

where

$$a = (3/4\pi)eZR^2$$

The nuclear quadrupole moment is given by

$$Q = (3Zer_o^2/(5\pi)^{1/2})(\beta+0.36\beta^2) \quad (17)$$

In the above it is the relative isotope shift between pairs of isotopes for a particular level which is determined. In practice it is the relative isotope shift in a transition which is measured. In order to compare experiment and theory it is necessary to extract relative shifts in the levels from the relative shifts of the

transition. This has been done by assigning the shift in a particular level to be zero [18]. The level chosen for this assignment often has a substantial relative shift and it is doubtful that any meaningful comparison between experiment and theory can be made this way. Alternatively an estimated value of the relative shift in one level may be used [23]. For some particular transitions, for example transitions involving the change of a d to an f electron, it can be shown by comparing the relative transition isotope shift (RTIS) for several transitions with different upper terms that the shift in the upper level is zero and thus the relative level isotope shift (RLIS) in the lower level is measured directly. This can then be used to derive the RLIS from the measured RTIS on transitions with other upper level configurations and so on. This type of procedure has been applied to strontium [2].

Agreement between the results of ab initio calculations and experiment has been poor to date. More often the theorist uses the experimental results as a guideline to explore which nuclear model gives the closest agreement between experiment and theory. Thus the measurement of isotope shifts is important to increasing understanding of the structure of nuclei.

Some progress has been made in separating specific mass shifts from field shift contributions by the following semi-empirical approach. After subtracting the normal mass shift contribution the residual isotope shift between two isotopes, i and j, with mass numbers A_i and A_j and for a line x is given by

$$\Delta\nu_{ij}^{x} = K^{x}A_{ij} + E^{x}C_{ij} \qquad (18)$$

where

$$A_{ij} = (A_j - A_i)/A_jA_i$$

In the first term, which describes the specific mass shift, K^x depends only on the wavefunctions of the electronic states of the transition. The second term corresponds to the field shift and is also the product of a purely electronic part E^x and a purely nuclear part C_{ij}. The electronic contribution, E^x, is here proportional to the difference of the electronic densities at the nucleus of the two levels of the transition.

The ratio $\Delta\nu_{ij}^x/\Delta\nu_{kl}^x$ of the shifts of two different isotope pairs, i,j and k,l, in line x would be the same for all lines if either the mass effect or the field effect were zero. Its constancy or otherwise is a means of determining if it is valid to neglect mass effects in heavier atoms or to neglect field effects in lighter atoms. Variation in this quantity, now that it is being measured with better accuracy, appears as a general rule. It has been unambiguously observed in elements as light as calcium and as heavy as plutonium [13].

King [16] devised a method of obtaining information about the ratio of field shifts on two lines. The shift $\Delta\nu_{ij}$ is replaced by a modified shift $\Delta\nu_{ij}'$, according to

$$\Delta\nu_{ij}' = \Delta\nu_{ij}(A_{rs}/A_{ij}) \tag{19}$$

where

$$A_{rs} = (A_s - A_r)/A_rA_s$$

is the nuclear factor of the specific mass shift, for a particular pair of isotopes, taken as reference. For each isotope pair, $\Delta\nu_{ij}'^y$ is plotted against $\Delta\nu_{ij}'^x$ for all available isotope pairs (ij). The points associated with the various isotope pairs lie on a straight line since according to equation (18) their coordinates obey

$$\Delta\nu_{ij}'^y = (E^y/E^x)\Delta\nu_{ij}'^x + [K^y - K^x(E^y/E^x)]A_{rs} \tag{20}$$

The diagram is known as a "King plot", and the straight line connecting the plotted points as the "King line". The gradient of this line is an experimental quantity yielding the ratio E^y/E^x of the field shifts of the two lines; it is a pure field shift quantity. The intercept, $m' = A_{rs}[K^y - K^x(E^y/E^x)]$, is a pure mass shift quantity when the value of E^y/E^x is substituted in.

The values of the isotope shift constant determined from experiment, for transitions involving a change in the number of s electrons, C_{exp}, are usually referred to as βC_{exp} where β is placed before C_{exp} to indicate that the observed shift may be reduced due to screening effects by the electrons involved in the transition on the remainder of the electron configuration. This β is quite different from the deformation parameter and is an unfortunate choice of symbol. As it is used exclusively in the literature it will be retained here. For example if a 6p electron is excited to a higher energy state, the screening which it exerts on the $(6s)^2$ shell is reduced and the 6s electrons are coupled more closely to the nucleus. It is possible to allow for some screening effects. Brix and Kopfermann [10] predict a reduction in the isotope shift of a 6s electron to be 20% for screening by a 5d or 6s electron and 10% for screening by a 6p electron. In the present studies it is an isotope shift purely due to a change in the screening electrons that is observed. On a transition involving the change in the screening on a 6s electron from a 5d to a 6p electron a transition isotope shift about 10% of the 6s isotope shift would result .

5.4 Previous Results From Isotope Shift Measurements in Tungsten

Isotope shifts between the three abundant even isotopes of tungsten have been previously measured by studying the emission from a liquid nitrogen cooled, W hollow cathode discharge, using a high finesse Fabry Perot etalon. Fifty five transitions in the wavelength range 601.28-370.79nm have been studied [17-25]. A schematic of the level splittings for the isotopes giving rise to the even isotope splittings and the hyperfine components is shown in figure 5.7. Ten of the transitions studied have a $^7S_3$ lower level . The results obtained from these transitions are summarised in Table I. Where uncertainties are not quoted in Table I these are $\pm$60 MHz. The transition isotope shifts observed fall into two categories; one group with a shift of the order of 2 GHz arising from a change in the number of s electrons as the configuration changes from $5d^5 6s \rightarrow 5d^3 6s^2 6p$, and a second group of shifts of less than 1 GHz for a configuration change $5d^5 6s \rightarrow 5d^4 6s6p$ where the number of s electrons is unchanged and the transition shift arises from changes in the screening of the s electrons.

For a single level in tungsten the lower mass number isotope is lower in energy. As the W^{182} isotope peak always occurs at a higher frequency than the W^{184} peak which is in turn higher than the W^{186} peak for the $^7S_3$ transitions the RLIS in the lower level exceeds that in the upper level (see figure 5.7).

The isotope shift between W^{182} and W^{180} has been measured on two transitions at 426.94nm and 404.5nm using cathode material enhanced in W^{180}. The relative shifts, $[\Delta(182\text{-}184)]/[\Delta(180\text{-}182)]$, obtained were 1.38 [21], 1.52 [22], 1.45 [25] and 1.38 [23].

Table I

Previous Isotope Shift Measurements on $^7S_3$ - Transitions

λ /nm	Upper level	Δ(184-182) /MHz	Δ(186-184) /MHz	$\frac{\Delta(184-182)}{\Delta(186-184)}$	Ref.
475.76	239_2	930	750	1.24	[20]
430.21	261_2	690	600	1.15	[20]
429.46	262_2	990	840	1.18	[20]
426.94	263_2	2820	2430	1.16	[18]
		2850	2364	1.206	[20]
		2742 (±40)	2430 (±40)	1.128	[25]
407.44	274_3	540	480	1.13	[20]
404.56	276_2	1860	1710	1.09	[18]
		1878 (±20)	1788 (±15)	1.050	[20]
		1881	1788	1.052	[25]
400.88	278_4	540	600	0.90	[20]
381.75	291_3	2820	2370	1.19	[20]
		2763 (±30)	2310 (±30)	1.196	[25]
380.92	291_2	2010	1920	1.05	[20]
370.79	299_3	2070	1800	1.15	[20]

The nuclear spin of W^{183} was determined to be 1/2 from studies of the hyperfine components using tungsten enriched to about 90% in W^{183} [19]. Two intense hyperfine components were observed for transitions involving levels with total angular momenta J between 0 and 5 implying $2I + 1 = 2$. The two intense hyperfine components were almost coincident with the W^{182} and W^{184} even isotope peak positions, observed using naturally occurring tungsten. This explained why the hyperfine components were not observed in these spectra. Vreeland and Murakawa [22] found that the hyperfine components were not coincident with the even isotope peaks on certain transitions. The two intense hyperfine components were not resolved separately but from centre of gravity considerations they were able to predict the hyperfine component positions. Their results for one transition are shown in figure 5.8. The intensities of the hyperfine components shown in figures 5.7 and 5.8 are those obtained from wave mechanics [26].

Blaise and Gluck [23] made an estimate of βC_{exp} from their experimental results using the Lande-Goudsmit-Fermi-Segre (LGFS) formula for calculating $|\Psi(0)|^2$ and assuming the mass shift to be negligible. The LGFS formula gives the s-state probability density at $r = 0$ to be

$$|\Psi_s(0)|^2 = Z_i Z_o^2 / [\, a_H^3 (n^*)^3] \qquad (21)$$

where $Z_i e$ is the effective nuclear charge, $Z_o e$ is the external atomic charge and where

$$n^* = n - \Delta$$

is the effective quantum number (obtained by equating the term value energy to $-R_\infty Z_o^2/(n^*)^2$), n is the principal quantum number and Δ is the quantum defect. Using the result

$$1/n^{*3}(dn^*/dn) = 0.596 \pm 0.06$$

this gives

$$\beta C_{exp} = \Delta\nu_{6s}/(0.596) \qquad (22)$$

The value of $\Delta\nu_{6s}$ was derived from the measured isotope shifts on a number of transitions involving an increment in the number of 6s electrons by one. Blaise and Gluck [23] compared their results with C_{th}, the volume field effect, for $r_o = 1.2\times10^{-15}$m. Table II summarises their results.

The intrinsic quadrupole moments and the deformation parameters β, for tungsten nuclei have been derived from measured transition probabilities for the first excited state of the nuclei [27], excited by bombardment with 3MeV protons. The results are summarised in Table III.

5.5 Saturated Absorption Spectra

For the present investigations on the $^7S_3$-369_2 and $^7S_3$-368_3 transitions a standard saturated absorption spectrometer arrangement is employed as described in section 5.2 and depicted in figure 5.3. The hollow cathode discharge tube used is illustrated in figure 5.9a. It has a solid tungsten cathode (3mm internal diameter and 20mm long) inserted into a block of copper which is welded to glass to metal seal material which in turn is connected to a cannellated rod of copper. A glass dewar is formed about the copper rod by way of a glass to metal seal and this is filled with liquid nitrogen to cool the discharge. The windows are 1" diameter quartz discs and the anodes are nickel wire. The cooling achieved with this tube was not very efficient at the running currents found to give optimum signals and a modified design using a larger volume of copper (drilled with holes to increase

Table II

Comparison of Experiment and Theory for Tungsten [23]

	Isotope Pair		
	180-182	182-184	184-186
$\beta C_{exp}(x10^{-3} cm^{-1})$	93	133	117
$C_{th}(x10^{-3} cm^{-1}$	310	308	306
$\beta C_{exp}/C_{th}$	0.30	0.43	0.38

Table III

Quadrupole Moments and Deformation Paramaters for Tungsten Nuclei

	E2(keV)	$Q_o(x10^{-24} cm^2)$	β
W^{182}	100.07	6.34	0.236
W^{183}	46.48	6.37	0.236
W^{184}	111.13	6.04	0.224
W^{186}	122.48	5.99	0.220

its surface area) and a shorter distance between the cooled metal and the cathode has been proposed for future experiments and is depicted in figure 5.9b.

The saturated absorption spectra of the 294.440 nm and 294.698 nm lines are shown in figures 5.10 and 5.11. The transmission peaks of a 30cm confocal interferometer (constructed for the purpose of calibrating these spectra, FSR - 250MHz) generated by the fundamental beam are also shown. To avoid UV intensity fluctuations, due to dust particles in the laser cavity, the cavity was partially sealed using a perspex cover designed for the purpose and flushed with nitrogen to remove most of the dust. Then the enclosed cavity was maintained at a slightly positive N_2 pressure to keep dust out. The stabilised laser linewidth when scanning, with the frequency doubling elements in the cavity, was 350kHz (corresponding to 700kHz in the UV). This is considerably larger than the stabilised linewidth of 150kHz obtained without the frequency doubling elements. These spectra were obtained with the current optimised (40 - 50 mA) and using the maximum available UV intensity without focusing (10 mW mm^{-2} at the entrance to the discharge) in the saturating beam. A time constant of 100 ms was used on a Brookdeal Model 401A phase sensitive detector to condition the signal. Similar spectra were obtained for a saturating beam intensity of 3 mW mm^{-2} but the signal magnitude was reduced by a factor of five and the signal to noise ratio was similarly reduced. For saturating beam intensities below 3 mW mm^{-2} the sharp features were lost on the background, and only a Doppler broadened profile was observed at a saturating beam intensity of 0.5 mW mm^{-2}. There was no evidence of power broadening of the sub-Doppler features with the UV power available.

The broad Doppler-limited pedestal underneath the Doppler-free spectra originates from velocity changing collisions which occur during the lifetime of the metastable lower level. These have the effect of broadening the hole burned in the velocity distribution as atoms of the velocities adjacent to those being pumped fill in the hole.

A comparison is made between the linear absorption profile and the saturated absorption spectrum for λ = 294.698 nm in figure 5.12. The linear absorption was of the order of 8%.

The even isotope shifts and hyperfine splitting between the two most intense hyperfine components obtained from twenty-eight scans at λ= 294.440nm and twelve scans at λ = 294.698 nm are given in table IV. The numbers in brackets are the standard deviations. The large standard deviations in the larger splittings arise from the nonlinearity of the laser scan. Further improvement was not possible by careful alignment, and modification of the laser optics and electronics would be required to overcome this problem. Alternatively computerised data collection would allow the linearisation of scans by computation and would also allow algorithms for determining the centre of the lines more accurately than can be done by eye, to be utilised. Also given in Table IV is the ratio of the splittings for the 182-184 and 184-186 pairs of isotopes. This ratio is determined with an accuracy comparable with that in previous experiments on other transitions (summarised in Table I) and is in agreement with previous values.

Table IV

Results of the Saturated Absorption Study at 294.4 and 294.7nm

	Wavelength/nm	
	294.440	294.698
Upper Level	368_2	369_3
Δ (182-184)/MHz	113(3)	117(2)
Δ (184-186)/MHz	99(2)	106(3)
Δ (183a-183b)/MHz	2136(12)	1406(6)
$\frac{\Delta\ (182-184)}{\Delta\ (184-186)}$	1.14±0.05	1.10±0.05

Table V

Abundances Deduced from Peak Heights of the Spectra

	% Abundance from peak heights above zero (±0.1%)		% Abundance from peak heights above background (±0.4%)		Natural Abundance
	I	II	I	II	
λ =294.440nm					
182	27.5	27.5	24.8	27.1	26.4
183a	8.4		13.2		
183b	6.0		8.5		
(183)	14.4	14.4	21.7	14.4	14.4
184	30.0	30.0	27.1	29.7	30.6
186	28.1	28.1	26.4	28.8	28.4
λ =294.698nm					
182	25.9	27.0	25.4	26.3	26.4
183a	11.7		9.0		
183b	6.1		8.2		
(183)	17.8	14.4	17.2	14.4	14.4
184	28.9	30.0	29.5	30.5	30.6
186	27.4	28.5	27.9	28.8	28.4

It is difficult to interpret the peak heights when there is a large background contribution from the effect of velocity changing collisions. Cooling the discharge did enhance the magnitude of the signal observed by up to 100% for currents of 25 mA, but without reducing the relative background contribution. As the discharge current was increased, which gave better definition of the saturated absorption peaks, the enhancement due to cooling was lost. The cathode was no longer being cooled at these higher currents.

Two methods were used to consider the ratios of the peak heights. Firstly the peak heights above the zero signal were measured and the abundance of each isotope was predicted from these. The same was done for measuring the peak heights with the background subtracted by drawing the best straight line across the base of the peak to the background. As the abundance of W^{183} was usually overestimated in these calculations the abundances of the even isotopes were calculated from the peak heights obtained in the two ways described with the W^{183} abundance defined as 14.4%. The results of these calculations are summarised in table V.

Only for λ = 294.440 nm, with the peak heights measured from the zero signal level, is the predicted W^{183} abundance correct and also spread between the hyperfine states in the proportions expected from the theoretical intensity ratios. But for all derivations the abundances of the even isotopes are in reasonable agreement with the naturally occurring abundances. The agreement is better when the W^{183} abundance is given its expected value.

The full width at half maximum of all the even isotope peaks on both transitions is (38±2) MHz. The spread of the measured widths for the two hyperfine components is larger being (45-64) MHz with the average being 48 MHz. The increased uncertainty arises from the difficulty in determining the background level for these peaks.

The values of gA, the statistical weight multiplied by the transition probability, have been tabulated for many transitions in tungsten, though not for all the transitions involving either of the upper levels of interest here [28]. The sum of the gA values for the five transitions which are most intense in emission, arising from the 369_2 level is about 64×10^8 s^{-1}. The value of g for this level is 5. Thus the sum of the A values for this transitions is $13 \times 10^8 s^{-1}$ and the natural linewidth deduced is 200 MHz. This is larger than the linewidth observed. All the lower levels for these transitions are metastable or the ground state and therefore may have significant population densities in the hollow cathode discharge. The upper level lifetime may thus be increased by radiation trapping, leading to a narrower "natural" linewidth. Alternatively the transition probabilities may be incorrect. Radiation trapping would also explain the observation of broader lines for the W^{183} hyperfine components as the radiation trapping for these transitions will be less than for the even isotope transitions due to the lower density of W^{183} metastables.

Figures are not available for the collision cross section between the $^7S_3$ state of tungsten and neon. Nor has the quadratic Stark effect on the $^7S_3$, 368_3 and 369_2 states been investigated, but by comparison with other atomic species (Hg in Ne[4] and Sr in Ne [2]) Stark broadening and impact broadening should only contribute a few MHz to the linewidth. Neon is used because it produces the smallest

impact broadening of all noble gases [2]. Thus the resolution achieved is consistent with that expected from the natural linewidth reduced by radiation trapping.

Some information about the expected hyperfine spectra on these two transitions can be obtained from the present results. On the $^7S_3$-368_3 transition the position of the centre of gravity of the four W^{183} hyperfine components can be calculated knowing the separation of the two strong hyperfine components only. Considering the two intense hyperfine components only, the centre of gravity is given by

$$17.4\,\nu_{cg} = 7.4\,\nu$$

where ν is the separation of the intense hyperfine components and ν_{cg} is the centre of gravity measured relative to the strongest hyperfine component. The two weak hyperfine components can be included without explicitly knowing the frequency splitting because of symmetry. Including the two weak hyperfine components this gives

$$18.14\,\nu_{cg} = 7.77\nu$$

Substituting the experimental value of ν (1405 MHz), the first expression gives ν_{cg} = 597.5 MHz while the second gives ν_{cg} = 601.8 MHz. Thus the two weak hyperfine components shift the centre of gravity away from the strongest hyperfine component by an additional ~5 MHz. Taking the centre of gravity as the mid point between the W^{182}-W^{184} isotope peaks the experimentally determined centre of gravity for the W^{183} isotope is 600 MHz, measured from the most intense hyperfine component. The good agreement on this transition between this experimental value and that obtained using the theoretical intensity ratios and the hyperfine splitting to determine the centre of gravity suggests that this approach may be applied to the $^7S_3$-369_2 transition to determine the exact magnitude of the hyperfine splitting in the upper and lower levels. Results from this can then be used to determine the splittings on the $^7S_3$-368_3

transition.

The mid-point between the W^{182}-W^{184} isotope peaks measured from the position of the strong hyperfine component, for the $^7S_3$-369_2 transition, is 901 MHz. The centre of gravity for the hyperfine components of this transition is given by

$$10\nu_{cg} - 7(2136.1 - \nu_{cg}) - 0.5(\nu_1 - \nu_{cg}) = 0$$

using the experimentally determined hyperfine splitting, ν = 2136.1 MHz. Substituting the experimentally determined centre of gravity this implies ν_1, the hyperfine splitting in the $^7S_3$ level is 1630 MHz. But ν_1 is sensitively dependent on the position of the centre of gravity and varies from 1420-1770 MHz for the centre of gravity in the range 895-905 MHz. So the estimated $^7S_3$ hyperfine splitting is not obtained to better than 200MHz in this way. However, within the predicted uncertainty the $^7S_3$ hyperfine splitting implies that the upper level is inverted as the splitting in the ground state is smaller than the difference of the two splittings. For the value 1630 MHz this implies that F = 5/2 level lies 506 MHz below the F = 3/2 level.

The $^7S_3$ hyperfine splitting has been previously estimated [20] as 1950 MHz and this value also implies an inverted upper level although the F = 5/2 state would only lie 186 MHz above the F = 3/2 state. The $^7S_3$ hyperfine splitting would need to exceed 2136 MHz before a non-inverted upper level would be predicted. The values for the various hyperfine splittings predicted by this analysis are summarised in Table VI.

Table VI

Values of the Hyperfine Splittings Deduced from Centre of Gravity Considerations

ν_{cg} (MHz)	hfs $^7S_3$ (MHz)	hfs 369_2 (MHz)	hfs 368_3 (MHz)
895	1420	-716	+15
901	1630	-506	+225
905	1770	-366	+365
910.2	1950	-186	+545

Table VII

Ratio of Field Shifts for Pairs of Transitions from King Plots

Transitions nm	Field Shift Ratio E^y/E^x	Mass Shift Intercept m' (MHz)
$\frac{294.698}{294.440}$	0.77±0.04	30±4
$\frac{426.94}{294.440}$	26±4	-130±460
$\frac{426.94}{294.440}$	37±4	-1460±450

The spectra for the values obtained with the experimentally determined centre of gravity are shown in figure 5.13.

No crossover resonances are observed midway between the two resolved hyperfine components on either of the transitions studied. As the hyperfine splitting is of the order of the Doppler width (~1700 MHz) crossover resonances are not expected.

An experiment is planned using a 96.3% W^{183} sample to attempt to resolve a third hyperfine component on either of these transitions in the hope that the hyperfine splittings can be determined with some accuracy.

King plots constructed by the method outlined in section 5.3 are drawn in figure 5.14 for the transition pairs 294.440nm:294.698nm, 294.440nm:426.94nm and 294.698nm:426.94nm. The splittings for the $5d^5 6s\,^7S_3$ - $5d^3 6s^2 6p$ transition at 426.94nm are taken from reference [18] and depicted in figure 5.8. This transition is chosen as the upper level configuration is the same as that for the two transitions studied, except it has one less 5d electron and one more 6s electron. The points are clustered closely together so the accuracy in relative shifts deduced from these plots is poor. The ratio of the field shifts and the intercepts obtained are summarised in table VII.

The field shift on the transition when a second 6s electron is formed is 30 - 40 times that observed when a 6s electron changes from being shielded by a 5d electron to being shielded by a 6p electron. Using the isotope shift of a 6s electron in tungsten derived by Blaise and Gluck [23] the measured isotope shifts on the 294.440nm and 294.698nm transitions correspond to a 5% decrease in the isotope

shift of the 6s electron due to being shielded by a 6p rather than a 5d electron. This is about half the reduction of 10% predicted by Brix and Kopfermann [10].

The two upper levels give rise to significantly different shielding of the 6s electron even though they have the same configuration as is shown by the ratio of the field shifts on the two transitions.

5.6 Summary

The even isotope splittings on two transitions, at 294.440nm and 294.698nm in WI have been resolved by saturated absorption and measured with standard deviations of 2-3 MHz. All the splittings are small, of the order of 100 MHz, as is expected on transitions where there is no change in the number of s electrons. The saturated absorption peaks have a FWHM of about 40 MHz which is limited by the natural lifetime of the upper levels increased by radiation trapping.

The relative isotope shift, $\Delta(182\text{-}184)/\Delta(184\text{-}186)$ was measured as 1.14 ± 0.05 on the 294.440nm transition and as 1.10 ± 0.05 on the 294.698nm transition. These are in good agreement with the values obtained on transitions with large even isotope splittings which can be resolved by Doppler limited studies in cooled discharges.

The saturated absorption even isotope peak heights are in reasonable agreement with those expected from the isotope abundances.

The two most intense hyperfine components arising from the odd isotope W^{183} with nuclear spin I=1/2 have also been resolved. These are somewhat broader than the even isotope peaks (50 MHz). From centre of gravity considerations the hyperfine splittings on all three levels involved in the two transitions have been predicted. All predictions of the hyperfine level splittings in tungsten have been made assuming the centre of gravity for the W^{183} hyperfine components falls midway between the W^{182} and W^{184} even isotope peaks. As the splittings obtained are very sensitive to small changes in the centre of gravity it is important to test this assumption more precisely. A saturated absorption experiment using a sample of 96.3% W^{183} is planned when this material becomes available. If any one of the three weak hyperfine components associated with these two transitions can be resolved it will be possible to obtain the hyperfine splittings for these three levels and also to re-evaluate the hyperfine splittings on a number of other transitions which have been studied classically.

The frequency precision in the present investigation is limited by the non-linearity of the ring dye laser frequency scan and the use of a confocal interferometer for frequency calibration. These limitations can be overcome by using optical heterodyning techniques in conjunction with crossed atomic/laser beam experiments. Two narrow linewidth lasers are required. One laser is locked to the centre of a spectral feature or to a reference line. The second laser is locked to another spectral feature (or offset locked in small frequency steps). The difference in the two optical frequencies can be measured directly by mixing the two laser beams on a point contact metal diode. Difference frequencies up to 200 THz can be measured directly [38].

References

1. A Siegel, J E Lawler, B Couillaud and T W Hänsch (1981), Phys.Rev.23A, 2457.
2. C J Lorenzen and K Niemax (1982), Optics Commun.43, 26
3. N Beverini, M Galli, M Inguscio, F Strumia and G Bionducci (1982), Optics Commun.43, 261
4. C E Wagstaff and M H Dunn (1980), Optics Commun. 35, 353.
5. B Couillaud, L A Bloomfield, J E Lawler, A Siegel and T W Hänsch (1980), Optics Commun. 35, 359.
6. C R Webster, L Woste and R N Zare (1980), Optics Commun. 35, 435.
7. J A R Griffith, G R Isaak, R New, M P Ralls and C P van Zyl (1979), J.Phys.B:Atom.Molec 12, L1.
8. P E G Baird, S A Blundell, G Burrows, C J Foot, G Meisel, D N Stacey and G K Woodgate (1983), J.Phys.B:Atom.Molec 16, 2485.
9. O Laporte and J E Mack (1943), Phys.Rev. 63, 246.
10. P Brix and H Kopfermann (1958), Rev.Mod.Phys. 30, 517.
11. G Breit (1958), Rev.Mod.Phys. 30, 507.
12. D N Stacey (1966), Rep.Prog.Phys. 29, 171.
13. J Bauche and R J Champeau (Academic Press, New York 1976), Advances in Atomic and Molecular Physics 12, 39.
14. I I Sobelman (Springer, 1979), Atomic Spectra and Radiative Transitions, p 170.
15. E E Fradkin (1962), Sov.Phys.JETP 15, 550.
16. W H King (1963), J.Opt.Soc.Am. 53, 822-7.
17. N S Grace and K R More (1934), Phys.Rev. 45, 166.
18. H Kopfermann and D Meyer (1948), Z.Phys. 124, 685.
19. G R Fowles (1950), Phys.Rev. 78, 744.
20. K Murakawa (1953), J.Phys.Soc.Japan 8, 215.
21. K Murakawa (1956), J.Phys.Soc.Japan 11, 778.
22. J A Vreeland and K Murakawa (1958), J.Phys.Soc.Japan 13, 663.

23. J Blaise and G Gluck (1959), Le Journal de Physique et le Radium 20, 466.

24. S George, J E Fredrickson and A W Tucker (1971), Am.J.Phys. 39, 135.

25. N K Odintsova and A R Striganov (1978), Opt.Spectrosc. 43, 356.

26. C Candler (Cambridge University Press, 2nd Ed.1964), Atomic Spectra, pg.311.

27. O Hansen, M C Oleson, O Skilbreid and B Elbek (1961), Nuc.Phys. 25, 634.

28. C H Corliss and W R Bozman (1962), NBS Monograph 53.

29. K Shimoda (ed.) (Springer Verlag, 1976), High Resolution Laser Spectroscopy (Topics in Applied Physics 13).

30. T W Hänsch (North Holland Publishing, 1977), Proc.Int.School Physics, Enrico Fermi Course 64, "Nonlinear Optics" (N Bloembergen, ed.).

31. W Demtroder (Springer Verlag, 1981), Laser Spectroscopy (Chemical Physics 5).

32. M D Levenson (Academic Press, 1982), Introduction to Nonlinear Laser Spectroscopy.

33. M S Sorem and A L Schawlow (1972), Opt.Commun. 5, 148.

34. E V Baklanov and V P Chebotaev (1971), Sov.Phys.JETP 33, 300.

35. P R Berman (1977), Advances in Atom. and Molec.Phys. 13, 57.

36. C E Wieman (1977), Thesis (Stanford).

37. T W Hänsch, I S Shahin and A L Schawlow (1971), Phys.Rev.Lett. 27, 707.

38. K M Baird (Jan, 1983), Physics Today, p52.

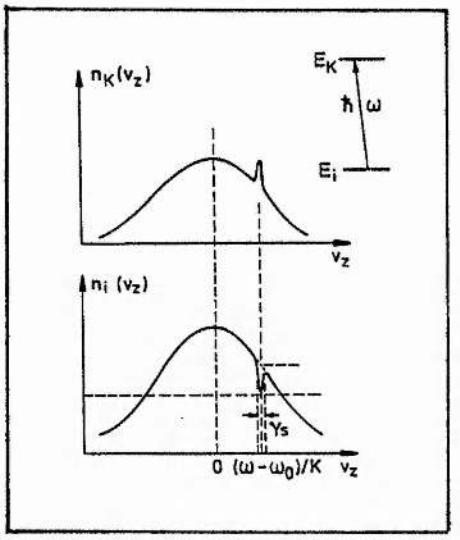

Figure 5.1 Hole burning in the lower level population distribution $n_i(v_z)$ of an inhomogeneously broadened transition due to the absorption of a strong saturating beam. There is a corresponding peak in the population distribution of the upper level (after Demtroder [31]).

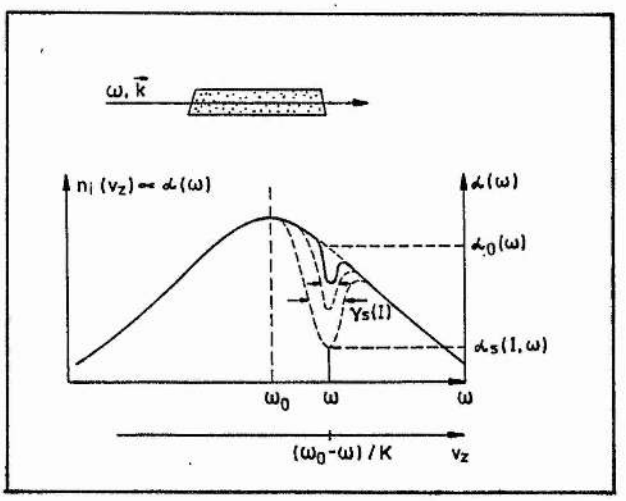

Figure 5.2 Increase of the hole width as the saturating intensity is increased (after Demtroder [31]).

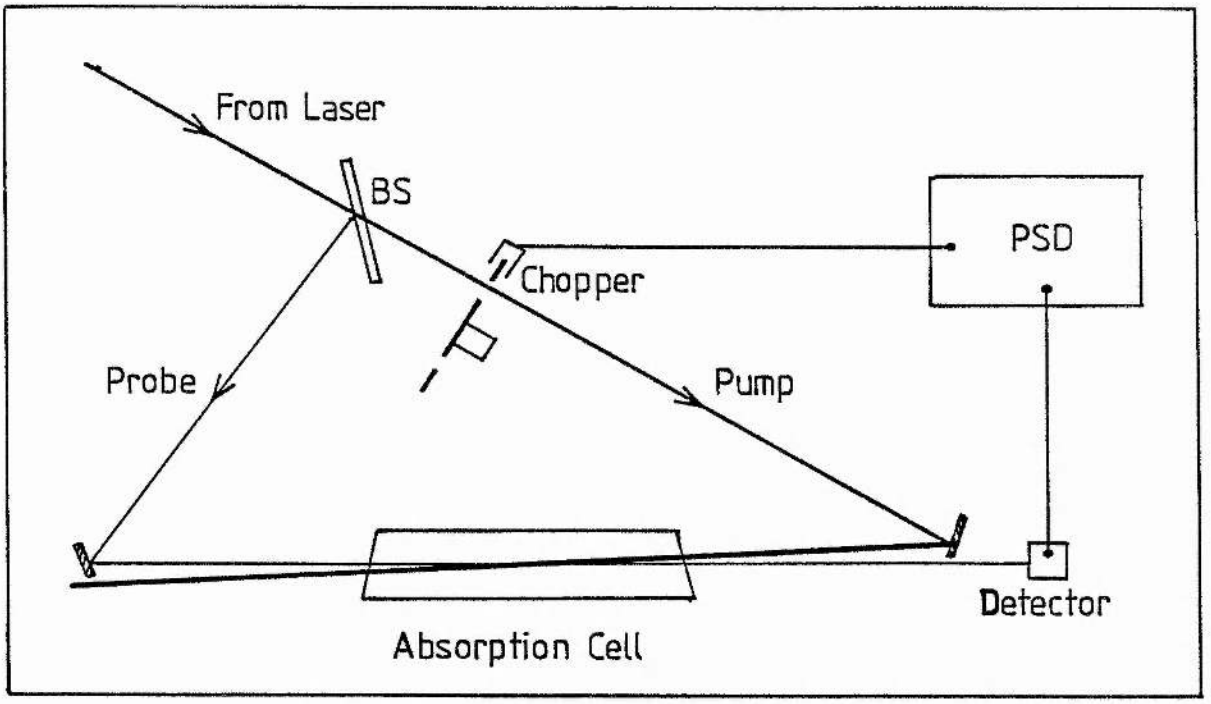

Figure 5.3 Saturated absorption spectrometer. BS-quartz beam splitter (uncoated).

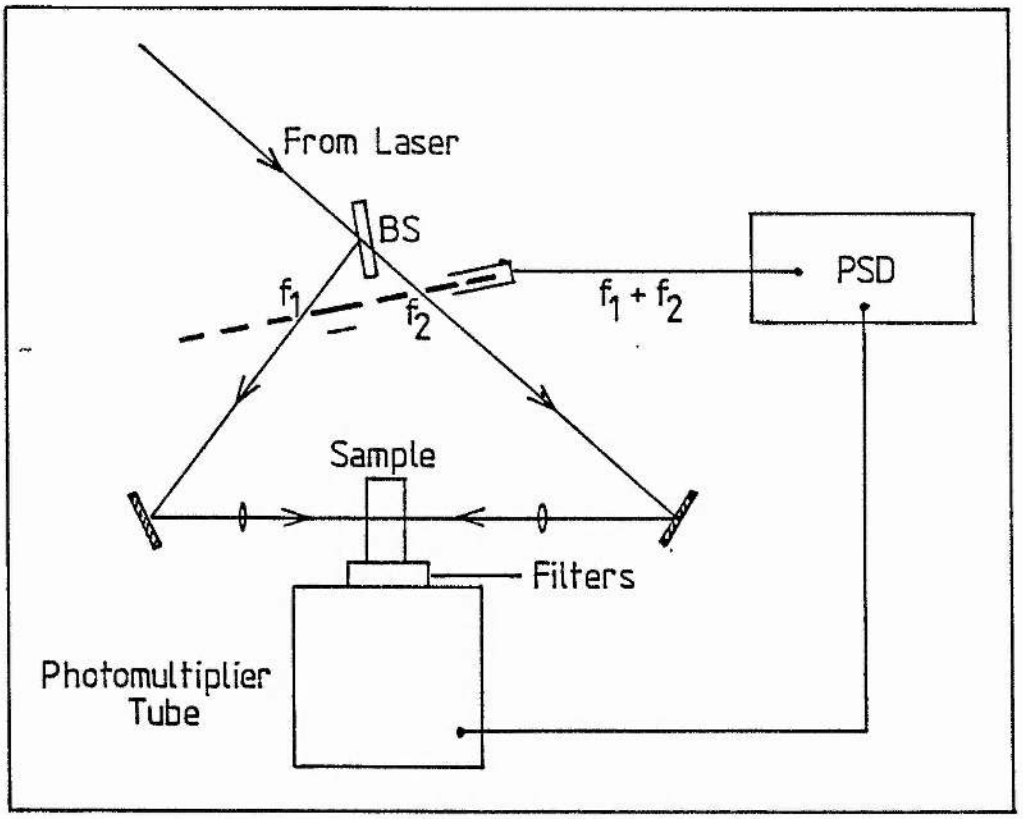

Figure 5.4 Intermodulated fluorescence. BS-50% beam splitter.

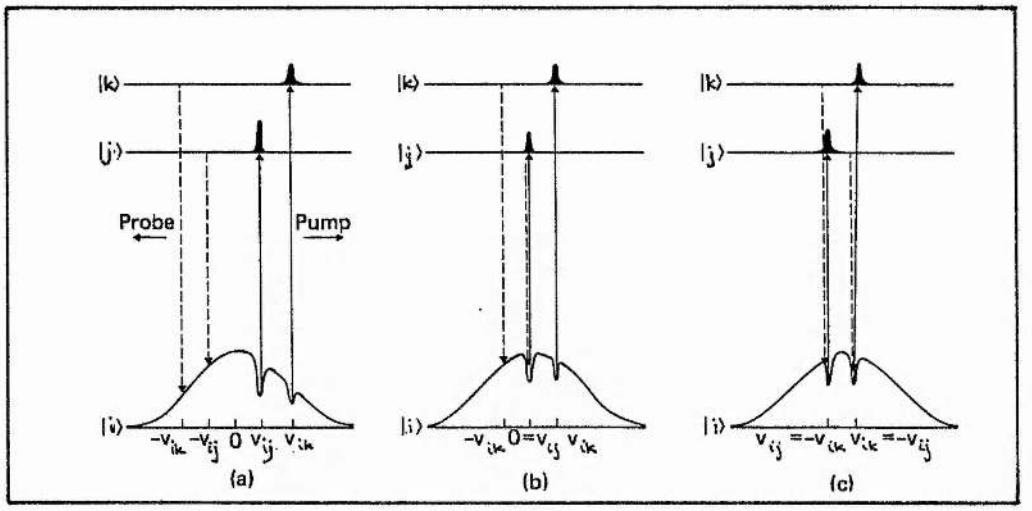

Figure 5.5 Bennet holes, the Lamb dip and crossover resonance for two coupled transitions (a)The waves are off resonance and the probe beam absorption is unperturbed (b)The Lamb dip condition for the $|i\rangle - |j\rangle$ transition. (c)The velocity group pumped on one transition is probed on the other transition resulting in a crossover peak (after Levenson [32]).

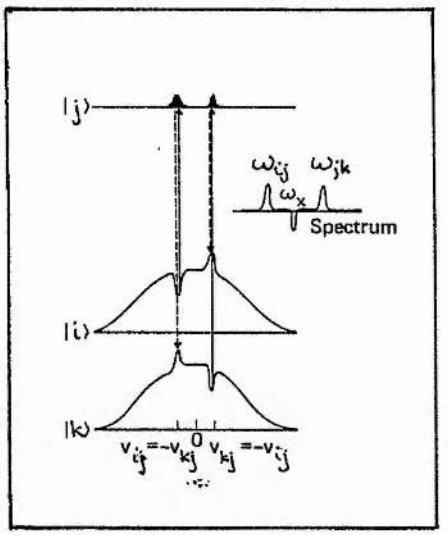

Figure 5.6 Crossover resonance due to optical pumping. The pump wave depopulates one velocity group in each of two low lying states. Atoms decaying from the upper level produce peaks in the velocity distribution at the velocity corresponding to the hole in the other lower state. When the probe wave is resonant with a velocity group with an increased population, the absorption is increased and an inverted cross over peak results.

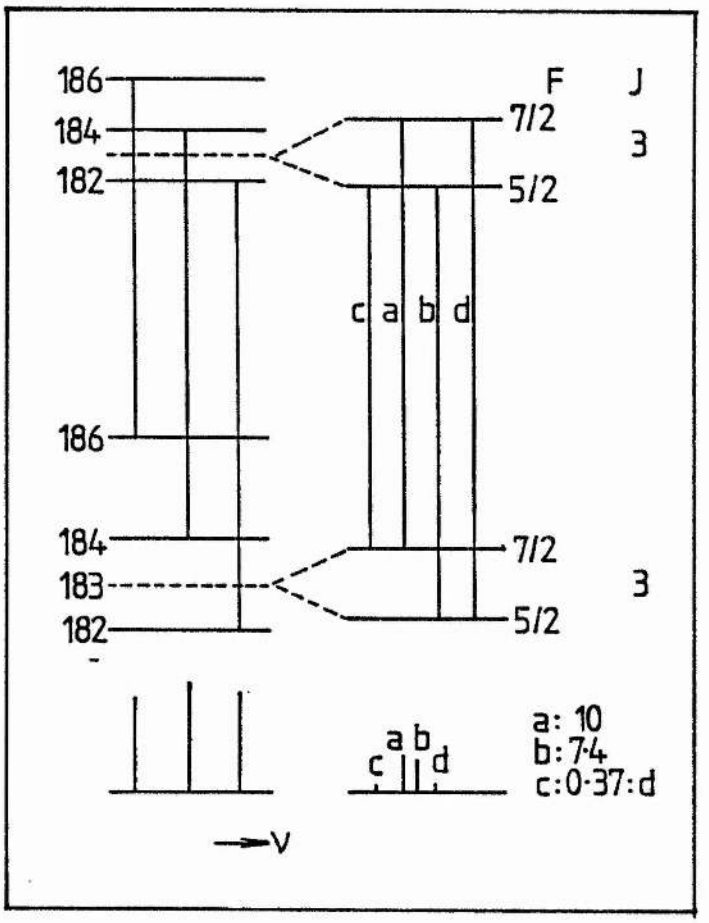

Figure 5.7 Schematic diagram showing the expected spectrum of a tungsten transition due to isotope shift and hyperfine splitting.

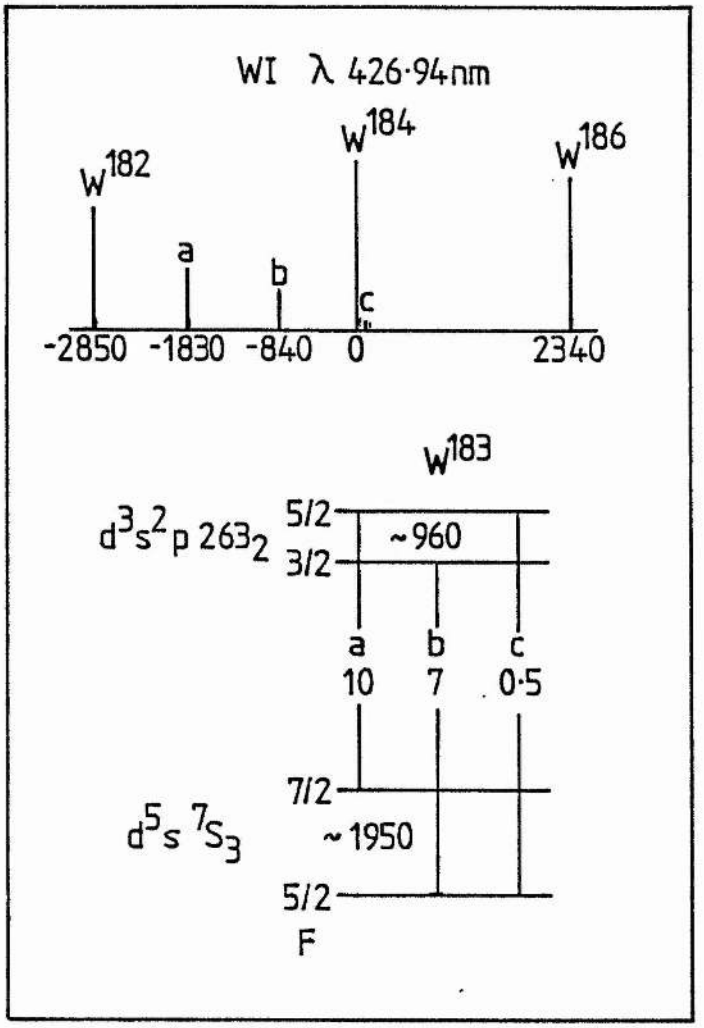

Figure 5.8 The spectrum and level diagram for the 426.94 nm W^{183} I transition (after Vreeland and Murakawa [22]).

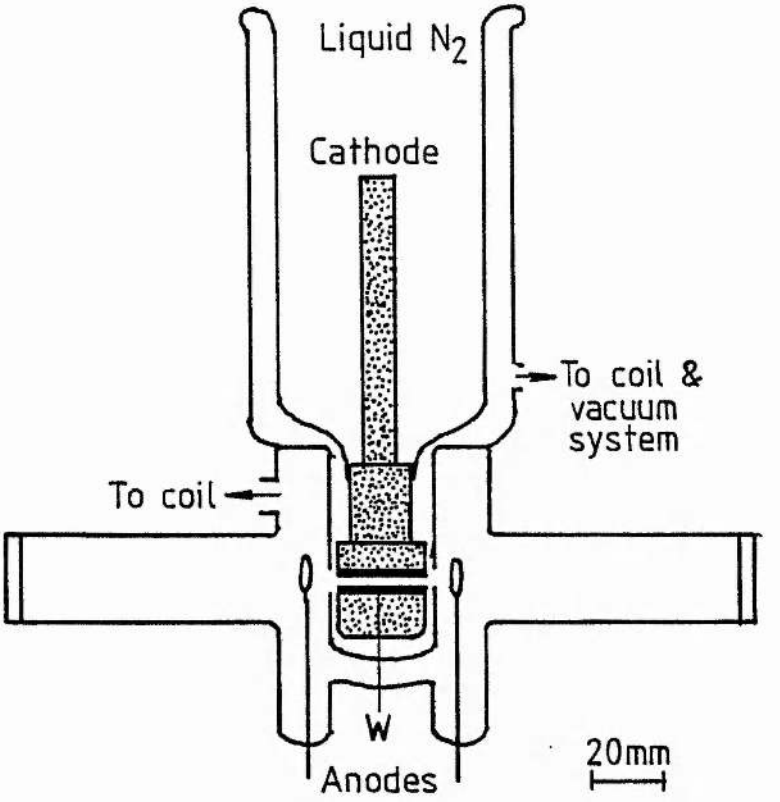

Figure 5.9(a) Liquid nitrogen cooled W hollow cathode discharge as used in the present experimental investigation.

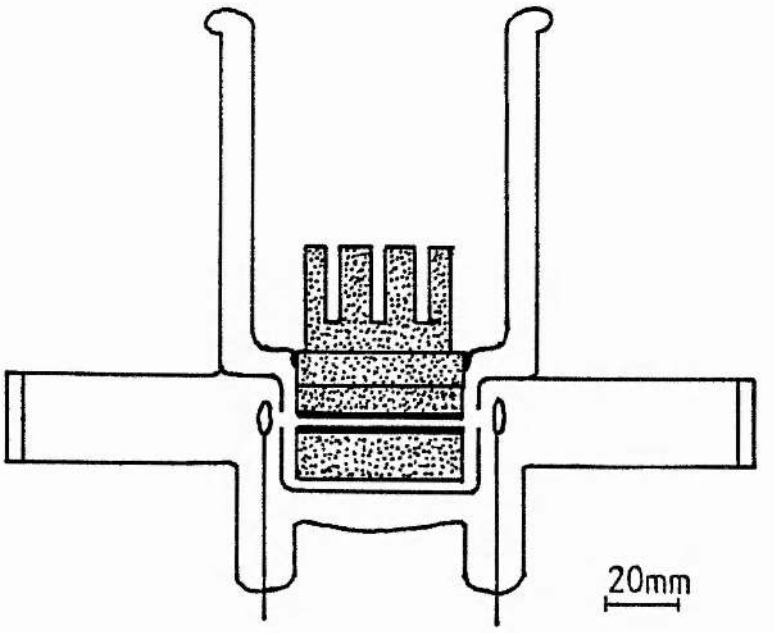

Figure 5.9(b) Proposed liquid nitrogen cooled hollow cathode discharge to give more efficient cooling of the cathode.

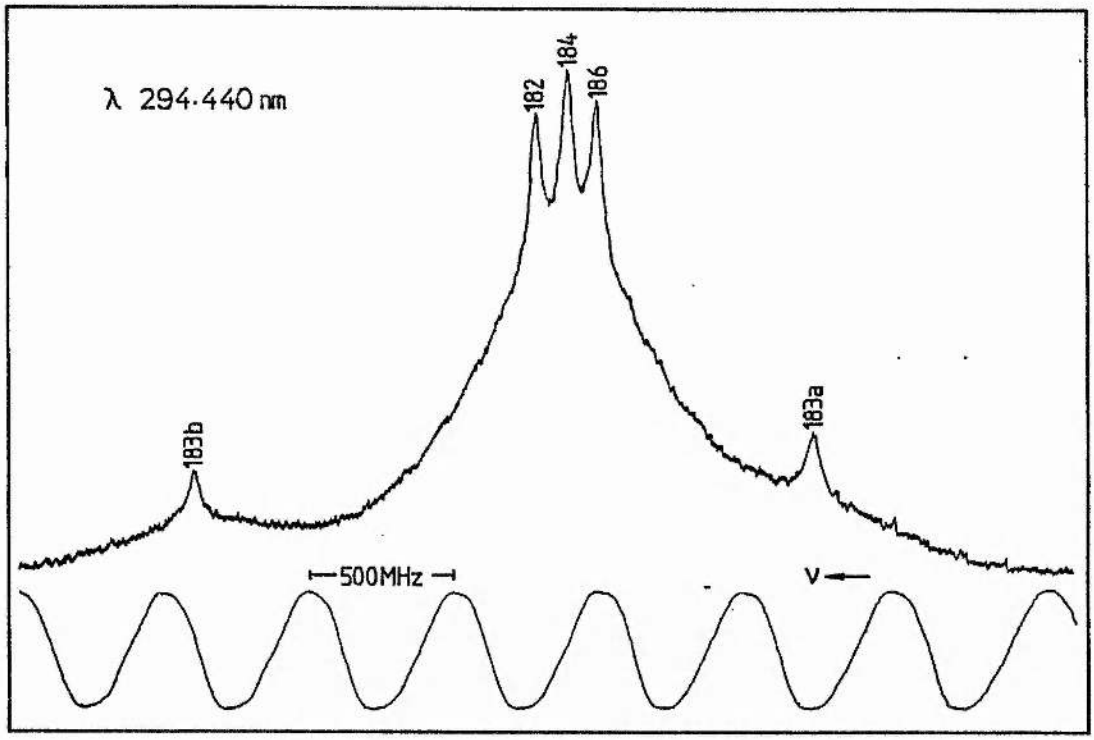

Figure 5.10 Saturated absorption spectrum for the $d^5 s^7 S_3 - d^4 sp^3 6 9_2$ transition at 294.440 nm in WI. Also shown is the trace from a 30 cm confocal interferometer monitoring the fundamental radiation. Distance between the peaks corresponds to a 500 MHz shift in the UV frequency.

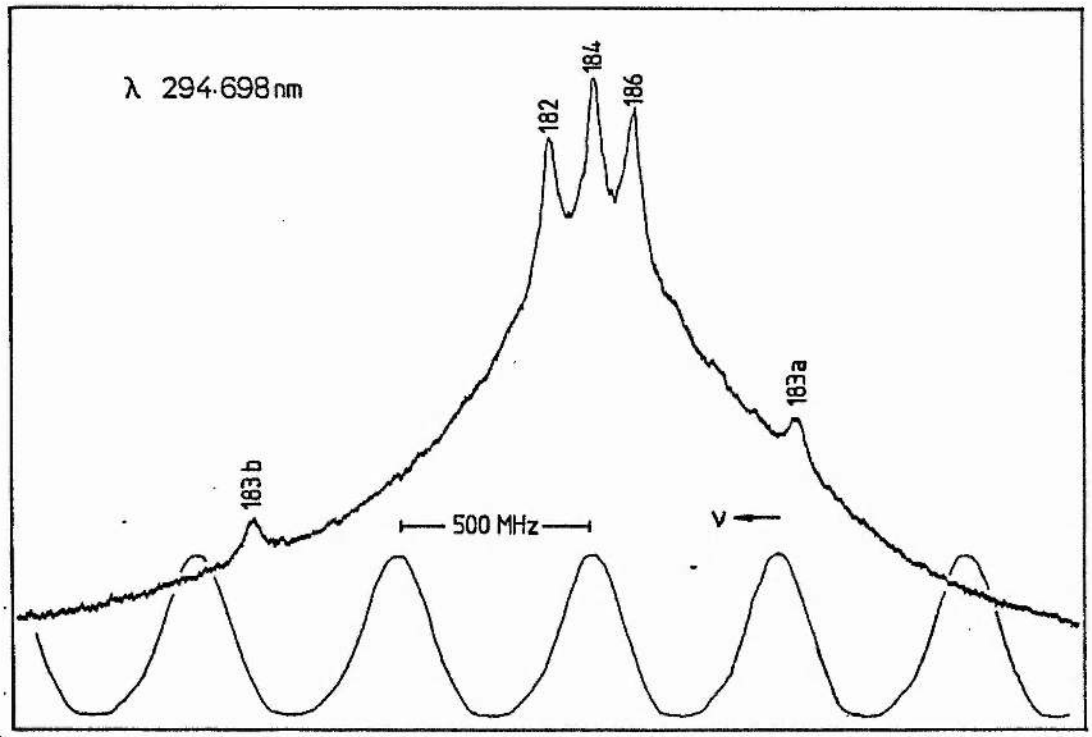

Figure 5.11 Saturated absorption spectrum for the $d^5 s^7 S_3 - d^4 sp^3 6 8_3$ transition at 294.698 nm in WI. Reference interferometer transmission is also shown. Distance between the peaks corresponds to a 500 MHz shift in the UV frequency.

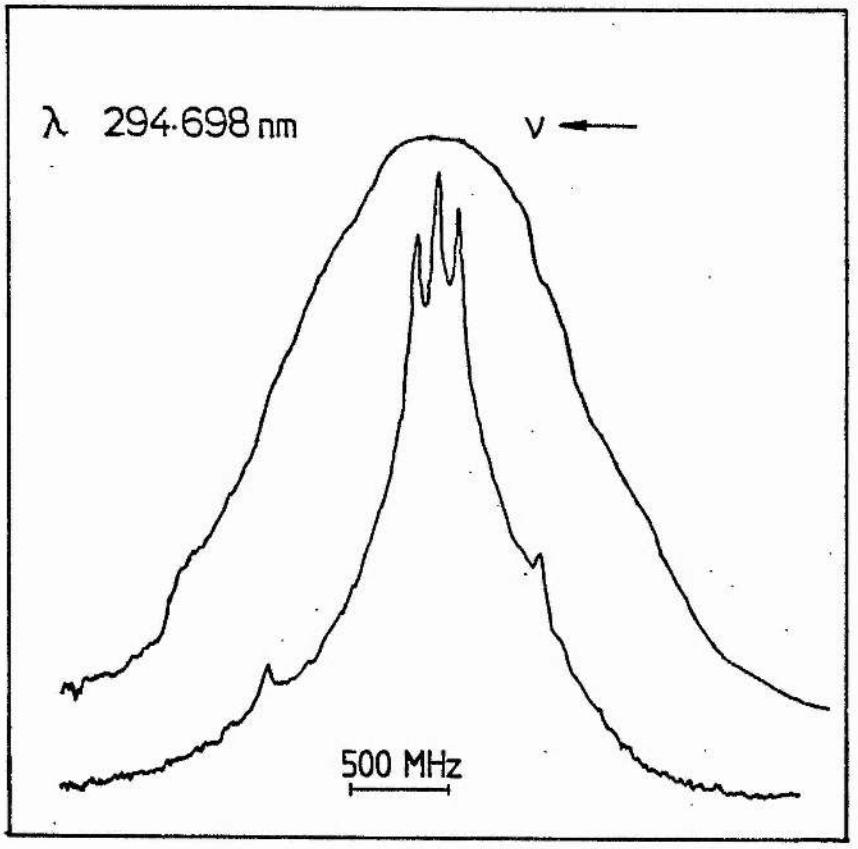

Figure 5.12 The upper trace shows the linear absorption line profile on the 294.698 nm transition. The saturated absorption profile is shown in the lower trace for comparison.

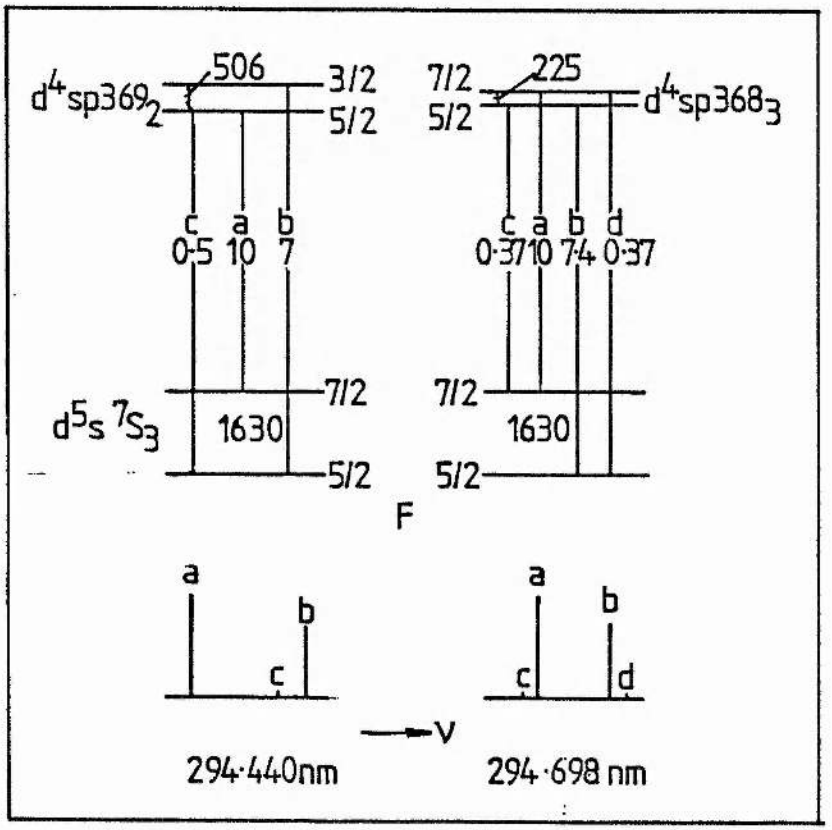

Figure 5.13 Hyperfine splittings, predicted, on the two transitions at 294.44nm and 294.70nm.

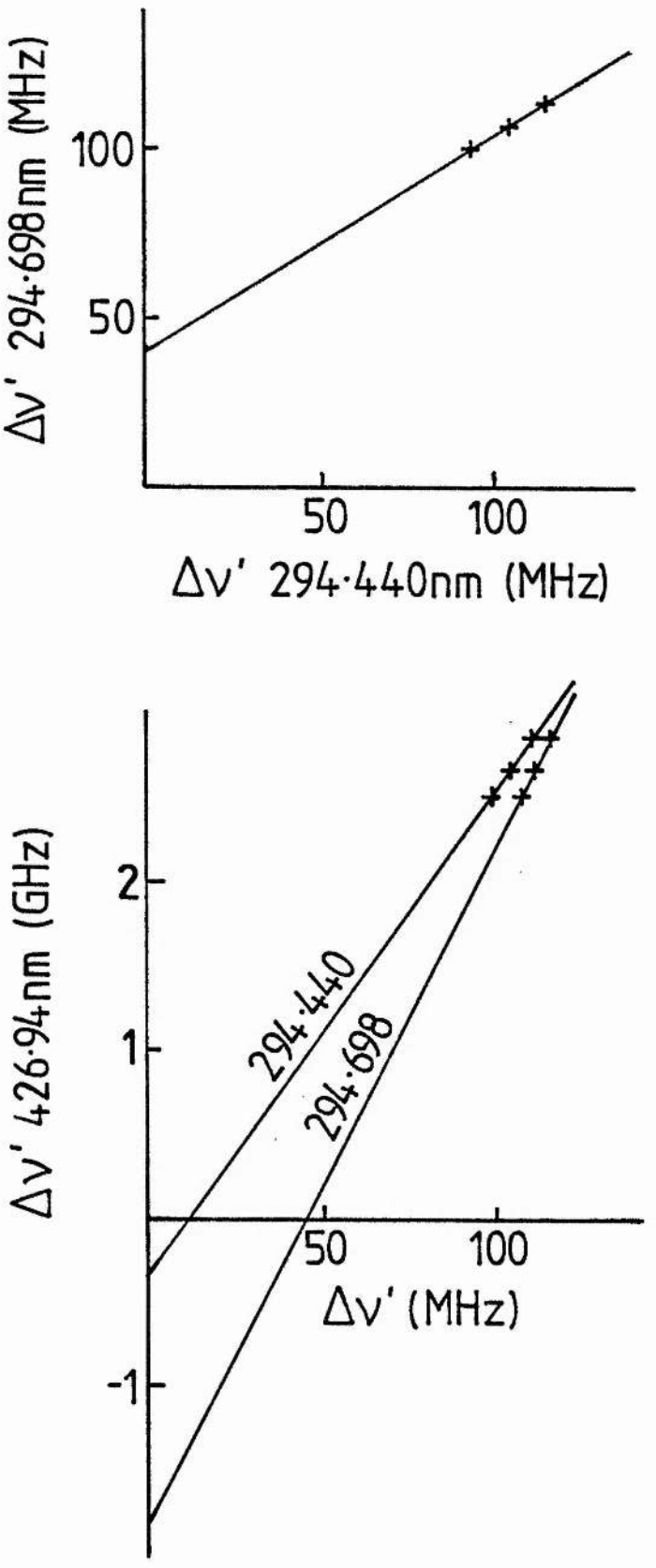

Figure 5.14 King plots.

Appendix A

The Wavemeter

Introduction

High precision measurement of laser wavelengths using corner cube interferometers is now a well established technique [1],[2]. The interferometer is a modified, travelling Michelson interferometer. Two laser beams, one of known wavelength, pass in opposite directions along the same physical path within the interferometer and their intensities, after interference, are monitored separately. As one arm of the interferometer is lengthened at a constant speed a sinusoidal intensity signal of constant frequency is generated, for each beam. The number of fringes for each wavelength can be counted over any path difference

$$d = N_1\lambda_1/2 = N_2\lambda_2/2 \tag{A.1}$$

and the unknown wavelength calculated

$$\lambda_2 = (N_1/N_2)\lambda_1 \tag{A.2}$$

where λ_1 and λ_2 are the reference and unknown air wavelengths, respectively and N_1 and N_2 are the number of fringes for the reference wavelength and unknown wavelength respectively formed in distance, d.

To achieve precisions of 1 part in 10^8 an iodine stabilised He-Ne laser, stable to 1 part in 10^{10}, is usually used as the reference laser and the fringes are multiplied by up to 100 and phase locked. The level of sophistication resulting is only justifiable where accurate measurement of wavelengths is a primary objective of the research. In applications where a dye laser wavelength is to be tuned

onto a Doppler broadened atomic or molecular transition, as here, an accuracy of 1 part in 10^6 is sufficient. A much simpler instrument can meet this requirement. Such a single corner cube interferometer is described here.

By using a preset number of pulses from the unknown wavelength interference fringes, as a gate for the reference pulses, it is possible to obtain electronically a direct readout of the unknown wavelength. A preset count can be calculated, taking account of dispersion in air, to give a direct reading of the fundamental dye laser wavelength or second harmonic generated from it, while using the fundamental laser beam in the wavemeter interferometer to generate the interference fringes. The electronic circuits designed to achieve this are described.

The Interferometer

(Allister I Ferguson and Karl Wickert (Kaiserslautern) are credited with much of the design and construction of the mechanical apparatus.)

The practical wavemeter is shown, approximately to scale, in figures 1 and 2. The optical layout is given schematically in figure 3. The reference laser is a single frequency, thermally stabilised He-Ne laser(LU12, Barr and Stroud Ltd.) [3-6], stable to 1MHz. The wavemeter base is a 150mm wide aluminium girder. Two 20mm diameter steel rods supported above this provide the track on which the corner cube carrier(CCC), mounted on ball races, travels. The wavemeter base is raised and supported at one end so that a linear rather than closed loop connection between the drive wheel and CCC can

be utilised. This connection is made of a length of magnetic recording tape. This minimises the oscillations induced in the velocity of the CCC when the direction of travel along the track changes. A reversible synchronous motor (Rayleigh Instruments MB04 5176) and gearbox (MB02 2073) are used to drive the CCC along the track at 3.7cm s^{-1}. An ac relay (RS 348-762) is used in conjunction with two lever operated, SPDT switches (RS 337-863), one at each end of the track, to change the direction of motion of the CCC when it reaches an end.

The interferometer consists of a corner cube reflector (Edmund scientific, 014161), beamsplitters (Klinger Scientific, number 014161), mirrors (Ealing, number 23-5853) and iris diaphragms (Ealing, number 22-3305). Beamsplitter 2 is mounted on a transverse travel slide (Ealing, 22-7611) mounted at 45° to the axis of the wavemeter. Interference fringes are detected by HP 5082-4220 pin photodiodes.

Method of Alignment

All labels refer to figure 3.

The Reference Beam

Place a screen (a piece of angle iron covered in graph paper is ideal) at point A.

Adjust the position of the laser and the tilts of M1 and M2 so that the beam reflected from the corner cube falls on the same spot on the screen as the corner cube is translated. Fine adjustments of M1 and M2 are achieved systematically in the following way:

a. Vertical adjustment - If the spot falling on the screen drops as the optical path difference increases then with the smallest

path difference lower the spot on the screen with M1 and restore its position with M2. Conversely for the spot rising, raise it a small amount with M1 and restore with M2.

b. Horizontal adjustment - If the spot moves to the right with increasing path difference, with the corner cube close to the mirrors shift the spot a small amount to the right with M1 and correct with M2.

Check that the beams entering and leaving the corner cube are at the same height.

Adjust the tilt of BS1 so that the reflected beam is approximately horizontal and perpendicular to the straight through beam.

Translate BS2 until the beams from BS1 and the corner cube overlap at the coated surface of BS2.

Adjust the tilt of BS2 so that the two beams overlap on both sides of the interferometer for at least 2m. (A mirror at 45° placed behind BS2 facilitates this).

Circular fringes should be observed in the interfering beams.

Check that circular fringes are observed for maximum path difference. If not it is necessary to go through the alignment procedure again.

Note that all the alignment adjustments are made with the optical path difference between the two arms of the interferometer at a minimum.

Put PD1 in place and check that the amplitude of the amplified photodiode signal does not vary more than is consistent with the expansion of the spot size, as the corner cube is translated. Note the reference laser must be stabilised for this.

Adjust the amplification so that the signal amplitude does not

exceed 0.7V. This is necessary because the signal is capacitively coupled to a positive voltage supply, signal conditioning circuit.

The Dye Laser Beam

Adjust the tilt of M3 so that the exiting reference beam is centralised on iris P2.

Place P1 about 2m away with the reference beam falling centrally on it.

Adjust the tilts of BS3 and M4 (following a similar scheme for fine adjustments as that described above) so that the dye laser beam falls centrally on P1 and P2. If this adjustment is carried out carefully enough the dye laser beam should be automatically aligned when it enters the wavemeter and circular fringes should be observed at point B.

The intensity as the corner cube is translated is then detected by PD2. The gain for the signal is adjusted to give a signal with amplitude <0.7V.

The Preset Count

The reference vacuum wavelength is known and the unknown vacuum wavelength is given by [2]

$$\lambda_{vac} = \lambda_{ref,vac} N_{ref}/N \qquad (A.3)$$

This assumes that the path difference for both laser beams is identical. The refractive index of air is different at the two wavelengths and therefore the optical path difference is different even when both beams exactly overlap in space. Correcting for this gives

$$\lambda_{vac} = \lambda_{ref,vac}(N_{ref}/N)(n(\lambda_{vac},T,P,F)/n(\lambda_{ref,vac},T,P,F)) \tag{A.4}$$

$$n(\lambda,T,P,F) = \delta + 1$$

where

$$\delta = \delta_o g - f$$

$$\delta_o = 6432.8\times10^{-8} + (2949810\times10^{-4}\lambda^2/(146\times10^{-6}\lambda^2-1)) + (25540\times10^{-1}4\lambda^2/(41\times10^{-6}\lambda^2-1)) \quad (\lambda \text{ in nm})$$

$$g = (P(1+(1.049-0.015T)P\times10^{-6}))/(720.8826(1+0.003661T))$$

(T in °C, P in Torr) (A.5)

$$f = F(0.0624\times10^{-6}-0.00068/\lambda^2)/(1+0.00366T)$$

$$F = \phi F_{max}/100$$

where ϕ is the % humidity and F_{max} is the saturated water vapour pressure at temperature T, in Torr.

$$\lambda_{air}(15\,°C,760\text{ Torr}) = \lambda_{vac}/(\delta_o+1) \tag{A.6}$$

$$\lambda_{air}(T,P,F) = \lambda_{vac}/n(\lambda_{vac},T,P,F) \tag{A.7}$$

It is desired to obtain a direct reading of the unknown wavelength. If

$$N = \lambda_{ref,vac}n(\lambda_{vac},T,P,F)/n(\lambda_{ref,vac},T,P,f)$$

then a direct reading of the vacuum, unknown wavelength is obtained

$$\lambda_{vac} = N_{ref} \tag{A.8}$$

Most wavelength tables list the wavelength in air at a pressure of 760 Torr and temperature of 15 °C and so to obtain this wavelength as a direct reading

$$N_{air}(760\text{ Torr},15\,°C) = N_{vac}/n(\lambda_{vac},15\,°C,760\text{ Torr}) \tag{A.9}$$

The preset count value for the wavelength in air under these

conditions is

$$N_{air} = {}_{ref,vac}/n(\lambda_{ref,vac},T,P,F) \qquad (A.10)$$

The program written to evaluate these preset count values is listed below. Calculations of the preset count to obtain the standard wavelength in air (Table I) are the same for wavelengths around 300nm and 600nm and hence the second harmonic wavelength can be obtained using the fundamental laser beam in the wavemeter by halving the preset count for the fundamental wavelength.

The Electronics

The preamplifier circuit for the photodiode signal is shown in figure 4. The output from this circuit is input to the decoupling circuit in figure 5 [7]. The use of this buffer overcomes problems of preamplifier instability caused by the input capacitance of the triggering electronics etc. The output from the MC10116 is a square wave of amplitude 1.0V set on a dc level of 4.0V. This is input to the circuit shown in figure 6 the output of which is a train of TTL pulses suitable for counting.

The circuit for controlling the two counters is shown in figure 7. This allows both the counters to be gated for a period of time determined by the operator or for a count to be started by the operator and stopped when the number of unknown wavelength pulses reaches the preset value. Figure 8 shows the preset counter circuit. The enabled reference wavelength pulses are input at pin 15 of the LSD 4029B. The current count is constantly compared with the preset count and when they coincide a pulse is output from pin 3 of the

MSD 40085B. This pulse stops the count. The time delay between preset being reached and the count being stopped leads to one extra pulse being counted and this is taken into account in setting the preset count. The reference counter is a simple decade counter circuit shown in figure 9.

The counter circuits were produced photographically, the preset counter being a double sided PCB and the reference counter single sided. Copies of the graphics layouts for the boards are shown in figures 10 & 11.

References

1. F V Kowalski, R T Hawkins and A L Schawlow (1976), J.Opt.Soc.Am. 66, 965.

   F V Kowalski, R E Teets, W Demtroder and A L Schawlow (1978), J.Opt.Soc.Am. 68, 1611.

   F V Kowalski (1978), Thesis (Stanford).

2. K Wickert (1979), Diplomb Thesis (Kaiserslautern).

3. R Balhorn, H Kunzmann and F Lebowsky (1972), Appl.Opt. 11, 742.

4. S J Bennet, R E Ward and D C Wilson (1973), Appl.Opt. 12, 1406.

5. S K Gordon and S F Jacobs (1974), Appl.Opt. 13, 231.

6. N A Clark (1976), Appl.Opt. 15, 1375.

7. M Tooley and D Whitfield (1979), Wireless World January, p44.

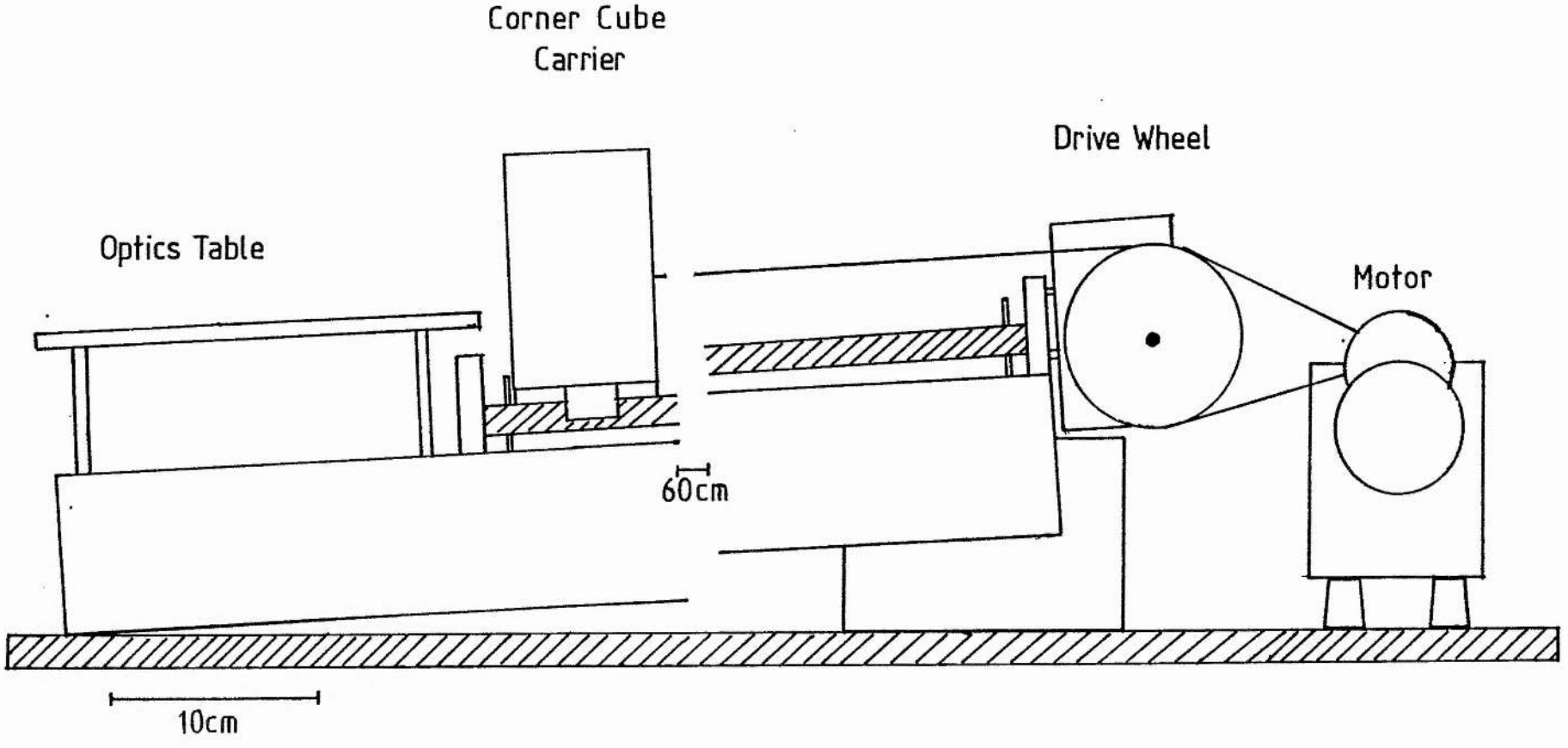

Figure 1 Side view of wavemeter, approximately to scale.

Figure 2 Top view of wavemeter, approximately to scale.

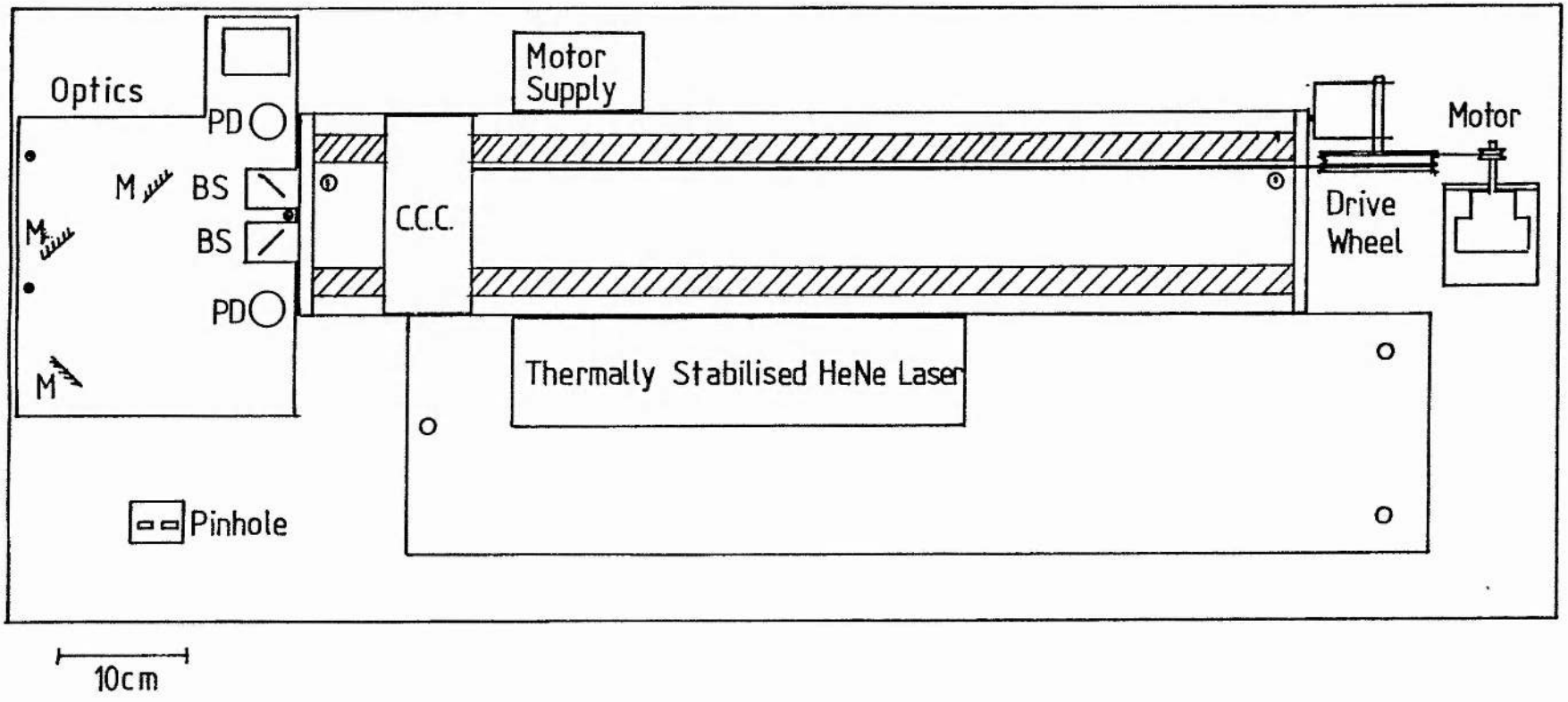

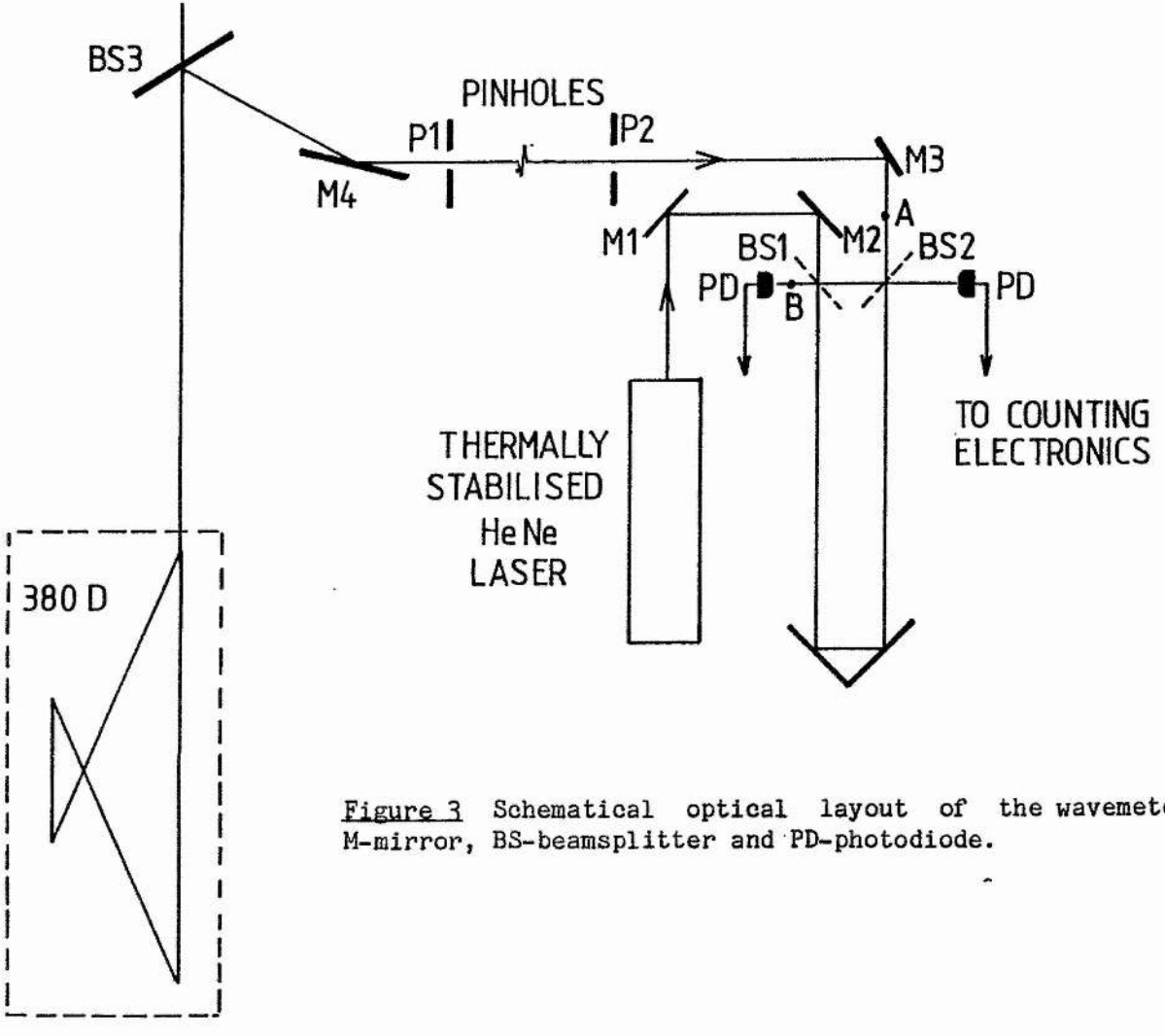

Figure 3 Schematical optical layout of the wavemeter. P-pinhole, M-mirror, BS-beamsplitter and PD-photodiode.

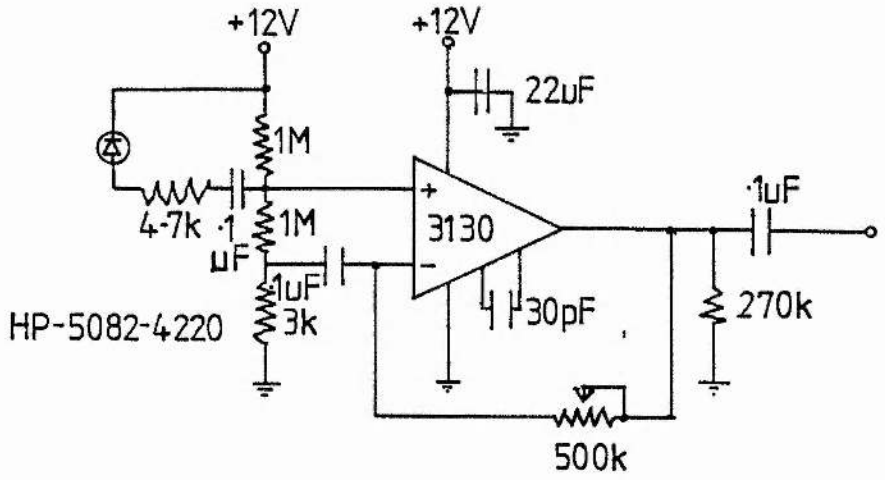

Figure 4 Photodiode signal preamplifier.

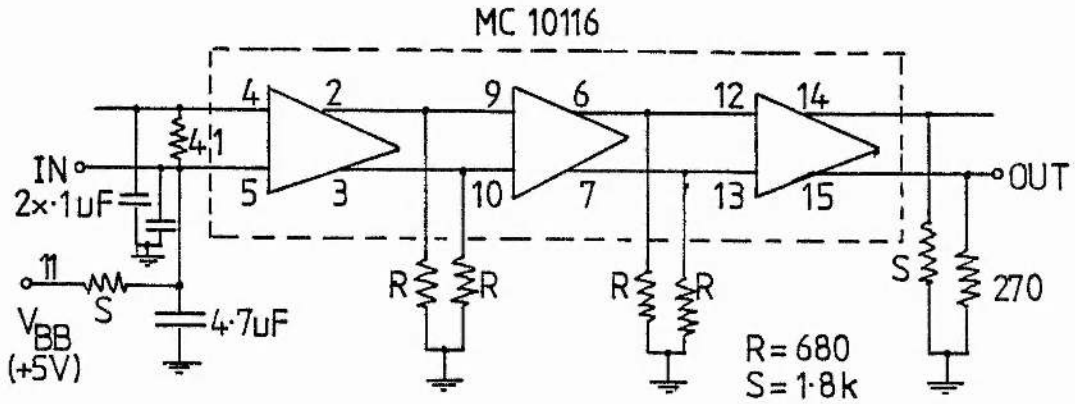

Figure 5 Circuit for decoupling the preamplifier stage from the counting stage.

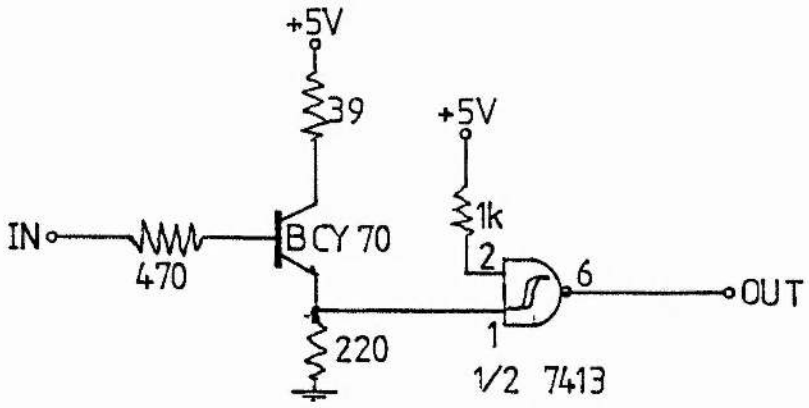

Figure 6 Triggering circuit.

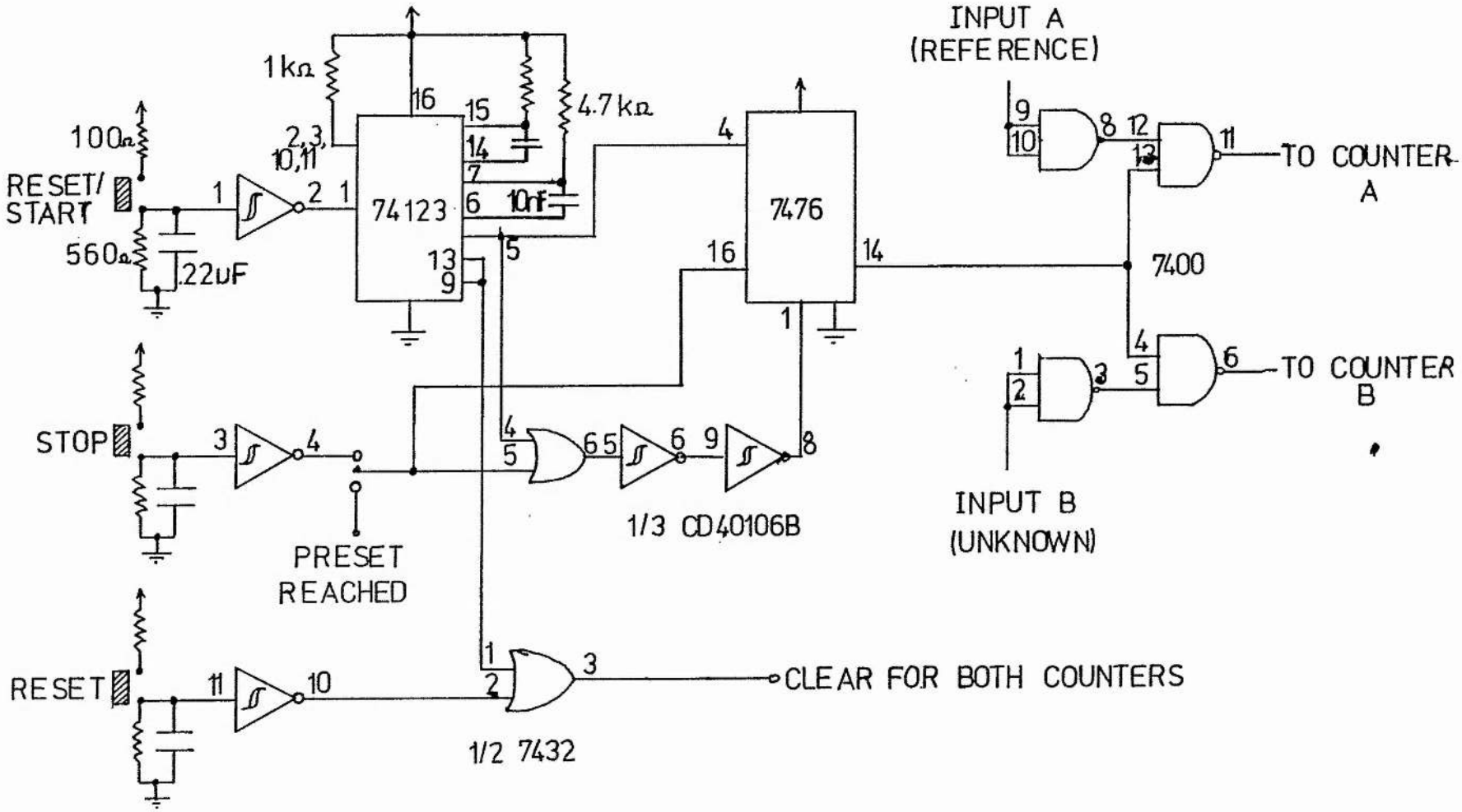

Figure 7 Control circuit.

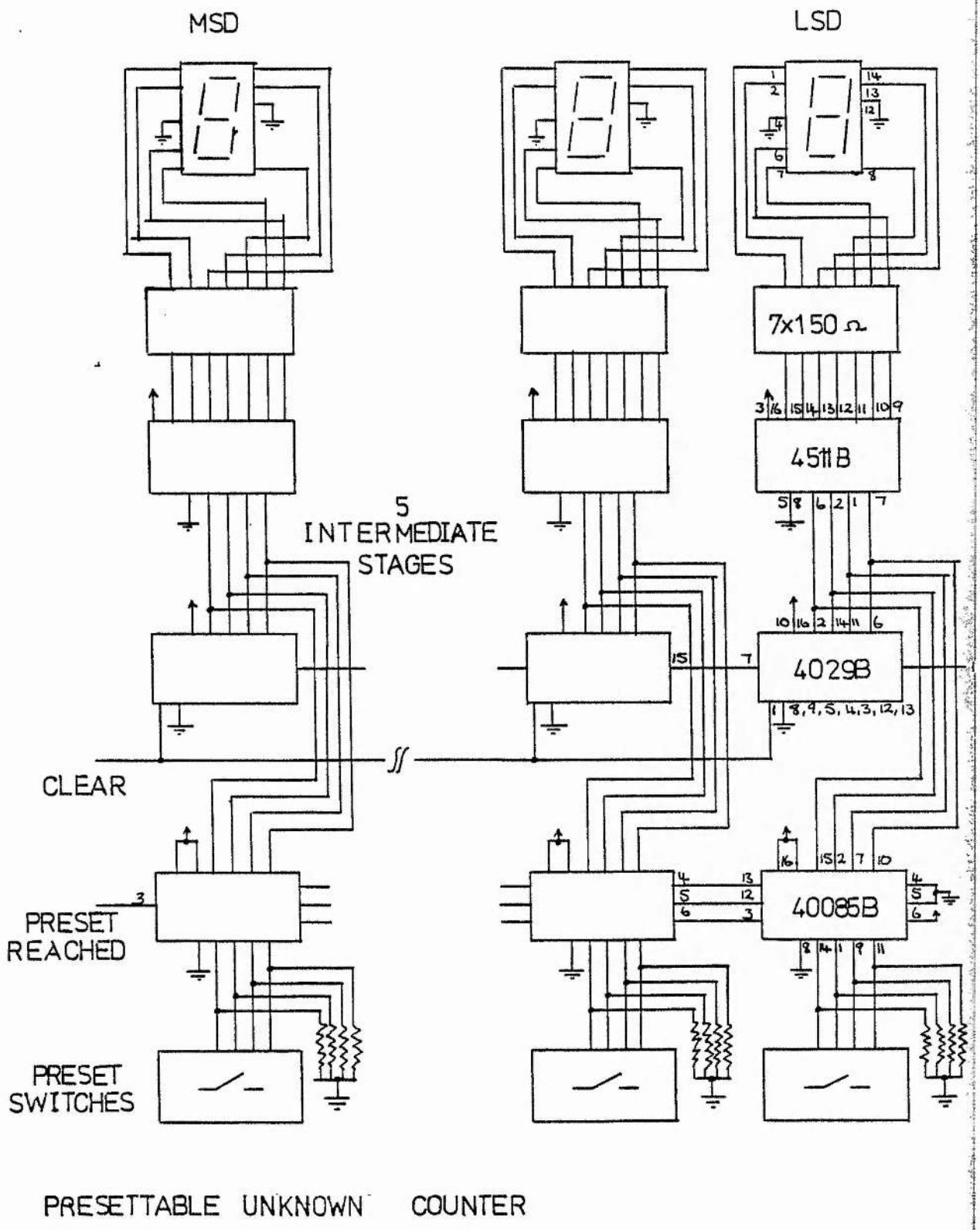

Figure 8 Presettable counter-for counting unknown fringes.

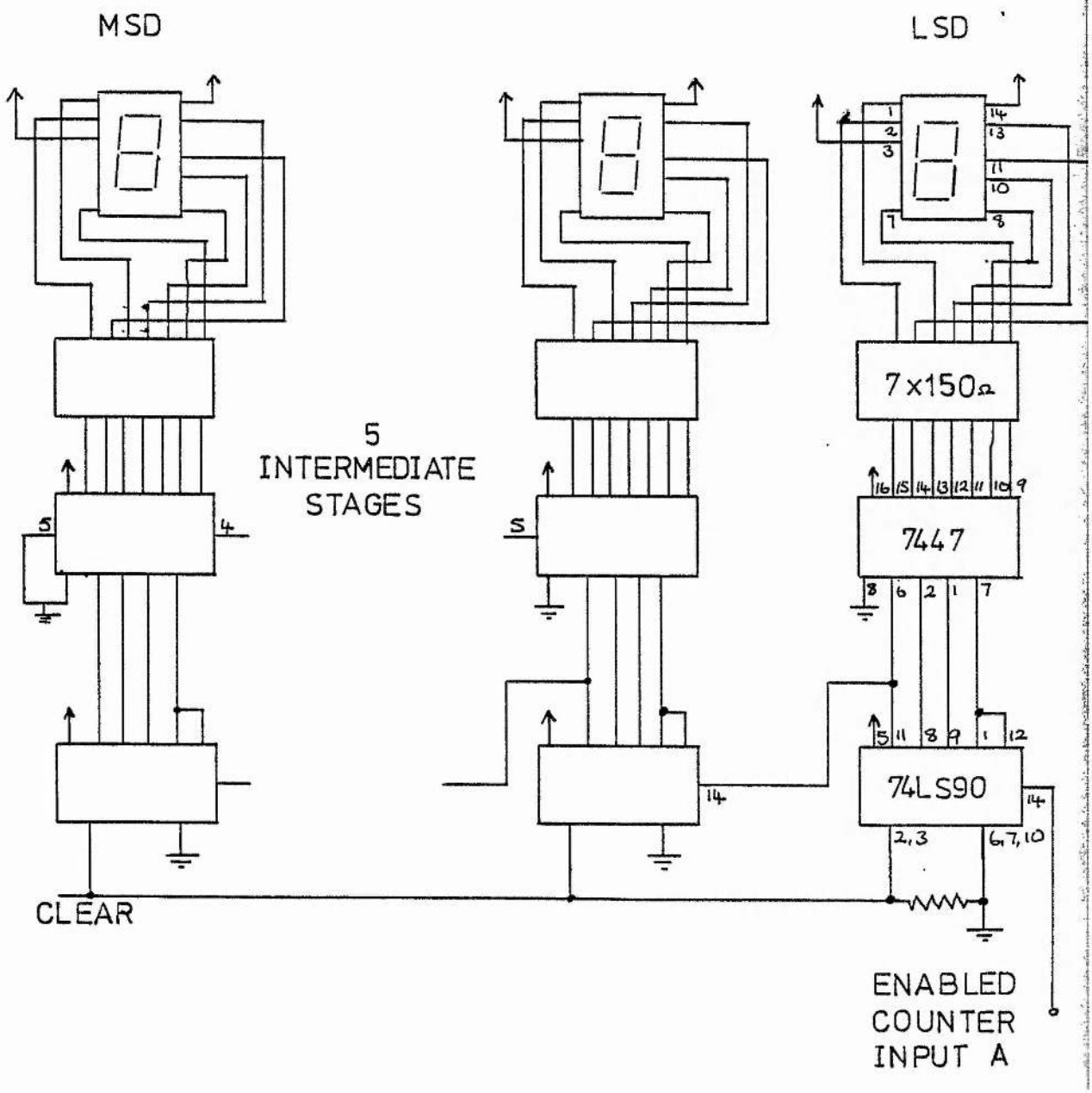

Figure 9 Decade counter-for counting reference fringes.

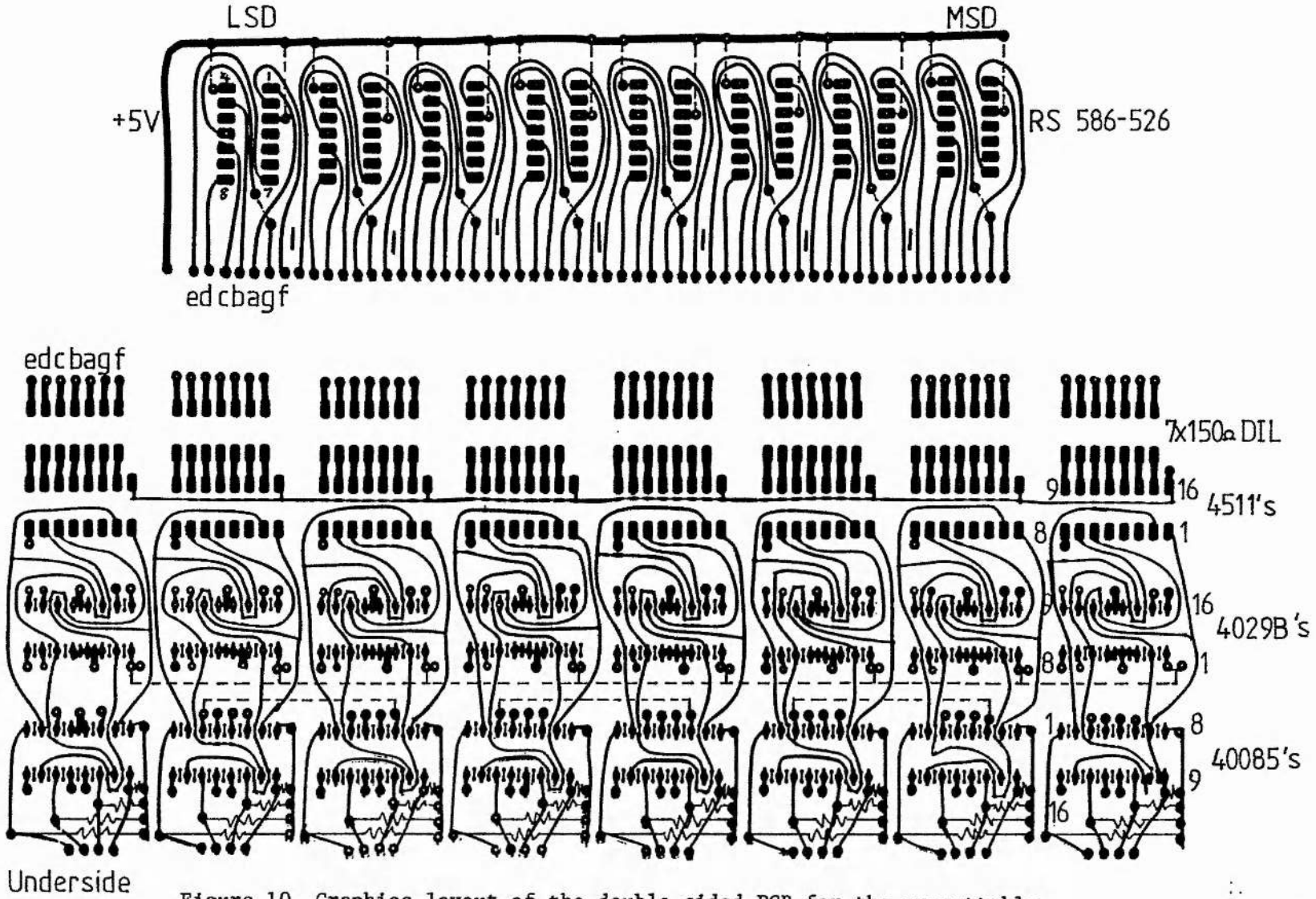

Figure 10 Graphics layout of the double sided PCB for the presettable counter (unknown wavelength). Dashed lines denote wire connections. LSD-least significant digit, MSD-most significant digit, DIL-dual in line package.

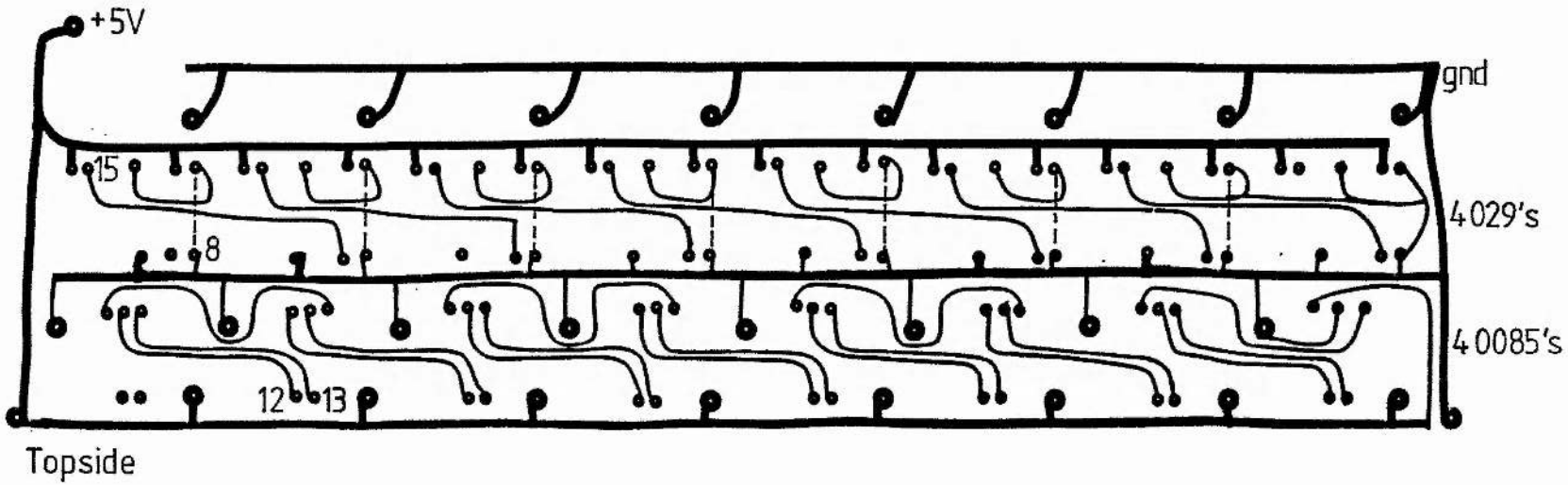
+5V
gnd
15
8
4029's
4 0085's
12
13
Topside

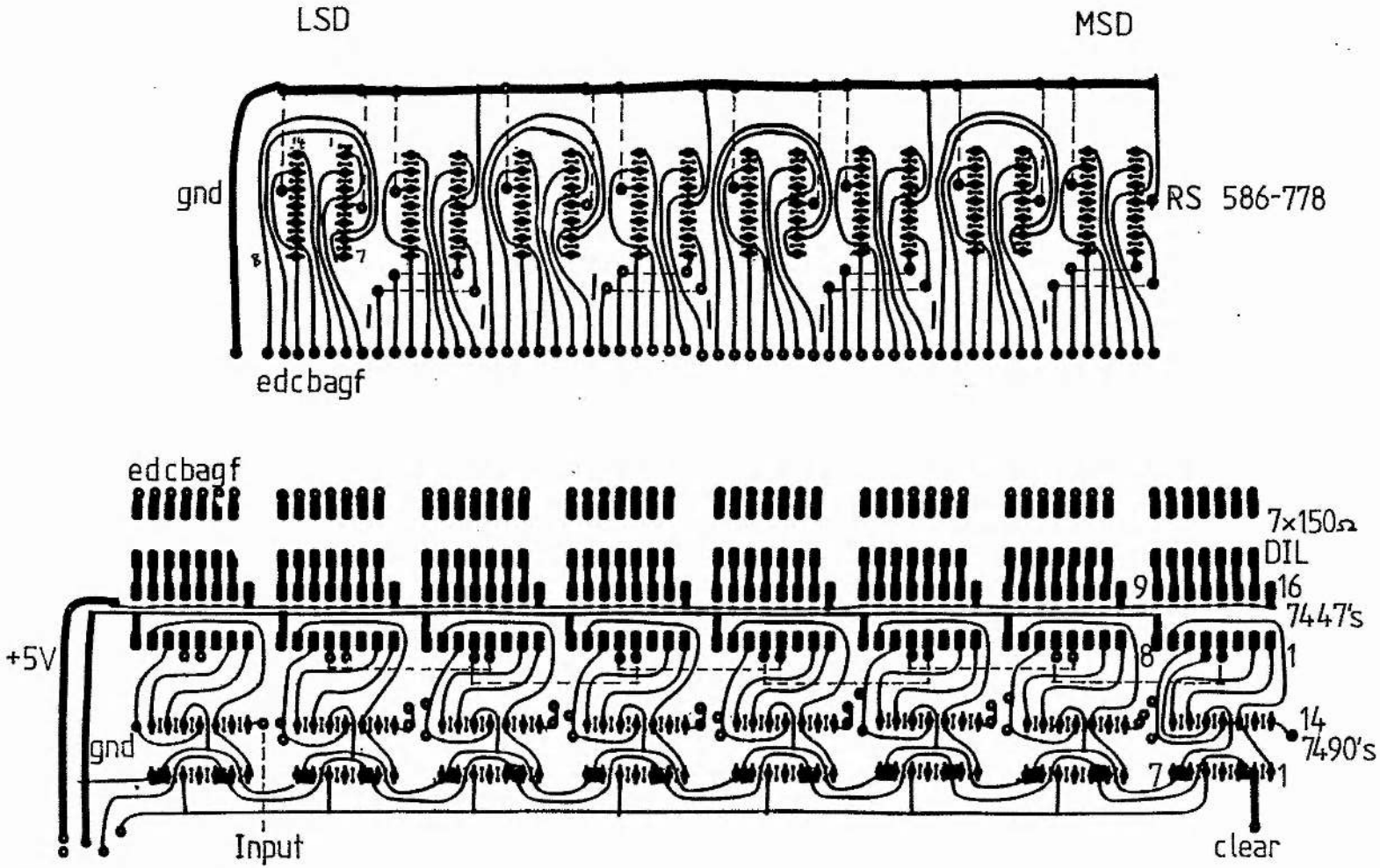

Figure 11 Graphics layout of the single sided PCB for the decade counter (reference wavelength).

Table I

Preset Count

Pressure=760 Torr

Reference Wavelength=632.9916nm

Humidity=100%

T/ °C	Laser /nm	M(vac)	M(air,std.)	M(sh)
15.0	250.0000	633.0073	632.8165	316.4082
15.0	300.0000	633.0011	632.8166	316.4083
15.0	350.0000	632.9976	632.8166	316.4083
15.0	400.0000	632.9955	632.8165	316.4083
15.0	450.0000	632.9941	632.8166	316.4083
15.0	500.0000	632.9931	632.8166	316.4083
15.0	550.0000	632.9924	632.8166	316.4083
15.0	600.0000	632.9918	632.8166	316.4083
20.0	250.0000	633.0070	632.8162	316.4081
20.0	300.0000	633.0009	632.8164	316.4082
20.0	350.0000	632.9976	632.8165	316.4083
20.0	400.0000	632.9954	632.8165	316.4082
20.0	450.0000	632.9941	632.8166	316.4083
20.0	500.0000	632.9931	632.8166	316.4083
20.0	550.0000	632.9924	632.8166	316.4083
20.0	600.0000	632.9919	632.8167	316.4083
25.0	250.0000	633.0067	632.8159	316.4079
25.0	300.0000	633.0006	632.8161	316.4081
25.0	350.0000	632.9973	632.8163	316.4081
25.0	400.0000	632.9954	632.8164	316.4082
25.0	450.0000	632.9940	632.8165	316.4083
25.0	500.0000	632.9930	632.8165	316.4082
25.0	550.0000	632.9923	632.8165	316.4082
25.0	600.0000	632.9918	632.8166	316.4083

```
c*****************************************
      PROGRAM SET
c*****************************************
      dimension fm(3)
      COMMON F,G,A,B,C,D,E,H,H1,G1
      OPEN(UNIT=1,NAME='SETCNT',TYPE='NEW')
  100 FORMAT(20x,f5.1,5x,f8.4,3(5x,f8.4))
      fm(1)=12.788
      fm(2)=17.535
      fm(3)=23.759
      P=760.
      do 3 m=1,3
      t=10.+real(m)*5.
      L=100
      f=real(1)*fm(m)/100
      G1=1.+(.003661*T)
      G3=720.8826*G1
      G2=P*(1.+(1.049-(.015*T))*P*1.E-6)
      G=G2/G3
      A=6432.8E-8
      B=2949810.E-14
      C=146.E-6
      D=25540.E-14
      E=41.E-6
      H=.0624E-6
      H1=6.8E-4
      x=632.9916
      CALL REFRAC(X,RN1,D5)
C X is the vacuum reference wavelength
      DO 1 K=250,600,50
      Y=REAL(K)
      CALL REFRAC(Y,RN4,D4)
c Y is the vacuum measured wavelength
      RM1=X*(RN4/RN1)
      RM2=RM1/(D4)
      rm3=rm2/2
      write(1,100)t,y,rm1,rm2,rm3
    1 CONTINUE
    3 continue
      CLOSE(UNIT=1)
      END
c*****************************************
      SUBROUTINE REFRAC(Q,RN,D1)
c*****************************************
      COMMON F,G,A,B,C,D,E,H,H1,G1
      Z=Q*Q
      D2=A+((B*Z)/(C*Z-1))+((D*Z)/(E*Z-1))
      F1=((H-(H1/Z))/G1)*F
      RN=1.+D2*G+F1
      D1=1.+D2
      RETURN
      END
```

Appendix B

Stability Region Calculations - Computer Programs

See section 2.4 for a detailed discussion of how to calculate the stability regions for the tangential and sagittal planes of the 380D cavity.

PROGRAM STABCONT - This program calculates the spot size for the jet and crystal foci in both the tangential and sagittal planes, for cavity reductions about the jet and crystal respectively.

PROGRAM TANJACR - This program is used to calculate the waist positions relative to M1 and M3, in the cavity. This version calculates the waist positions for the tangential plane using cavity reductions about the jet and crystal. Other versions do the same for the sagittal plane or for reductions of the cavity about other regions in the cavity.

The two-dimensional contour plots featured in section 2.4 were generated from the data files produced by the above programs using the SURFACE graphics package.

```
c*************************************************************
      Program STABCONT
c*************************************************************
      common d12,d13,d23,wjet2,wcrys2
      common/one/f10,f20,f30
      common/two/rnj,rna,rnc,rnr,rlj,rla,rlc,rlr,rj,ra,rc,rr,d2,d5
      common/three/f1,f2,f3,fo1,fo2,fo3
c Input all quantities in centimetres
      rnj=1.43
      rna=1.5
      rnc=1.52
      rnr=1.5
      type 320
  320 format(' Input the lengths of the jet,ast.comp.,xtal &rhomb'$)
      accept *,rlj,rla,rlc,rlr
      type *,rlj,rla,rlc,rlr
      type 330
  330 format(' Input the separation between the jet & ast.comp.'$)
      accept *,d2
      type 340
  340 format(' Input the separation between the xtal & rhomb '$)
      accept *,d5
      ang=.992546
      ang1=.98965274
      rj=rlj/rnj
      ra=rla/rna
      rc=rlc/rnc
      rr=rlr/rnr
c f1,f2,f3 are the focal lengths of equivalent lenses for
c the curved mirrors in the Spectraphysics 380D ring cavity.
      f10=1.75
      f20=5.0
      f30=11.4
c The tangential focal lengths:
      f1=f10*ang1
      f2=f20*ang
      f3=f30*ang
c The sagittal focal lengths:
      fo1=f10/ang1
      fo2=f20/ang
      fo3=f30/ang
c d12,d13,d23 are the separations of the mirror pairs.
c
      open(unit=3,name='focdat',type='new')
cTranslating M1 in .25mm steps
C And translating M3 in 2.mm steps
      do 1 I=0,40
      d23=30.5+real(i)/5.
      do 2 J=0,40
      d12=7.9+real(j)/40.
      d13=77.6+real(i)/5.+real(j)/40.
      call calcspot
      call spot
    2 continue
    1 continue
      end
c
c*********************************************************
      subroutine calcspot
c*********************************************************
      common d12,d13,d23,wjet2,wcrys2
      common/one/f10,f20,f30
c First calculate the ABCD matrix for evaluating the jet focus
      a11=1.
      a12=-1/f10
      a21=d13
      a22=1-d13/f10
      b11=a11-(1/f30)*a21
      b12=a12-(1/f30)*a22
      c21=d23*b11+a21
      c22=d23*b12+a22
      e11=b11-(1/f20)*c21
      e12=b12-(1/f20)*c22
      fjet=-1/e12
      pjet1=(1-e11)/e12
      pjet2=(1-c22)/e12
      djet=d12-pjet1-pjet2
      sjet=djet*(4*fjet-djet)/4
      wjet1=djet/2+pjet2
      wjet2=djet/2+pjet1
c
```

```
c Evaluating the focus at the auxillary waist
        g11=1.
        g12=-1/f20
        g21=d12
        g22=1-d12/f20
        h11=g11-g21/f10
        h12=g12-g22/f10
        p21=d13*h11+g21
        p22=d13*h12+g22
        q11=h11-p21/f30
        q12=h12-p22/f30
        fcrys=-1/q12
        pcrys1=(1-q11)/q12
        pcrys2=(1-p22)/q12
        dcrys=d23-pcrys1-pcrys2
        scrys=dcrys*(4*fcrys-dcrys)/4
        wcrys2=dcrys/2+pcrys2
        wcrys3=dcrys/2+pcrys1
        end
c*****************************************************************
        subroutine spot
c*****************************************************************
        common d12,d13,d23,wjet2,wcrys2
        common/two/rnj,rna,rnc,rnr,rlj,rla,rlc,rlr,rj,ra,rc,rr,d2,d5
        common/three/f1,f2,f3,fo1,fo2,fo3
        d7=d13
        d1=wjet2-(rlj/2)
        d6=wcrys2-(rlc/2)
        d4=d23-(d6+d5+rlc+rlr)
        d3=d12-(d2+d1+rlj+rla)
c
c The calculations for the jet in the tangential plane
        a33=1/rnj
        a34=d1*rnj
        a43=-1/(f1*rnj)
        a44=rnj-d1*rnj/f1
        b33=a33+(d7*a43)
        b34=a34+d7*a44
        b43=a43-b33/f3
        b44=a44-b34/f3
        c33=b33+d6*b43
        c34=b34+d6*b44
        c43=b43/rnc
        c44=b44/rnc
        c33=c33*rnc
        c34=c34*rnc
        e33=c33+rc*c43
        e34=c34+rc*c44
        e33=e33/rnc
        e34=e34/rnc
        e43=c43*rnc
        e44=c44*rnc
        f33=e33+d5*c43
        f34=e34+d5*c44
        f33=f33*rnr
        f34=f34*rnr
        f43=e43/rnr
        f44=e44/rnr
        g33=f33+rr*f43
        g34=f34+rr*f44
        g33=g33/rnr
        g34=g34/rnr
        g43=f43*rnr
        g44=f44*rnr
        h33=g33+d4*g43
        h34=g34+d4*g44
        h43=g43-h33/f2
        h44=g44-h34/f2
        p33=h33+d3*h43
        p34=h34+d3*h44
        p33=p33*rna
        p34=p34*rna
        p43=h43/rna
        p44=h44/rna
        q33=p33+ra*p43
        q34=p34+ra*p44
        q33=q33/rna
        q34=q34/rna
        q43=p43*rna
        q44=p44*rna
        r33=q33+d2*q43
        r34=q34+d2*q44
        r43=q43/rnj
        r44=q44/rnj
        r33=r33*rnj
        r34=r34*rnj
        fjet=-1/r43
        pjet1=rnj*(1-r44)/r43
        pjet2=rnj*(1-r33)/r43
        djet=(rlj-pjet1-pjet2)/rnj
        sjet1=djet*(4*fjet-djet)/4
        wjet3=(rlj+pjet2-pjet1)/2
        wjet4=(rlj-pjet2+pjet1)/2
c
```

```
c Calculations for the crystal in the tangential plane
      a55=1/rnc
      a56=d5*rnc
      a66=rnc
      a65=0.
      a55=a55*rnr
      a56=a56*rnr
      a65=a65/rnr
      a66=a66/rnr
      b55=a55+rr*a65
      b56=a56+rr*a66
      b55=b55/rnr
      b56=b56/rnr
      b65=a65*rnr
      b66=a66*rnr
      c55=b55+d4*b65
      c56=b56+d4*b66
      c65=b65-c55/f2
      c66=b66-c56/f2
      e55=c55+d3*c65
      e56=c56+d3*c66
      e55=e55*rna
      e56=e56*rna
      e65=c65/rna
      e66=c66/rna
      f55=e55+ra*e65
      f56=e56+ra*e66
      f55=f55/rna
      f56=f56/rna
      f65=e65*rna
      f66=e66*rna
      g55=f55+f65*d2
      g56=f56+f66*d2
      g55=g55*rnj
      g56=g56*rnj
      g65=f65/rnj
      g66=f66/rnj
      h55=g55+rj*g65
      h56=g56+rj*g66
      h55=h55/rnj
      h56=h56/rnj
      h65=g65*rnj
      h66=g66*rnj
      p55=h55+d1*h65
      p56=h56+d1*h66
      p65=h65-p55/f1
      p66=h66-p56/f1
      q55=p55+p65*d7
      q56=p56+p66*d7
      q65=p65-q55/f3
      q66=p66-q56/f3
      r55=q55+d6*q65
      r56=q56+d6*q66
      r55=r55*rnc
      r56=r56*rnc
      r65=q65/rnc
      r66=q66/rnc
      if(rlc.le.0.)then rnc=1.
      fcrys=-1/r65
      pcrys1=rnc*(1-r66)/r65
      pcrys2=rnc*(1-r55)/r65
      dcrys=(rlc-pcrys1-pcrys2)/rnc
      scrys1=dcrys*(4*fcrys-dcrys)/4
      wcrys3=(rlc-pcrys1+pcrys2)/2
      wcrys4=(rlc+pcrys1-pcrys2)/2
      rnc=1.52
      type*,sjet1,r33,r44,scrys1,r55,r66

c The calculations for the jet in the sagittal plane
      a33=1.
      a34=d1
      a43=-1/fo1
      a44=1-d1/fo1
      b33=a33+(d7*a43)
      b34=a34+d7*a44
      b43=a43-b33/fo3
      b44=a44-b34/fo3
      c33=b33+d6*b43
      c34=b34+d6*b44
      c43=b43
      c44=b44
      e33=c33+rc*c43
      e34=c34+rc*c44
      e43=c43
      e44=c44
      f33=e33+d5*e43
      f34=e34+d5*e44
      f43=e43
      f44=e44
      g33=f33+rr*f43
      g34=f34+rr*f44
      g43=f43
      g44=f44
      h33=g33+d4*g43
      h34=g34+d4*g44
      h43=g43-h33/fo2
      h44=g44-h34/fo2
      p33=h33+d3*h43
      p34=h34+d3*h44
      p43=h43
      p44=h44
      q33=p33+ra*p43
      q34=p34+ra*p44
      q43=p43
      q44=p44
      r33=q33+d2*q43
      r34=q34+d2*q44
      r44=q44
      r43=q43
      fjet=-1/r43
      pjet1=rnj*(1-r44)/r43
      pjet2=rnj*(1-r33)/r43
      djet=(rlj-pjet1-pjet2)/rnj
      sjet2=djet*(4*fjet-djet)/4
      wjet5=(rlj+pjet2-pjet1)/2
      wjet6=(rlj-pjet2+pjet1)/2
  400 format(4 f15.9)
c
c Calculations for the crystal in the sagittal plane
      a55=1.
      a56=d5
      a66=1.
      a65=0.
      b55=a55+rr*a65
      b56=a56+rr*a66
      c55=b55+d4*a65
      c56=b56+d4*a66
      c65=a65-c55/fo2
      c66=a66-c56/fo2
      e55=c55+d3*c65
      e56=c56+d3*c66
      f55=e55+ra*c65
      f56=e56+ra*c66
      g55=f55+c65*d2
      g56=f56+c66*d2
      h55=g55+rj*c65
      h56=g56+rj*c66
      p55=h55+d1*c65
      p56=h56+d1*c66
      p65=c65-p55/fo1
      p66=c66-p56/fo1
      q55=p55+p65*d7
      q56=p56+p66*d7
      q65=p65-q55/fo3
      q66=p66-q56/fo3
      r55=q55+d6*q65
      r56=q56+d6*q66
      r65=q65
      r66=q66
      if(rlc.le.0.0) then rnc=1.
      fcrys=-1/r65
      pcrys1=rnc*(1-r66)/r65
      pcrys2=rnc*(1-r55)/r65
      dcrys=(rlc-pcrys1-pcrys2)/rnc
      scrys2=dcrys*(4*fcrys-dcrys)/4
      wcrys5=(rlc+pcrys2-pcrys1)/2
      wcrys6=(rlc+pcrys1-pcrys2)/2
      rnc=1.52
      write(3,400)sjet1,sjet2,scrys1,scrys2
  500 end
$
```

```
c*************************************************************
      Program TANJACR
c*************************************************************
      common d12,d13,d23,wjet2,wcrys2
      common/one/f10,f20,f30
      common/two/rnj,rna,rnc,rnr,rlj,rla,rlc,rlr,rj,ra,rc,rr,d2,d5
      common/three/f1,f2,f3,fo1,fo2,fo3
c Input all quantities in centimetres
      rnj=1.43
      rna=1.5
      rnc=1.52
      rnr=1.5
      type 320
  320 format(' Input the lengths of the jet,ast.comp.,xtal &rhomb'$)
      accept *,rlj,rla,rlc,rlr
      type *,rlj,rla,rlc,rlr
      type 330
  330 format(' Input the separation between the jet & ast.comp.'$)
      accept *,d2
      type 340
  340 format(' Input the separation between the xtal & rhomb '$)
      accept *,d5
      ang=.992546
      angl=.98965274
      rj=rlj/rnj
      ra=rla/rna
      rc=rlc/rnc
      rr=rlr/rnr
c f1,f2,f3 are the focal lengths of equivalent lenses for
c the curved mirrors in the Spectraphysics 380D ring cavity.
      f10=1.75
      f20=5.00
      f30=11.4
c The tangential focal lengths:
      f1=f10*angl
      f2=f20*ang
      f3=f30*ang
c d12,d13,d23 are the separations of the mirror pairs.
c
      open(unit=1,name='wajacr',type='new')
c Translating M3 in 2 mm steps
cTranslating M1 in .25mm steps
      do 1 I=0,40
      d23=30.5+real(I)/5.
      do 2 J=0,40
      d12=7.9+real(J)/40.
      d13=77.6+real(I)/5.+real(J)/40.
      call calcspot
      call spot
    2 continue
    1 continue
      end
c
c*************************************************************
      subroutine calcspot
c*************************************************************
      common d12,d13,d23,wjet2,wcrys2
      common/one/f10,f20,f30
c First calculate the ABCD matrix for evaluating the jet focus
      a11=1.
      a12=-1/f10
      a21=d13
      a22=1-d13/f10
      b11=a11-(1/f30)*a21
      b12=a12-(1/f30)*a22
      c21=d23*b11+a21
      c22=d23*b12+a22
      e11=b11-(1/f20)*c21
      e12=b12-(1/f20)*c22
      fjet=-1/e12
      pjet1=(1-e11)/e12
      pjet2=(1-c22)/e12
      djet=d12-pjet1-pjet2
      sjet=djet*(4*fjet-djet)/4
      wjet1=djet/2+pjet2
      wjet2=djet/2+pjet1
c
c Evaluating the focus at the auxillary waist
      g11=1.
      g12=-1/f20
      g21=d12
      g22=1-d12/f20
      h11=g11-g21/f10
      h12=g12-g22/f10
      p21=d13*h11+g21
      p22=d13*h12+g22
      q11=h11-p21/f30
      q12=h12-p22/f30
      fcrys=-1/q12
      pcrys1=(1-q11)/q12
      pcrys2=(1-p22)/q12
      dcrys=d23-pcrys1-pcrys2
      scrys=dcrys*(4*fcrys-dcrys)/4
      wcrys2=dcrys/2+pcrys2
      wcrys3=dcrys/2+pcrys1
```

```
c*****************************************************************
      subroutine spot
c*****************************************************************
      common d12,d13,d23,wjet2,wcrys2
      common/two/rnj,rna,rnc,rnr,rlj,rla,rlc,rlr,rj,ra,rc,rr,d2,d5
      common/three/f1,f2,f3,fo1,fo2,fo3
      d7=d13
      d1=wjet2-(rlj/2)
      d6=wcrys2-(rlc/2)
c
c The calculations for the jet in the tangential plane
      d11=d1
      d61=d6
      do 5 M=1,2
      d31=d12-(d11+d2+rlj+rla)
      d41=d23-(d61+d5+rlc+rlr)
      a33=1/rnj
      a34=d11*rnj
      a43=-1/(f1*rnj)
      a44=rnj-d11*rnj/f1
      b33=a33+(d7*a43)
      b34=a34+d7*a44
      b43=a43-b33/f3
      b44=a44-b34/f3
      c33=b33+d61*b43
      c34=b34+d61*b44
      c43=b43/rnc
      c44=b44/rnc
      c33=c33*rnc
      c34=c34*rnc
      e33=c33+rc*c43
      e34=c34+rc*c44
      e33=e33/rnc
      e34=e34/rnc
      e43=c43*rnc
      e44=c44*rnc
      f33=e33+d5*e43
      f34=e34+d5*e44
      f33=f33*rnr
      f34=f34*rnr
      f43=e43/rnr
      f44=e44/rnr
      g33=f33+rr*f43
      g34=f34+rr*f44
      g33=g33/rnr
      g34=g34/rnr
      g43=f43*rnr
      g44=f44*rnr
      h33=g33+d41*g43
      h34=g34+d41*g44
      h43=g43-h33/f2
      h44=g44-h34/f2
      p33=h33+d31*h43
      p34=h34+d31*h44
      p33=p33*rna
      p34=p34*rna
      p43=h43/rna
      p44=h44/rna
      q33=p33+ra*p43
      q34=p34+ra*p44
      q33=q33/rna
      q34=q34/rna
      q43=p43*rna
      q44=p44*rna
      r33=q33+d2*q43
      r34=q34+d2*q44
      r43=q43/rnj
      r44=q44/rnj
      r33=r33*rnj
      r34=r34*rnj
      fjet=-1/r43
      pjet1=(1-r44)/r43
      pjet2=(1-r33)/r43
      djet=(rlj-pjet1-pjet2)
      sjet1=djet*(4*fjet-djet)/4
      wjet4=(rlj+pjet1-pjet2)/2
      d11=wjet4+d11-(rlj/2)

c Calculations for the crystal in the tangential plane
      d31=d12-(d11+d2+rlj+rla)
      d41=d23-(d61+d5+rlc+rlr)
      a55=1/rnc
      a56=d5*rnc
      a66=rnc
      a65=0.
      a55=rnr*a55
      a56=a56*rnr
      a66=a66/rnr
      a65=a65/rnr
      b55=a55+rr*a65
      b56=a56+rr*a66
      b55=b55/rnr
      b56=b56/rnr
      b65=a65*rnr
      b66=a66*rnr
      c55=b55+d41*b65
      c56=b56+d41*b66
      c65=b65-c55/f2
      c66=b66-c56/f2
      e55=c55+d31*c65
      e56=c56+d31*c66
      e55=e55*rna
      e56=e56*rna
      e65=c65/rna
      e66=c66/rna
      f55=e55+ra*e65
      f56=e56+ra*e66
      f55=f55/rna
      f56=f56/rna
      f65=e65*rna
      f66=e66*rna
      g55=f55+f65*d2
      g56=f56+f66*d2
      g55=g55*rnj
      g56=g56*rnj
      g65=f65/rnj
      g66=f66/rnj
      h55=g55+rj*g65
      h56=g56+rj*g66
      h55=h55/rnj
      h56=h56/rnj
      h65=g65*rnj
      h66=g66*rnj
      p55=h55+d11*h65
      p56=h56+d11*h66
      p65=h65-p55/f1
      p66=h66-p56/f1
      q55=p55+p65*d7
      q56=p56+p66*d7
      q65=p65-q55/f3
      q66=p66-q56/f3
      r55=q55+d61*q65
      r56=q56+d61*q66
      r55=r55*rnc
      r56=r56*rnc
      r65=q65/rnc
      r66=q66/rnc
      fcrys=-1/r65
      pcrys1=(1-r66)/r65
      pcrys2=(1-r55)/r65
      dcrys=(rlc-pcrys1-pcrys2)
      scrys1=dcrys*(4*fcrys-dcrys)/4
      wcrys3=(rlc-pcrys1+pcrys2)/2
      d61=d61+wcrys3-rlc/2
    5 continue
      write(1,300)d11+rlj/2,sjet1,d61+rlc/2,scrys1
  300 format(4 f12.6)
  500 end
```

Alignment Procedure for Incorporating the Frequency Doubling Elements

1. With the 9.4% transmitting output coupler (TOC) as M4, align the dye laser, to give single mode operation, according to the instructions in the Spectra-Physics 380D manual, except remove the standard astigmatism compensator and ensure M3 is the high UV transmitting mirror.

2. Reduce the Ar^+ pump power to 2W.

3. Replace the 9.4% TOC with the 0.14% TOC. Use the UDT PIN10-UVCAL photodiode, placed behind a 1% NDF, to monitor the fundamental power.

4. Screw the quartz compensating rhomb onto the rotary stage nearest the jet.

5. Place the crystal oven, with the aperture for the crystal approximately parallel to the base plate, on to the second rotary stage.

6. Connect the crystal oven to the temperature control box.

7. Rotate the crystal oven about its axis to recover overlap of the fluorescent spots on mirror M3.

8. Reoptimise the focus of M2. Place a card about 9" behind the fundamental output coupler and minimise the size of the spot from M3 by translating M2 away from the jet.

9. Lasing should be achieved by adjusting the tilt of M2. Optimise

the fundamental power by small adjustments of M3, M4 and M_{pump}. Check that the laser is operating single mode.

10. Check the beam path through the quartz compensating rhomb. If this is not parallel to the sides of the rhomb then the relative orientation of the crystal and rhomb is not optimum. In this case see step 15.

11. Rotate the crystal about its axis by a small amount in a noted direction, until lasing is just about extinguished. Reoptimise power by tilting M2 followed by M3 and M4. If there is an improvement in the fundamental power continue to rotate the crystal oven in this direction until no further improvement is obtained. If there is a reduction in the power rotate the oven in the opposite direction, iteratively, until maximum power is obtained. The optimised power should not be less than 80% of that measured in step 2.

12. Select phase match temperature and switch on heater.

13. Rotate the BRF to obtain phase match. Measure the UV generated by placing PIN 100-UVCAL photodiode behind a UV filter. Maximise the measured power by rotating the dual galvo-plates (using the scan position control on the 381 electronics box). A UV power of 3-7 mW obtained at this point is acceptable.

14. Adjust the pump power to achieve the desired UV power.

15. The adjustment to achieve optimum relative orientation of the crystal and rhomb is best made by minimising the laser threshold. Rotate the rhomb using the rotational adjustment of its stage, by a small amount. Then rotate the rhomb to re-establish lasing. If the

threshold has been reduced continue to rotate the crystal in the same direction. Otherwise rotate it in the opposite direction. The angle on the crystal rotatory stage is usually 116° for optimum relative orientation of the crystal and rhomb. Return to step 11.

Figure 1 Schematic diagram of the base plate with the crystal and rhomb positioning devices shown. This plate is screwed to the cavity invar rods using a 'V' and plane for location. The double-axis translation stages are Ealing number 35-1718 and the miniature rotary stages are Ealing number 35-1742.

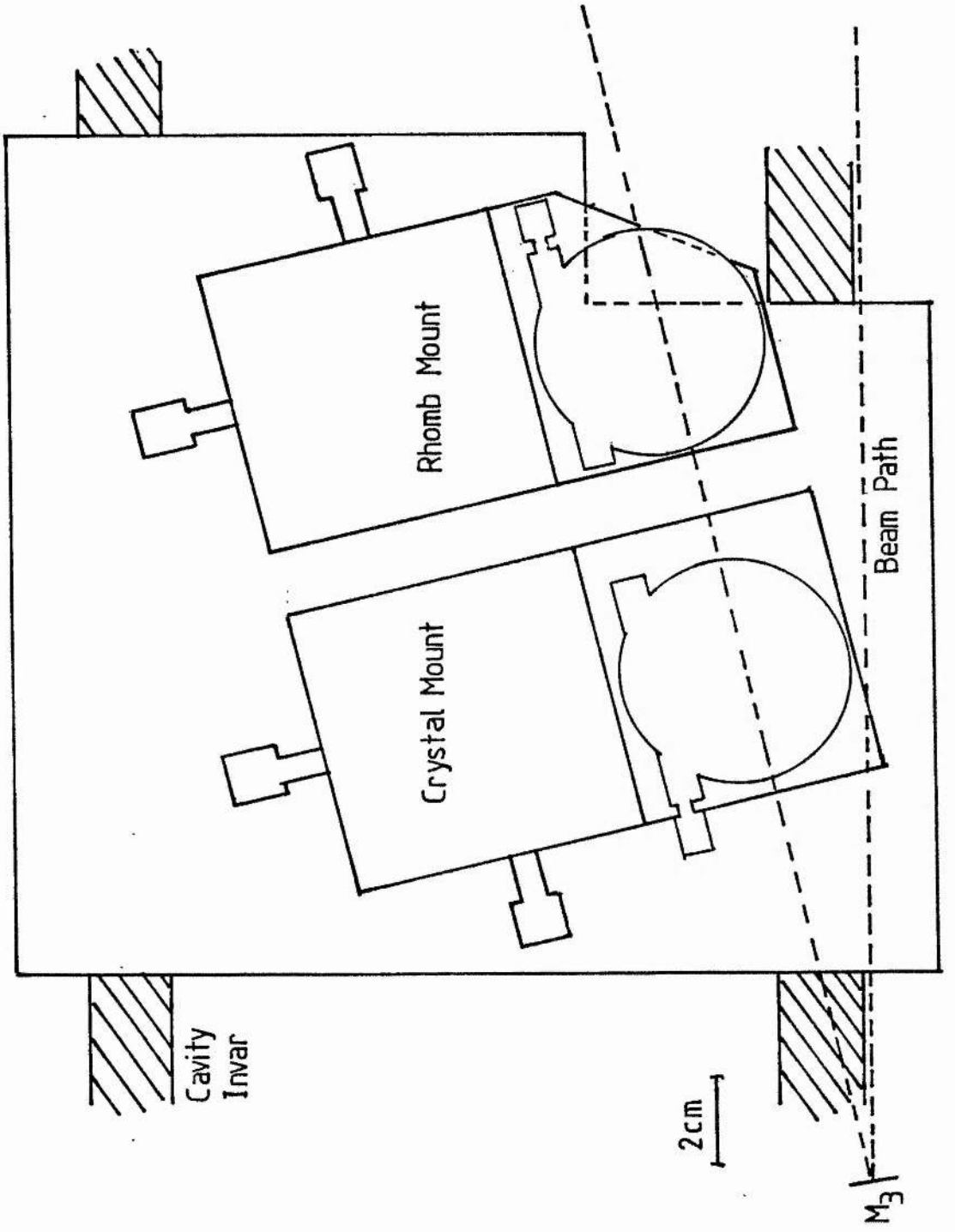

Appendix C

Computer Programs Used in Analysing Helium 2^3S Metastable Densities

1. CREHEL

This program calculates the metastable density from the absorption measurements taken from chart recordings. A linear correction is made for the variation in the uv intensity during a laser frequency scan. Two values of the metastable density are obtained, one for each side of the line profile.

2. BROWNE6

This program calculates the 2^3S metastable density from equation (3.6) when all rate coefficients are provided.

3. DETGAM1

For each experimentally determined metastable density this program calculates the range of α values required to match the range of γ values 5×10^{-9} cm^3 s^{-1} to 1×10^{-7} cm^3 s^{-1}, for use in program LASTHE.

4. LASTHE

The 2^3S metastable density is calculated from equation (3.6) as α and γ are stepped in value, by small increments, within the ranges specified above. The difference between this calculated value and the experimental value to be fitted, is calculated. Initially a limit is set for a maximum of this difference and of the set of α and γ pairs leading to a metastable density which satisfy this, the one with the minimum of this difference is written to a file.

5. COLEXCOA

This program uses the best value of γ, obtained by the fitting procedure outlined in section 3.4, and the experimental metastable density data to calculate the value of α.

6. COMDOP

The data for figures 3.1 and 3.2 were generated by this program.

```
c*********************************************
      PROGRAM CREHEL
C*********************************************
c To create a file of absorption measurements from
c linear absorption data and to calculate the
c Doppler width of the absorption coefficient and
c the triplet metastable densities.
      open (unit=1, name='hela', type='new')
      const=3.213e12
c const=sqrt(pi/ln2)*G1/Gu*(8pi/2(lambda**2*Au1)
c for Au1=3.1e6 per sec.
      type 200
  200 format(' Input the pressure and # of data points  '$)
      accept*,p,j
      write(1,50)p,j
      do 1 I=1,j
        type 250
  250   format('  Input I,v1,v2,v3,v4,v5,v6,dw  '$)
        accept*,ri,v1,v2,v3,v4,v5,v6,dw
c dw is the full width at half maximum of the absorption
c profile from which the Doppler width of the absorption
c coefficient may be deduced.
        rt1=(v2*v4)/(v1*v5)
        rt2=0.5*rt1+0.5
        rt3=(v2*v6)/(v3*v5)
        rt4=0.5*rt3+0.5
        rko1=-(1/2.3)*log(rt1)
        rko2=-(1/2.3)*log(rt2)
        rko3=-(1/2.3)*log(rt3)
        rko4=-(1/2.3)*log(rt4)
        r1=rko2/rko1
        x=alog(r1)
        y=-1.0*x
        dw1=(1.665*dw/2)/(sqrt(y))
        rn1=rko1*dw1*const
        r2=rko4/rko3
        x=alog(r2)
        y=-1.0*x
        dw2=(1.665*dw/2)/(sqrt(y))
        rn2=rko3*dw2*const
        write(1,150),ri,dw,dw1,dw2,rn1,rn2
    1 continue
  150 format(f5.1,3 f6.2,2 e13.3)
   50 format(f6.3,i3)
      close(unit=1)
      end
$
```

```
c*********************************************
      program BROWNE6
c*********************************************
c Calculating He(23S) metastable atom densities
c using the model developed by Dunn & Browne
      open(unit=1,name='meta',type='new')
      open(unit=2,name='ced',type='old')
  100 format(f8.5)
  200 format(3 f9.4,f10.4,6 (1x,e12.6))
  300 format(3 f9.4)
      type 450
  450 format('  alpha=x1*(E/p-x2),input x1 & x2  '$)
      accept*,x1,x2
      do 3 K=1,5
      type 400
  400 format('  Input the pressure  '$)
      accept*,p
      write(1,100)p
      do 1 I=1,8
      read(2,300)ri,ep,dw
      alpha=x1*(ep-x2)
      t=((dw/(7.16*1018.6e-4))**2)*4
      rno=3.5E16*P*(300/t)
      rne=1.e11*ri/ep
      tau=3.0e4/p
      delta=1.5e-9
      gamma=4.2e-9
      b=(tau+gamma*rne)
      a=delta
      c=-alpha*rno*rne
      rnml=(-b+sqrt(b**2-4*a*c))/(2*a)
      write(1,200)ri,ep,dw,t,alpha,gamma,rne,rno,rnml
    1 continue
    3 continue
      close(unit=1)
      close(unit=2)
      end
```

```
c***********************************************
      program DETGAM1
c***********************************************
c Calculating He(23S) metastable atom densities
      DIMENSION ERR(20),rm(8),gamma1(20)
      open(unit=1,name='meta',type='new')
      open(unit=2,name='ced',type='old')
  100 format(f8.5)
  460 FORMAT(10 (F9.5))
  465 format(e16.8)
  200 format(3 f9.4,f10.4,6 (1x,e12.6))
  300 format(3 f9.4,f7.3)
      type 450
  450 format(' alpha=x1*(E/p-x2),input x1 & x2 '$)
      accept*,x1,x2
      do 7 n=1,20
      gamma1(n)=(real(n)/2.)*1.e-8
    7 continue
  400 format(10 e10.3)
      do 2 1=1,5
      type 150
  150 format(' Pressure=? '$)
      accept*,p
      do 1 I=1,8
      read(2,300)ri,ep,dw,rm(I)
      alpha=x1*(ep-x2)
      rinc=alpha/10.
      t=((dw/(7.16*1018.6e-4))**2)*4
      rno=3.5E16*P*(300/t)
      rne=1.e11*ri/ep
      tau=3.0e4/p
      delta=1.5e-9
      do 6 k=-5,5
      alpha1=alpha+real(K)*rinc
      do 9 m=1,20
      b=(tau+gamma1(m)*rne)
      a=delta
      c=-alpha1*rno*rne
      rnm1=(-b+sqrt(b**2-4*a*c))/(2*a)
      err(m)=rm(i)-(rnm1/1.e12)
    9 continue
      write(1,465)alpha1
      write(1,460)(err(J),J=1,20)
    6 continue
    1 continue
    2 continue
      close(unit=1)
      close(unit=2)
      end
```

```
c*********************************************
      program LASTHE
c*********************************************
c Calculating He(23S) metastable atom densities
      open(unit=1,name='meta',type='new')
      open(unit=2,name='ced',type='old')
  100 format(f8.5)
  460 FORMAT(5 E16.8)
  200 format(3 f9.4,f10.4,6 (1x,e12.6))
  300 format(3 f9.4,f7.3)
      do 3 N=1,5
      type 450
  450 format(' alphamin,alphamax= ? '$)
      accept*,x1,x2
      rinc=(x2-x1)/50
      type 470
  470 format(' max allowed diff '$)
      accept*,rlim
      error=rlim
      type 150
  150 format(' Pressure=? '$)
      accept*,p
      write(1,100)p
      do 1 I=1,8
      read(2,300)ri,ep,dw,rm
      write(1,300)ri,ep,dw,rm
      t=((dw/(7.16*1018.6e-4))**2)*4
      rno=3.5E16*P*(300/t)
      rne=1.e11*ri/ep
      tau=3.0e4/p
      delta=1.5e-9
      do 6 k=0,50
      alpha=x1+real(K)*rinc
      error=rlim
      do 9 m=4,100,4
      gamma=real(M)*1.e-9
      b=(tau+gamma*rne)
      a=delta
      c=-alpha*rno*rne
      rnm1=(-b+sqrt(b**2-4*a*c))/(2*a)
      err=rm-(rnm1/1.e12)
      if(abs(err).lt.rlim)then
        if(abs(err).lt.abs(error))then
          error=err
          alphal=alpha
          gammal=gamma
          rnm=rnm1
        end if
      end if
    9 continue
      if(error.ne.rlim)write(1,460)alphal,gammal,rnm,error
    6 continue
    1 continue
    3 continue
      close(unit=1)
      close(unit=2)
      end
```

```
c*********************************************
      program COLEXCOA
c*********************************************
c Calculating the metastable excitation coeff. for
c groundstate-electron collisions
      open(unit=1,name='meta',type='new')
      open(unit=2,name='ced',type='old')
  100 format(f8.5)
  200 format(3 f9.4,f10.4,5 (1x,e12.6))
  300 format(3 f9.4,f6.1)
      do 3 K=1,5
      type 400
  400 format('  Input the pressure  '$)
      accept*,p
      write(1,100)p
      type 450
  450 format('  Input gamma  '$)
      accept*,gamma
      type 460
  460 format('  Alpha=x1*(E/p-x2), inputx1 & x2  '$)
      accept*,x1,x2
      do 1 I=1,8
      read(2,300)ri,ep,dw,rnm
      rnm=rnm*1.e12
      t=((dw/(7.16*1018.6e-4))**2)*4
      rno=3.5E16*P*(300/t)
      rnel=1.e11*ri/ep
      tau=3.0e4/p
      delta=1.5e-9
      alpha=x1*(ep-x2)
      rne=((tau+delta*rnm)*rnm)/(alpha*rno-gamma*rnm)
      write(1,200)ri,ep,dw,t,rnm,gamma,alpha,rnel,rne
    1 continue
    3 continue
      close(unit=1)
      close(unit=2)
      end
```

```
c*****************************************
c          PROGRAM COMDOP
c*****************************************
        dimension B(10),C(10),D(6,501)
        common del2,d
        open(unit=1,name='cdop',type='new')
        type 100
  100   format('  Temperature=?   '$)
        accept *,T
        type 200
  200   format('  No. of fine structure components=?  '$)
        accept *,num
        type 300
  300   format('  Atomic weight=?  '$)
        accept *,A
        type 350
  350   format('  Shift freq. and intensity ratios for components')
  400   format('  Freq. shift=?  '$)
  500   format('  Intensity=?  '$)
        do 1  I=1,num
        type 400
        accept *,b(I)
        type 500
        accept *,c(I)
    1   continue
        type 800
  800   format('  Centre frequency=?  ')
        accept *,v
        del=7.16*v*1.e5*(sqrt(T/A))*1.2
        del2=del*del
  900   format(i5,3 f12.4)
        do 3 j=1,num
        call dopp(j,b(j),c(j))
    3   continue
        do 4 k=1,501
        d(4,K)=d(1,k)+d(2,k)+d(3,K)
    4   continue
        comp=0.
        do 5 k=1,501
        if(d(4,k).gt.comp) then
        comp=d(4,k)
        no=k-251
        end if
    5   continue
        call dopp(5,real(no),comp)
        do 7 k=1,501
        d(6,k)=d(5,k)-d(4,k)
    7   continue
        do 6 k=1,501
        write(1,900) k-251,d(4,k),d(5,k),d(6,k)
    6   continue
        end
c
        subroutine dopp(I,w,aint)
        common del2,D
        dimension D(6,501)
        do 5 k=1,501
        rk=real(K)-251.
        D(I,k)=aint*exp((-4*(4*(rk-w))**2*1.e14)/del2)
c Frequency being stepped in 40 MHz intervals
c Therefore scan is over range -10GHz to +10 GHz
    5   continue
        return
        end
```

Appendix D

Change in the Electron Density in a Discharge

To relate the measured change in the voltage across a ballast resistor in series with a discharge tube, to the change in the current, when using a constant voltage supply, it is necessary to include the effect of the changing drift velocity of the electrons due to the changing voltage across the discharge. Consider the circuit in the figure.

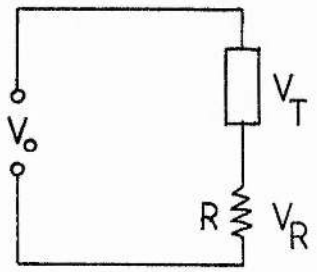

We have

$$V_o = iR + V_T$$

and

$$i = An_e e\upsilon_D$$

where A is the cross sectional area of the discharge, n_e is the electron density, e the electronic charge and υ_D the drift velocity of the electrons. The drift velocity is well approximated by a linear function of E/p

$$\upsilon_D = CV_T$$

Thus we have

$$V_R = RAn_e e\upsilon_D$$

and the differential of this is

$$\delta V_R = RAe(\upsilon_D \delta n_e + n_e \delta \upsilon_D)$$

Rearrangement and substitution give

$$\delta V_R = RAe\upsilon_D \delta n_e / [1-(\delta\upsilon_D/\upsilon_D)/(\delta V_R/V_R)] \qquad (1)$$

But we have

$$\delta\upsilon_D = C\delta V_T = -C\delta V_R$$

and

$$\delta\upsilon_D/\upsilon_D = -\delta V_R/(V_o - V_R)$$

Substituting this expression into equation (1) and rearranging gives

$$\delta V_R/V_R = \delta n_e/n_e(V_T/V_o)$$

The measured change in voltage across the ballast resistor corresponds to a fraction of the change in the electron density. The voltage across the tube is (305 ± 6)V for the current range 2.5-22mA, for a pressure of 1.5 Torr in the neon positive column under study in Chapter 4. The power supply voltage increases from 900-3000 V to supply this current range. Thus the fractional change in V_R must be multiplied by a correction factor between 3 and 10 to obtain the fractional change in electron density. For a current of 5mA and pressure of 1.5 Torr this correction gives about a 2% change in the electron density.

Appendix E

Method of Solving Neon Positive Column Rate Equations

The rate equations describing the $1s_5$, $1s_4$, $1s_3$ and $2p_2$ level populations in a neon positive column are given in section 4.5.1. When the laser is off all terms in $B(\nu)I$ vanish. The steady state solutions with the laser on or off are obtained by expressing all the populations densities in terms of the $1s_5$ population density as follows:

$$\text{From eqn.(4.6)} \qquad N_6 = f_1(N_5)$$

$$\text{then from eqn.(4.5)} \qquad N_3 = f_2(N_6) = f_3(N_5)$$

$$\text{then from eqn.(4.4)} \qquad N_4 = f_4(N_6) = f_5(N_5)$$

$$\text{then from eqn.(4.3)} \qquad N_5 = f_6(N_5)$$

The resulting expression is solved for N_5 which is then substituted into the other expressions to obtain N_4, N_3 and N_6. Once the steady state values are known these can be used as initial conditions for obtaining the time resolved behaviour. Starting with the steady state solution with the laser off and giving $B(\nu)I$ a non zero value, the increment in N_i is obtained from

$$dN_i = (f_i)dt$$

and is approximated by

$$\Delta N_i = (f_i)\Delta t$$

where suitable increments Δt are chosen by trial and error. The programs used to generate the results presented in chapter 4 are listed below. Program UNE gives the population density as a function of $B(\nu)I$. Program UNINEOG gives the population densities as a function of time as the laser is switched off. Program UNINEOGON gives the population densities as a function of time as the laser is switched on.

```
c*******************************************
      program UNE
c*******************************************
c Model for neon optogalvanic effect including
c the radiative levels in the 1s group.
      double precision alpha3,alpha4,alpha5,alpha6,a62,a63,a64,a65
      double precision bi,g1,g2,g34,g45,g57,g37,g67,beta
      double precision rno,rne,rn3,rn4,rn5,rn6,O,P,Q,R,S,T,U,V,W
      double precision A,B,C,a40,x1,x2,x3,rn7,r30,r50,r40
      open(UNIT=1, name='uneog',type='new')
      a62=2.25d7
      a63=1.46d7
      a64=5.61d6
      a65=1.15d7
      a40=1.30d4
      beta=9.d-10
      rno=3.22d16
      g1=5d0
      g2=3.d0
      g67=2.d-8
      g37=6.d-9
      g57=6.d-9
      g34=0.d0
      g45=0.d0
      tau3=5.d3
      tau5=5.d3
      type 50
   50 format(' Input alpha6-the exc.coeff for 2p2 '$)
      accept*,alpha6
      type 100
  100 format(' Input alpha5-the exc.coeff for 1s5 '$)
      accept*,alpha5
      type 200
  200 format(' Input alpha3-the exc.coeff. for 1s3 '$)
      accept*,alpha3
      type 300
  300 format(' Input alpha4-the exc.coeff. for 1s4 '$)
      accept*,alpha4
      type 400
  400 format(' Input the electron density '$)
      accept*,rne
      type 420
  420 format(' Input b3 '$)
      accept*,b3
      bi=0.d0
      O=alpha6*rne*rno/(bi*g1/g2+g67*rne+a62+a63+a64+a65)
      P=bi/(bi*g1/g2+g67*rne+a62+a63+a64+a65)
      Q=a63/(g34*rne+g37*rne+tau3)
      R=(alpha3*rno*rne)/((g34+g37)*rne+tau3)
      S=alpha4*rno*rne/(a40+g45*rne)
      T=(g34*rne)/(a40+g45*rne)
      U=a64/(g45*rne+a40)
      A=-beta
      B=g45*rne*(T*Q*P+U*P)+(a65+bi*g1/g2)*P-(g57*rne+tau5+bi)
      C=(a65+bi*g1/g2)*O+alpha5*rno*rne+g45*rne*(T*Q*O+T*R+U*O+S)
      rn5=(-B-dsqrt(B**2d0-4d0*A*C))/(2d0*A)
      rn4=T*(Q*(P*rn5+O)+R)+S+U*(P*rn5+O)
      rn3=Q*(P*rn5+O)+R
      rn6=P*rn5+O
      x1=beta*(rn5**2.d0)
      x2=b3*(rn3**2.d0)
      x3=(g67*rn6+g37*rn3+g57*rn5+g37*rn4)*rne
      rn7=x1+x2+x3
      type*,rn6,rn5,rn4,rn3
      r50=rn5
```

```
      r40=rn4
      r30=rn3
      DO 1 I=0,12
      DO 2 J=2,10
      bi=DFLOAT(J)*(10.D0**DFLOAT(I))
      O=alpha6*rne*rno/(bi*g1/g2+g67*rne+a62+a63+a64+a65)
      P=bi/(bi*g1/g2+g67*rne+a62+a63+a64+a65)
      Q=a63/(g34*rne+g37*rne+2.d0*tau3)
      R=(alpha3*rno*rne+tau3*r30)/((g34+g37)*rne+2.d0*tau3)
      S=alpha4*rno*rne/(a40+g45*rne)
      T=(g34*rne)/(a40+g45*rne)
      U=a64/(g45*rne+a40)
      A=-beta
      B=g45*rne*(T*Q*P+U*P)+(a65+bi*g1/g2)*P-(g57*rne+2.d0*tau5+bi)
      C=(a65+bi*g1/g2)*O+alpha5*rno*rne+g45*rne*(T*Q*O+T*R+U*O+S)
      C=C+tau5*r50
      rn5=(-B-dsqrt(B**2d0-4d0*A*C))/(2d0*A)
      rn4=T*(Q*(P*rn5+O)+R)+S+U*(P*rn5+O)
      rn3=Q*(P*rn5+O)+R
      rn6=P*rn5+O
      x1=beta*(rn5**2.d0)
      x2=b3*(rn3**2.d0)
      x3=(g67*rn6+g37*rn3+g57*rn5+g37*rn4)*rne
      rn7=x1+x2+x3
      WRITE(1,800)bi,RN6,RN5,RN4,RN3,rn7
    2 CONTINUE
    1 CONTINUE
  800 FORMAT(6 E13.6)
      close(unit=1)
      end
```

```
c*******************************************
      program UNINEOG
c*******************************************
c Model for neon optogalvanic effect including
c the radiative levels in the 1s group.
      double precision alpha3,alpha4,alpha5,alpha6,a62,a63,a64,a65
      double precision bi,g1,g2,g34,g45,g57,g37,g67,beta
      double precision rno,rne,rn3,rn4,rn5,rn6,O,P,Q,R,S,T,U,V,W
      double precision A,B,C,a40,tau3,tau5,r50,r30,big,TAU
      dimension big(5)
      common bi,g1,g2,g34,g45,g57,g37,g67,beta,alpha3,alpha4,alpha5
      common a62,a63,a64,a65,a40,rno,rne,O,P,Q,R,S,T
      common U,V,W,A,B,C,alpha6,tau3,tau5,r50,r30,tau,b3
      open(UNIT=1, name='uneogon',type='new')
      big(1)=1.d4
      big(2)=1.d5
      big(3)=1.d6
      big(4)=5.d6
      big(5)=1.d7
      g1=5.d0
      g2=3.d0
      a62=2.25d7
      a63=1.46d7
      a64=5.61d6
      a65=4.76d7
      a40=1.30d4
      beta=9.d-10
      b3=2.d-9
      rno=3.22d16
      g67=2.d-8
      g37=6.d-9
      g57=6.d-9
      g34=0.d0
      g45=0.d0
      tau3=5.d3
      tau5=5.d3
      type 50
 50   format(' Input alpha6-the exc.coeff for 2p2 '$)
      accept*,alpha6
      type 100
100   format(' Input alpha5-the exc.coeff for 1s5 '$)
      accept*,alpha5
      type 200
200   format(' Input alpha3-the exc.coeff. for 1s3 '$)
      accept*,alpha3
      type 300
300   format(' Input alpha4-the exc.coeff. for 1s4 '$)
      accept*,alpha4
      type 400
400   format(' Input the electron density '$)
      accept*,rne
      type 500
500   format(' Input tau '$)
      accept*,tau
      do 1 I=1,5
      bi=big(I)
      rn6=(alpha6*rno*rne)/(g67*rne+a62+a63+a64+a65)
      Q=(alpha3*rno*rne)/((g34+g37)*rne+tau3)
      R=a63/((g34+g37)*rne+tau3)
      rn3=Q+R*rn6
      r30=rn3
```

```
      U=a64/(a40+g45*rne)
      S=g34*rne/(a40+g45*rne)
      T=(alpha4*rno*rne)/(a40+g45*rne)
      rn4=S*rn3+T+U*rn6
      A=beta
      B=(tau5+g57*rne)
      C=alpha5*rno*rne+a65*rn6+g45*rne*rn4
      r50=(-B+dsqrt((B**2d0)+4d0*A*C))/(2d0*A)
      O=alpha6*rne*rno/(bi*g1/g2+g67*rne+a62+a63+a64+a65)
      P=bi/(bi*g1/g2+g67*rne+a62+a63+a64+a65)
      Q=a63/(g34*rne+g37*rne+2.d0*tau3)
      R=(alpha3*rno*rne+tau3*r30)/((g34+g37)*rne+2.d0*tau3)
      S=(alpha4*rno*rne)/(a40+g45*rne)
      T=(g34*rne)/(a40+g45*rne)
      U=a64/(g45*rne+a40)
      A=-beta
      B=g45*rne*(T*Q*P+U*P)+(a65+bi*g1/g2)*P-(g57*rne+tau+tau5+bi)
      C=(a65+bi*g1/g2)*O+alpha5*rno*rne+g45*rne*(T*Q*O+T*R+U*O+S)
      C=C+tau*r50
      rn5=(-B-dsqrt(B**2.d0-4.d0*A*C))/(2.d0*A)
      rn4=T*(Q*(P*rn5+O)+R)+S+U*(P*rn5+O)
      rn3=Q*(P*rn5+O)+R
      rn6=P*rn5+O
      call off(rn6,rn5,rn4,rn3)
 1    continue
600   format(6 e15.6)
      close(unit=1)
      end
c*************************************************
      subroutine OFF(r6,r5,r4,r3)
c*************************************************
      double precision alpha3,alpha4,alpha5,alpha6,a62,a63,a64,a65
      double precision bi,g1,g2,g34,g45,g57,g37,g67,beta,r77
      double precision rno,rne,r33,r44,r55,r66,O,P,Q,R,S,T,U,V,W
      double precision A,B,C,a40,dr6,dr5,dr4,dr3,r7,r8,r9,delta,delt
      double precision tau3,tau5,r6,r5,r4,r3,r10,r11,r50,r30,tau
      common bi,g1,g2,g34,g45,g57,g37,g67,beta,alpha3,alpha4,alpha5
      common a62,a63,a64,a65,a40,rno,rne,O,P,Q,R,S,T
      common U,V,W,A,B,C,alpha6,tau3,tau5,r50,r30,tau,b3
      r66=r6
      r55=r5
      r44=r4
      r33=r3
      delta=1.d-12
      do 1 I=1,10000
      dr6=(alpha6*rno*rne-(g67*rne+a62+a63+a64+a65)*r66)*delta
      dr5=(alpha5*rno*rne+a65*r66+g45*r44*rne-(tau+tau5)*r55
     1       -g57*rne*r55-beta*r55**2d0+tau*r50)*delta
      dr4=((alpha4*rno+g34*r33-g45*r44)*rne+a64*r66-a40*r44)*delta
      dr3=((alpha3*rno-(g34+g37)*r33)*rne+a63*r66-2.d0*tau3*r33
     1        +tau3*r30)*delta
      r66=r66+dr6
      r55=r55+dr5
      r44=r44+dr4
      r33=r33+dr3
 1    continue
      delt=1.d-8
      r77=beta*r55**2.d0+b3*r33**2.d0+rne*(g37*(r33+r44+r55)+g67*r66)
      write(1,300)delt,r66,r55,r44,r33,r77
      delta=1.d-11
```

```
      do 2 J=1,4
      do 3 K=1,90
      do 4 L=1,100
      dr6=(alpha6*rno*rne-(g67*rne+a62+a63+a64+a65)*r66)*delta
      dr5=(alpha5*rno*rne+a65*r66+g45*r44*rne-(tau+tau5)*r55
     1       -g57*rne*r55-beta*r55**2d0+tau*r50)*delta
      dr4=((alpha4*rno+g34*r33-g45*r44)*rne+a64*r66-a40*r44)*delta
      dr3=((alpha3*rno-(g34+g37)*r33)*rne+a63*r66-2.d0*tau3*r33
     1        +tau3*r30)*delta
      r66=r66+dr6
      r55=r55+dr5
      r44=r44+dr4
      r33=r33+dr3
 4    continue
      delt=delt+delta*100.
      r77=beta*r55**2.d0+b3*r33**2.d0+rne*(g37*(r33+r44+r55)+g67*r66)
      write(1,300)delt,r66,r55,r44,r33,r77
 3    continue
      delta=delta*10.
 2    continue
      delta=delta/10
      do 5 M=1,90
      do 6 N=1,1000
      dr6=(alpha6*rno*rne-(g67*rne+a62+a63+a64+a65)*r66)*delta
      dr5=(alpha5*rno*rne+a65*r66+g45*r44*rne-(tau+tau5)*r55
     1       -g57*rne*r55-beta*r55**2d0+tau*r50)*delta
      dr4=((alpha4*rno+g34*r33-g45*r44)*rne+a64*r66-a40*r44)*delta
      dr3=((alpha3*rno-(g34+g37)*r33)*rne+a63*r66-2.d0*tau3*r33
     1        +tau3*r30)*delta
      r66=r66+dr6
      r55=r55+dr5
      r44=r44+dr4
      r33=r33+dr3
 6    continue
      delt=delt+delta*1000.
      r77=beta*r55**2.d0+b3*r33**2.d0+rne*(g37*(r33+r44+r55)+g67*r66)
      write(1,300)delt,r66,r55,r44,r33,r77
 5    continue
300   format(6 e15.6)
      end
$
```

```
c*****************************************
      program UNINEOGON
c*****************************************
c Model for neon optogalvanic effect including
c the radiative levels in the 1s group.
      double precision alpha3,alpha4,alpha5,alpha6,a62,a63,a64,a65
      double precision bi,g1,g2,g34,g45,g57,g37,g67,beta
      double precision rno,rne,rn3,rn4,rn5,rn6,P,Q,R,S,T,U,V,W
      double precision A,B,C,a40,tau3,tau5,tau,big
      dimension big(5)
      common bi,g1,g2,g34,g45,g57,g37,g67,beta,alpha3,alpha4,alpha5
      common a62,a63,a64,a65,a40,rno,rne,P,Q,R,S,T,b3
      common U,V,W,A,B,C,alpha6,tau3,tau5,tau
      open(UNIT=1, name='uneogON',type='new')
      big(1)=1.d4
      big(2)=1.d5
      big(3)=1.d6
      big(4)=5.d6
      big(5)=1.d7
      g1=5.d0
      g2=3.d0
      a62=2.25d7
      a63=1.46d7
      a64=5.61d6
      a65=4.76d7
      a40=1.30d4
      beta=9.d-10
      b3=2.d-9
      rno=3.22d16
      g67=2.d-8
      g37=6.d-9
      g57=6.d-9
      g34=0.d0
      g45=0.d0
      tau3=5.d3
      tau5=5.d3
      type  50
 50   format(' Input alpha6-the exc.coeff for 2p2 '$)
      accept*,alpha6
      type 100
100   format(' Input alpha5-the exc.coeff for 1s5 '$)
      accept*,alpha5
      type 200
200   format(' Input alpha3-the exc.coeff. for 1s3 '$)
      accept*,alpha3
      type 300
300   format(' Input alpha4-the exc.coeff. for 1s4 '$)
      accept*,alpha4
      type 400
400   format(' Input the electron density '$)
      accept*,rne
      type 500
500   format(' Input tau '$)
      accept*,tau
      do 1 I=1,5
      bi=BIG(I)
      rn6=(alpha6*rno*rne)/(g67*rne+a62+a63+a64+a65)
      Q=(alpha3*rno*rne)/((g34+g37)*rne+tau3)
      R=a63/((g34+g37)*rne+tau3)
      rn3=Q+R*rn6
      U=a64/(a40+g45*rne)
      S=g34*rne/(a40+g45*rne)
      T=(alpha4*rno*rne)/(a40+g45*rne)
      rn4=S*rn3+T+U*rn6
```

```
      A=beta
      B=(tau5+g57*rne)
      C=alpha5*rno*rne+a65*rn6+g45*rne*rn4
      rn5=(-B+dsqrt((B**2d0)+4d0*A*C))/(2d0*A)
      call on(rn6,rn5,rn4,rn3)
    1 continue
  600 format(6 e15.6)
      close(unit=1)
      end
c*************************************************
      subroutine ON(r6,r5,r4,r3)
c*************************************************
      double precision alpha3,alpha4,alpha5,alpha6,a62,a63,a64,a65
      double precision bi,g1,g2,g34,g45,g57,g37,g67,beta
      double precision rno,rne,r33,r44,r55,r66,P,Q,R,S,T,U,V,W
      double precision A,B,C,a40,dr6,dr5,dr4,dr3,r7,r8,r9,delta,delt
      double precision tau3,tau5,r3,r4,r5,r6,r10,r11,tau
      common bi,g1,g2,g34,g45,g57,g37,g67,beta,alpha3,alpha4,alpha5
      common a62,a63,a64,a65,a40,rno,rne,P,Q,R,S,T,b3
      common U,V,W,A,B,C,alpha6,tau3,tau5,tau
      r66=r6
      r55=r5
      r44=r4
      r33=r3
      DELTA=1.D-12
      do 1 I=1,10000
      dr6=(alpha6*rno*rne-(g67*rne+a62+a63+a64+a65)*r66+
     1    bi*(r55-g1/g2*r66))*delta
      dr5=(alpha5*rno*rne+a65*r66+g45*r44*rne-tau5*r55+tau*(r5-r55)
     1       -g57*rne*r55-beta*r55**2d0-bi*(r55-g1/g2*r66))*delta
      dr4=((alpha4*rno+g34*r33-g45*r44)*rne+a64*r66-a40*r44)*delta
      dr3=((alpha3*rno-(g34+g37)*r33)*rne+a63*r66-tau3*r33
     1   +tau3*(r3-r33))*delta
      r66=r66+dr6
      r55=r55+dr5
      r44=r44+dr4
      r33=r33+dr3
    1 continue
      delt=1.d-8
      r77=rne*(g37*(r33+r44+r55)+g67*r66)+beta*r55**2.d0+b3*r33**2.d0
      write(1,300)delt,r66,r55,r44,r33,r77
      delta=1.d-11
      do 2 J=1,4
      do 3 K=1,90
      do 4 L=1,100
      dr6=(alpha6*rno*rne-(g67*rne+a62+a63+a64+a65)*r66+
     1    bi*(r55-g1/g2*r66))*delta
      dr5=(alpha5*rno*rne+a65*r66+g45*r44*rne-tau5*r55+tau*(r5-r55)
     1       -g57*rne*r55-beta*r55**2d0-bi*(r55-g1/g2*r66))*delta
      dr4=((alpha4*rno+g34*r33-g45*r44)*rne+a64*r66-a40*r44)*delta
      dr3=((alpha3*rno-(g34+g37)*r33)*rne+a63*r66-tau3*r33
     1   +tau3*(r3-r33))*delta
      r66=r66+dr6
      r55=r55+dr5
      r44=r44+dr4
      r33=r33+dr3
    4 continue
      delt=delt+delta*100.
      r77=rne*(g37*(r33+r44+r55)+g67*r66)+beta*r55**2.d0+b3*r33**2.d0
      write(1,300)delt,r66,r55,r44,r33,r77
    3 continue
      delta=delta*10.
    2 continue
```

```
      delta=delta/10.
      do 5 M=1,90
      do 6 N=1,1000
      dr6=(alpha6*rno*rne-(g67*rne+a62+a63+a64+a65)*r66+
     1    bi*(r55-g1/g2*r66))*delta
      dr5=(alpha5*rno*rne+a65*r66+g45*r44*rne-tau5*r55+tau*(r5-r55)
     1       -g57*rne*r55-beta*r55**2d0-bi*(r55-g1/g2*r66))*delta
      dr4=((alpha4*rno+g34*r33-g45*r44)*rne+a64*r66-a40*r44)*delta
      dr3=((alpha3*rno-(g34+g37)*r33)*rne+a63*r66-tau3*r33
     1   +tau3*(r3-r33))*delta
      r66=r66+dr6
      r55=r55+dr5
      r44=r44+dr4
      r33=r33+dr3
    6 continue
      delt=delt+delta*1000.
      r77=rne*(g37*(r33+r44+r55)+g67*r66)+beta*r55**2.d0+b3*r33**2.d0
      write(1,300)delt,r66,r55,r44,r33,r77
    5 continue
  300 format(6 e15.6)
      end
$
```